Chair of Physical Metallurgy and Metallic Materials

Doctoral Thesis

Temperature effect during mechanical alloying on the yttria evolution in the processing of an ODS FeCrMnNiCo alloy

Dipl.-Ing. Michael Mayer, BSc

October 2022

AFFIDAVIT

I declare on oath that I wrote this thesis independently, did not use other than the specified sources and aids, and did not otherwise use any unauthorized aids.

I declare that I have read, understood, and complied with the guidelines of the senate of the Montanuniversität Leoben for "Good Scientific Practice".

Furthermore, I declare that the electronic and printed version of the submitted thesis are identical, both, formally and with regard to content.

Date 11.10.2022

Signature Author
Michael Mayer

Preface

The current work is submitted for the purpose of obtaining the degree "Doktor der montanistischen Wissenschaften" at the "Montanuniversität Leoben" and was supervised by ao. Univ. Prof. DI Dr. mont. Reinhold Ebner and Univ. Prof. DI Dr. techn. Martin Stockinger. The project was realized in the time between November 2018 and April 2022.

Acknowledgment

Abstract

In order to improve the efficiency of thermodynamic processes, higher operation temperatures are required, which, however, are mainly limited by the maximum application temperature of the nowadays-used materials. The most effective strengthening mechanism for metal alloys at elevated temperatures represents the incorporation of nanometer-sized oxides, also known as oxide-dispersion-strengthening. Nevertheless, the production of this alloy class via mechanical alloying is still time-consuming and therefore, expensive, limiting the economic feasibility. In this context, this thesis investigates the effect of cryogenic mechanical alloying as a possible means to improve the efficiency of mechanical alloying and gives insights into the mechanism of mechanical alloying of an fcc FeCrMnNiCo oxide-dispersion strengthened alloy.

Pre-alloyed gas-atomized FeCrMnNiCo powders were milled with 1 m.% Y_2O_3 using a novel cryogenic milling setup and the powders were analyzed using state-of-the-art methods including high-resolution scanning electron microscopy, high-energy X-ray diffraction, transmission electron microscopy, atom probe tomography and positron annihilation spectroscopy. The powders were consolidated via spark plasma sintering and inductive heating within the synchrotron beamline in order to analyze the oxide-precipitation and defect evolution during consolidation ex-situ and in-situ.

Cryogenic mechanical alloying was found to increase defect densities of the fcc FeCrMnNiCo matrix and is suggested to improve the refinement of yttria during mechanical alloying and thus increases the milling efficiency towards shorter milling times. Furthermore, the refinement of yttria is assumed to occur in two different size ranges of yttria, with 10 nm as the transition, while in both ranges, cryomilling reduces the size of yttria. Investigation regarding crystal structure identified yttria larger 10 nm as crushed remnants of the initial yttria, whereas independent of the milling temperature, approximately two-thirds of the added yttria is smaller than 10 nm and postulated to be dissolved into the matrix forming nanoclusters. The formation and stability of these nanoclusters were further suggested to be strongly

related to vacancies, and thus, increased vacancy densities within the cryomilled sample suggest smaller and more stable nanoclusters after milling at cryogenic temperatures. These more stable nanoclusters are proposed to cause a later precipitation of Y and O during heating which further results in a higher fraction of $YCrO_3$ within the cryomilled sample, whereas after room temperature milling, mostly Y_2O_3 formed. It is further suggested that the proposed increased cluster stability retains the, in defects stored, internal energy towards a higher temperature during heating promoting abnormal grain growth in the cryomilled specimen, whereas this effect was not observed in the room temperature milled specimen.

Kurzzusammenfassung

Um die Effizienz der thermodynamischen Prozesse zu verbessern, sind höhere Betriebstemperaturen erforderlich, die jedoch hauptsächlich durch die maximale Anwendungstemperatur der heute verwendeten Werkstoffe begrenzt sind. Der effektivste Verfestigungsmechanismus für Metalllegierungen bei erhöhten Temperaturen stellt die Einbringung von nanometergroßen Oxiden dar, auch bekannt als Oxid-Dispersions-Verstärkung. Die Herstellung dieser Legierungsklasse durch mechanisches Legieren ist jedoch nach wie vor zeitaufwendig und damit teuer, was die wirtschaftliche Rentabilität einschränkt. Aus diesem Grund wird in dieser Arbeit die Wirkung des kryogenen mechanischen Legierens als mögliche Verbesserung der Effizienz des mechanischen Legierens untersucht und ein Einblick in den Mechanismus des mechanischen Legierens einer fcc FeCrMnNiCo oxiddispersionsverfestigten Legierung gegeben.

Vorlegierte, gasverdüste FeCrMnNiCo-Pulver wurden mit 1 m.% Y_2O_3 in einer neuartigen kryogenen Mahlanlage gemahlen und mit modernsten Methoden wie hochauflösender Rasterelektronenmikroskopie, hochenergetischer Röntgenbeugung, Transmissionselektronenmikroskopie, Atomsondentomographie und Positronen-Annihilationsspektroskopie analysiert. Die Pulver wurden mittels Spark Plasma Sintering und induktiver Erwärmung innerhalb der Synchrotron-Beamline verfestigt, um die Oxidausscheidung und Defektentwicklung während der Verfestigung ex-situ und in-situ zu analysieren.

Es wurde festgestellt, dass kryogenes mechanisches Legieren die Defektdichte der fcc FeCrMnNiCo-Matrix erhöht. Es wird vermutet, dass es die Verfeinerung von Yttriumoxid während des mechanischen Legierens verbessert und somit die Mahleffizienz in Richtung kürzerer Mahlzeiten erhöht. Darüber hinaus wird angenommen, dass die Verfeinerung von Yttriumoxid in zwei verschiedenen Größenbereichen von Yttriumoxid stattfindet, wobei 10 nm der Übergang ist, während in beiden Bereichen das Kryomahlen die Größe von Yttriumoxid reduziert. Bei der Untersuchung der Kristallstruktur wurde Yttriumoxid mit einer Größe von mehr als 10 nm als zerkleinerte Reste des ursprünglichen Yttriumoxids identifiziert, während unabhängig von der

Mahltemperatur etwa zwei Drittel des hinzugefügten Yttriumoxids kleiner als 10 nm sind und in der Matrix gelöst werden und Nanocluster bilden. Die Bildung und Stabilität dieser Nanocluster hängt vermutlich eng mit den Leerstellen zusammen, so dass eine höhere Leerstellendichte in der kryomillierten Probe auf kleinere und stabilere Nanocluster nach dem Mahlen bei kryogenen Temperaturen schließen lässt. Es wird angenommen, dass diese stabileren Nanocluster eine spätere Ausscheidung von Y und O während des Erhitzens bewirken, was wiederum zu einem höheren Anteil an $YCrO_3$ in der kryogemahlenen Probe führt, während sich nach dem Mahlen bei Raumtemperatur hauptsächlich Y_2O_3 gebildet hat. Es wird ferner angenommen, dass die vorgeschlagene erhöhte Stabilität der Cluster die in den Defekten gespeicherte innere Energie während des Erhitzens erst bei einer höheren Temperatur freigibt, was ein abnormales Kornwachstum in der kryogefrorenen Probe zur Folge hat. Dieser Effekt wurde bei der bei Raumtemperatur gemahlenen Probe nicht beobachtet.

List of abbreviations

APT   Atom probe tomography

bcc   Body centered cubic

BSE   Backscatter electron

CT   Cryogenic temperature

EDS   Energy dispersive spectrometry

fcc   Face centered cubic

FWHM   Full-Width-Half-Maximum

HEA   High entropy alloy

HR-TEM   High-resolution transmission electron microscope

MA   Mechanical alloying

ODS   Oxide dispersion strengthening

PALS   Positron annihilation lifetime spectroscopy

PAS-DB   Positron annihilation spectroscopy Doppler broadening

RT   Room temperature

SE   Secondary electron

SEM   Scanning electron microscope

SFP   Stacking fault probability

SPS   Spark plasma sintering

TEM   Transmission electron microscope

Table of content

1 Introduction and motivation

Since the very beginning of humanity, the history of humans has been tightly connected with the discovery of new materials. Some chapters in history are even named after these materials, such as the Bronze Age or Iron Age, emphasizing the importance of these newly discovered materials for the evolution of humanity [1]. Nevertheless, even in modern ages, materials are one of the driving forces of innovations and key to tackling challenges modern societies face. The most recent of these challenges is undoubtedly global warming or climate change demanding new technologies for reduced CO_2 emissions. Besides new energy sources – i.e. energy transition – a key role is devoted to increasing the efficiency of existing processes to cut down CO_2 emissions. For example, according to the International Council on Clean Transportation (ICCT) [2], air travel produces approximately 3% of the global CO_2 emissions and is among the fastest-growing sources of greenhouse gases. Alternative energy sources are under development, but conventional jet turbines will play a major role also in the following decades, especially for intercontinental flights. Although the global pandemic caused by COVID-19 decreased air traffic, the number of flights is expected to rise again, even above the pre-pandemic level [3]. Therefore, in order to make air travel environmentally friendlier by decreasing CO_2 emissions, the efficiency of jet engines is in focus to be increased.

Generally, the efficiency of thermodynamic processes, present in, e.g. jet engines and power plants, is increased with higher operation temperatures [4]. However, these operation temperatures are exceptionally limited by the used materials, and therefore, materials sustaining higher loads at elevated and high temperatures could reduce CO_2 emissions significantly. Nowadays, used Ni-based superalloys have already reached their application limit and require therefore enhanced cooling solutions to increase the operating temperature and, consequently, the efficiency of the turbine further [5,6]. However, even though these cooling solutions increase the overall efficiency, they also cause inefficiency losses decreasing the potentially reachable efficiency [4,7]. Figure 1 presents the ideal theoretical performance of a jet engine as a function of the turbine inlet temperature. At higher temperatures,

the inefficiency losses due to cooling of the blades increase and thus, the overall potential cannot be fully utilized. Therefore, new classes of materials are in focus of research over the last decades to be applied at higher temperatures than nowadays used Ni-based alloys.
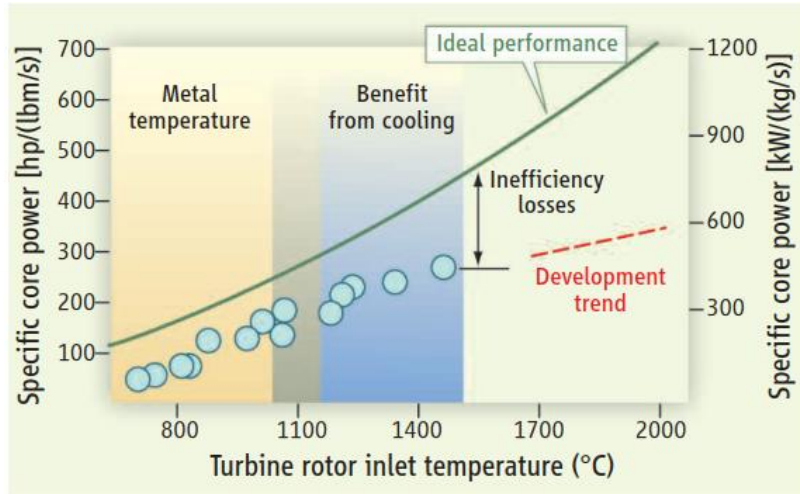
Figure 1: Inefficiency loss due to cooling of the blades of Ni-based superalloys [4].

Among the most promising candidates for future advanced high-temperature materials are the new class of high entropy alloys. In history so far, alloy design was based on one main element alloyed with other elements to increase its performance – i.e. steel, Ni-based alloys and aluminum alloys. Conversely, high entropy alloys consist of five or more elements with relatively equal concentrations. This novel alloy design has caught increased attention as, in many cases, it exhibits a single-phase solid solution with good ductility [8,9]. Among the first high entropy alloys and the most known representative of this class, is the FeCrMnNiCo alloy. This so-called Cantor alloy, named after its developer, forms a single-phase cubic face-centered structure [10] and is reported to have a low diffusivity qualifying it for applications that require creep resistance [8]. However, this alloy lacks the strength at high temperatures to be a competitive replacement for Ni-based superalloys and consequently, additional strengthening is required.

There are several strengthening mechanisms in metallic alloys, but oxide-dispersion strengthening (ODS) is the most effective at high temperatures [11]. This mechanism relies on the incorporation of small but highly stable oxide particles, mostly yttria, that effectively impede

the motion of dislocations at temperatures even above 1000°C [12]. However, these highly stable oxides are immiscible in the matrix, which means in turn that this strengthening mechanism cannot be produced via melting metallurgy but requires powder metallurgy. Therefore, oxide-dispersion strengthened materials are produced via mechanical alloying of a matrix powder with minor additions of oxide particles, typically between 0.5 and 1.5 m.% of oxides. However, this process is time-consuming and consequently expensive limiting the potential of this strengthening mechanism [13].

In this context, this work aims to improve the efficiency of mechanical alloying of an ODS-HEA by investigating the process as well as to get an in-depth understanding of the governing mechanisms of incorporating yttria into the fcc FeCrMnNiCo matrix. Low deformation temperatures are reported to increase the defect density of this alloy [14], which is suggested to foster the dissolution of yttria [15]. Furthermore, a detailed understanding of the mechanisms during mechanical alloying allows further improvements in the process as well as alloy design. Another important part of the process chain, the precipitation during the subsequent consolidation, is examined in order to expand knowledge on the production of high-entropy alloys for high-temperature applications.

2 State of the art

The purpose of this chapter is to provide the reader with a comprehensive overview of the main topics covered in the thesis in order to provide a better understanding of the subjects being discussed. Described topics include an overview of high-entropy alloys (HEA), which was the matrix alloying system used in this thesis, as well as the material strengthening concept of oxide dispersion strengthening (ODS) which was used as a high-temperature strengthening mechanism. Furthermore, focus is laid on the manufacturing process of mechanical alloying, as it is essential in the processing of ODS-materials and plays a dominant role in this thesis.

2.1 High entropy alloys

Conversely to classic alloy design with a basis material and additional alloying elements, high entropy alloys are defined as alloys consisting of five or more elements with concentrations between 5 and 35 atomic percent while exhibiting a single-phase microstructure. The name originates from the first idea that the high mixing entropy stabilizes the single-phase solid solution, also known as the high entropy effect [8,10]. However, nowadays it is assumed that the increased entropy reduces the number of arising phases, but other effects such as short-range ordering play a much more critical role in stabilizing the single-phase solid solution [9,16].

Another proposed core effect of high entropy alloys, which is especially important for applications at high temperatures, is the so-called sluggish diffusion effect [8]. It is expected that in high entropy alloys, neighboring atoms are different, and as a result, the local atomic configuration consists of low-energy sites and high-energy sites for diffusing atoms. If atoms move to a low-energy site, they become trapped and diffusion is slowed down [8]. However, other studies report contradictory results as no significant change in the diffusion coefficient compared to the elemental metals is found when the data is normalized at T_m [16].

2.1.1 Cantor Alloy (FeCrMnNiCo)

The most known representative of this new class of materials is the equiatomic $Fe_{20}Cr_{20}Mn_{20}Ni_{20}Co_{20}$ [at.%] or so-called Cantor alloy, named after it's discoverer [10].

<u>Microstructure and phase stability of the FeCrMnNiCo alloy:</u>

The Cantor alloy is reported to solidify dendritically but forms a face-centered cubic (fcc) single-phase solid solution upon homogenization which was taken as proof that this is the stable state [17,18]. This unexpected single-phase fcc microstructure has caught significant attention to investigate the stability of this phase. In this context, Laurent et al. [18] showed that slow cooling leads to a dendritic solidification structure as shown in the Fe X-ray map in Figure 2a where the color scale indicates the intensity of Fe. The dendrites are reported to be enriched in Fe, Cr and Co while the inner-dendritic area is enriched in Ni and Mn. Subsequent annealing at 1100°C for 6h homogenizes the morphology as depicted in Figure 2b with no areas with increased Fe content (red areas) and was seen as a proof that this is the stable state of the alloy even at room temperature [18].
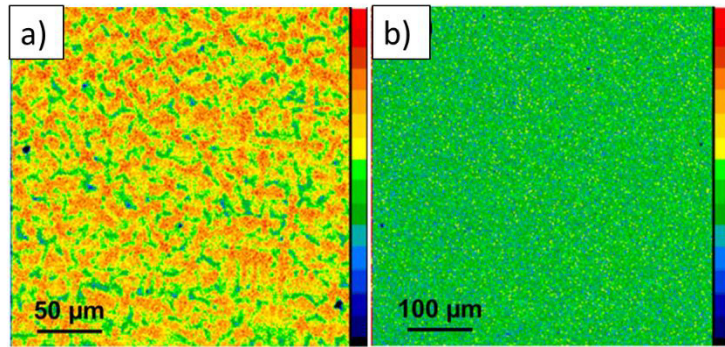
Figure 2: Fe X-ray maps of the FeCrMnNiCo alloy at different production states obtained by Electron-Probe-Micro-Analysis indicating the dendritic structure after slow cooling and the effect of homogenization: a) induction melted, b) subsequent annealing for 6h at 1100°C [18].

Opposing the theory that the Cantor alloy's stable state is the single-phase solid solution, some studies showed that upon annealing at elevated temperatures up to 500 days [19,20] or in highly deformed

materials, such as mechanical alloyed materials, even after annealing for 5 min at 450°C, precipitations are formed [21]. In high pressure torsion deformed materials, Schuh et al. [21] observed that Mn and Cr primarily segregate due to their low diffusion coefficient and form a NiMn-phase and σ-phases or $Cr_{23}C_6$ when C is present as an impurity. With longer annealing times, also Fe- and Co-rich phases precipitate in his severely deformed samples as shown in Figure 3.
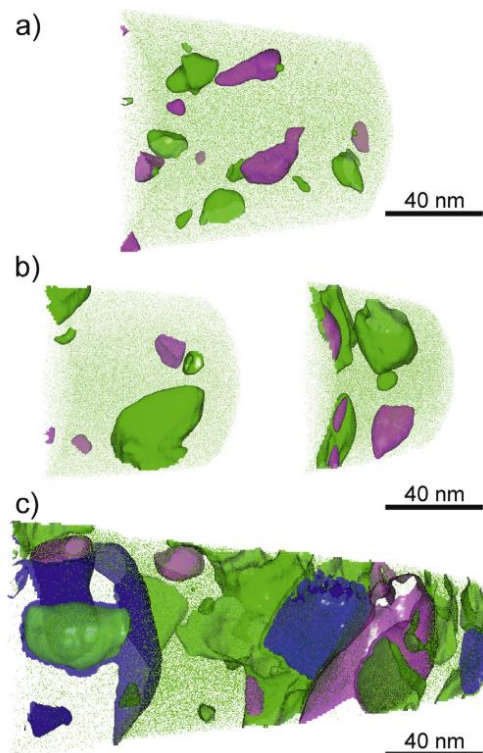
Figure 3: Precipitates formed in the FeCrMnNiCo alloy after annealing for a) 5 min, b) and c) 15h at 450°C. Green areas are enriched with Ni and Mn, purple areas with Cr and blue areas with Co [21].

On the other hand, heat treatments above approximately 800°C do not form precipitates even at annealing times of 500 days and previously formed precipitates dissolve back into the matrix, indicating that the fcc microstructure of the FeCrMnNiCo alloy is stable above 800°C [20,21]. Based on these observations, Otto et al. [20] proposed a schematic time-temperature-transformation (TTT) diagram for this alloy's phase stability, which is presented in Figure 4.
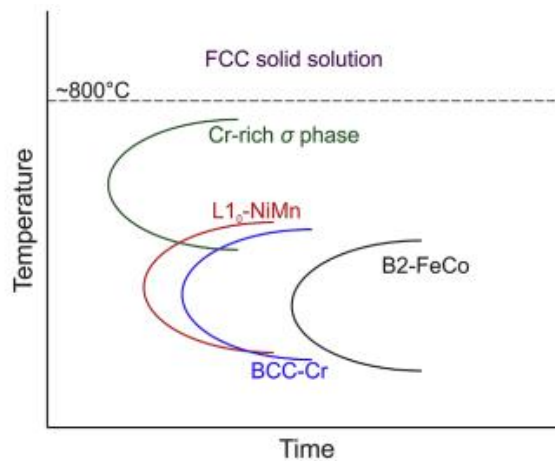
These results show that the FeCrMnNiCo single-phase solid solution is stable above 800°C but forms various phases below this temperature as the diffusion-assisted process is significantly faster for severely deformed samples [20,21]. These findings concerning the phase instability below 800°C significantly affected the investigations in this thesis as heating and, more importantly, cooling was conducted at fast rates to avoid precipitation of second phases. For mechanically alloyed powders, this is of upmost importance as these highly deformed materials are expected to accelerate phase precipitation.

Mechanical properties of the FeCrMnNiCo alloy:

Mechanical alloying represents continuous deformation of the used powders which further means that the process strongly relates to their mechanical properties. Therefore, the following chapter gives a brief overview of the state-of-the-art of mechanical properties of the FeCrMnNiCo alloy used in this thesis.

The mechanical properties of the FeCrMnNiCo alloy are reported to be strongly temperature-dependent [22–24], as depicted by representative stress-strain curves in Figure 5 from 77 K to 1073 K testing temperatures. Even at a testing temperature of 1073 K, the alloy exhibits lower ductility than the specimen at 77 K. Therefore, low deformation temperatures increase strength and elongation to fracture compared to room temperature tensile tests.
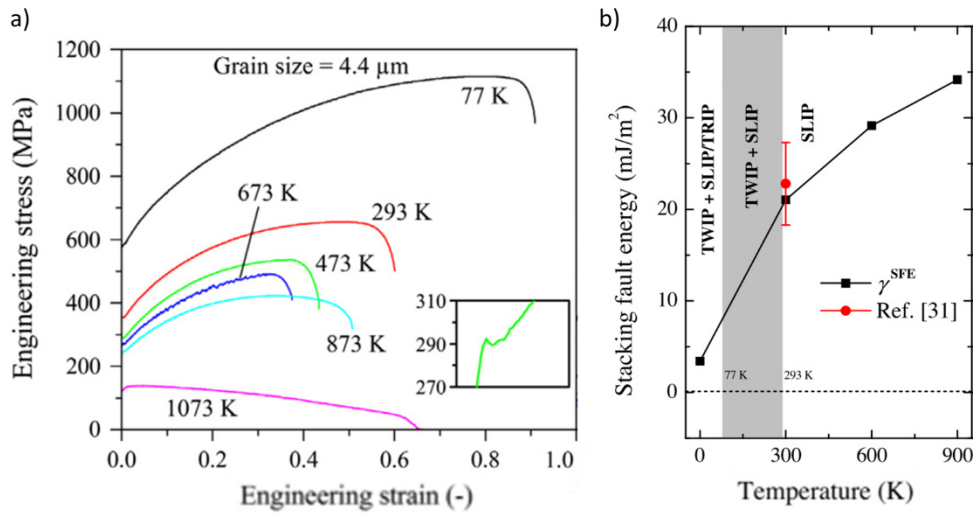
Figure 5: a) Temperature-dependent stress-strain chart of the FeCrMnNiCo alloy
(Cantor alloy) exhibiting improved mechanical properties at low temperatures [22].
b) Calculated temperature-dependent stacking fault energy showing a transition to twinning
deformation below room temperature [25].

The increased strength and elongation to fracture is reported to be a consequence of this alloy's low and temperature-dependent stacking fault energy [25,26] as it influences the transition from dislocation slip to twinning deformation. The SFE describes the energy needed to introduce a stacking fault, i.e. to change the stacking sequence of one atomic plane. For the FeCrMnNiCo alloy, the SFE has been measured and calculated as 21 mJ/m² at RT, a low value compared to steels [25]. According to Huang et. al using ab-initio calculations, which results are presented in Figure 5, twinning as a new deformation mechanism increasingly develops as the temperature is lowered below RT and the SFE decreases [25,27]. This results in an increased formation of mechanically activated twins and thus, increased strain hardening at low temperatures while at elevated temperatures, dislocation slip is dominant but strongly localized within a limited set of {111} planes [22].

8
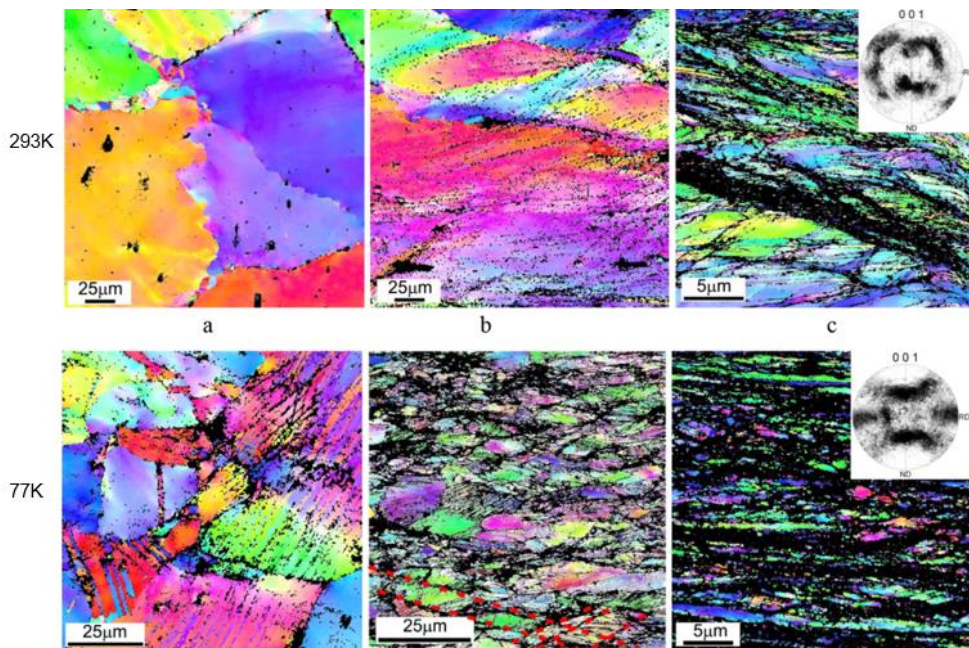
Figure 6: Different degrees of deformation during rolling of the Cantor alloy at room temperature (293 K) and at cryogenic conditions (77 K) indicating increased twinning activity at 77K. a) 15%, b) 40% and c) 80% thickness reduction [14].

The influence of cryogenic deformation temperatures of the FeCrMnNiCo alloy was further studied by Stepanov et al. [14] who used TEM investigations at RT- and cryo-rolled specimen observing a higher fraction of twinned grains but lower dislocation densities. EBSD images of his specimen are presented in Figure 6, depicting more twins in the cryo-deformed sample at the same thickness reduction. This indicates that twinning is easier activated at 77 K, while higher strains are needed to activate twinning deformation at 293 K [14]. Therefore, this low and temperature dependent SFE strongly influences the mechanical properties of the FeCrMnNiCo alloy and significantly affects the milling behavior at RT and cryogenic temperatures, which is further described in chapter 2.3.3.

2.2 Oxide dispersion strengthening

In order to obtain improved high-temperature mechanical properties of the Cantor alloy such as increased strength and creep resistance, additional strengthening is necessary. Among several strengthening mechanisms available for metallic alloys, the strengthening of materials with the incorporation of highly stable and small particles is the most effective at high temperatures. This so-called oxide-dispersion strengthening is based on the hindering of dislocation motion upon plastic deformation. The effectiveness of this mechanism depends on the size and number density as well as on the coherency and thermal stability of these particles [11,12].

While coherent precipitates can be less effective at higher temperatures, the small and incoherent dispersions in ODS alloys are reported to impede dislocations' motion [11,12]. Arzt [12] proposed that this phenomenon is based on the so-called pinning effect of the incoherent interface after a dislocation passed the dispersoid via climbing. Therefore, dislocations are observed to stick to the particle after passing it, which is presented in Figure 7.
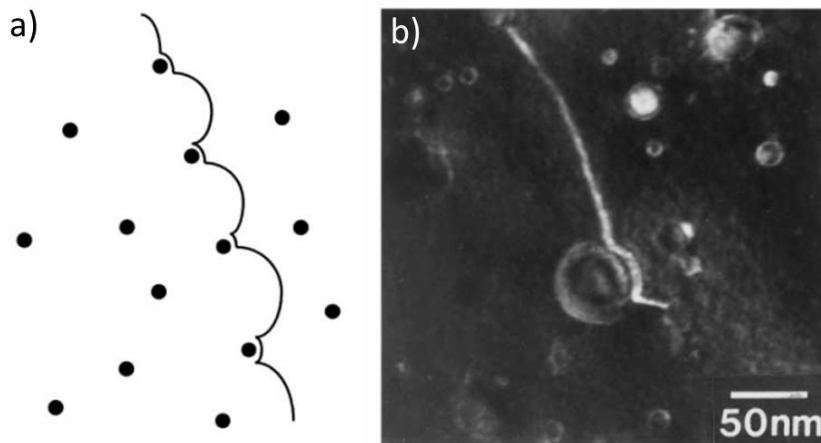
Figure 7: a) Schematic illustration of the attractive pinning force of dispersoids onto a dislocation [12]. b) TEM picture showing this pinning effect [12].

According to Arzt [12], this effect is attributed to the partial relaxation of the dislocation strain field by diffusion on the dispersoid-matrix interface. As a result, the particles exert an attractive force on the dislocation forcing it to bow out, as presented in Figure 7a as a

10

schematic image and observed via TEM in Figure 7b [12]. This mechanism provided improved high temperature strength and creep resistance and was mostly applied for steels [28–30].

However, some works already focused on adding yttria to form oxide dispersion strengthened high-entropy alloys via mechanical alloying at room temperature [31–33]. The results of Hadraba et al. [31] presented in Figure 8 suggest improved tensile properties at RT and at 800°C as a result of the addition of yttria to an FeCrMnNiCo alloy. In his study, the addition of 0.3 m.% of yttria increased the strength by about 70 % at 800°C. Focusing on compressive creep, Dobeš et al. [33] observed a reduction of the creep rate by more than two orders of magnitude in the investigated range from 973 K to 1073 K in his ODS-FeCrMnNiCo alloy.
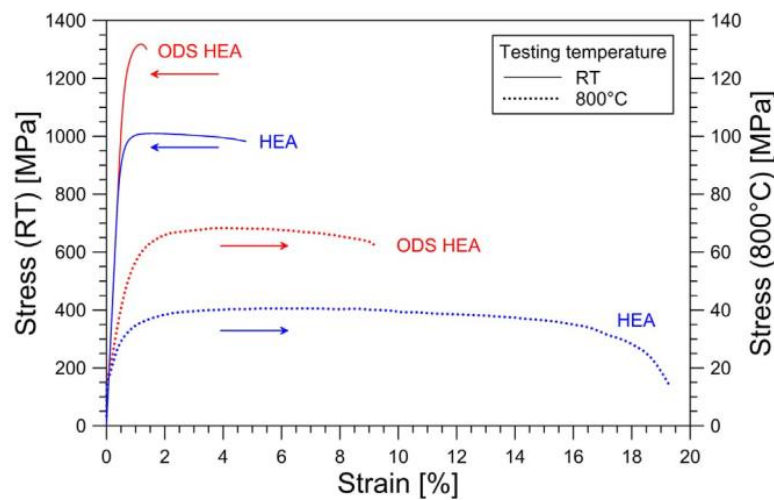
Figure 8: Stress-strain curve of a Cantor alloy with and without oxide dispersions tested at RT and at 800°C [31].

Gwalani et al. [32] used a Cantor alloy with minor additions of Al and compared different yttria contents and the influence of consolidation parameters on the yield strength at room temperature. The results show an increase in the RT yield strength by adding yttria as well as by lowering the grain size with different consolidation parameters. The authors further concluded that the amount of added yttria has just a minor effect on the yield strength at room temperature. These studies indicate the potential of oxide dispersion strengthening as high-temperature strengthening mechanism in high entropy alloys.

11
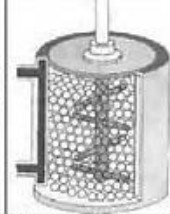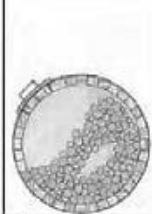
2.3 Mechanical alloying of ODS powders

As a result of the high stability and immiscibility of the incorporated oxides, the production of ODS powders needs to be accomplished via mechanical alloying. The elemental or pre-alloyed matrix powders are milled together with oxide particles such as yttria to produce composite powders via severe plastic deformation [13]. After mechanical alloying, the milled powders are densified, or so-called consolidated, which is described in detail in chapter 2.4.

Raw powders → Mechanical alloying → Consolidating → Final product

Figure 9: Schematic illustration of the process route for the production of ODS-materials via mechanical alloying.

For mechanical alloying, several types of mills are available, differentiating in how they facilitate powders and grinding media movement. Figure 10 shows a brief overview of available systems from which, the attritor ball mill, considered a high-energy ball mill, will be explained in detail as this type is used in this thesis.

Device	Simoloyer®	Planetary Ball Mill	Attritor®	Drum (ball) mill
Maximum diameter [m]	0.9	0.2	1	3
Maximum total volume [l]	400	8	1000	20000
Maximum relative velocity [m/s]	14	5	4.5 - 5.1	< 5
Graphic (cross section)				

Simoloyer® is a brand of Zoz GmbH, Germany; Attritor® is a brand of Union Process, USA;

Figure 10: Overview of typical ball mills used for mechanical alloying and their size parameters [13].

A schematic of an attritor ball mill is shown in Figure 11a consisting of a container filled with the powder and grinding media – typically

balls – and a rotational shaft with pins. Upon rotating, the pins stir the grinding media and the powders, resulting in frequent collisions of the grinding media with trapped powder particles in-between as illustrated in Figure 11b [13]. Compared to the traditional melting metallurgy, mechanical alloying is an entirely solid state process where alloying occurs by repeated deformation of powder particles that are trapped between the grinding media [13].
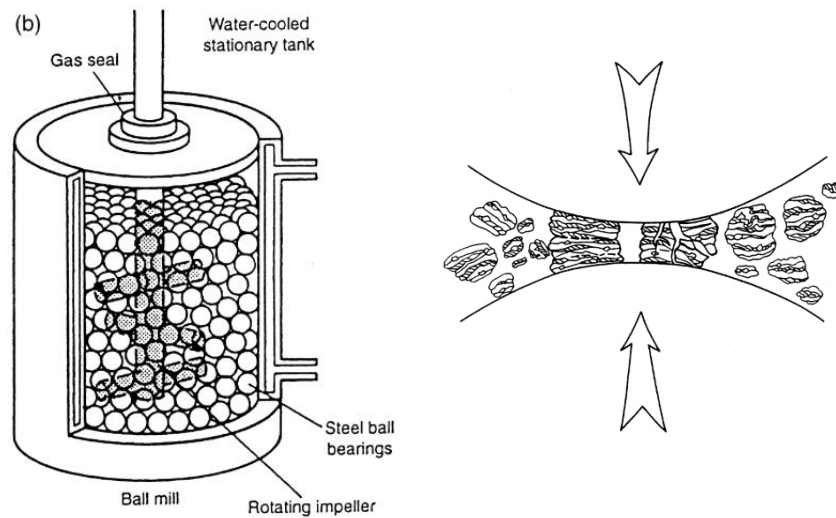
Figure 11: a) Illustration of an Attritor ball mill [13]. *b) Schematic picture of trapped metal powder between two grinding balls during mechanical alloying* [13].

These collision events are the basic principle of mechanical alloying upon which, repeated cold welding and fracturing of the in-between trapped powder particles occurs. With this rapid energizing by severe plastic deformation and subsequent quenching, alloying of the particles takes place. Furthermore, oxide particles get refined and homogeneously distributed, and high densities of lattice defects such as dislocations, nanograins and vacancies [13,34–37] are introduced. A typical plot of crystallite size and lattice strain, two specific indicators for lattice defects, vs. milling time during room temperature milling, is shown in Figure 12b. By this plot, an increase of the lattice strain and a decrease of the crystallite size as a function of milling time especially during the first hours of milling is reported.
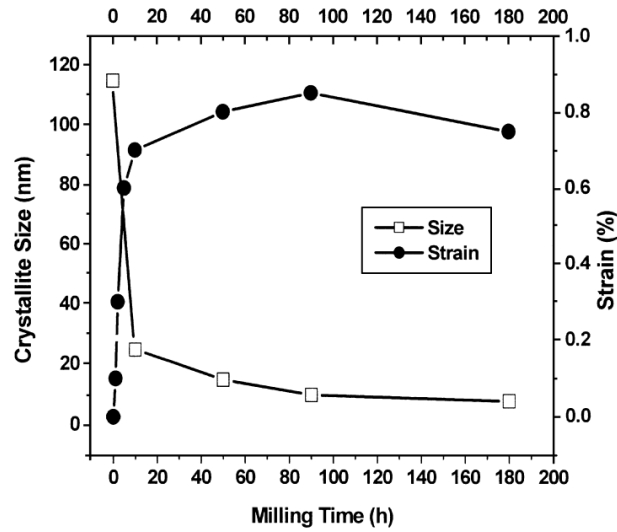
Figure 12: Plot of crystallite size and lattice strain vs. milling time during room temperature milling of Mo [38].

Concerning the mechanism of mechanical alloying, based on the involved materials, the process can be classified into three different milling systems [13]:

- Ductile with ductile
- Ductile with brittle
- Brittle with brittle

Typically, ODS materials represent the ductile-brittle system with a ductile metal powder as a matrix component and the brittle oxide powder.

2.3.1   Stages of mechanical alloying

According to Surayanana [13], the whole process can be described in three subsequent stages.

First stage:

The softer powder is flattened, and a lamellae structure develops. Hard particles such as oxides decrease in size and get trapped between the lamellae interfaces, as shown in Figure 13a [13].

14

<u>Second stage:</u>

Cold-welding, fracturing and refinement of the powder size dominate in this stage. Also, the microstructure gets finer, and defects such as grain boundaries, dislocations and vacancies increase significantly while oxide dispersions become more uniform, as presented in Figure 13b [13].
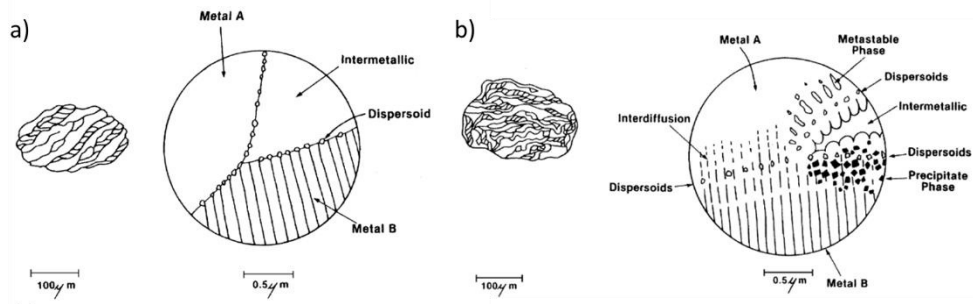
Figure 13: a) The first stage of mechanical alloying indicates a lamellae structure with oxide particles at the interfaces. b) The second stage of mechanical alloying schematically shows finer lamellae structure and increased defect densities [13].

<u>Third and final stage:</u>

True mechanical alloying occurs in this stage by forming a solid solution. For this process, different theories exist to better describe different powder combinations. The model of R.B. Schwarz [39] relies on a high number of dislocations acting as diffusion paths for forming a solid solution. Figure 14 shows the model in three subsequent stages. In the first stage presented in Figure 14a, a clean interface between particle A and particle B develops and dislocations pile-up at the interface. During the subsequent stage depicted in Figure 14b, atoms from particle B diffuse into particle A via pipe diffusion in the dislocation paths. They furthermore pin the dislocations allowing more atoms to diffuse into particle B [39]. If the force of the ball-ball collisions exceed the pinning force of the solutes, the dislocations move leaving the diffused atoms as interstitials or substitutionals which is shown in Figure 14c [39].
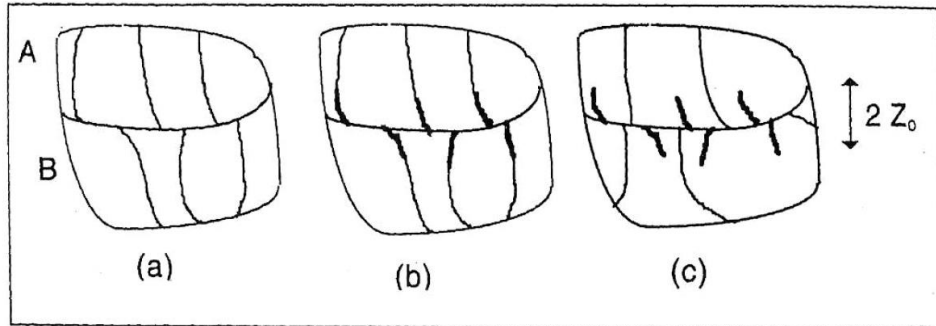
Figure 14: Principle of the diffusive mixing theory of Schwarz for the components A and B [39].

Ashkenazy [40] studied the mixing mechanism of different precipitates in copper using molecular dynamics calculations and agrees with the study of R.B Schwarz for material combinations with the same crystal structure [40]. However, if the precipitates exhibit different crystal structures, i.e. a particle with bcc-structure is embedded in an fcc matrix, the dislocations cannot pass through the matrix-particle interface. As a result, dislocations pile up at the interfaces resulting in high stresses, upon which, the interface relaxes, forming an amorphous shell around the particle. However, the exact mixing or dissolution mechanism is still unclear, but "shuffling" rearrangements of the atoms are proposed to take place [40].

Many previous works focused on a detailed analysis of the mixing behavior of yttria within a metal matrix. Most of the research trying to answer the question of whether yttria dissolves or gets finely dispersed deals with bcc ODS steels, while just few works on fcc alloys were done. Some studies proposed a dissolution at lattice defects where especially vacancies are reported to play a crucial role in the dissolution of yttria [15,41–43]. Using positron annihilation spectroscopy (PAS), Ressel et al. [15] found that the vicinity of vacancies of mechanically alloyed ODS steel powders is enriched with yttria, concluding a dissolution of yttria at vacancies and thermodynamic and first-principle calculations showed that O and Y are strongly attracted by vacancies in bcc steels [15,44–47]. Furthermore, first-principle calculations yielded that O lowers the formation energy of O enriched nanoclusters containing Y and other solutes in close proximity below that of the stable oxide [44]. These findings were confirmed by Xu et

16

al. [43] using PAS and Atom Probe Tomography (APT) as in his samples without vacancies, no nanoclusters were observed while the sample exhibiting high vacancy densities showed small and stable O-enriched nanoclusters.

Another theory concerning the dissolution of yttria by Kimura et al. [48] proposes an amorphous phase around the nanometric crystallites enriched with Y and O, as presented in Figure 15. For this theory, yttria as well as the crystallite size need to be refined to nanometric scale providing a sufficient driving force for the decomposition of yttria into these amorphous areas.

In all of the above described theories, lattice defects are reported to play a crucial role in the refinement and dissolution of yttria during mechanical alloying. In this context, this thesis laid special focus on the investigation of the amount and type of lattice defects in the processing of the used ODS-HEA.
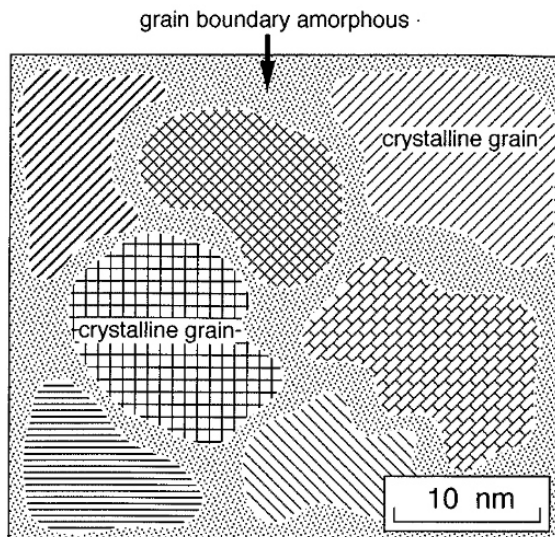
Figure 15: Schematic illustration of the model proposed by Kimura et al. showing the crystallites surrounded by an amorphous phase enriched with Y and O [48].

Contrary to the above-stated publications, Phaniraj [49] concluded that yttria did not dissolve at milling times up to 18 hours for the investigated austenitic steel. His conclusions for adding 5 m.% yttria are based on XRD and XPS, where yttria can still be found in these measurements.

2.3.2 Nanostructured materials

Mechanical alloying, a process of severe plastic deformation, does not only produce metal alloys but also fosters grain refinement down to the nanometric scale [13]. These nanostructured materials exhibit grain sizes of a few nanometers, typically 1-100 nm [13]. As schematically presented in Figure 16, the grain sizes are so small that a significant volume of the microstructure in nanocrystalline materials is composed of interfaces. These interfaces are mainly grain boundaries, which are depicted as white particles in Figure 16. Consequently, nanocrystalline materials exhibit properties that are significantly different from, and often improved over, their conventional coarse-grained polycrystalline counterparts such as

- increased strength and higher hardness
- extremely high diffusion rates and therefore
- reduced sintering times [13,50].
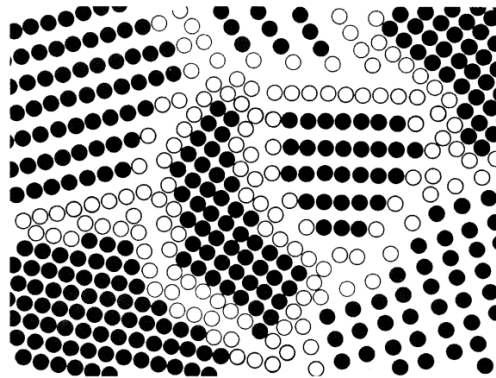
Figure 16: Illustration of nanocrystalline materials showing a high volume fraction of grain boundaries marked in white [13].

A model for the formation of nanocrystalline materials via mechanical alloying is presented in Figure 17 and can be described as follows:

Upon heavy deformation, shear bands form and cause strongly localized deformation resulting in extremely high dislocation densities [50–53]. These dislocations arrange as dislocation cells at a given strain to lower their energy. With further deformation – i.e. milling – these

18

cell walls transform into small-angle boundaries and upon further heavy deformation into high-angle grain boundaries via rotation of the grains [50–52].

High Density Dislocation Cells   Strain-induced High-angle Boundaries
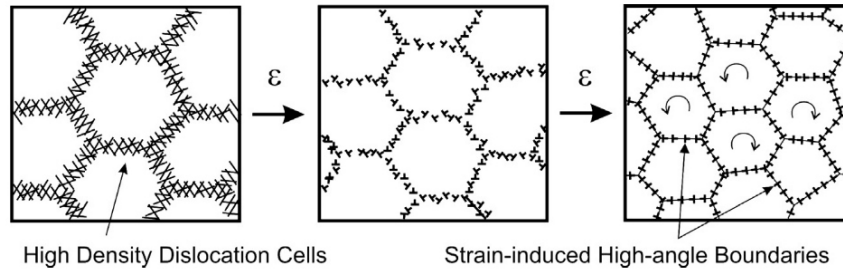
Figure 17: Schematic model of the formation of nanograins during severe plastic deformation [53].

The minimum obtainable grain size can be described as a balance between the defect or dislocation structure and the dislocation annihilation and recombination by thermal processes [51,54]. Mohamed [54] created a theoretical model to predict the minimum grain size obtainable by ball milling as a function of various material parameters. According to his model, the concentration of vacancies is also several orders higher than equilibrium. Dislocations contribute to pipe diffusion while vacancies are utilized to the occurrence of serrated flow resulting from dynamic strain aging. The model fits quite well with experimental data and yields that the minimum grain size is a function of the hardness, the activation energy for recovery, the stacking fault energy and the melting temperature [54]. The latter was already observed elsewhere [51].

At RT and below RT, nanocrystalline materials exhibit improved properties, while at higher temperatures above 0.55 T_m, this advantage dismisses due to a rapid grain coarsening [55]. As a result, after MA, nanostructured composite powders are expected but their improved mechanical properties are not anticipated to prevail after sintering.

2.3.3 Effect of cryomilling on the production of ODS-Alloys

Cryomilling means the milling of powders at temperatures below -150°C [56], however, even though several studies used cryomilling, detailed investigations of the direct effect of cryogenic mechanical alloying are rare. Nevertheless, published articles report of an accelerated refinement of the powder particles which is proposed to be a result of suppressed cold-welding of the powder particles [57]. Furthermore, lower deformation temperature are reported to suppress recovery and recrystallization leading to lower crystallite sizes and increased defect densities after cryogenic mechanical alloying [56,58,59] suggesting reduced milling times necessary to obtain a comparable microstructure [57].

Furthermore, Kim et al. [60] showed through small-angle neutron scattering (SANS) higher number densities of precipitated oxide particles within steels – i.e. smaller particles - after consolidation compared to steels milled at room temperature, suggesting a beneficial effect of low milling temperatures on the production of ODS steels.

Even though milling temperatures of the aggregate are kept at low temperatures, it must be mentioned that locally much higher temperatures appear, which can hardly be estimated. For example, in Ni-based alloys, the global temperatures during room temperature milling range from 100 to 215°C dependent on the cooling solution while locally, during the ball collisions, temperatures of up to 1000°C are estimated [13].

2.4 Consolidation of mechanically alloyed powders

In order to obtain practical components out of the milled powders, powders are compacted to dense materials via a process called consolidation. As shown in Figure 18, the process can be divided into sinter-based approaches by simply heating the powders below the melting temperature, pressure-based approaches with a uniaxial or hydrostatically applied pressure in a step before heating as well as the combination of both – i.e. hybrid densification. Furthermore, different solutions to facilitate heating can be applied such as an external heat

source – i.e. oven – or internal heating by applying as electric current through the powder which is the basis of spark plasma sintering (SPS). In this thesis, powders were consolidated via SPS while for in-situ consolidation investigations, pressureless external heating was applied.
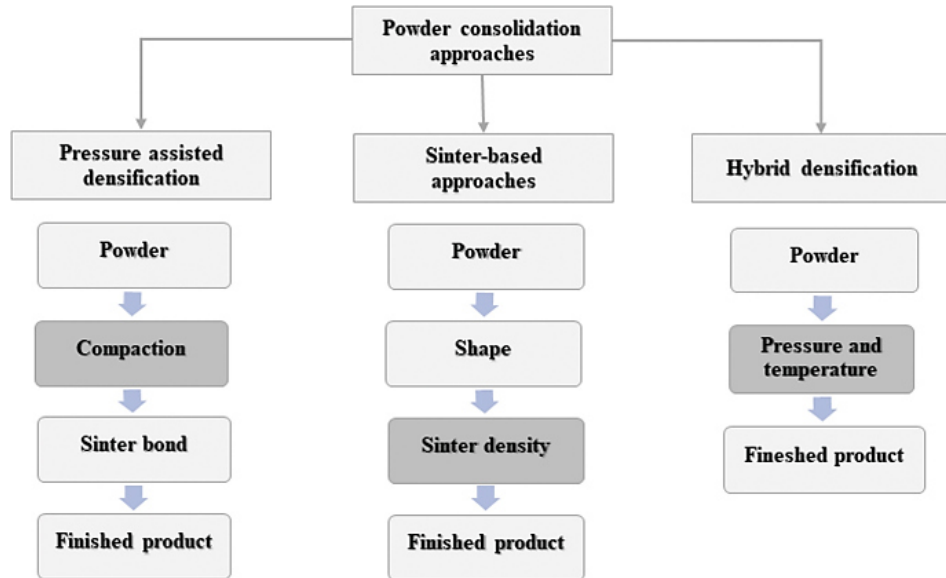
Figure 18: Schematic categorization of different consolidation approaches [61].

Beside the compaction of powders, in oxide dispersion strengthened materials (ODS), the re-precipitation of dissolved oxide particles occurs during consolidation forming the desired small nanometer-sized particles.

2.4.1   Pressureless sintering of powders

During pressureless sintering, powders are heated within a die until the desired density is reached. Heating provokes diffusion processes such as volume, surface and grain boundary diffusion to minimize the surface energy resulting in the formation of necks between the powder particles, which is presented in Figure 19. The occuring diffusion processes strongly depend on the powder material as well as the applied process parameters such as temperature and atmosphere. Regardless the governing sinter processes, upon longer sintering times, the connections between the particles increase, consequently reducing the pores until the driving force for reducing the porosity is too weak. Therefore, the sinter parameters, temperature and duration must be

21

carefully chosen for each powder where particle size and chemistry are among the main influencing parameters [62].
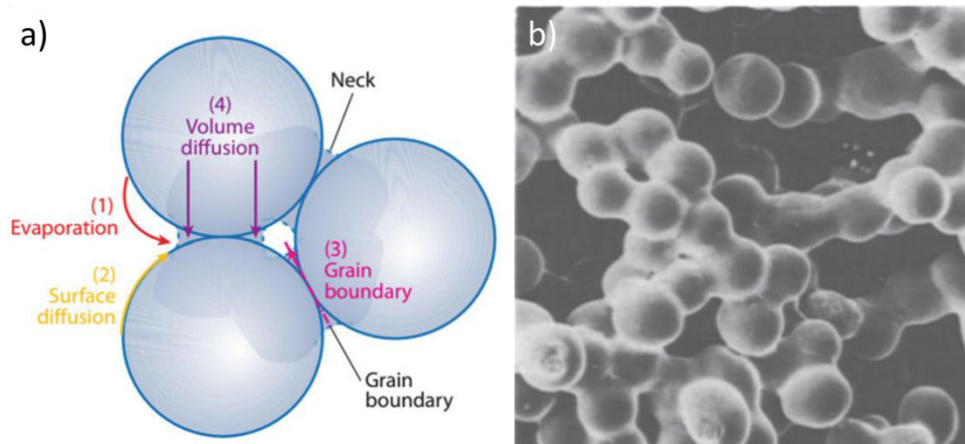
Figure 19: a) Illustration of the involved diffusion processes during sintering [63]. b) SEM image of formed necks during sintering of Cu-powders for 8h at 1300 K [62].

2.4.2　Hybrid densification

On the other hand, hot pressing (HP) also involves pressure during sintering, allowing high sinter densities, especially for powders that are difficult to sinter. Hot pressing might also reduce the necessary sinter temperature and consequently suppresses grain growth. The pressure during hot pressing is usually applied uniaxially, while hot isostatic pressing (HIP) utilizes a hydrostatic pressure [62].

A consolidation process used in this work is called spark plasma sintering (SPS) and will be explained in more detail. This process is similar to hot pressing (HP) but differs in how the heat is transmitted into the sample. For HP, an external heat source heats up the material while at SPS, a pulsed current passes through the sample and the die. Therefore, the powders are heated from the outside and inside which is illustrated in Figure 20. In comparison to HP and other sintering techniques, SPS exhibits higher heating rates and shorter sintering times due to the electric heat transmission into the powders. As a result, the process times are in the range of several minutes while for conventional sintering techniques, several hours are necessary. These short sintering times but also the applied pressure results in retarded

grain growth consequently allowing the production of nanostructured materials [63].
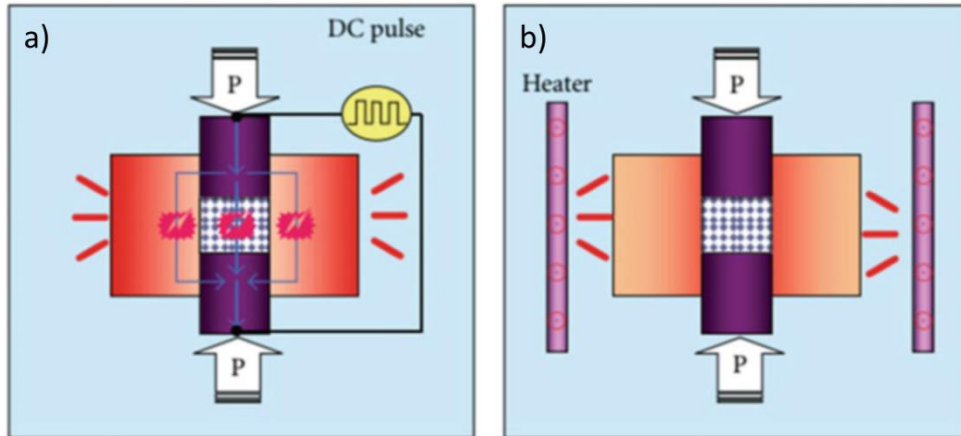
Figure 20: Comparison of a) SPS and b) HP indicating the different ways of heating the sample [63].

It is widely accepted that Joule-heating of the electric current through the powder heats the specimen at a high rate [63]. However, whether discharges in the gaps between the powders occur, causing a spark and a plasma field or not is still under debate [64,65]. Nevertheless, studies reported partially melted areas at the gaps between powders after SPS, which was reportedly not found after HP and HIP using the same parameters, indicating locally very high temperatures and possibly the presence of a spark [65]. However, as yttria is immiscible in the matrix alloy, it is expected to segregate in the melt and appears as large and inhomogeneously distributed oxides in the melted areas after consolidation. Such a result is not desirable due to the loss of the ODS-effect and consequently, a significant reduction of the high temperature mechanical properties has to be expected.

2.4.3   Oxide precipitation during consolidation

After mechanical alloying, a metastable supersaturated solid solution containing Y and O is present in the milled powders, for which heating during consolidation provokes precipitation towards a more stable state [66]. In the case of ODS, this more stable state is the precipitation of yttria but is dependent on the alloy and the available amount of

23

oxygen. Therefore, also other oxides such as complex Y-Ti-O were observed to precipitate [43,67], and, if enough Cr is available, $YCrO_3$ was reported [67–69]. Investigating the sintering temperature dependent oxide precipitation, Zhang et al. conducted SANS measurements after heating ferritic steels finding only Y_2O_3 to precipitate below 1000°C sinter temperature whereas Y_2O_3 along $YCrO_3$ precipitated together above 1000°C as shown in Figure 21a. Kawamura [70] further reported this co-existence of both oxides by investigating the ternary phase diagram of the system Cr-Y-O, which is presented in Figure 21b for 1025°C. Concerning the precipitation and phase stability of these oxides, Chung et. al [68] observed larger $YCrO_3$ at grain boundaries whereas Y_2O_3 formed smaller precipitates within the grains suggesting a lower tendency towards coarsening for Y_2O_3 compared to $YCrO_3$. The type of precipitated oxide is expected to influence the mechanical properties and is therefore of high interest for this thesis.
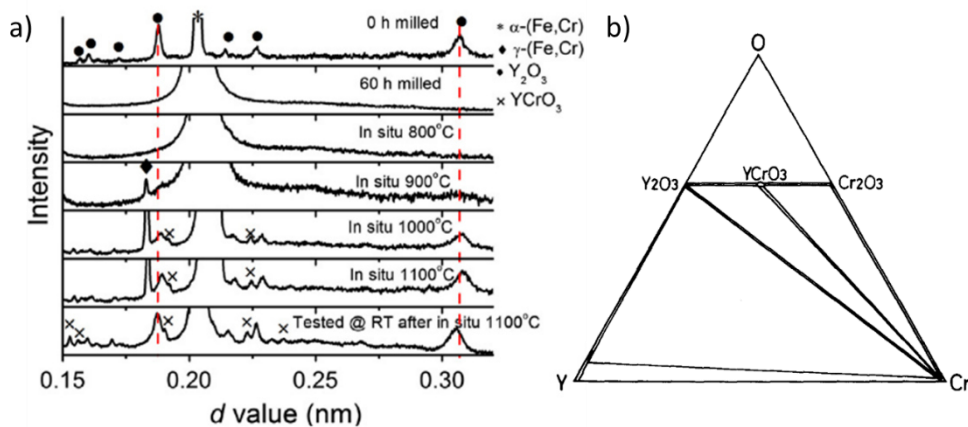
Figure 21: a) SANS powder diffraction pattern before and after milling and after annealing at different temperatures for 1h showing solely yttria precipitates below 1000°C whereas from 1000°C on, also $YCrO_3$ precipitates [71]. b) Ternary phase diagram of the system Y-Cr-O at 1025°C [70].

The results of Zhang et al. show a precipitation of yttria after annealing at 900°C for 1h. However, some studies reported nanoclusters in a size of 2 nm that are highly stable and therefore did not precipitate up to approx. 1400°C with the addition of Ti [72].

2.4.4   Lattice defect annihilation during consolidation

Beside oxide precipitation during heating, lattice defects introduced during the deformation of metals partially annihilate, which can be easily seen by a lower Full-Width-Half-Maximum (FWHM) in XRD pattern after a heat treatment compared to the one before. This behavior is presented in Figure 22, depicting an XRD diffraction pattern of as-milled powders together with powders subsequently SPS treated and annealed. In this image, less intense and broader peaks are observed in the milled powders (MA 80h) whereas the peak height increases and narrows after SPS indicating a significant decrease of lattice defects [73].
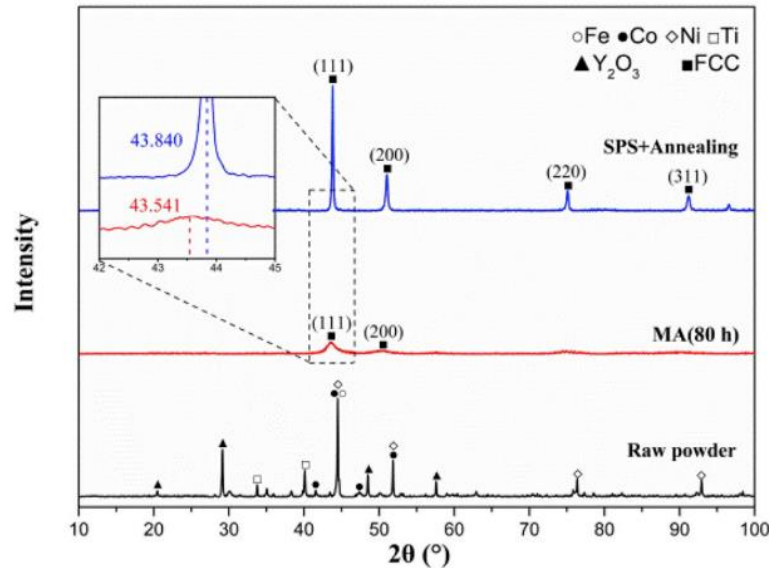
Figure 22: XRD diffraction pattern of the raw powder, the as-milled ODS-FeCoNi HEA powder and the same powder SPS treated at 1100°C and subsequently annealed at 850°C [73].

As described in chapter 2.3.2, materials deformed by severe plastic deformation such as ball-milled powders typically exhibit high defect densities together with nanometer-sized grains which is, however, a metastable state [13,74]. Therefore, upon heating or consolidation of the milled powders, defects recover while the size of these grains is expected to increase via recrystallization [75] which is an essential aspect for high temperature applications [76].

Recovery refers to the partial restoration of the microstructure to the state before deformation and occurs before recrystallization. In deformed materials, point defects and dislocation are present. However, point defects already annihilate at low temperatures and are thus not considered in the description of the processes of recovery and recrystallization. Dislocation recovery represents a series of events to minimize the stored energy such as annihilation and rearrangement of dislocations. Dislocations of opposite burgers vector on different glide planes annihilate by glide, climb and cross-slip leading to an overall decrease of the dislocation density. Cross-slip is, however, reduced in materials with a low SFE hindering dislocations to recover and thus, promoting recrystallization [75]. Furthermore, dislocations can also minimize their energy by forming low energy and low-angle grain boundaries and therefore, subgrains. These subgrains can further grow to reduce their energy. The process of recovery is schematically shown in Figure 23a-b [75].

To initiate recrystallization, nucleation of subgrains with low internal energy has to occur, as presented schematically in Figure 23c. These grains then grow on the extend of others [75].
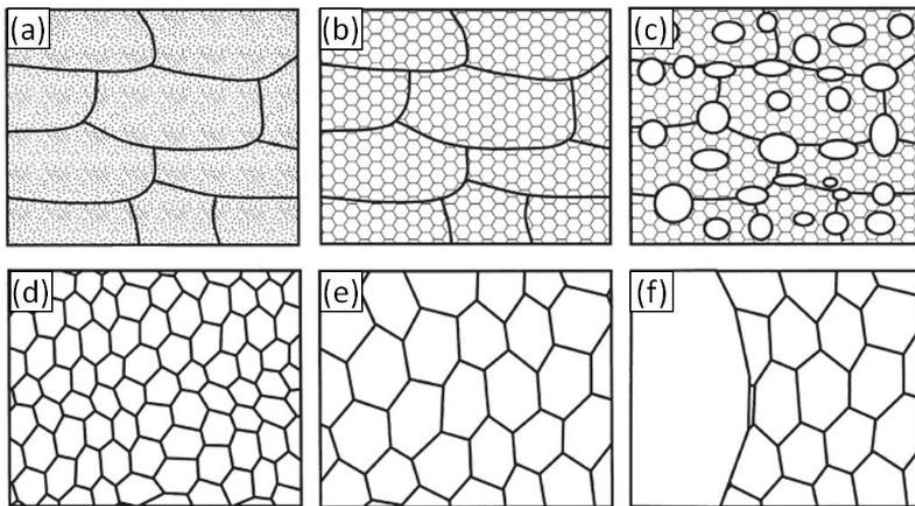
Figure 23: Illustration of the different microstructural states during annealing of deformed alloys. a) deformed, b) recovered, c) beginning of recrystallization, d) fully recrystallized e) grain growth, f) abnormal grain growth or secondary recrystallization [75].

The driving force of recrystallization is the minimization of internal energy provided by lattice defects and small-angle grain boundaries, whereas precipitates retard grain growth as shown in the following equation [75]:

$$P = P_D + P_C - P_Z$$

For particle strengthened materials, the pressure on the grain boundary P results from the pressure of dislocations P_D, grain boundaries P_C and particles P_Z. Following this equation, an equilibrium grain size is achieved once the driving force gets weaker than the pinning pressure of the precipitates. This so-called normal grain growth is expected to occur uniformly within the sample, as depicted in Figure 24, exemplarily showing an increased mean grain size after annealing [75].

Figure 24 further shows the bimodal grain size increase during abnormal grain growth, also called secondary recrystallization [77]. In contrast to normal grain growth where the particle size distribution is increased globally towards larger mean values, for abnormal grain growth, a little number of grains grow on the extend of others resulting in a bimodal grain size distribution if the annealing time is not long enough.
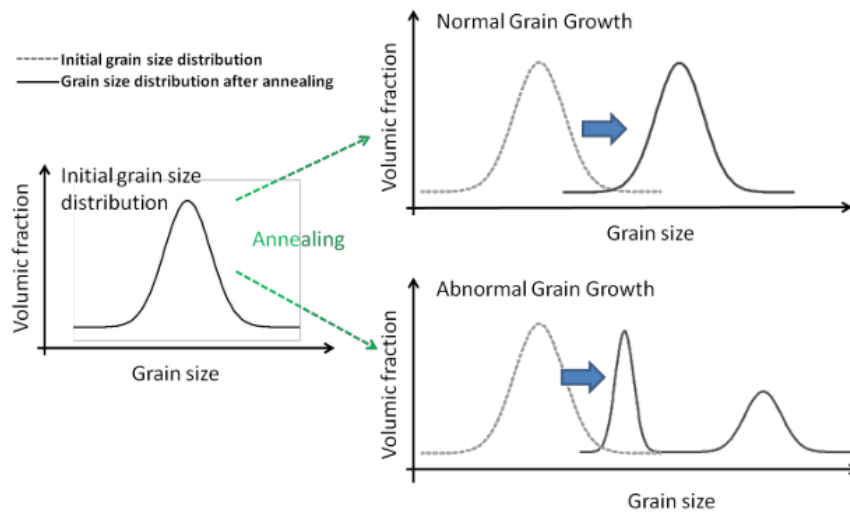
Figure 24: Schematic illustration of the grain size increase during normal grain growth and the bimodal distribution after abnormal grain growth [77].

The exact mechanism behind abnormal grain growth is still not well understood. In many cases, preservation of lattice defects - e.g. by hindering grain boundaries from moving or dislocations to annihilate - up to high temperatures was proposed to promote secondary recrystallization as the stored energy gets released at elevated temperatures providing sufficient driving force for rapid grain growth [74,78]. In this context, literature reported a low initial grain size to promote the nucleation for secondary recrystallization whereas, in analogy to normal grain growth, the driving force was mostly attributed to the reduction of internal energy [74,78]. Furthermore, smaller precipitates and solute atoms such as boron or nitrogen [79] are reported to retard grain growth while precipitate coarsening or - dissolution is expected to promote the formation of abnormal grains [74,79,80].
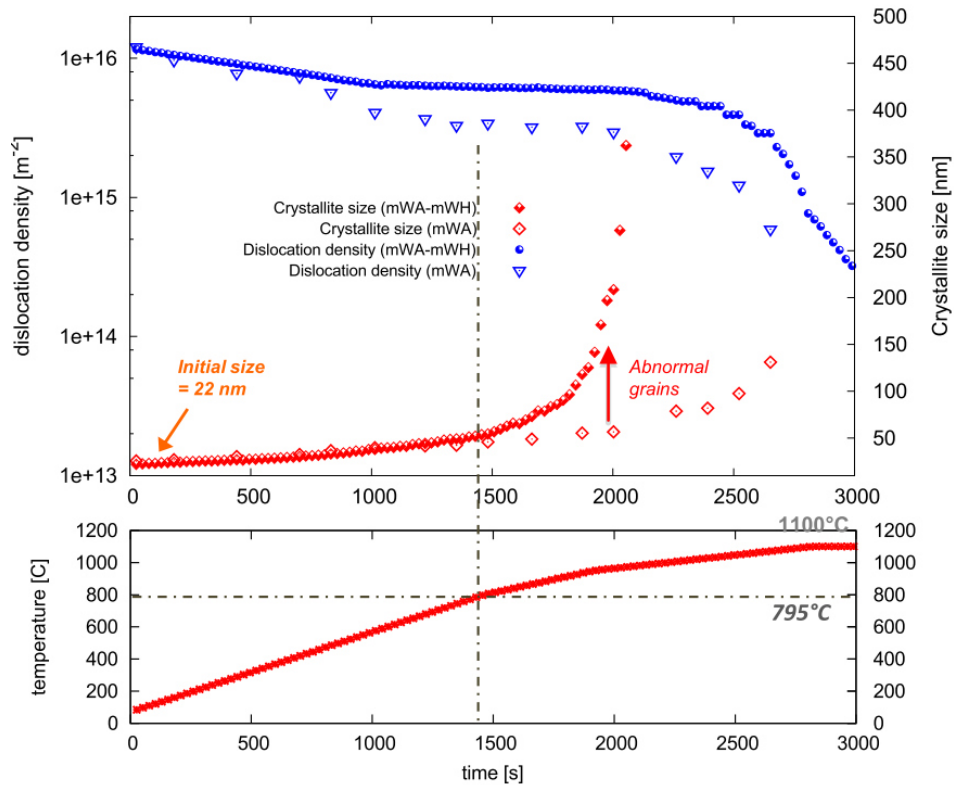
Figure 25: Decreasing dislocation density and increasing crystallite size in an ODS ferritic powder obtained from in-situ synchrotron high-energy X-ray measurements and analyzed by two different evaluation methods: the modified Warren-Averbach method (mWA) and a coupled method of modified Warren-Averbach with modified Williamson-Hall (mWA-mWH). The mWH and mWA methods are explained in chapter 3.2.5 whereas details to the mWH-mWA method can be found in [81]. The trend of the crystallite size calculated using the "mWA-mWH approach" indicates secondary recrystallization in this ODS ferritic powder [81].

Sallez et al. [81] used in-situ XRD measurements to investigate grain growth during heating of a ferritic ODS steel powder. The authors observed an increase in the crystallite size from 20 to 50 nm during isothermal recovery at low temperatures, whereas, in their samples, recrystallization starts at 800℃. However, heating above 850℃ resulted in abnormal grain growth, which the authors attributed to heterogeneous microstructure after milling and the high stored energy. Figure 25 depicts the in-situ XRD results of Sallez et. al showing a drastic increase of the crystallite size indicating abnormal grain growth. This assumption was confirmed by SEM microstructure images showing some abnormally large grains with nanocrystalline areas in-between. The dislocation density in his samples decreased upon heating but reached a steady-state plateau between 650℃ and 800℃, which,

29

according to Sallez et al., shows the transition between recovery and recrystallization.

3 Experimental

This chapter elaborates on the used processing and investigation techniques, trying to give a brief description of the methods as well as used parameters allowing reproduction of the experiments.

3.1 Used material

3.1.1 Powders

For mechanical alloying, $Fe_{20}Cr_{20}Mn_{20}Ni_{20}Co_{20}$ [at.%] powders were prepared using gas-atomization at Nanoval GmbH & Co. KG, yielding a chemical composition given in Table 1. A representative SEM image of the powder before mechanical alloying is depicted in Figure 26a showing a d_{50} particle size of 25.5 µm. The powders were mixed with 1 m.% Y_2O_3 exhibiting a d_{90} of 1.16 µm which is shown in Figure 26b.

Table 1: Chemical composition of the gas-atomized powders. Ni, Co, Fe, Mn and Cr were measured using ICP/OES and O was determined using hot extraction.

	Ni	Co	Fe	Mn	Cr	O
m.%	20.2	21.3	20.2	19.9	18.3	0.11
at.%	19.2	20.2	20.2	20.3	19.7	0.38
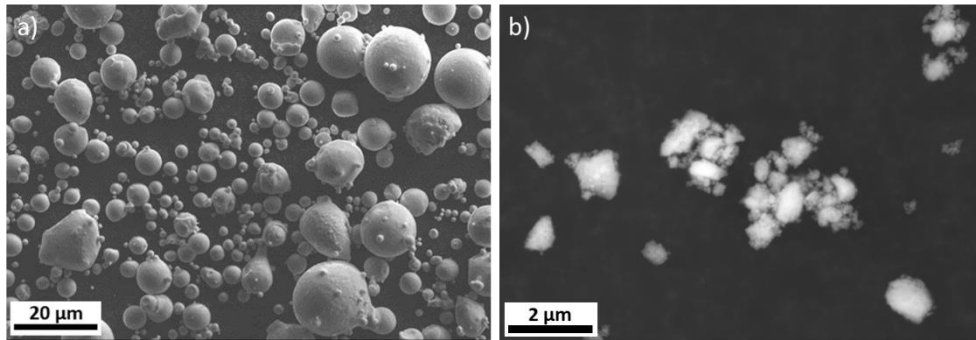
Figure 26: Representative SEM images of the initial powder. a) FeCrMnNiCo and b) Y_2O_3.

3.1.2 Mechanical alloying

Milling was performed at the Materials Center Leoben (MCL) within a novel high-energy attritor ball mill with a schematic of the milling setup presented in Figure 27.
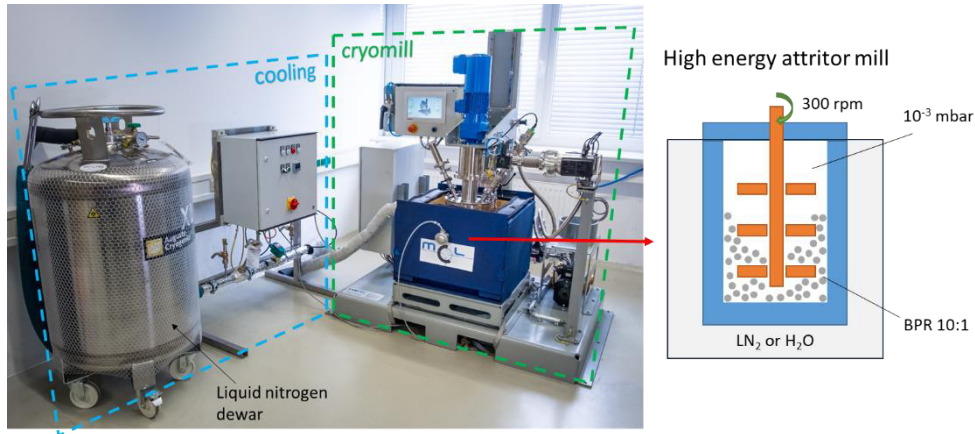
Figure 27: Milling setup including the most important process parameters.

The powders were milled within a grinding vial made of stainless steel (X6CrNiMoTi17-12-2), the same material was used for the shaft and the pins. The mill was operated at 300 rpm using Inconel 825 balls with a diameter of 6.35 mm and a ball-to-powder-weight-ratio (BPR) of 10:1 – i.e. 5 kg of grinding media with 0.5 kg of powder. The used materials in the milling setup were carefully chosen to prevent contamination of the milled powders with unwanted elements due to abrasion of balls, vial and pins. To avoid atmospheric contamination, a vacuum of 10^{-3} mbar was applied during the whole process. Cooling was maintained from the outside of the milling vial. For RT milling, water was used to keep RT around the vial and for milling at cryogenic temperatures, the cooling box outside the milling vial was held at -150°C using liquid nitrogen.

Table 2: Variations of the milling parameters and the corresponding nomenclature of the milled specimen. RT represents approx. 25°C and CT -150°C milling temperature around the grinding vial.

	0h	10h	18h	48h	54h	168h
RT	unmilled	10h/RT	18h/RT	48h/RT		168h/RT
CT		10h/CT	18h/CT	48h/CT	48h/RT + 6h/CT	

Table 2 presents the produced samples. Milling times ranged from 10h to 168h for RT and from 10h to 48h for cryomilling but also the combination of both milling temperatures was applied to one specimen where 6h of cryomilling was added to 48h of milling at RT.

32

3.1.3   Consolidation

In order to investigate the precipitation of yttria and the microstructural evolution, the milled samples were consolidated via spark-plasma sintering (SPS) at RHP-Technology GmbH using a DSP518 from Dr. Fritsch Sondermaschinen GmbH. A more detailed description of the process can be found in chapter 2.4. During this process, powders are put into a graphite die and external pressure and an electric field were applied whereas a vacuum prevented oxidation during the process.

Table 3: Measured densities of the consolidated samples using the Archimedes principle.

	unmilled	*48h/RT*	*48h/RT+6h/CT*	*48h/CT*
density	100%	98%	99%	99%

In this work, 650 g of the selected milled powders were spark plasma sintered using a heating rate of 100 K/min up to 1100°C, a pressure of 30 MPa and 30 min holding time before cooling. The finally achieved sample had a diameter of 78 mm and a height of approximately 15 mm. The density measured using the Archimedes principle is shown in Table 3, yielding more than 98% for all consolidated samples.

3.2   Investigation methods

3.2.1   Scanning electron microscopy

Scanning electron microscopy (SEM) has become a versatile investigation method in the field of materials science. Its strength lies in the possibility of combining different analysis techniques such as microscopic images, crystallography and chemistry in a single device allowing access to correlative investigations.

In a SEM, an electron beam scans the sample interacting with the specimen at every location sending out specific signals. The primary electrons from the electron beam interact with the specimen via elastic or inelastic scattering giving various information about the sample. Elastically scattered primary electrons eventually escape the sample after experiencing scattering and deflection by the atoms in the sample as backscattered electrons (BSE) and are detected by a semiconductor

detector located around the primary beam. The observed contrast of BSE gives information about specimen composition as the deflection of the BSE depends on the Z-value of the elements in the sample [82].

Inelastic scattering of primary electrons or BSE in the sample causes the excitation of weakly bound electrons, which can escape into the vacuum if generated close to the sample surface as so-called secondary electrons (SE). Two types of SE show inherent sample properties, SE1 and SE2, differentiated by the generating electrons and schematically presented in Figure 28 [83]. SE1 are generated by the primary electron beam close to the point of impact. On the other hand, SE2 are generated by BSE traveling through the specimen and potentially escape close to the surface but much further laterally from the incident electron beam. The third type of SE, SE3, are emitted when the escaped BSE strike the objective pieces or the chamber wall contributing to the background signal. SE give information about the topographic contrast [82,83], but, depending on the SEM parameters, different phases can also be identified. This results from different work-functions of different phases resulting in phases exiting more SE and consequently appearing brighter than others, a feature used in this thesis to easily detect and analyze oxide particles [84].
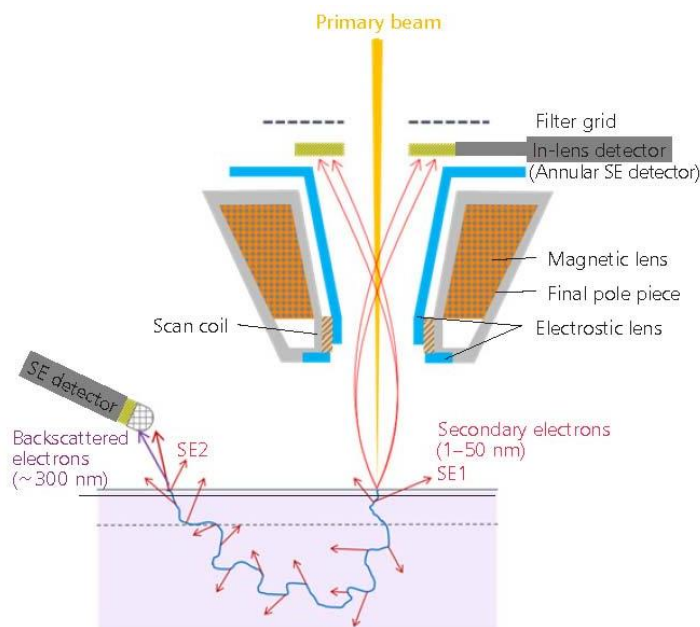
Figure 28: Illustration of the interaction of the electron beam with the specimen and detectors for secondary electrons [85].

The most common SE detector is the Everhart-Thornley detector attracting both, SE1 and SE2 by a biased grid. However, this limits the achievable resolution due to the laterally displaced SE2. Therefore, in order to improve the resolution, the application of in-lens detectors shown in Figure 28 allows the generation of images by solely measuring SE1. This improves the resolution limit of SE to the geometric dimensions of the electron beam [82,85]. Therefore, beside the simple detection of oxide particles, in this thesis the in-lens detector is used to allow the detection and analysis of smaller oxide particles down to approx. 17 nm.

Another possibility to increase the spatial resolution is to operate a SEM in transmission mode, also known as scanning transmission electron microscopy (STEM). For this, the specimen needs to be thin enough for electrons to pass through, which are collected by a detector below the specimen. Using this technique, magnifications of 500kx and more can be realized. However, the sample preparation is difficult and time-consuming, limiting the applicability [82].

Beside mass-contrast, SEM also allows for quantitative chemical measurements using energy dispersive spectroscopy (EDS). The energy of the electron beam is transferred to an inner shell electron in the specimen which gets ejected, resulting in an unstable state. Consequently, this unstable state is compensated by an outer shell electron losing energy by emitting an X-ray with elemental specific energy. Collecting these X-rays allows the determination of local chemical composition. As in this thesis, especially small oxide particles are analyzed, an important aspect of EDS concerning the spatial resolution is the voltage of the beam. Higher beam voltage increases the volume the electrons interact with, which means in turn, that the chemical information is collected from a larger volume decreasing the minimum achievable spatial resolution. One way to estimate this so-called interaction volume is to conduct Monte-Carlo simulations of the specific alloy as presented in Figure 29 for the FeCrMnNiCo alloy used in this thesis [82].
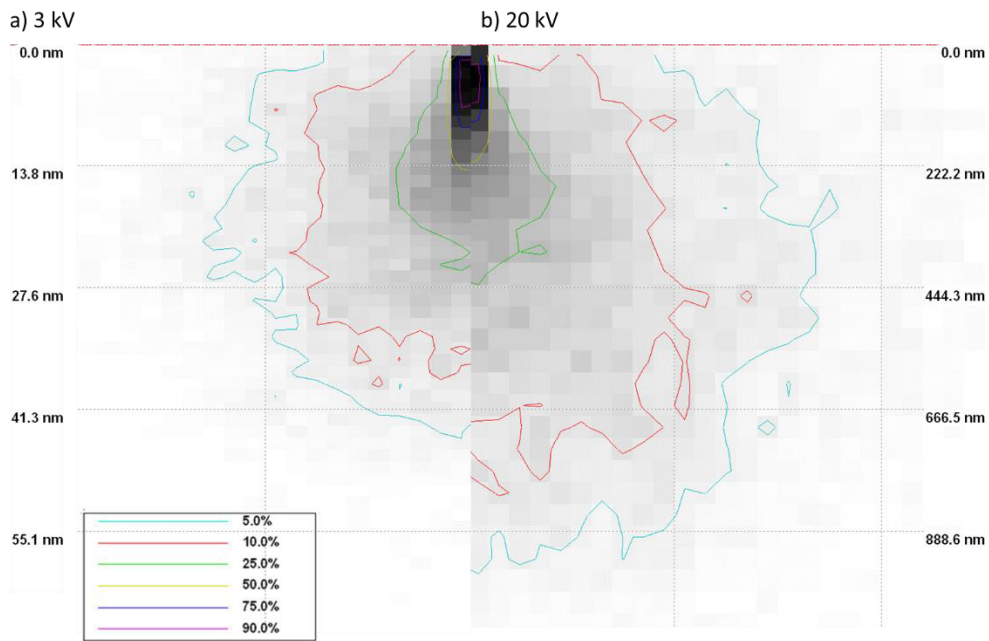
Figure 29: Monte-Carlo simulation of the percentage-weighted travel distance of primary electrons in a FeCrMnNiCo + 1 m.% Y_2O_3 alloy – i.e. the percentage of primary electrons traveling a certain distance. Acceleration voltage: a) 3 kV and b) 20 kV. The electron beam diameter for simulation was chosen as 1 nm. Note the different scale bars.

Figure 29 depicts the Monte-Carlo simulation of the distance primary electrons travel within the FeCrMnNiCo alloy for 3kV and 20kV acceleration voltage. While the travel distance that only 10% of the primary electrons reach – i.e. 90% of the electrons travel shorter distances, red line – is about 30 nm for 3kV, 20kV results in approx. 600 nm. During travelling through the material, electrons loose energy, eventually even below the excitation energy for characteristic X-rays. As a result, the size of the activation volume, from which elemental specific X-ray are excited, is expected to be slightly smaller than the travel distance of primary electrons depicted in Figure 29. Furthermore, generated X-rays are partially absorbed before leaving the specimen slightly weakening the chemical signal, especially for areas deeper in the sample. However, as most of the electrons do not travel far into the specimen, both errors are expected to be insignificant for the purpose of this thesis.

Furthermore, for higher voltages, signals from stronger bond electron shells are obtained making a chemical indication much easier due to less overlap between the obtained peaks. An example of

36

overlapping peaks at a low acceleration voltage of 3 kV is presented in Figure 30 showing an overlap of the O and Cr peak. Even though the O-peak in Figure 30b seems slightly broader suggesting increased Cr within the spectra, no exact Cr peak is observed making a differentiation between $YCrO_3$ and Y_2O_3 hard and therefore not trustworthy. Therefore, the best acceleration voltage has to be defined from case to case [82].
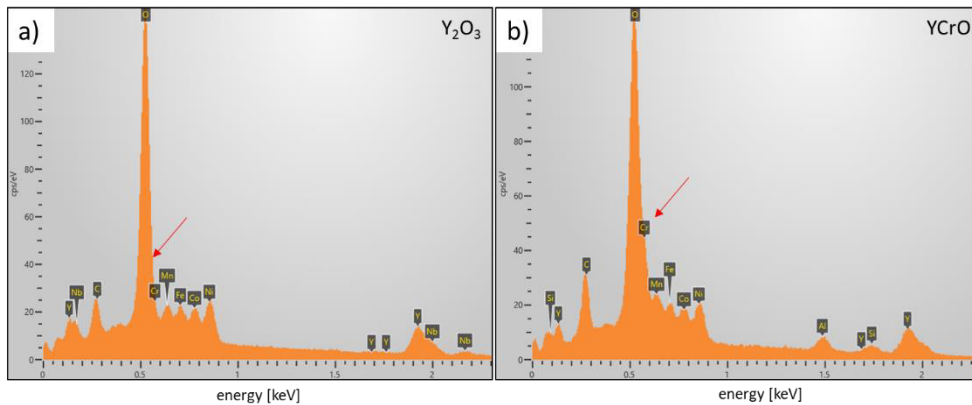
Figure 30: Comparison of two at 3 kV acceleration voltage obtained EDS spectra showing similar energies of O and Cr and a resulting different oxide classification for a) Y_2O_3 and b) $YCrO_3$.

In this thesis, the morphology of the powder particles was investigated at the MCL using a Zeiss Evo Ma25 while cross-sections of the powders were analyzed a Zeiss GeminiSEM® 450. In order to obtain particle size distributions, the SEM images of the milled powders were analyzed using an in-house python code from which, mean particle sizes and the 25% and 75% quantiles were calculated. The cross-sections were prepared using standard metallographic methods including active oxide suspensions (OPS). In order to analyze the oxide dispersions within the powders, for each specimen, SE in-lens images at three different powder particles and at three magnifications for each particle (1 kX, 3 kX and 10 kX) were taken to enhance the power in statistics. These images were then analyzed using an in-house python code (Python 3.7) with respect to size and oxide phase fraction (see Figure 31). Even though the usage of an In-lens detector allows a lateral resolution of the of the size of the electron beam, in this code, particles smaller three pixels (17 nm at the highest magnification) were generally excluded due to a high chance of being faulty detected. To

37

account for different observed areas, the measured particle densities were corrected using an area factor.
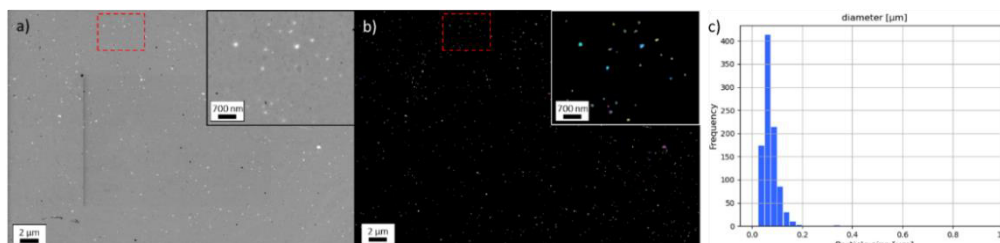
Figure 31: Illustration of oxide particle analysis using the in-house python code. a) Representative in-lens SEM image with the magnified area. b) Analyzed image output and c) particle size histogram output of the python script.

The overall chemical composition was analyzed in large areas in the same images as the particle analysis using a mirror-less Oxford Instruments Ultim Extreme detector and 20 kV acceleration voltage. From the obtained chemical results, the mean values and the standard deviation for each element were calculated.

3.2.2   Transmission electron microscopy

Similar to STEM, in a transmission electron microscope (TEM), electrons pass through the specimen onto a detector on the other side. However, the difference to a STEM is that in a TEM no scanning of the electron beam is needed as the image is generated directly by the beam. Furthermore, compared to STEM in a SEM, in TEM, higher acceleration voltages of 300 kV are applied. TEM can be used for high-resolution microscopy down to atomic resolution (HR-TEM) as well as for investigations regarding crystal structure [86,87]. For the latter, a diffraction pattern of the whole image can be obtained but also by focusing the beam on a single spot, a diffraction index of a single spot is possible. In a TEM, chemical analysis based on EDS has increased resolution due to the thin specimen and the high voltage resulting in practically no activation volume. By this, the lateral resolution of TEM-EDS can be a few nm [86,87]. This advantage is, however, a problem as well for TEM-EDS. Due to the thin specimens and thus low volume, lower X-ray statistics are gained, limiting this method's chemical sensitivity [87].

38

Samples for this work were prepared using focused-ion-beam (FIB) lift-outs in a SEM [88,89] and analyzed at the Erich-Schmid institute for materials science in Leoben. Lift-outs were taken from the cross-sections of the milled powders in-between visible oxides in order to solely analyze the matrix. For the TEM investigations, a JEOL JEM-2200 FS, with an acceleration voltage of 200 kV was used. For accurate phase characterization, a combination of high-resolution TEM (HRTEM) imaging and selected area diffraction (SAD) was used. The microstructure was imaged using scanning TEM (STEM).

3.2.3   Atom probe tomography

Atom probe tomography (APT) allows the three-dimensional chemical investigation of specimens at nearly atomic resolution and is, therefore, a useful tool for the chemical analysis of precipitates and other microstructural features such as grain boundaries. Specimens need to be shaped into a small tip with a tip radius of just 50 nm before investigation. Figure 32 depicts the concept of APT showing the tip and a pulsing electric field between the tip and an electrode. By this field, atoms of the tip evaporate forming ions, which are accelerated onto a detector. The obtained time of flight, the position at the detector and the mass-to-charge-ratio of the ions, allows a reconstruction of the tips [90].
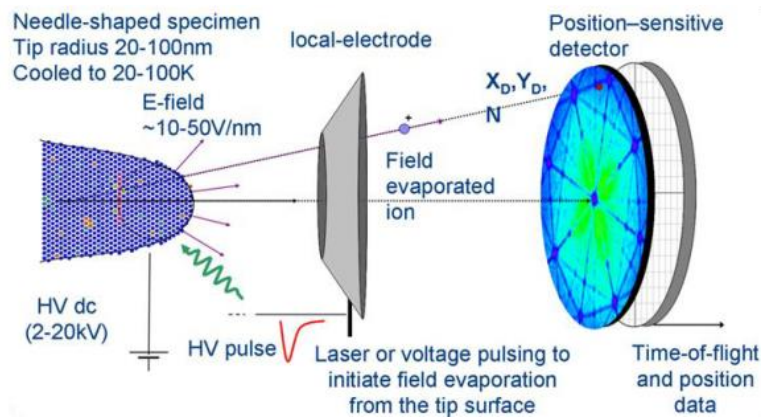
Figure 32: Schematic setup of APT showing the specimen tip, electrode and detector [90].

However, the detector of the used APT has an efficiency rate of approx. 37 % [91] indicating that not all of the evaporated atoms finally contribute to the obtained signal. Nevertheless, this efficiency

rate is independent on the type of ion and therefore allows a trustworthy chemical analysis. A special artefact in APT regarding second phase particles is the so-called local magnification effect occurring when two phases have different evaporation field strengths. This leads to a modification of the ion trajectories causing overlaps, especially at interfaces. When the differences in the evaporation field strengths is small, only interfaces are affected but for small particles with larger differences, even the core may be affected. This overlap in trajectories causes the detection of matrix elements within particles or clusters and vice-versa and therefore alters the chemical composition and size of particles, precipitates or clusters [92,93].

Table 4: Evaporation field of the FeCrMnNiCo matrix elements and Y and their ratio to Y [94]. The mean evaporation field of the equiatomic FeCrMnNiCo matrix is calculated as 32 V/nm and the corresponding ratio to Y is approx. 0.75.

Element	Fe	Cr	Mn	Ni	Co	Y
Evaporation field strength [V/nm]	33	27	30	35	37	24
Ratio of Y to matrix element	0.72	0.89	0.80	0.68	0.65	-

To estimate the influence of the local magnification effect on the Y-enriched clusters observed in this thesis, Table 4 gives the values of the evaporation field of the matrix elements together with Y as well as the ratio of the evaporation fields of Y to the matrix elements. All ratios are below one which means, according to Lawitzki et al. [95], that the sizes of the clusters are underestimated and appear smaller than they actually are. Taking the simulated influence of the ratio of evaporation fields on the cluster size from [95] and by considering a mean evaporation field of the FeCrMnNiCo matrix, the clusters in this thesis are approx. 25% larger than measured by APT.

In this thesis, APT tips of the milled powders were prepared using FIB lift-outs in a SEM [96,97] at cross-sections prepared for the SEM investigations. Sample preparation, APT-analysis and evaluation of the data was conducted at the department for materials science at the Montanuniversität Leoben. Lift-outs for each specimen were taken from similar positions in-between visible oxide particles in order to measure the matrix composition. The lift-out had a size of 10 x 2 x 3 µm³ and was subsequently cut into three parts which were located on

a pre-tip for final thinning. APT investigations were conducted at a LEAP 3000 X HR System from CAMECA in voltage mode and at 200 kHz, 50 K. The data was reconstructed using IVAS 3.6.8 from CAMECA and a K-value of 5. For the analysis of the clustering behavior of Y and O, the maximum separation method [98] was applied, for which the input parameters were obtained by the nearest-neighbor distribution as described in [99] combined with a cluster count distribution which is outlined in [100]. The volume fraction of the clusters was calculated using a method according to [101].

3.2.4   Positron annihilation spectroscopy

Being the anti-particle of electrons, positrons can be effectively used to study defects with high sensitivity. The technique of positron annihilation spectroscopy (PAS) is based on the effect that a γ-ray is emitted once the electron and positron recombine within the sample giving information about the type of defect as well as the local chemical surrounding [102,103]. The schematic principle is depicted in Figure 33a showing a positron entering the specimen.
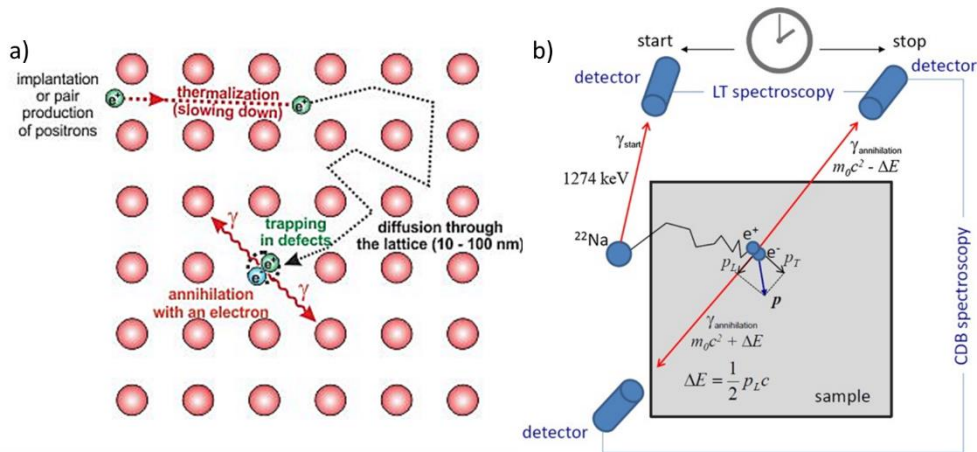
Figure 33: a) Illustration of a positron interacting with the specimen until annihilation [104]*. b) Measurement setup for lifetime measurement and Doppler-broadening* [102]*.*

At PAS, positrons are usually generated in a [22]Na source also emitting a γ-ray for each generated positron. The positron then tunnels approx. 100 μm through the specimen where it slows down and diffuses further where it gets trapped and eventually recombines with an electron sending out an γ-ray. The time between the generation of the

first γ-ray and the annihilation γ-ray gives the positron lifetime used for Positron-Annihilation-Lifetime-Spectroscopy (PALS). The lifetime is in the range of picoseconds and a measure of the size of the trapped position. If the positron was trapped at larger open volumes, larger lifetimes are measured as an electron needs more time to reach the positron [102,103]. Figure 34 depicts an example lifetime spectra including the fit of different contributing lifetimes such as the bulk lifetime (free positrons), the source contribution and the lifetime of positron at dislocations. Deconvolution of the spectra allows the separation of each contribution to obtain the lifetimes of each component.
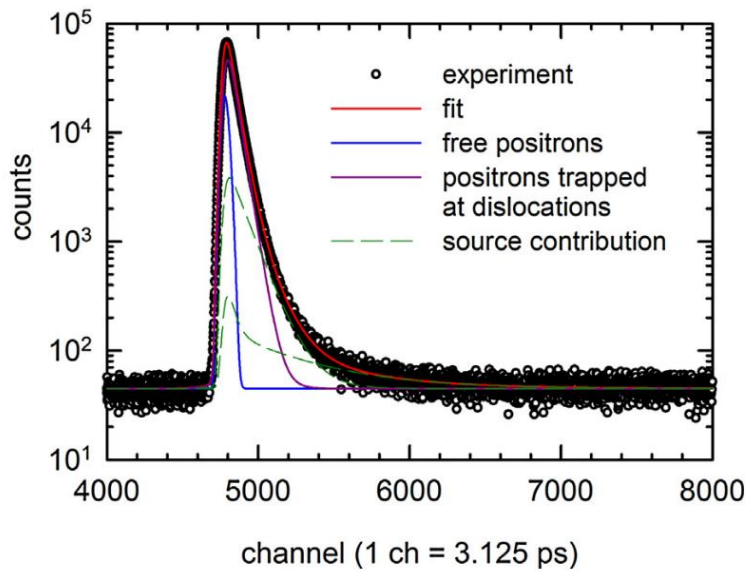
Figure 34: Example PALS spectra with fits for free electrons, source contributions and the annihilation at dislocations showing the contributions to the experimental spectra [102].

Besides the lifetime of the positron, also the energy of the annihilation γ-ray can be measured giving information about the chemical surrounding of the annihilation site. The reason for this is that the annihilating electron transfers its energy and momentum, an indicator for the atom, to the γ-ray. This so-called Doppler-broadening (PAS-DB) is a relative technique as no quantitative chemistry determination is possible. Therefore, besides the investigated samples, reference samples need to be measured and the obtained chemical signatures are compared [102,103].

Prior to PAS measurements, the powders were pressed to small disks using a pressure of 3 GPa, the minimum pressure necessary to achieve a mechanically stable specimen. In this context, the deformation of the powders is not expected to affect the investigation as positrons tunnel deep enough into the sample to avoid the highly deformed areas at the surface of the powder particles. For PAS measurements, conducted at the institute of materials physics at the Graz University of Technology, two disks of each sample were used and a ^{22}Na source in aluminum foil was sandwiched between them. For obtaining the positron lifetime spectra, an analog fast-fast positron lifetime spectrometer with a time resolution function of 163 ps (full-width-half-maximum) was used, at which, for each measurement, more than 10^6 counts were acquired. Background correction and fitting of the spectra were conducted using the software PALSFIT [105].

3.2.5   X-ray diffraction

X-ray diffraction (XRD) is a versatile investigation method to analyze occurring phases and the crystallography of a specimen. The principle of XRD is based on Bragg's equation describing the diffraction condition for incident X-rays [106].

$$n\lambda = 2\,d\sin\theta$$

Based on this equation, for a given wavelength λ and lattice spacing d, the angle at which the incident beam is diffracted can be calculated [106]. Any variation of the diffraction angle causes a peak shift and broadening, indicating lattice imperfections or lattice defects that can be determined using theoretical models [107]. In this work, beside the lattice parameter obtained from the peak position and the Full-Width-Half-Maximum (FWHM), which is the width of the diffraction peak, advanced methods were used to calculate the dislocation density, crystallite size and stacking fault probability (SFP). The first of these methods is the so-called modified Williamson-Hall method (modWH) which is, as the name suggests, based on the Williamson-Hall plot (WH), but it considers the effect of dislocations on the pattern and can be used for calculating the crystallite size within a highly-deformed specimen [108,109]. In the highly deformed milled samples investigated in this thesis, the WH method is inaccurate due to poor fitting as

shown in Figure 35a. Considering dislocations by using the modWH significantly improves the fit quality shown in Figure 35b. A detailed instruction and description of the method was described by Ungár et. al [110].
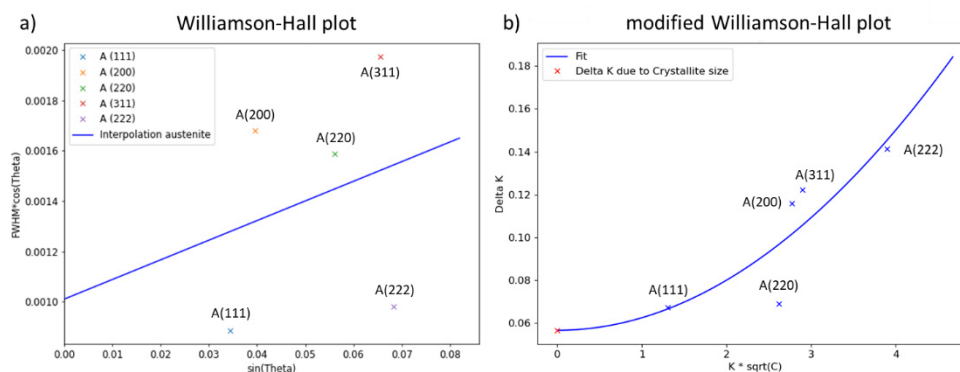
Figure 35: Comparison of the a) Williamson-Hall plot and b) modified Williamson-Hall plot for a milled specimen. This evaluation was obtained from HE-XRD measurements at RT.

The dislocation density was calculated using the modified Warren-Averbach method described elsewhere [110,111]. This method uses a Fourier analysis of the diffraction pattern allowing the decomposition of the peak in order to separate different peak broadening causes.

Figure 36: Indication of the direction of the peak shifts caused by planar faults [112].

The SFP α represents the probability of finding a stacking fault on any series of (111) planes in a fcc material. The calculation of this parameter is based on the asymmetric peak shift caused by planar faults using the unmilled powder as a reference. Therefore, in contrast to lattice parameter changes, where all peaks shift towards higher or lower angles, planar faults shift peaks in different directions, as depicted by the arrows in Figure 36.

The definition of the SFP and a description of the calculation are based on Paterson [112] and Warren [113]. The formula to calculate the SFP is given below:

$$\alpha = \frac{\Delta(2\overset{\circ}{\theta}_{200} - 2\overset{\circ}{\theta}_{111}) * \pi^2}{90\sqrt{3} * (\tan(\theta_{200}) * f_{200} - \tan(\theta_{111}) * f_{111})}$$

Here, $\Delta(2\overset{\circ}{\theta}_{200} - 2\overset{\circ}{\theta}_{111})$ represents the difference of the (111) and (200) peak separation of the measured sample and the reference sample. θ_{111} and θ_{111} are the peak positions of the peaks of the milled powders. All peak positions are given in [°] and f_{111} and f_{222} are crystallographic factors given in [113]. In contrast to the previous methods, modWH and modWA, where the peak broadening and peak position was used, calculating the SFP solely relies on the peak position.

Another interesting feature, the beginning and strength of recrystallization during heating, can be obtained by investigating the spottiness of the synchrotron diffraction rings as described by Moreno [114]. Typically, a solid diffraction ring indicates the presence of a high number density of small and differently orientated grains. In contrast, larger grains in the same volume provide a lower amount of scattering statistics resulting in fewer but more intense diffraction spots, which are shown in Figure 37. Using this principle allows to follow the growth of crystallites upon in-situ heating of specimen by plotting the intensity along the azimuthal angle for a diffraction ring and counting the number of exceptionally bright diffraction spots using the method of Moreno [114] with an example depicted in Figure 37. Therefore, the beginning and strength of recrystallization upon heating of the milled powders can be determined.
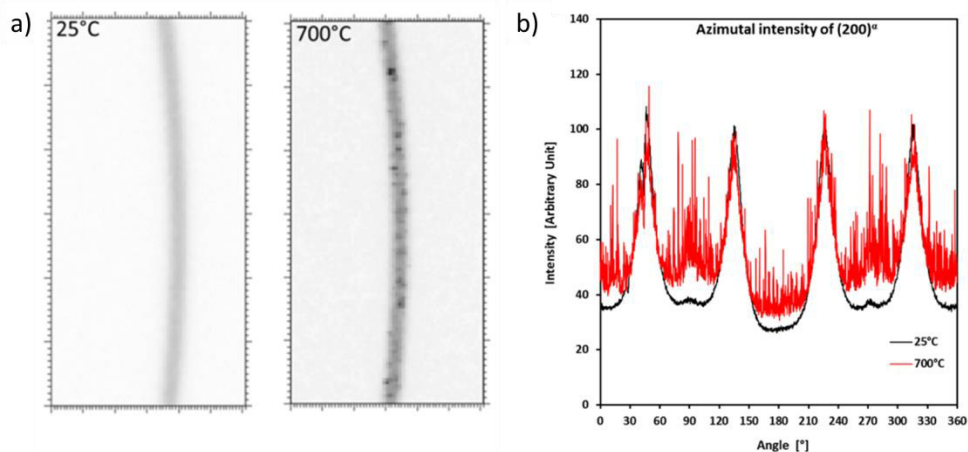
Figure 37: a) Part of a diffraction ring at 25°C and after heating at 700°C and b) the evaluation of the azimuthal intensity in order to count the number of spots [114].

In this thesis, XRD measurements were carried out at the MCL using a Bruker D8 discover and CuKα radiation. Instrumental broadening was measured using a LaB_6 powder according to the National Institute of Standards and Technology [115] and considered for the calculations. Furthermore, in-situ investigations were carried out using High-Energy X-ray diffraction (HE-XRD) at the HEMS beamline of PETRA III [116] at Deutsches Elektronen-Synchrotron (DESY) in Hamburg using high-energy synchrotron radiation. To obtain a monochromatic X-ray wavelength from the continuous synchrotron spectra, a Si single crystal monochromator is used where only a wavelength fulfilling Bragg's equation [106] gets diffracted. However, according to the *n* in Bragg's equation, harmonic wavelengths at half the desired wavelength also get diffracted contribution to the X-ray spectra. These harmonic wavelengths show intensities of only 1% of the main wavelength, but due to the high intensity of synchrotron radiation, they cause so-called harmonic peaks, i.e. additional reflexes at half the diffraction angle of the main wavelength. Figure 38 shows the diffraction pattern of the 48h/CT specimen in logarithmic representation showing the main peaks and the corresponding harmonic peaks at half the diffraction angle correspondingly labeled from a-f.

46
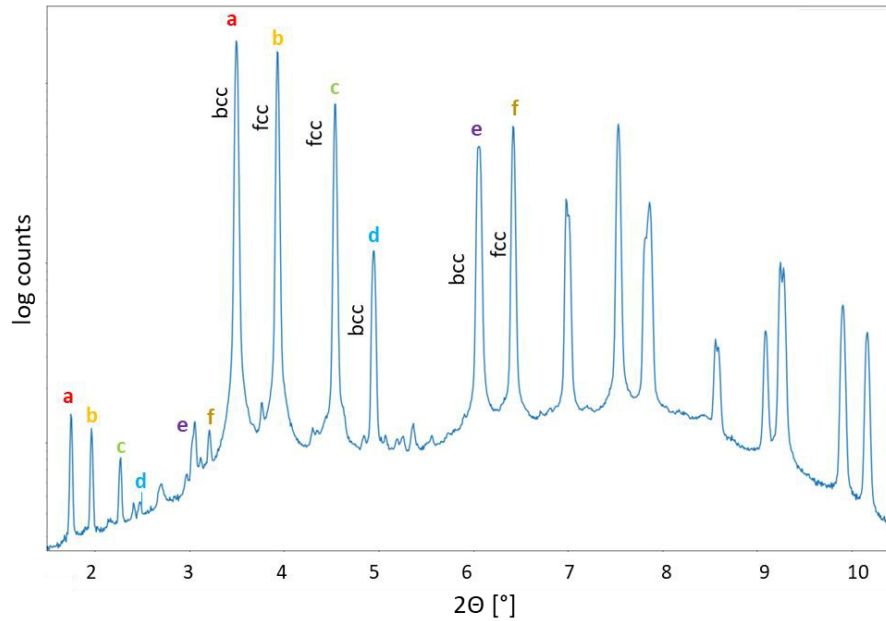
Figure 38: Representative diffraction pattern of the heated 48h/CT sample showing the main bcc and fcc peaks labeled from a-f with the corresponding harmonic peaks at half of the diffraction angle as the main peaks.

Figure 39 depicts the setup for HE-XRD experiments. The powders were put into a Nb capsule in order to facilitate the heating within a dilatometer of the type Netzsch DIL 402 CD. To prevent oxidation, the dilatometer was evacuated to approx. 10^{-4} mbar. The heating rate was chosen to simulate the SPS process, whereas the holding time was reduced from 30 min to 15 min. Therefore, the powders were heated to 1100°C with a heating rate of 100 K/min and held at this temperature for 15 min. Subsequently, the samples were cooled at 100 K/min. The detector distance was chosen as 1.4 m and the beamline yielded the main wavelength of the used beam of 0.14235 Å. In order to obtain a 1D diffraction pattern, the 2D diffraction image was integrated over the whole angle, as presented in Figure 39.
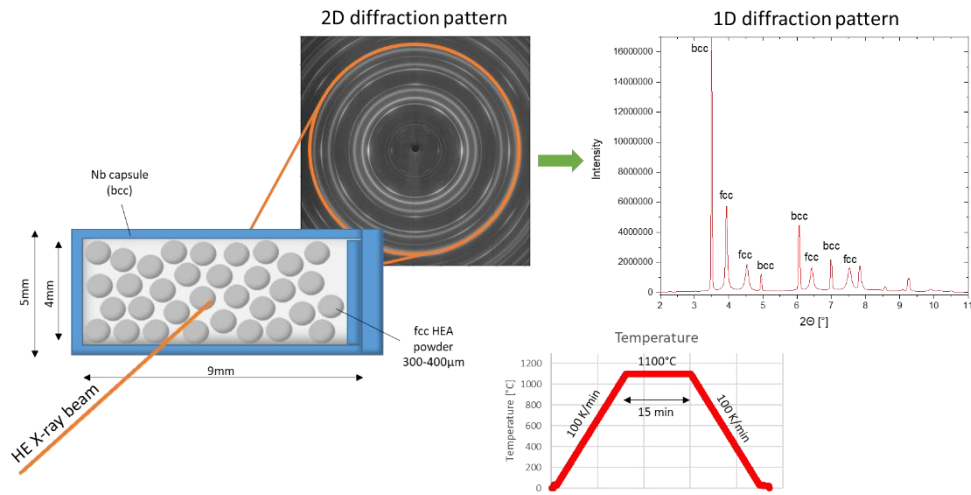
Figure 39: Illustration of the experimental setup, parameters and procedure for in-situ HE-XRD measurements.

The peak properties such as the FWHM and peak position were obtained from a Pseudo-Voight fit, and the crystallite size, dislocation density and SFP were calculated by applying the above methods in an in-house python script (Python 3.7). For lattice parameter investigations, the peak positions were corrected by the influence of planar faults using a method described by Warren [113]. To determine the different arising peaks, the software Bruker DIFFRAC EVA was used, where the obtained diffraction peaks were compared with a database. Recrystallization was investigated by applying the spottiness algorithm of Moreno using the same in-house python script.

It has to be mentioned that for all of the above-described methods, uncertainties concerning the quantitative results exist, mostly due to their complexity. However, all patterns were measured and analyzed using the same parameters and the same python code and are therefore expected to deliver qualitative comparable results.

4 Results and Discussion

In order to describe the temperature-dependent mechanism of the refinement and dissolution of yttria during mechanical alloying in an fcc FeCrMnNiCo high entropy alloy, results of particle size investigations, microstructural development and yttria refinement during mechanical alloying and detailed correlative examinations of the clustering behavior of yttria at atomic scale are presented and discussed. Special focus is laid on the influence of cryogenic temperatures during mechanical alloying compared to room-temperature milling. Furthermore, the effect of cryomilling on the subsequent consolidation process is studied and results, including ex-situ and in-situ results of oxide precipitation and defect evolution, are discussed.

4.1 Temperature effect of the refinement and dissolution of yttria during mechanical alloying

The following chapter focuses on the incorporation of yttria into a FeCrMnNiCo matrix via mechanical alloying and analyzes the overall particle and microstructure evolution during the process. Furthermore, the refinement and dissolution of yttria dependent on milling time and temperature are studied in detail and conclusions regarding the dissolution of yttria at defects are drawn. The results presented below are summarizing the main findings from publication A (The Effect of Cryogenic Mechanical Alloying and Milling Duration on Powder Particles' Microstructure of an Oxide Dispersion Strengthened FeCrMnNiCo High-Entropy Alloy) and publication B (From microscopic to atomistic scale: Temperature effect on yttria distribution in milled FeCrMnNiCo powder particles).

4.1.1 Influence of the milling time and temperature on the powder particle's morphology and chemical composition

In order to investigate the comparability of the milled powders, three large-area EDS measurements at different positions on cross-sections of the milled powders were undertaken using a Hi-res EDS detector and are compared in Figure 40.
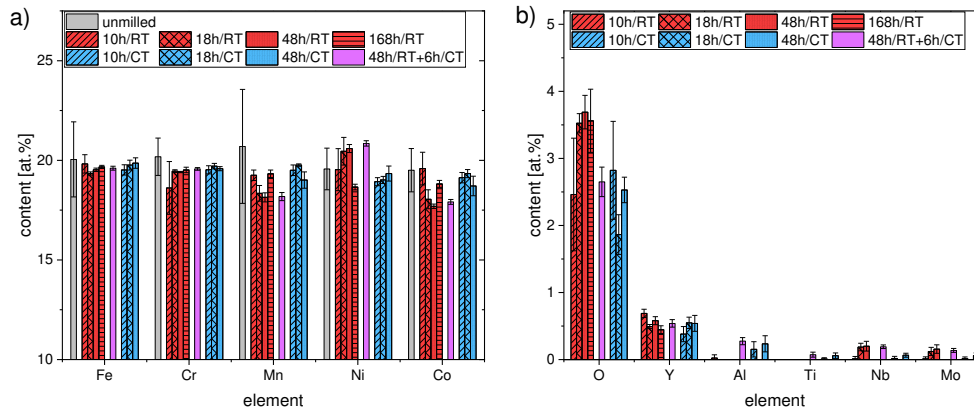
Figure 40: 20kV EDS global chemistry conducted on cross-sections of the at room temperature (RT) and cryogenic temperature (CT) milled powders for the a) matrix elements and b) yttria and other detected elements. The matrix elements exhibit a nearly equiatomic composition and all samples show similar Y contents.

The main elements such as Fe, Cr, Mn, Ni and Co show minor deviations from the equiatomic FeCrMnNiCo alloy, except for noticeable higher Ni content and lower Mn and Cr content in the room temperature milled (RT) samples. This might be due to contaminations from prior milling experiments with Inconel 718 and the abrasion of the milling balls made of Inconel 825. The existence of Nb and Mo, which are alloying elements of Inconel 718 and Inconel 825, in these samples further support this assumption. All chemical variations of the milled specimen show lower variations than the standard deviation of the unmilled specimen and are therefore assumed to be insignificant.

In order to evaluate the uptake of gases during the process, the milled samples as well as the starting powders were analyzed using combustion analysis. This method exhibits a higher accuracy for light

elements and gases compared to EDS. The results are presented in Figure 41 as a function of the milling time. By this plot, an increase of the oxygen content from approx. 0.30 m.%, which represents the at the powders adsorbed oxygen and the oxygen of yttria, up to 0.67 m.% with longer milling times is observed whereas the nitrogen content does not seem to be affected by the milling time. However, the cryomilled specimen (CT) exhibit increased nitrogen – approx. double the content - and slightly decreased oxygen contents compared to their room temperature milled (RT) counterparts. These observations indicate the intake of atmospheric gases into the milling chamber even though a vacuum of 10^{-3} mbar was applied during the whole process. Especially the increased N_2 content of the cryomilled samples confirms this interpretation as liquid nitrogen is used for cooling directly outside the grinding vial and therefore provides N_2 gases directly around the vial. The uptake of gases will be of interest in chapter 4.2 dealing with the consolidation – i.e. heating – and oxide and nitride formation of the powders.
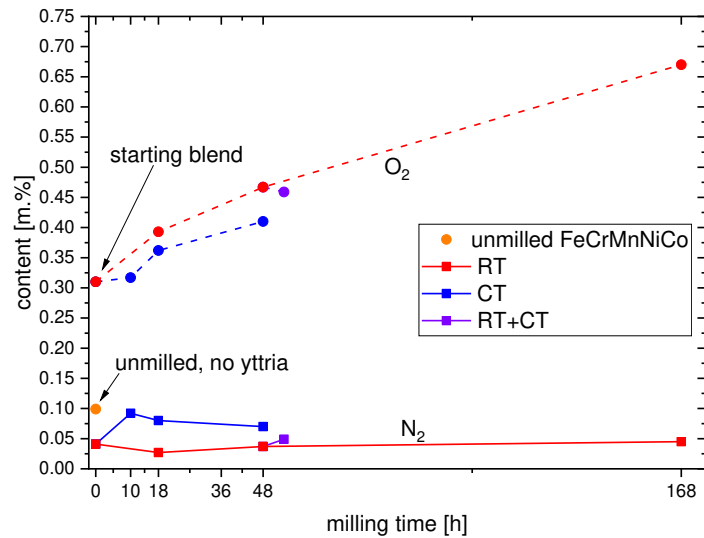
Figure 41: Oxygen and nitrogen content of the samples obtained from combustion analysis as a function of milling time and –temperature.

During mechanical alloying, powder particles get repeatedly fractured and cold-welded, and therefore, the powder particles' morphology and size are expected to be milling time and temperature dependent. Representative powder particles before milling and after

milling at different milling-temperatures and -times are presented in Figure 42 depicting a rather spherical shape of the particles.
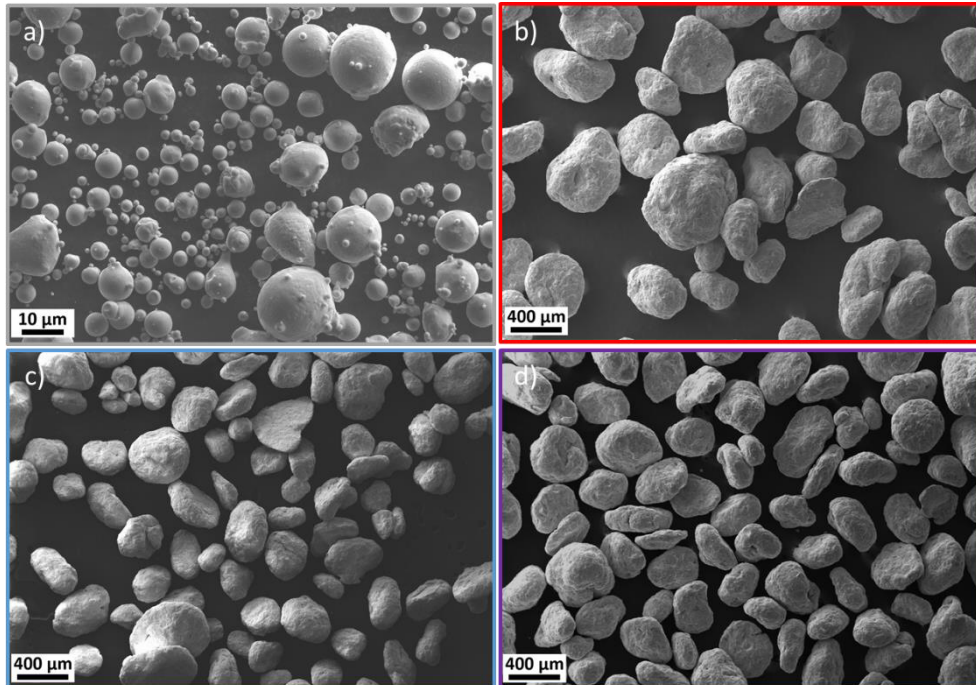
Figure 42: Representative SEM images of the a) gas-atomized powder, b) 48h/RT, c) 48h/CT and d) 48h/RT+6h/CT milled powders indicating a particle size increase upon milling and a decrease at cryogenic milling temperatures [35].

Furthermore, visually comparing the unmilled specimen in Figure 42a with the milled specimen suggests an increase of the particle size upon milling – note the different scale bars – while the 48h/RT specimen indicates the largest particles. This visual assumption is supported by the particle size analysis obtained from at least four SEM images taken from samples exposed to different milling conditions, see Figure 43. By this, a particle size of approx. 400 µm was obtained for the 48h/RT sample whereas the 48h/CT specimen achieves approx. 300 µm. Furthermore, by this image, an overall increase of the powder particle size upon milling was observed similar to other studies dealing with the milling of fcc materials [117].
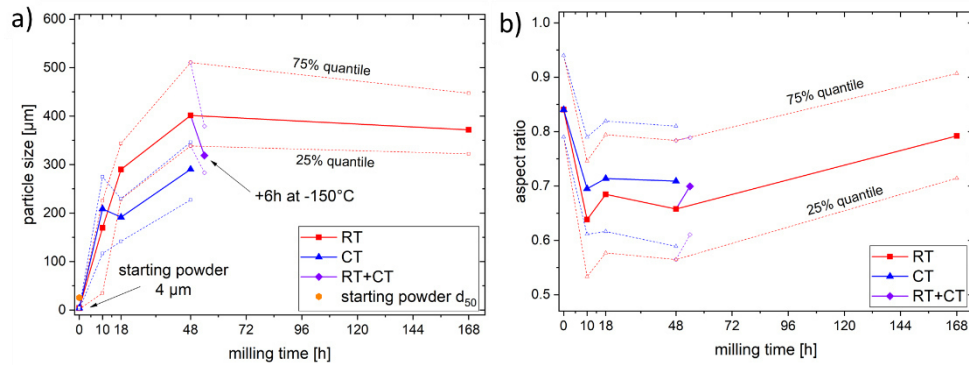
Figure 43: a) Powder particle size as a function of the milling time for the RT and cryomilled powders showing an increase with milling time and a decrease at lower milling temperatures. b) Aspect ratio against the milling time indicating no significant temperature dependence [35].

However, while no milling temperature dependent difference in the particle size can be observed for 10h of milling, this difference increases during further milling, as the cryomilled powder exhibit significantly smaller particles upon milling times beyond 18 h. This effect of cryogenic temperatures is also represented by the 48h/RT+6h/CT specimen, where 6h of milling at CT after milling for 48h at RT significantly reduces the achieved particle size. This temperature-dependent particle size allows assumptions regarding the temperature-dependent deformation mechanism of the used FeCrMnNiCo alloy, which is an important parameter for the refinement and dissolution of yttria during mechanical alloying. According to Suryanarayana [13], during mechanical alloying, powder particles get continuously cold-welded and subsequently fractured as a result of work-hardening, eventually reaching a steady-state particle size where cold welding and fracturing events occur at the same rate. Therefore, smaller particle sizes at lower milling temperatures of the same powder suggest a shift of this balance towards increased fracture events leading to smaller particles. This means in turn, that these FeCrMnNiCo powder particles exhibit an increased work hardening ability and higher strength at lower milling temperatures, which was previously reported in [22,24,118] and is directly related to deformation twinning [119].

Another important aspect of the morphology of powders, especially for the powder flow, is the shape or so-called aspect ratio. The aspect ratio represents whether the particles are spherical or flat with values

of one or close to zero, respectively. The evaluated aspect ratio as a function of milling time and temperature is presented in Figure 43b. Considering the 25% and 75% quantiles, no significant difference between the RT and CT milled powders was observed but powders tend to get slightly flattened upon milling. However, an achieved aspect ratio of approx. 0.7 shows a almost spherical shape of the milled particles that qualifies for potential additive manufacturing applications [120,121].

Previous studies for milled fcc alloys found both morphologies, flat or flaky particle shape [117,122] and spherical particles [69,123–125] and even a combination of both morphology types has been reported [126,127] so far. Suryanarayana [13] suggested that the powder particles' morphology is related to the BPR (ball-to-powder-mass-ratio) and proposed spherical particle shapes for BPRs above 10:1, whereas a lower BPR tends to form flaky particles. However, a comparison of the BPRs of above-mentioned literature and considering the results of this work disagrees with this hypothesis as in all cases, a BPR of 10:1 or larger was used. Consequently, other parameters such as the applied rotational speed, the overall design of the milling apparatus, (length and number of the milling pins and their distance to the milling vial) as well as the size of the milling balls might influence the powder particle's aspect ratio.

4.1.2 Milling temperature dependent yttria size distribution from macro- to nanoscale

At longer milling times, yttria particles are expected to refine within the matrix powder as a result of the continuous cold welding and fracturing of the powder. Therefore, in order to investigate the size and phase fraction of yttria, cross-sections of all milled specimens were analyzed and representative SE in-lens Hi-res SEM images are shown in Figure 44, depicting yttria particles as white spots. The RT milled samples are presented in Figure 44a-d, and the cryomilled samples are shown in Figure 44e-g. The combination of both milling temperatures is depicted in Figure 44h. Regarding milling time, visual inspection of the yttria particles suggests a decrease of the yttria phase fraction upon longer milling times and the dispersions seem more uniformly

distributed. The 18h milled samples for both milling temperatures exhibit a typical lamellae structure indicating the second stage of mechanical alloying as described by Suryanarayana [13] but at this stage, no temperature dependence on the lamellae structure was observed.

A comparison of the 48h/RT, the 48h/CT and the 48h/RT+6h/CT specimen presented in Figure 44c, g and h respectively indicates a lower yttria phase fraction in the 48h/CT specimen compared to the 48h/RT sample. This decrease together with an overall comparable Y content as presented in Figure 40 indicates an increased refinement of yttria below the SEM resolution limit of 17 nm, representing 3 pixels in the 10k magnified in-lens SEM image as described in chapter 3.2.1.
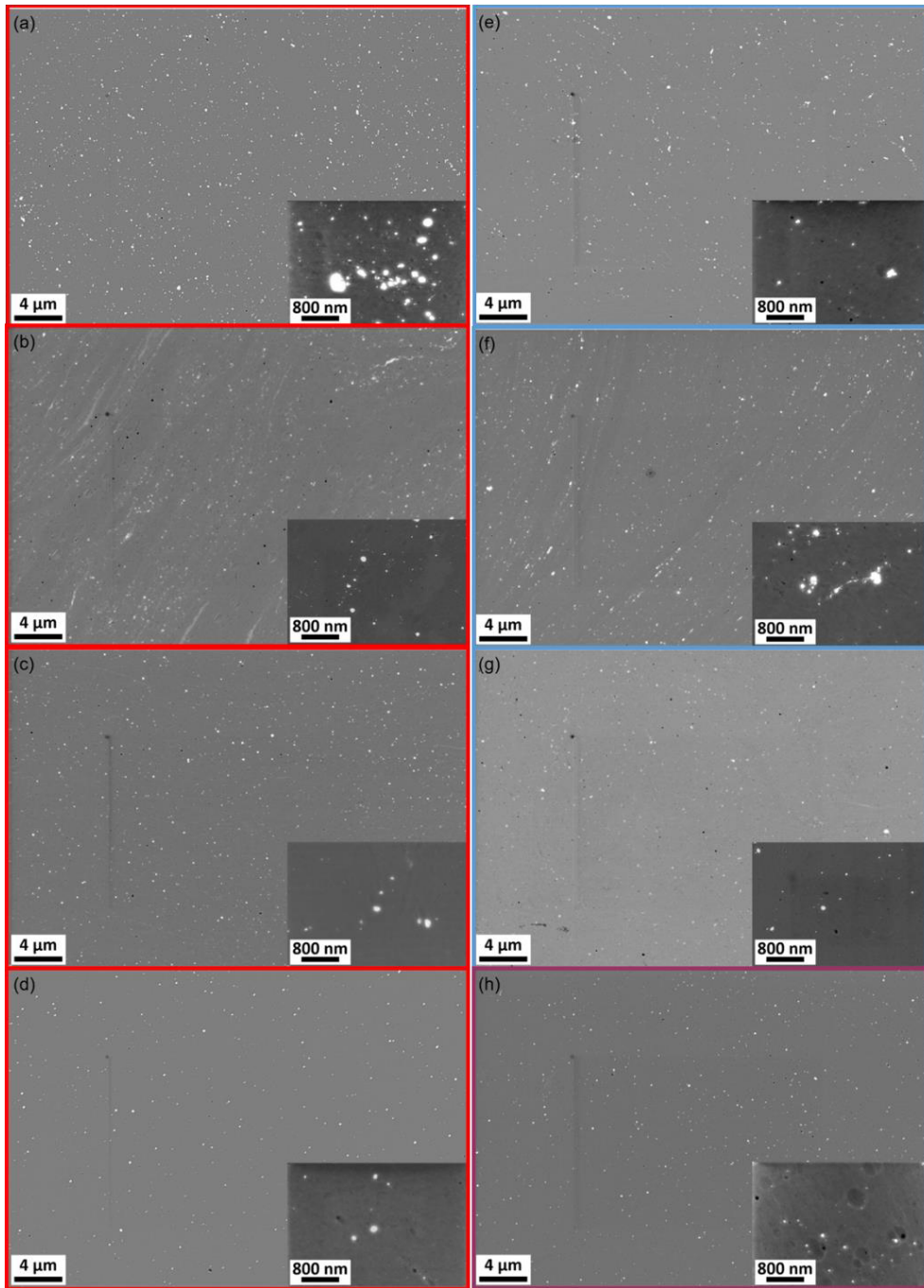
Figure 44: In-lens SE HR-SEM images indicating yttria as white spots for the a) 10 h, b) 18 h, c) 48 h, d) 168 h samples milled at RT; and e) 10 h, f) 18 h, g) 48 h specimen milled at CT; and h) the sample milled for 48 h at RT and a subsequent milling for 6 h at CT. The observable phase-fraction of yttria decreases at longer milling times and cryogenic milling temperatures [35].

To quantify the above hypothesis, the phase fraction of detectable yttria was determined at several positions and three different magnifications and compared with the initially added yttria. The resulting phase fractions presented in Figure 45 imply a lower amount of by HR-SEM detectable yttria – i.e. particles larger than 17 nm – at longer milling times. Therefore, an increased amount of yttria particles in the cryomilled specimen is smaller than 17 nm or supersaturated in the matrix. This observation can be seen more clearly if the detected phase fraction is compared with the overall amount of yttria as measured by EDS as presented in Figure 40. By this, for the 48h/CT specimen, a percentage of 87 vol.% of the added yttria is below the detection limit while for the 48h/RT sample, approximately 70% are not detectable again implying an increased refinement during CT milling. Even milling for 168h at RT yields just 83% of undetected yttria suggesting a faster and more effective refinement of yttria at low milling temperatures. Furthermore, by investigating the standard deviation of the phase fraction of the milled powders, a significant decrease of inhomogeneity within the milled powders is observed indicating a more homogeneous distribution at longer milling times.

Detailed investigation of the refinement of yttria is shown Figure 45b-c which shows the relative particle size distribution of the detected yttria particles, with each data point representing a diameter range of 10 nm. At shorter milling times, the relative particle size does not show significant differences but as the yttria phase fraction decreases, particles seem to get refined at all measured length scales. However, at longer milling times, pronounced differences between the different milling temperatures are observed, as cryomilling appears to reduce the oxide particle size close to the detection limit of the HR-SEM as marked by arrows. On the contrary, the 48h/RT and 168h/RT specimen exhibit the highest fraction close to the detection limit and the 48h/RT+6h/CT sample indicates a transition state confirming the temperature effect of lowering the particles close to the detection limit.
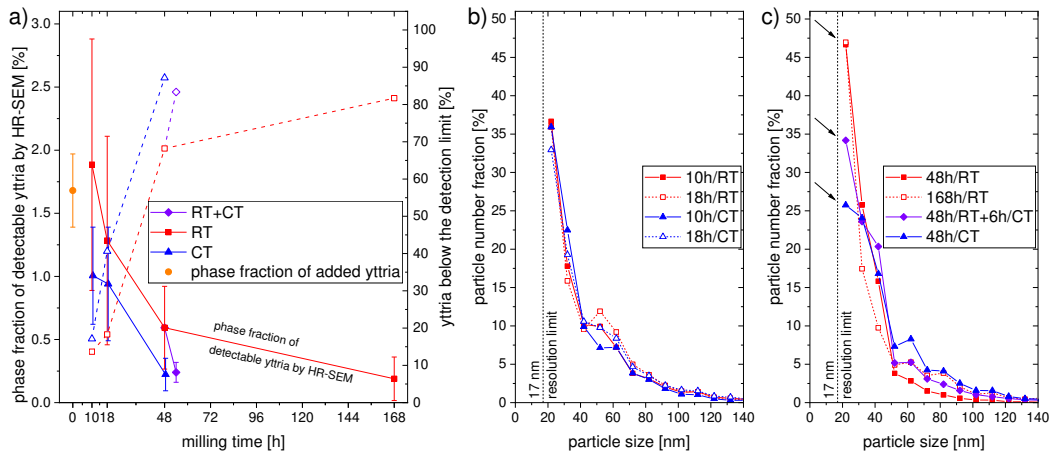
Figure 45: a) Phase fraction of detectable yttria (solid line) by HR-SEM and calculated percent of yttria below the detection limit (dotted line) of the HR-SEM (smaller than 17 nm) presented as a function of the milling time for specimens milled at RT and CT. The initially added yttria phase fraction was calculated from the associated overall Y content measured by EDS. b) Milling time and –temperature independent particle size distributions for 10 h and 18 h milling time at room temperature (RT) and cryogenic temperature (CT). c) The particle size distributions of the 48h/CT, 48h/RT+6h/CT, 48h/RT and 168h/RT milled samples showing a decrease of the smallest particle fraction at lower milling temperatures as indicated by arrows [35].

In order to extend these observations towards smaller yttria sizes, the area below 17 nm was investigated using TEM-EDS mapping, but due to the small investigated area, these measurements lack the statistical power to be included in the analysis obtained from in-lens SEM images. Nevertheless, Figure 46 depicts STEM-EDS and TEM-EDS maps of the 48h/RT, 48h/RT+6hCT and 48h/CT specimens allowing assumptions on the refinement of yttria at length scales below 17 nm.
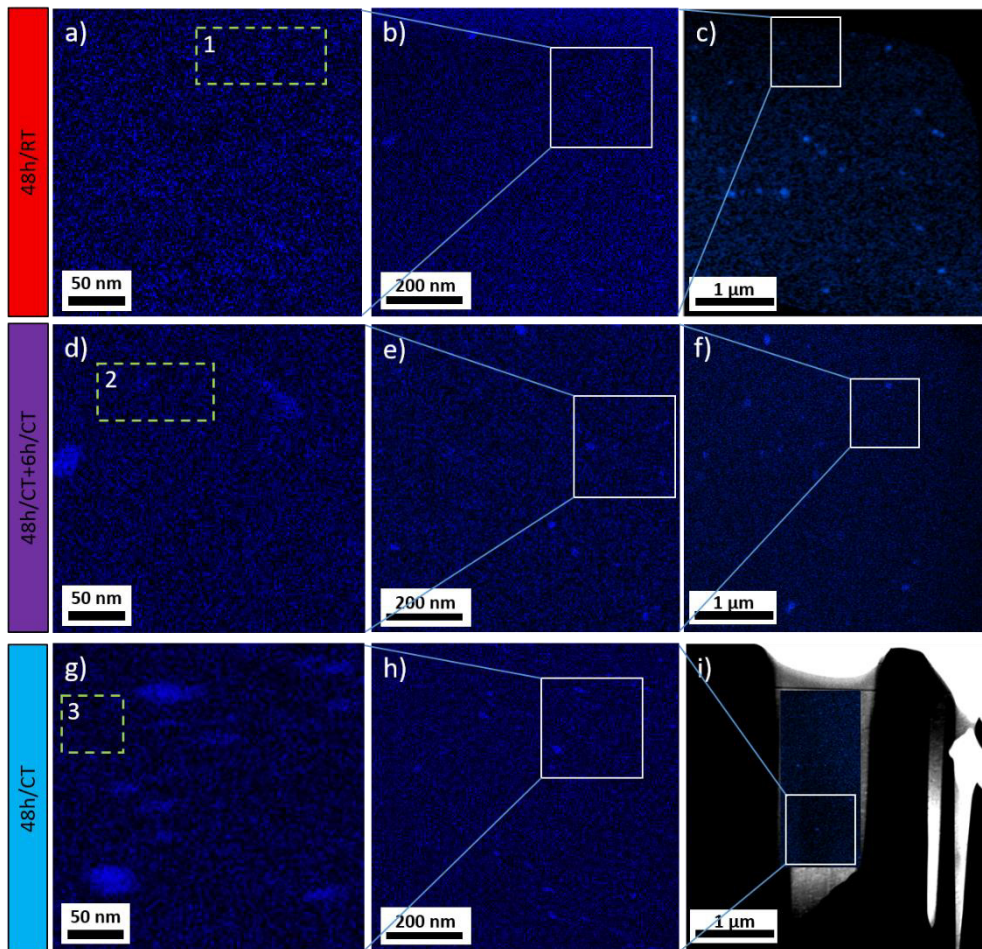
Figure 46: Y-TEM-EDS maps of the 48h/RT (a, b), 48h/RT+6h/CT (d, e) and 48h/CT (g, h) specimens at two different magnifications and the corresponding Y-STEM-EDS-maps (c, f, i) showing a higher fraction of fine yttria particles in the samples milled at CT. The dashed areas (1-3) represent the area from where the matrix chemistry was measured. Results of the Y-matrix content yield 1) 0.42 at.%Y, 2) 0.41 at.%Y and 3) 0.39 at.%Y showing no significant difference between the measured specimen [publication B].

By inspecting the 48h/RT specimen presented in Figure 46a-c, the lowest magnification exhibits the highest fraction of yttria whereas no detectable yttria particles appear in the highest magnification. It has to be mentioned that the shown pictures are representatives of various analyzed positions. In contrast to the room temperature milled sample, the 48h/CT specimen suggests an increased number density of yttria particles at the highest magnification in Figure 46g implying a stronger refinement of yttria during cryomilling. The smallest by this method detectable particle exhibited a size of 10 nm in diameter. The assumption of increased refinement upon cryomilling is again supported by investigating the 48h/RT+6h/CT specimen indicating

59

an in-between state concerning the number fraction of detectable yttria particles. Therefore, the results obtained from in-lens SEM images can be extended towards smaller particle sizes indicating increased refinement of yttria at cryogenic milling temperatures.

As yttria exhibits a higher yield strength of 7 GPa [128] compared to a heavily deformed FeCrMnNiCo alloy at RT exhibiting 2 GPa [21], a simple crushing of yttria is not expected. Nevertheless, according to Ashkenazy [40], the refinement behavior of incoherent particles in a ductile matrix - such as yttria in fcc - is based on dislocations piling up at the particle-matrix interface, forming an amorphous shell around the particle. High stresses at this interface then cause the interface's relaxation and refining. Literature on the temperature-dependent deformation behavior of the FeCrMnNiCo alloy, [22,24,118] together with results in chapter 4.1.1, suggest increased work-hardening and strength at low deformation temperatures – i.e. milling temperatures – possibly indicating higher defect densities. Therefore, at this length scale, increased defect densities and strength of the matrix are suggested to lead to increased refinement of yttria as described by Ashkenazy [40]. The observation that the 48h/RT+6h/CT specimen represents an in-between state between RT and CT milling concerning the yttria size distribution confirms this hypothesis. It is proposed that the yttria size for particles larger 10 nm exhibit a temperature dependent equilibrium where the transition from RT to CT is not yet finished after milling for 6h at CT after 48h at RT.

However, the smallest by these methods observed particle size yielded approximately 10 nm and inspecting the TEM-EDS measurements in Figure 46, which represent the matrix composition in-between yttria, shows high amounts of undetected Y in the matrix. Comparing the, within the detection limit comparable, yttria content of approximately 0.40 at.% with the initially added 0.55 at.% Y yields that approx. two-thirds of the added yttria is milling temperature independently refined below 10 nm.

Therefore, in order to shed light onto the yttria distribution below 10 nm, APT measurements were conducted. APT is a powerful technique to chemically analyze a small volume to get insights into the

clustering behavior of selected elements. Figure 47 presents the results of a Y and O cluster search algorithm of the APT-tips of the 48h/RT, 48h/RT+6h/CT and the 48h/CT specimens shown in Figure 47a-c, respectively. The overall Y content of each tip, as depicted in the top of each image, confirms the matrix TEM-EDS results by exhibiting no significant variation between the milled samples.
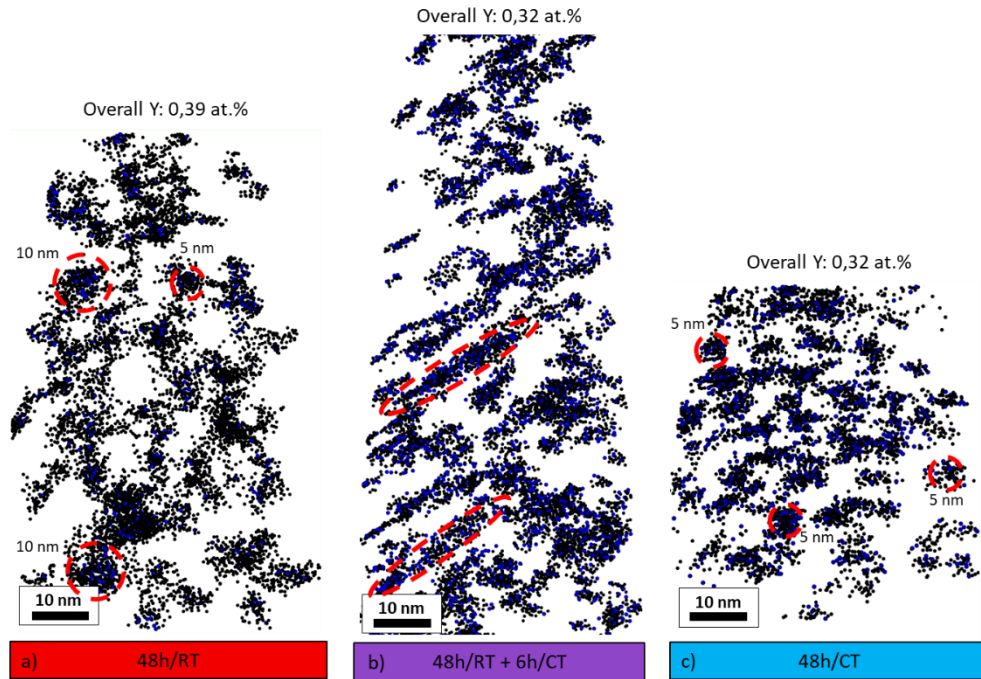
Figure 47: Cluster analysis for Y and O of the APT tips of the a) 48h/RT, b) 48h/RT+6h/CT, and c) 48h/CT specimen indicating smaller cluster sizes for the CT specimen while the combination of both milling temperatures shows a transition state. The respective Y-content of the entire tip is shown above each tip and marked areas indicate selected clusters with their corresponding size [publication B].

Investigating the size and structure of the clusters indicates network-like structures due to which a quantitative analysis of the cluster size could not be applied. Nevertheless, by visual comparison, clusters in the 48h/CT specimen appear smaller compared to the 48h/RT sample while the clusters of the 48h/RT+6h/CT exhibits elongated shapes. These elongated cluster shapes are suggested to represent a state in-between the at room temperature and cryogenic temperature milled samples for which the transition from a RT to a CT equilibrium cluster size is not yet finished after 6h of milling at cryogenic temperatures. Visual concerning the size of the clusters (marked in Figure 47)

61

suggests maximum 10 nm sized clusters in the 48h/RT sample, while in the 48h/CT specimen, the smallest clusters appear to size approx. 5 nm. The observed elongated clusters in the 48h/RT+6h/CT sample could be interpreted as a transition progress from a RT equilibrium cluster size to a CT cluster size, which is not yet finished after 6h of cryomilling.

The overall volume fraction of clusters yields 4 vol.% for all three investigated powders and is thus, independent from the milling temperature. Furthermore, as described in chapter 3.2.3, artefacts occurring in the measurement of clustered elements cause an alternation of the size and chemistry of clusters (local magnification effects [129]). Based on an estimation for the current alloy, Y-enriched clusters are expected to be approx. 25% larger than measured by APT. As a result, the actual volume fraction of the clusters can be estimated to 5 vol.%. However, the theoretical volume fraction of the initially added yttria is significantly lower with a calculated value of 1.7 vol.%. This observation might already indicate a dissolution of yttria which will be discussed in chapter 4.1.3.

A correlation of the size of these clusters with TEM microstructure images is presented in Figure 48. The size and shape of the clusters obtained from the APT analysis correlate well with the black structures in the TEM image suggesting that these areas are Y and O enriched nanoclusters. Furthermore, Y is heavier than the matrix elements and is therefore expected to appear darker in the BF images supporting this assumption. Investigation of the images confirms the network-like structures and smaller cluster sizes for the cryomilled sample as obtained by APT and also indicates that the obtained clusters are located within the nanograins of the milled powders. Even though both investigation methods just yield visually estimated cluster sizes, the correlative use of both methods, which also investigate a similar sample thickness, strengthens the assumption that cryomilling results in smaller cluster sizes.
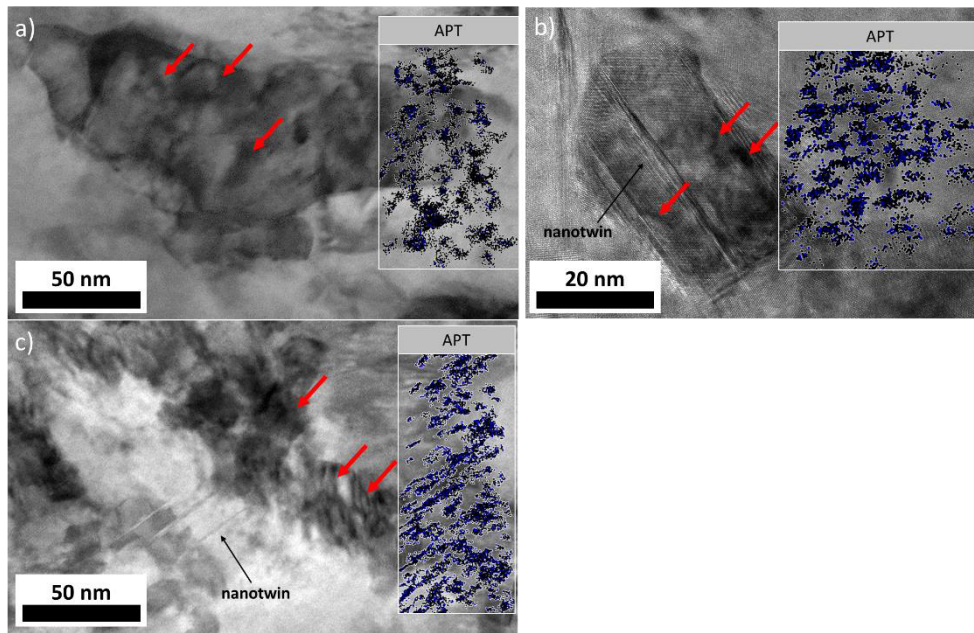
Figure 48: Size- and shape-correlation of BF-TEM-microstructure images with the results of the cluster search in APT-tips (in boxes on the right of each image) of a) 48h/RT, b) 48h/CT and c) 48h/RT+6h/CT. The correlation suggests that the black areas in the TEM images, indicated by red arrows, correspond to the nanoclusters observed in APT. Note that the APT-tips and TEM-lamellae were not prepared from the same position and that b) has a smaller scale bar .

Such clusters, also called nanoclusters, were already observed in mechanically alloyed steels in literature [36,130], forming distinct clusters [130,131] or percolated structures [18] in the size of a few nanometers. To estimate the size and stability of such nanoclusters, Zhao et al. [42] used first-principle theory at bcc steels proposing that strain originating from the presence of O-vacancy pairs is an important factor for smaller sizes and higher stability of these nanoclusters. As suggested previously, increased work-hardening and higher densities of lattice defects are proposed at cryogenic milling temperatures, resulting in increased lattice strains. This previous assumption therefore correlates well with the smaller cluster sizes proposed in the literature; the smaller cluster size in the 48h/CT sample is thus likely the result of higher lattice strains. However, the source of the strains cannot be concluded at this stage but will be discussed later in chapters 4.1.4 and 4.1.5. Investigation of the size and shape of the Y and O enriched nanoclusters in Figure 48 suggests that the by APT observed clusters are within the nanometric grains forming network-like structures comparable to the percolated aspect described by Brocq et.

al [18]. However, even though the observed shape correlates well with the theory of Kimura et al. suggesting amorphous phases around nanocrystalline grains, his hypothesis cannot be confirmed in this study as the hereby observed clusters seem to be located predominantly within nanograins. Furthermore, analysis regarding crystallinity will be discussed in chapter 4.1.3.

Figure 49 represents an attempt to illustrate the overall temperature dependent yttria size distribution based on the results of this work.
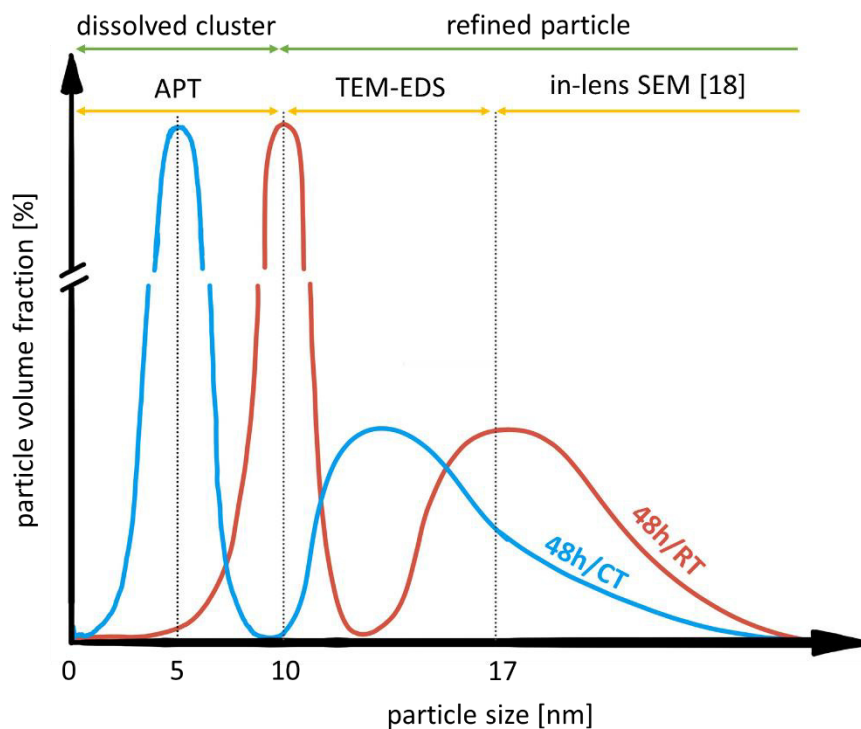
Figure 49: Illustration of the proposed yttria size distribution at all length scales after milling for 48h. By this, two-thirds of the yttria is refined below 10 nm (illustrated by the cut y-axis) while at both yttria size regimes, below and above 10 nm, yttria is smaller for the 48h/CT sample. Note that the 48h/RT+6h/CT sample is not depicted for a better visual presentation, but their size is expected to be in-between the other two specimens [publication B].

At both yttria length scales, larger and smaller 10 nm, yttria is proposed to exhibit an equilibrium size dependent on the strength and defect density of the matrix and therefore, on the milling temperature. To this end, based on the observation that approx. two-thirds of the added yttria is milling temperature independently refined below 10 nm,

64

two size regions for the refinement of yttria are proposed with 10 nm as a transition from nanoscale to mesoscale refinement.

4.1.3   Differentiation between particle and cluster of the observed yttria by crystallinity

The smallest by TEM-EDS detected particles sized approximately 10 nm while APT found small clusters with sizes of 5 nm in the 48h/CT sample. Now, the question arises whether these particles are crushed remnants of the initial yttria or already forming clusters with a changed crystal structure. Note that the author defines clusters as elemental enrichment within the matrix – i.e. without separate crystal structure – whereas particles exhibit their own crystal structure. However, to the best of the author's knowledge, no definition has been published so far and, in many cases, both terms are used together.

In order to evaluate this question, a diffraction map of the 48h/CT specimen, in which the particle refinement is most pronounced, was measured, and the results, together with a TEM-EDS map and bright-field (BF) and high-angle annular dark field (HAADF) images from the same location, are presented in Figure 50. Three representative diffraction patterns extracted from the diffraction map are depicted in Figure 50d.

In the HAADF image, yttria particles appear as black areas, which is confirmed by comparison with the TEM-EDS-map. The diffraction pattern depicted in Figure 50d-2 indicates the single-phase fcc matrix while Figure 50d-3 represents a larger yttria particle with approximately 40 nm. The corresponding diffraction pattern of one of the smallest by TEM-EDS detectable particles with approx. 10 nm is presented in Figure 50d-1. The diffraction patterns of both yttria particles indicate a similar and complex crystal structure as in both cases diffraction spots are close to the center whereas the fcc matrix has a distinct diffraction pattern. Therefore, by this comparison, it is assumed that the small 10 nm yttria particle possesses yttria crystal structure. Hence, the diffraction map reveals that particles down to approximately 10 nm exhibit yttria crystal structure. However, no smaller particles could be identified and no other structures besides fcc

were found indicating cluster formation below 10 nm. Nevertheless, it has to be mentioned that due to the thickness of the TEM lamellae of approx. 50 nm and the resulting uncertainties of the used method, the latter observation needs to be taken with care.
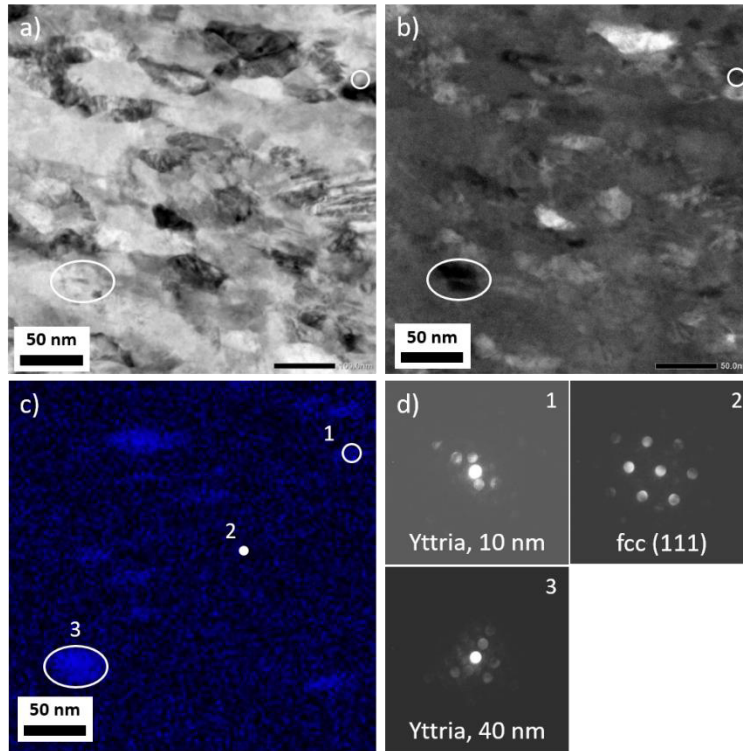
Figure 50: a) TEM-BF, b) TEM-HAADF, c) Y-TEM-EDS-map and d) selected diffraction patterns obtained from the diffraction map obtained from the 48h/CT sample in order to evaluate the matrix and yttria crystal structure. The results confirm an yttria crystal structure down to particles sizes of about 10 nm and therefore no dissolution of these yttria particles is suggested [publication B].

In order to obtain much broader information about the crystallinity, HE-XRD measurements were undertaken and the resulting representative diffraction pattern of the milled samples together with the heated 48h/RT specimen as a representative example are presented in Figure 51.
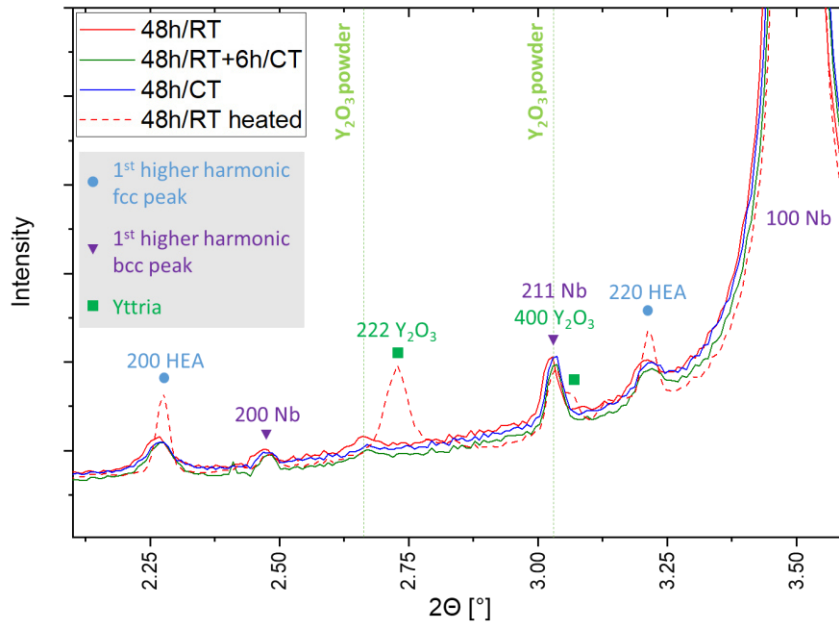
Figure 51: HE-XRD pattern of the milled specimen at RT and the 48h/RT sample after heating to 1100°C, holding for 15 min and subsequent cooling indicating the growth of the yttria peaks upon heating. The marked peak positions of Y₂O₃ powder were measured using Cu-radiation and recalculated to synchrotron wavelength. The peak positions of yttria after heating are shifted to slightly larger 2Θ angles [publication B].

Between the milled specimens, no significant difference is observed in the diffraction pattern. The yttria peaks marked in the image were obtained from the initial powder using a laboratory XRD and re-calculated to synchrotron wavelength. Evaluation shows a slight indication of a peak at a 2Θ of approx. 2.7° whereas the yttria peak at 3° overlaps with a harmonic Nb bcc peak of the capsule and is therefore not visible. However, after heating of the 48h/RT powder, both yttria peaks clearly increase in size and shift towards larger 2Θ angles indicating a lattice parameter decrease which was also reported by Zhang et. al [71]. This observation shows an increased amount of crystalline yttria in the heated specimen compared to the milled samples suggesting a high fraction of yttria without yttria crystal structure present after milling. Yttria below 10 nm in size is therefore likely to be present as clusters. Here it has to be mentioned that all other heated samples show the same trend but are not shown for a better visualization.

A dissolution of yttria into nanoclusters was already proposed by previous works [132–134] whereas Saber et al. [134] suggested a saturation of the matrix. In his work investigating ferritic ODS steels, the absence of yttria's crystalline diffraction reflexes obtained by TEM was interpreted that not dissolved yttria forms an amorphous phase, even if 10 m.% of yttria was added. The latter contrasts the results in this work finding yttria crystalline particles down to approx. 10 nm. However, based on the milling temperature independent fraction of yttria below 10 nm, a matrix saturation is proposed while the nearly undetected yttria peak in HE-XRD investigations suggests a dissolution into clusters for particles smaller 10 nm. To support the theory of a dissolution at small length scales, APT cluster analysis in chapter 4.1.2 found a significantly larger volume fraction of clusters than expected, even by considering APT artefacts. Such an increased volume fraction of Y and O enriched clusters means the uptake of matrix elements into the clusters and thus, suggests a mixing with matrix elements and therefore, a dissolution of Y and O into the matrix. Furthermore, in correlation with the proposed yttria size distribution in chapter 4.1.2, one-third of the added yttria is expected to be larger 10 nm, and therefore, to exhibit yttria crystal structure. The height of the corresponding yttria peak should therefore be one-third compared to the heated yttria peak, which was, however, not observed in the HE-XRD pattern. Nevertheless, according to Scherrer [135], small crystallite sizes broaden the peak which means in turn that the height of the peak decreases. Therefore, such small yttria particles with sizes of 10 nm are expected to significantly broaden the peak and thus, decrease the height of the peak. As a result, and in analogy to the size classification in chapter 4.1.2, it is assumed that particles above 10 nm are crushed remnants of the initial yttria while approx. two-thirds of the added yttria are refined below 10 nm and are dissolved as nanoclusters, without an own crystal structure.

4.1.4 Temperature dependence of introduced defects as a key for yttria distribution during mechanical alloying

As mechanical alloying is a process comprising severe plastic deformation, the evolution and type of defects is of great importance in order to understand the deformation behavior as well as the refinement and dissolution of yttria. Representative TEM microstructure images of the milled powders are presented in Figure 52, indicating a highly deformed nanocrystalline grain structure [136]. Visual comparison of the microstructures indicates smaller grain sizes in the 48h/CT specimen compared to the 48h/RT specimen whereas in the 48h/RT+6h/CT specimen, grain boundaries are not clearly visible. Grain sizes evaluated visually ranged from 50-100 nm in the 48h/RT sample to 20-40nm in the 48h/CT sample.
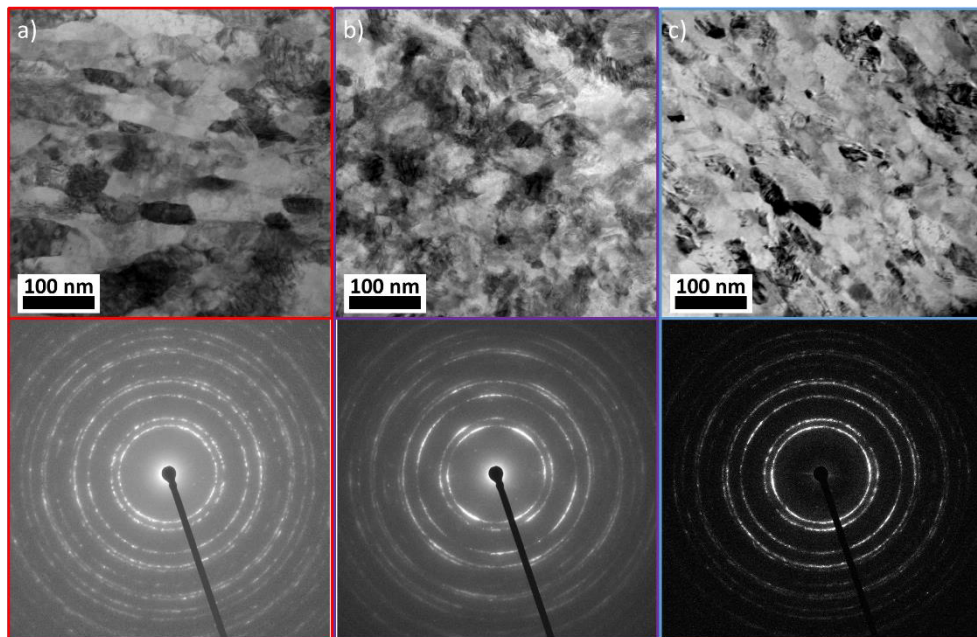
Figure 52: TEM-BF microstructure images with corresponding diffraction patterns of the a) 48h/RT, b) 48h/RT+6h/CT and c) 48h/CT specimen indicating smaller grains at lower milling temperatures [publication B].

The corresponding TEM diffraction patterns show increased spottiness of the 48h/RT specimen compared to the 48h/CT sample indicating less, and therefore, larger grains in the 48h/RT specimen. The diffraction rings of the 48h/RT+6h/CT sample with locally brighter areas indicate a deformation texture suggesting a non-uniform

deformation. Such a nanocrystalline microstructure was already reported by Schuh et. al [21] investigating a FeCrMnNiCo alloy produced via severe plastic deformation while such unclear "blurry" grain boundaries as exhibited by the 48h/RT+6h/CT sample are often associated with internal stresses related to the non-equilibrium state of grain boundaries in nanostructured materials [137]. Furthermore, the formation of nanocrystalline grains as well as their stable grain size is reported to be a result of high defect densities, especially dislocations [54] and stacking faults [14]. Therefore, at lower milling temperatures, less defect recovery and increased strength are suggested to develop higher defect densities resulting in smaller stable grain sizes in this ODS FeCrMnNiCo alloy.

To investigate this hypothesis, XRD measurements were conducted in order to get insights into the defect evolution during mechanical alloying of this ODS FeCrMnNiCo alloy. In this context, the full-width-half-maximum (FWHM) of the (111) peak of all milled specimens as well as representative diffraction patterns are presented in Figure 53. The diffraction pattern in Figure 53b depicts the unmilled powder as well as the 48h/RT, 48h/CT and 48h/RT+6h/CT samples. Investigating these patterns shows much smaller and broader peaks for all milled samples, with the 48h/CT specimen showing the broadest peaks. In order to quantify this observation, the FWHM, a fundamental parameter of lattice defects which increases with decreasing crystallite size as well as increasing lattice strain, is shown in Figure 53a at the example of the (111) reflection. The FWHM is significantly larger for all cryomilled specimen compared to their room temperature (RT) milled counterparts indicating higher defect densities or lower crystallite sizes for the cryogenic temperature (CT) milled samples. This temperature effect is also observed by inspecting the 48h/RT+6h/CT specimen where 6h of milling at CT after 48h of milling at RT increases the FWHM – and thus the density of lattice defects. Generally, lattice strains are caused by dislocations, stacking faults, vacancies, interstitial and substitutional elements [107]. Milling for 168h at RT yields the same FWHM as observed in the 48h/CT specimen suggesting an accelerated defect formation of this FeCrMnNiCo alloy at cryogenic milling temperatures.
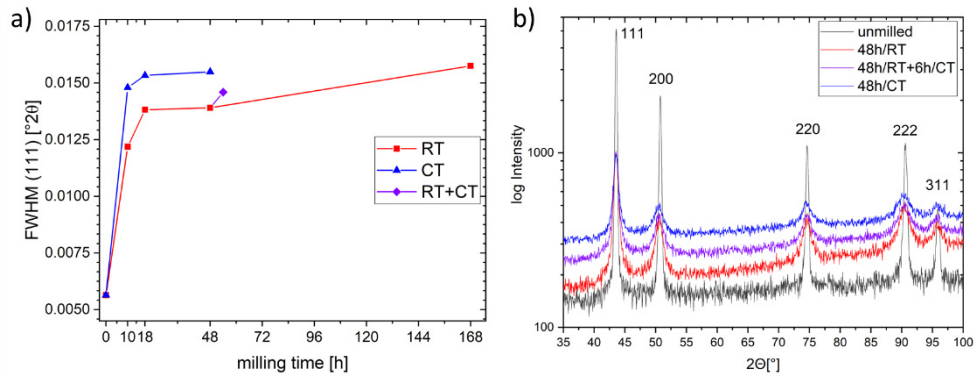
Figure 53: a) FWHM of the (111)-reflection for all milled samples as a function of milling duration at RT and CT as well as its combination, RT+CT. b) X-ray diffraction patterns of the unmilled, gas-atomized powder and the powders milled for 48h at RT, 48h at CT and the combination of both milling temperatures, respectively. Both figures confirm broader peaks after milling at CT compared to RT milling [35].

Furthermore, the FeCrMnNiCo alloy is reported to exhibit a low and strongly temperature-dependent stacking fault energy [23,25], upon which, stacking faults and twins can be easily formed during deformation. Therefore, Figure 54 presents the stacking fault probability (SFP) derived from XRD patterns of all samples as a function of milling time and temperature. The SFP is a measure for the formation of deformation induced stacking faults and describes the probability of finding a stacking fault between any two layers in the fcc stacking sequence [113]. An increased SFP suggests increased densities of stacking faults and thus defects, as they represent one specific type of defect. As for their formation dislocations are necessary [11], this might also indicate that also an increased dislocation density is present. Consequently, stacking faults and twins drastically influence the deformation behavior of metals as they contribute to deformation and represent barriers for dislocations which is strengthening the alloy [14,54,118].

71
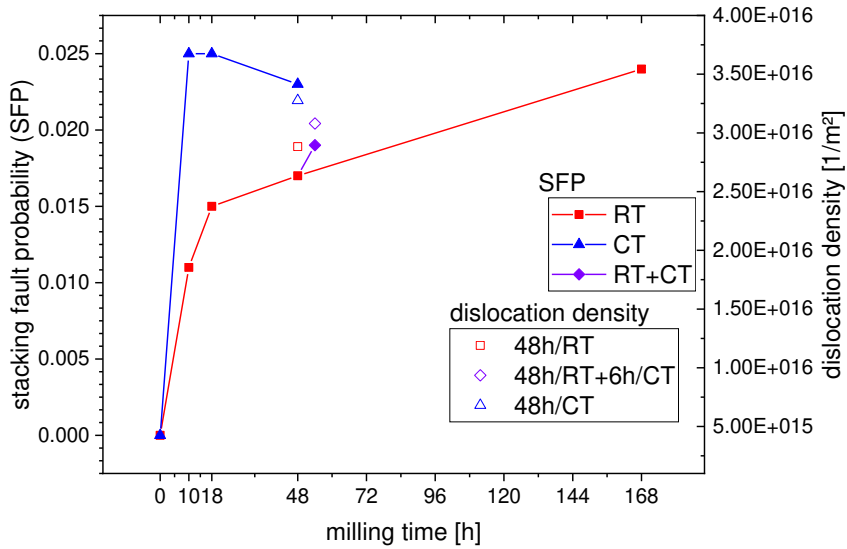
Figure 54: SFP calculated from the asymmetric peak shift of the (111) and (200) fcc reflections of the FeCrMnNiCo alloy as a function of milling duration at RT and CT, as well as its combination showing a higher SFP for the cryomilled specimen. The gas-atomized, unmilled sample was used as a reference for the undeformed state. The dislocation density depicted in this figure was calculated from HE-XRD measurements using the modified Warren-Averbach approach. It shows increased values for the 48h/CT sample in comparison to the 48h/RT specimen, whereas the 48h/RT+6h7CT sample lies in-between.

Investigation of Figure 54 reveals increased SFPs in all cryomilled samples compared to the RT milled powders. Milling at CT rapidly increases the SFP but stays rather constant at approximately 0.025 at longer milling times, which would mean that a stacking fault is present at every 40th atomic (111) plane. On the contrary, milling at RT shows smaller SFPs at all investigated milling times but eventually reaches a SFP close to the 48h/CT specimen at 168h of milling. The effect of low milling temperatures is confirmed by the fact that the 48h/RT+6h/CT sample shows a significantly increased SFP after only 6h of cryomilling of a 48h/RT sample. These findings are corroborated by Hi-res TEM microstructure images in Figure 48 showing the presence of nanotwins in both cryomilled specimens – 48h/CT and 48h/RT+6h/CT – whereas none were observed in the 48h/RT sample.

The dislocation density for the 48h/RT, 48h/RT+6h/CT and 48h/CT specimens, determined from HE-XRD measurements using a modified Warren-Averbach method, is depicted in Figure 54 superimposed to the SFP. All investigated specimens exhibit high dislocation densities in the order of 10^{16} m^{-2}, which is in the range of

72

e.g. martensite. However, similarly to the SFP, the 48h/CT sample shows the highest dislocation density, whereas the 48h/RT+6h/CT sample is in-between, showing a tendency towards slightly increased dislocation densities upon cryomilling.

These results of the SFP are in good agreement with recent studies of similar fcc materials [14,22,138,139] suggesting a higher fraction of twinned grains during deformation at low temperatures confirming a low and temperature-dependent stacking fault energy (SFE) as calculated by Huang et al. [25]. However, Stepanov et al. [14] observed lower dislocation densities as obtained by TEM, which is in contrast to the dislocation densities measured by HE-XRD measurements in this study. Nevertheless, the alloy investigated in this work was significantly higher deformed at higher deformation rates compared to the cold-rolled specimen of Stepanov et al. resulting in higher and possibly different defect structures and -densities. Regardless of the exact type and density of defects, both discussed types play a crucial part in the formation of nanocrystalline alloys by subdividing grains [14,34,50]. Therefore, increased defect densities such as planar faults and dislocations are suggested to be present in the cryomilled 48h/CT sample refining the grains and increasing the strength. The 48h/RT+6h/CT specimen indicates a transition state by apparently increased defect densities compared to the 48h/RT sample, whereas an accumulation and rearrangement of defects in order to subdivide grains has not yet taken place. This observation confirms interpretations of chapter 4.1.1, where increased strength due to increased defect densities in the cryomilled specimen was suggested to result in smaller powder particle sizes. Furthermore, these results are in good agreement with chapter 4.1.2 suggesting increased defect densities such as dislocations to be beneficial for the refinement and the stable particle size of yttria.

Beside dislocations and planar faults being responsible for the formation of nanostructured alloys, vacancies are reported to play a crucial role in the dissolution of yttria [43,133]. Therefore, in order to investigate the formation of vacancies, PALS (positron annihilation lifetime spectroscopy) measurements were conducted and compared with recent *ab-initio* calculations. According to our previous work [140],

the vacancy formation energy in the FeCrMnNiCo alloy linearly decreases with increasing lattice parameter. Table 5 shows the lattice parameter obtained by XRD measurements together with the calculated vacancy formation energies indicating an increase of the lattice parameter from 3,5978 Å for the RT milled sample to 3,6003 Å after cryomilling and, consequently, vacancy formation energies seems to decrease during cryomilling. The vacancy formation during mechanical alloying is activated by severe plastic deformation, which means in turn that vacancies are easier generated at cryogenic milling temperatures. Therefore, this observation suggests increased vacancy densities in the cryomilled specimen 48h/RT+6h/CT and 48h/CT compared to the 48h/RT sample.

Table 5: Lattice parameter of the milled specimen and the corresponding calculated vacancy formation energy indicating easier vacancy formation at lower milling temperatures. PALS results show an increase in the mean positron lifetime upon milling, which shows an increase in the open volume's size [publication B].

Specimen name	XRD lattice parameter [Å]	Vacancy formation Energy [eV]	Mean positron lifetime [ps]
unmilled, no yttria	3,5928	2,130	175
48h/RT	3,5978	2,113	200
48h/RT+6h/CT	3,5990	2,109	201
48h/CT	3,6003	2,104	200

In order to experimentally corroborate the existence of vacancies in the as-milled specimen, PALS measurements were conducted. PALS is a useful technique to examine open volumes such as vacancies by measuring the lifetime of positrons, which eventually get trapped at such open volumes within a sample. The results are presented in Table 5, showing an increase of the positron lifetime from 175 ps to approx. 200 ps after milling. According to literature, the bulk positron lifetime of the FeCrMnNiCo alloy is approx. 115 ps [141,142], whereas the lifetime of monovacancies is reported to be 170-180 ps [142,143] and divacancies exhibit lifetimes of 188 ps in Ni [144] and more than 200 ps for the FeCrMnNiCo alloy [143]. Therefore, the measured mean positron lifetimes suggest a higher amount of monovacancies present in the gas-atomized state, while milling is suggested to increase the

vacancy/volume size causing a mean lifetime value in the range divacancies. However, it has to be mentioned that the lifetimes stated in literature represent the corresponding lifetimes of single types of defects, such as dislocations or monovacancies, while in this study, a mean positron lifetime was obtained covering all types of defects. Hence, results show that the mean size of these open volumes is increasing during milling. However, no significant difference in the mean positron lifetime was observed between the milled specimens.Therefore, while the mean size of open volumes increases due to milling, no effect of the milling temperature was found. This could be either due to fact that the free volume concentration does not change or that so-called positron saturation trapping occurs. Nevertheless, due to the complex defect structure present after milling, the lifetime components of all types of defects superimpose and consequently, the fit of the spectrum could not be decomposed. Hence, no densities of each type of open volume could be measured.

To the best of the author's knowledge, no studies dealing with the temperature-dependent formation of mechanically generated vacancies have been published so far. Nevertheless, Ohkubo et al. [144] investigated the vacancy formation at RT in conventionally rolled Ni, showing that monovacancies are generated upon deformation while even stronger deformation did not increase the size of the vacancies. For high-speed deformation, mainly monovacancies but also low densities of vacancy clusters were observed. Other studies reported high vacancy densities after high-speed deformation of fcc thin foils proposing a vacancy-assisted deformation mechanism [145,146]. The ball-to-ball collisions during mechanical alloying occur at high deformation rates, and therefore, based on literature and results of PAS and *ab-initio* calculations [140], high densities of vacancies are expected after cryomilling. Furthermore, the hereby suggested increased vacancy densities in the cryomilled sample are in good agreement with chapter 4.1.2, implying that increased vacancy densities stabilize smaller nanoclusters. By this, cryomilling is suggested to increase the number of vacancies within the nanoclusters, consequently stabilizing smaller clusters.

4.1.5   Interaction of yttria with defects

As stated in chapter 4.1.3, it is suggested that approx. two-thirds of the added yttria is refined below 10 nm forming nanoclusters. In order to evaluate the mechanism of the cluster formation, this chapter analyses the APT cluster chemistry and correlates it with PAS-DB (positron annihilation spectroscopy doppler broadening) and literature. In this context, Figure 55a and b depict the ratio of the at.% of Y:O and the ratio of at.% of interstitial (O and N) to substitutional (Fe, Cr, Mn, Ni, Co, Y) elements within the clusters, respectively. The Y:O ratio shows yttria stoichiometric clusters for the 48h/RT and 48h/RT+6h/CT samples, while the ratio is significantly lower for the 48h/CT specimen. In the CT specimen, the ratio of substitutional elements, such as Fe, Cr, Mn, Ni, Co and Y, to interstitial elements such as O and N indicates a slight decrease of lattice elements in the matrix which is compensated by an increased amount of interstitial elements to maintain 100 at.% in total. However, O and N are not supposed to occupy lattice sites, and by taking into account that the volume fraction of the clusters is the same for all samples, as shown in chapter 4.1.2, this possibly indicates the presence of unoccupied lattice sites – i.e. vacancies – within the cryomilled sample.

Figure 55c shows the results of PAS-DB, an investigation technique to get insights into the chemical surrounding of annihilation sites such as open volumes or vacancies. This method compares the chemical signatures as a ratio to a reference state, which, in this study, is the unmilled powder mixed with 1 m.% yttria. Comparing the spectra of the milled specimen shows a clear trend of the cryomilled 48h/CT sample towards the signature of yttria, i.e. where all annihilation events happen within yttria. The 48h/RT sample indicates a less pronounced tendency, while the signature of the 48h/RT+6h/CT specimen is close to the 48h/CT sample but in-between the RT and CT specimen. Consequently, in the cryomilled specimen, more annihilation events occur in close proximity to yttria indicating yttria enrichments around vacancies, whereas this effect is less pronounced in the room temperature milled sample.
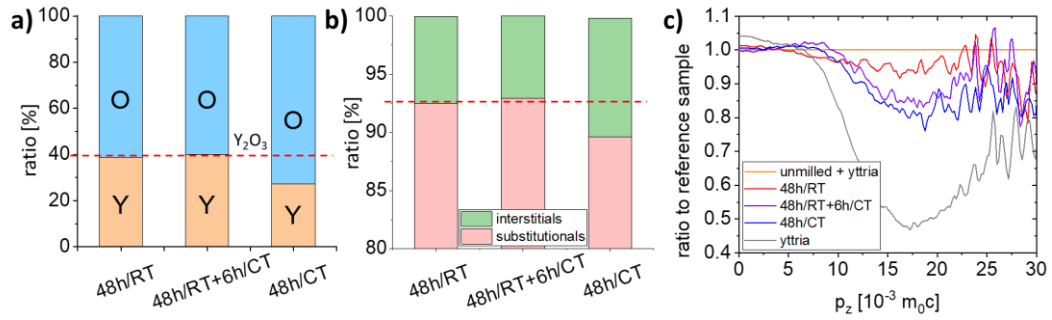
Figure 55: a) APT results of the ratio of at.% of Y:O of the clusters showing a lower Y:O ratio for the 48h/CT sample while the 48h/RT and the 48h/RT+6h/CT specimen yield yttria stoichiometry. b) Ratio of at.% of interstitial and substitutional elements within the clusters showing fewer matrix elements within the clusters for the 48h/CT sample. c) PAS-DB spectra showing the chemical signature of the milled specimens together with yttria relative to the unmilled powder mixed with 1 m.% yttria (1.0 line). The data indicates that the close vicinity of open volumes is decorated with yttria after milling, while for the cryomilled specimens, this effect is stronger [publication B].

Previous works suggested a dissolution of yttria at vacancies [15,36,44,130] or dislocations [147] in the late stages of mechanical alloying. According to first-principle calculations [44,148], vacancies strongly interact with oxygen, forming nanoclusters, whereas vacancies are reported to lower the formation energy of Y and O enriched nanoclusters below that of the stable oxide [15,44]. Even though these investigations were conducted for bcc steels, the results of Fang et al. [148] modeling the interaction of O with vacancies for the O-diffusion in Ni suggest that these calculations can be used for interpretations in this fcc FeCrMnNiCo alloy as well. To this end, the results of PAS-DB and the chemical ratios obtained by APT support the reported important role of vacancies in the formation of Y and O enriched nanoclusters by indicating the presence of vacancies within these clusters and extend these theories toward this fcc FeCrMnNiCo alloy. Furthermore, the results of this thesis suggest increased interaction of yttria with vacancies after cryomilling, possibly confirming the proposed higher vacancy densities within the cryomilled samples in chapter 4.1.4.

4.1.6 Summary of Temperature effect of the refinement and dissolution of yttria during mechanical alloying

This thesis showed that the powder particle size generally increases upon milling due to cold-welding of the ductile fcc FeCrMnNiCo powders even for cryogenic milling temperatures. Low milling temperatures, however, reduced the achieved final particle size compared to room temperature milling indicating a temperature dependent steady-state particle size. This observation is attributed to increased defect densities at cryogenic milling temperatures, such as mechanically formed twins and increased dislocation and vacancy densities, leading to a shift of the cold-welding and fracturing balance towards smaller powder particle sizes after cryomilling. The used milling setup in combination with the fcc FeCrMnNiCo alloy yielded relatively round particles for all samples, which is beneficial for the flowability and, therefore, the handling of the as-milled powders.

Furthermore, in Figure 49 it is postulated that independent of the milling temperature and after 48 h of milling, 10 nm represents a specific boundary, and therefore, the refinement and dissolution of yttria within the fcc FeCrMnNiCo alloy is suggested to be categorized into two yttria size regimes, larger and smaller 10 nm. Based on TEM and HE-XRD investigations, yttria larger 10 nm exhibits its initial complex yttria crystal structure and is therefore postulated to be crushed remnants of the initially added yttria. As a result, yttria larger 10 nm is suggested to refine as a result of high defect densities in the matrix but keeps its yttria crystal structure. As cryomilling increases the defect density within the milled powders, cryomilling possesses a beneficial effect on the rate of refinement during mechanical alloying but is also suggested to lower the achievable yttria size at this length scale. Inspecting the sample milled at 48h/RT and subsequently for 6h at CT suggests a state between milling at RT and CT. This observation suggests a transition from an RT to an CT equilibrium and therefore, a temperature-dependent equilibrium yttria size is proposed.

However, approx. two-thirds of the added yttria was observed to be in the second size regime below 10 nm forming network-like

nanoclusters within the grains of the fcc matrix and are, based on HE-XRD measurements, proposed to be dissolved. At this yttria size scale, cryomilling resulted in smaller cluster sizes with the smallest observed clusters exhibiting approx. 5 nm whereas RT milling yielded clusters with approx. 10 nm. Similar to particles larger 10 nm, the combination of both milling temperatures indicates a state in-between RT and CT milling, suggesting a temperature-dependent equilibrium cluster size. Based on PALS and *ab-initio* calculations of our previous work [140], this equilibrium cluster size is postulated to be a result of increased vacancy densities within the cryomilled samples, forming smaller and more stable clusters. To this end, this hypothesis is supported by PAS-DB and APT showing increased yttria interaction with vacancies in the cryomilled samples.

4.2 Microstructural processes during consolidation via spark plasma sintering (SPS)

This chapter deals with the subsequent consolidation – i.e. compaction – of the milled powders and focuses on the effect of cryomilling on the precipitation of oxides and microstructural changes during consolidation. In this context, powders were consolidated via SPS, a sintering technique allowing fast heating rates and short holding times, as well as inductively heated within a synchrotron beamline to allow *in-situ* investigation of the precipitation behavior. The as-milled material state discussed in this chapter is directly taken from the chapter before, and therefore, investigations and discussions in this chapter are based on the results of chapter 4.1.

4.2.1 Grain coarsening and oxide precipitation during Spark Plasma Sintering and inductive heating

It was previously shown that the milled powders exhibit a nanostructured microstructure with grain sizes of 10-100 nm dependent on the milling temperature. Nevertheless, this fine grain sizes are not reported to be the stable state and therefore, grain coarsening is anticipated during consolidating of the powders. In this context, low magnification backscatter SEM images of the Spark Plasma Sintered (SPSed) samples are presented in Figure 56a-c depicting an inhomogeneous bimodal grain size distribution within the consolidated samples. For the 48h/RT specimen shown in Figure 56a, this inhomogeneity is more pronounced whereas the 48h/RT+6h/CT and 48h/CT samples, presented in Figure 56b and c, respectively, exhibit just small areas of inhomogeneities which seem to be present at former powder particle surfaces. Figure 56d depicts a magnified picture of a coarse grained area in the consolidated 48h/CT specimen as a representative example. By this, larger grains that contain only minor amounts of yttria can be seen, whereas a high number density of precipitated yttria is observed within the nanograins.

The observations within the SPSed specimen described above show the pinning effect of yttria with respect to grain boundaries, but more importantly, it indicates a less homogeneous yttria distribution within

the as-milled 48h/RT specimen. As a result, milling at room temperature (RT) for 48h might not be enough to homogeneously distribute yttria within the milled powders, even though, this was suggested by investigations of the as-milled powders. Therefore, cryomilling, even for 6h after 48h of RT milling, is proposed to significantly increase the homogeneity of yttria within the milled powders. The 48h/RT+6h/CT and 48h/CT samples showed just minor inhomogeneities, which are located at conceivable former particle surfaces. It should be pointed out that the inhomogeneities of the 48h/RT sample might be similarly located but due to the significantly larger inhomogeneous areas, it is not possible to denote them as former powder particle boundaries. Such inhomogeneities at former particle surfaces is suggested to stem from surface effects during sintering, such as local melting. In literature it is, however, still under debate whether such local melting phenomena occur during SPS or not [64,65].

It must be mentioned that the black pores within these analyzed samples are only found in the outer part of the sintered samples from which the presented samples were taken. In the inner part of the consolidated specimen, nearly no pores but a comparable microstructure was detected.
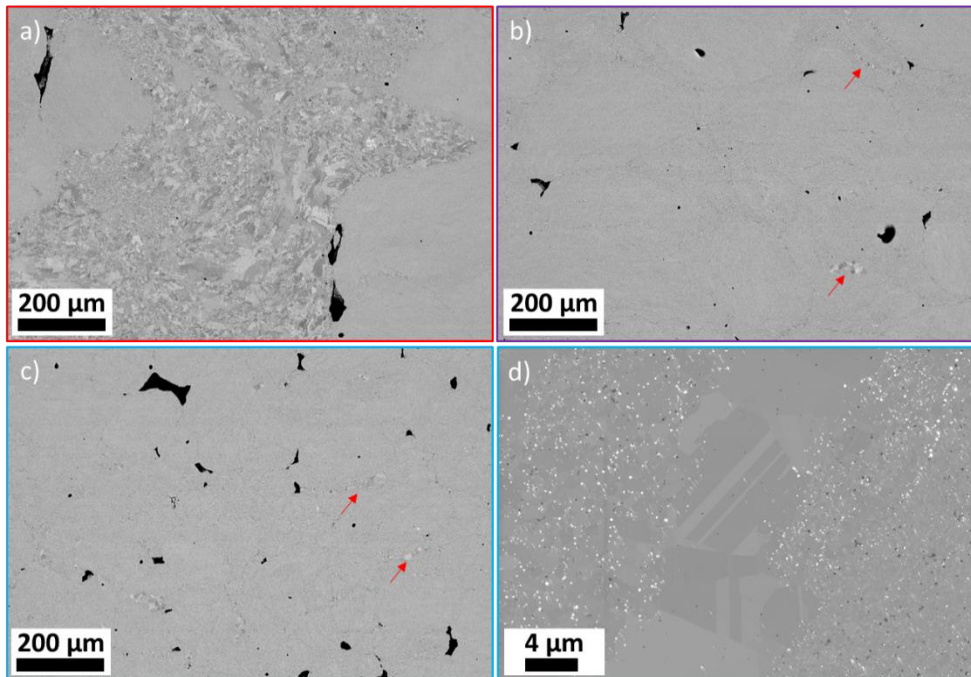
Figure 56: Low-magnification BSE SEM images of the a) consolidated 48h/RT sample indicating an inhomogeneous grain size distribution. b) Consolidated 48h/RT+6h/CT and c) consolidated 48h/CT specimen with small inhomogeneities marked by red arrows d) A detailed in-lens image of the consolidated 48h/CT sample as a representative example indicating nearly no yttria within coarse-grained regions showing the pinning effect of yttria with respect to grain boundaries.

Chapter 4.1 postulated that large amounts of yttria dissolve during mechanical alloying forming nanoclusters stabilized by vacancies. However, at elevated temperatures, at which the powders are consolidated, these clusters are expected to re-precipitate, forming finely dispersed nanometer-sized oxides such as yttria. Furthermore, chapter 4.1.1 showed a significant uptake of oxygen and nitrogen during milling which are both expected to affect the precipitation behavior during heating. Table 6 summarizes the O and N content of the 48h/RT, 48h/RT+6h/CT and 48h/CT specimen from chapter 4.1.1. It is observed that the oxygen content of the cryomilled 48h/CT specimen is slightly reduced, but an increased nitrogen content can be found in comparison with the 48h/RT specimen. The 48h/RT+6h/CT sample shows O- and N-contents in-between the other two specimen. It has to be mentioned that the presented oxygen content includes the oxygen incorporated by the addition of yttria which is expected to be 0.22 m.% O for the added 1 m.% Y_2O_3 and

therefore comparable to the amount of incorporated O during the process.

Table 6: Oxygen and nitrogen content of the 48h/RT, 48h/RT+6h/CT and 48h/CT specimen obtained via combustion analysis.

	48h/RT	48/RT+6h/CT	48h/CT
O [m.%]	0.467	0.459	0.410
N [m.%]	0.037	0.049	0.070

To investigate the oxide precipitation within the SPSed samples, only the nanograined regions within the consolidated samples were analyzed and microstructure backscatter images of the as-milled and SPSed samples are presented in Figure 57 showing a milling temperature independent increase of the grain size due to consolidation. However, even after consolidation, the samples exhibited small grain sizes of approx. 100 - 200 nm, which were determined by SEM. After consolidation, all specimens show large black precipitates which were identified by EDS investigation as Cr-Mn-O precipitates and only in the 48h/CT specimen, some were identified as Cr-N precipitates. These findings confirm the presence of excess oxygen and nitrogen in the sample even though a vacuum of 10^{-3} mbar was applied during milling. Visual inspection suggests that the phase fraction of the observed black precipitates is lowest in the 48h/RT sample. Hi-res in-lens images of the consolidated specimen shown as inserts in Figure 57b, d and f show finely precipitated yttria as white spots in the size of a few nanometers. However, EDS analysis identified some of these precipitates as Y-Cr-O. However, as mentioned in the methodological section of this work, due to the overlap of the O and Cr signal in EDS operated at 3 kV acceleration voltage, Cr and O are hard to distinguish and therefore, EDS cannot be used to distinguish between Y_2O_3 or possible Y-Cr-O precipitates.
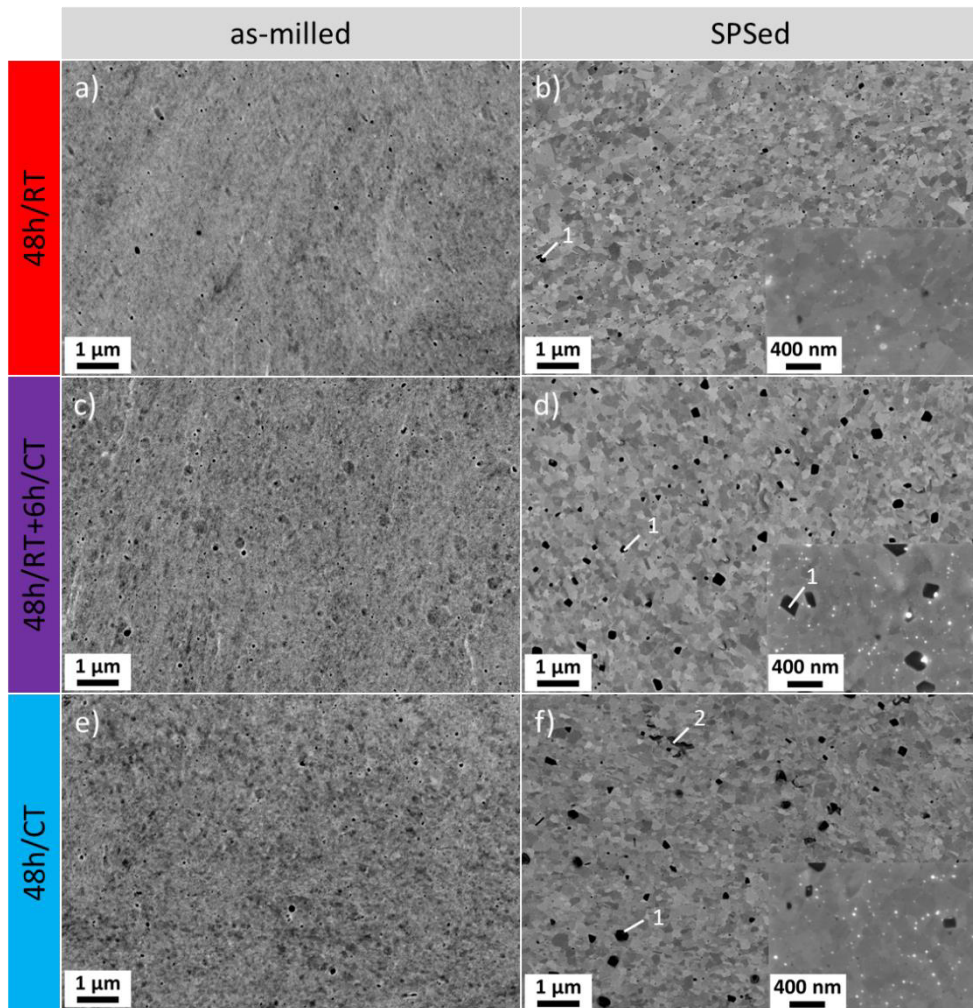
Figure 57: BSE microstructure images of the as-milled and SPSed powders with a) and b) showing the 48h/RT, c) and d) the 48h/RT+6h/CT sample and e) and f) the cryomilled 48h/CT specimen indicating an increase of the grain size due to consolidation. Inserts in b), d) and f) show Hi-res in-lens images of the microstructure indicating nanometer-sized yttria precipitates as white spots and other dark colored precipitates were identified to be Cr-Mn-O (1) and Cr-N (2) as indicated in b), d) and f).

In order to shed light on the precipitation of the oxide phases and to clearly identify the oxides, the powders were also inductively heated using the same heating rate as for SPS (100 K/min) but a shorter holding time - 15 min instead of 30 min –and were in-situ investigated using HE-XRD. Parts of the XRD patterns of the heated 48h/RT and 48h/CT samples are presented in Figure 58a. The identification of the peaks using the software DIFFRAC EVA found Y_2O_3 as well as $YCrO_3$ after heating, marked by green and blue symbols, together with first higher harmonic Nb bcc and FeCrMnNiCo fcc peaks. However, no

84

stoichiometry of Cr-Mn-O or CrN fitted in the obtained HE-XRD spectrum of the inductively heated specimen.

Comparing the Y_2O_3 and $YCrO_3$ peaks marked in Figure 58a show an increased amount of Y_2O_3 within the 48h/RT specimen – i.e. larger peak, whereas mostly $YCrO_3$ along a minor amount of Y_2O_3 precipitates in the 48h/CT sample during heating.

Figure 58b and Figure 58c show the height of the largest Y_2O_3 peak in the 48h/RT specimen and of the largest $YCrO_3$ peak in the 48h/CT specimen, respectively, as a function of the heating time/temperature. By this plot, it is observed that the peak height of the Y_2O_3 peak in the 48h/RT specimen starts to significantly increase at approx. 700°C while a similar behavior is observed for the $YCrO_3$ peak at the beginning of the holding time – i.e. at a temperature of 1100°C. In this context, Y_2O_3 is suggested to precipitate at approx. 700°C in the 48h/RT specimen, whereas $YCrO_3$ seems to precipitate at approx. 1100°C within the 48h/CT sample – at the beginning of the holding time.

As a result, after milling for 48h, cryogenic milling temperatures shift the main precipitated oxide phase from Y_2O_3 for the room temperature milled specimen towards $YCrO_3$ indicating a milling temperature dependent oxide precipitation within the investigated ODS FeCrMnNiCo alloy. Furthermore, both types of oxides were found to precipitate at different temperatures. It has to be mentioned that the 48h/RT+6h/CT specimen shows a similar behavior as the 48h/RT sample but is not depicted in Figure 58 for better visualization.
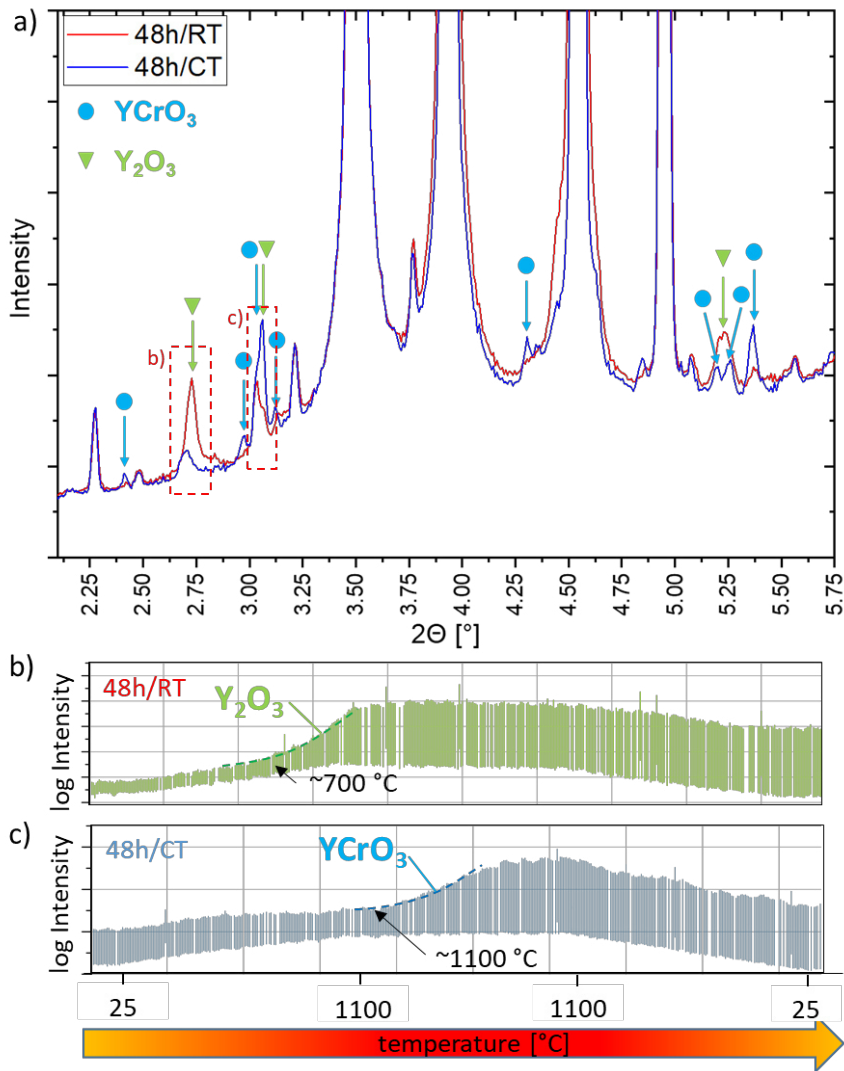
Figure 58: a) Part of the HE-XRD pattern of the 48h/RT and 48h/CT specimen after heating within the synchrotron beamline with marked Y_2O_3, $YCrO_4$ as well as bcc and fcc peaks showing different Y_2O_3 and $YCrO_3$ peak heights. b) In-situ investigation of the Y_2O_3 peak within the 48h/RT sample and c) the $YCrO_3$ peak within the 48h/CT specimen. Heating and cooling rate are 100K/min between RT and 1100°C, holding time at 1100°C is 15 min.

To the best of the author's knowledge, no investigations concerning the milling temperature dependent oxide precipitation have been conducted so far. Nevertheless, Chung et al. [68] investigated the cryomilled and subsequently SPSed FeCrMnNiCo alloy with the addition of Y_2O_3 and found precipitated Y_2O_3 within the grains as well as $YCrO_3$ at grain boundaries after SPS. The authors also observed Cr-Mn-O in a sample without Y_2O_3, but none was found in the specimen where Y_2O_3 was added. Zhang et al. [71] investigated the

86

precipitation of Y_2O_3 on a Fe-14Cr-10Y_2O_3 steel powder and found that Y_2O_3 precipitates after annealing at 900°C for 1h while no Y_2O_3 was found at lower annealing temperatures. The authors further observed $YCrO_3$ together with Y_2O_3 precipitations at higher temperatures above 1000°C. Kawamura et al. also reported this co-existence of Y_2O_3 and $YCrO_3$ at a temperature of 1025°C [70]. Therefore, the observation of co-existing Y_2O_3 and $YCrO_3$ in this work is in good agreement with literature. However, in this work, Y_2O_3 precipitates at a lower temperature compared to Zhang et al., possibly indicating different local chemical surroundings near the dissolved Y_2O_3 resulting in different precipitation kinetics as in bcc steels.

In the cryomilled 48h/CT sample, an increased amount of $YCrO_3$ precipitates at approx. 1100°C, whereas within the 48h/RT and 48h/RT+6h/CT specimen, mostly Y_2O_3 precipitates at approx. 700°C during heating. One possible explanation of the different types of precipitated oxide might be a higher amount of excess oxygen present in the 48h/CT specimen as $YCrO_3$ can form more oxides with the same amount of Y. However, the results of combustion analysis contradict this possible explanation as the 48h/CT specimen showed an even lower oxygen content than the 48h/RT sample. Therefore, this change in precipitated oxides is suggested to be related to the stability of the Y and O enriched nanoclusters after mechanical alloying. As concluded in chapter 4.1, cryomilling is suggested to result in more stable Y and O enriched nanoclusters which might cause a later precipitation upon heating compared to the 48h/RT and 48h/RT+6h/CT specimen. According to literature, at higher precipitation temperatures, the precipitation of $YCrO_3$ is favored over Y_2O_3 and therefore, more $YCrO_3$ and less Y_2O_3 precipitates in the 48h/CT specimen during inductive heating. A possible explanation for the observation of $YCrO_3$ at elevated precipitation temperatures might be related to a higher mobility of Cr atoms at higher temperatures. By this, Cr atoms are able to diffuse to the, from the clusters released, Y and O atoms consequently forming $YCrO_3$ whereas at lower temperatures, such phenomenon is less likely to occur.

Therefore, the results of this work confirm the proposed increased stability of the nanoclusters within the cryomilled 48h/CT sample in

comparison to the room temperature milled 48h/RT specimen. The observed difference between the SPSed and inductively heated specimen concerning the precipitation of Cr-Mn-O and Cr-N is discussed at the end of the next chapter.

4.2.2   Investigation   of   recrystallization   during consolidation

Mechanical alloying introduces high densities of lattice defects, as presented in chapter 4.1, which are supposed to recover and annihilate at elevated temperatures during consolidation. As a means of further elucidating the defect evolution during consolidation of this mechanically alloyed ODS FeCrMnNiCo alloy, the FWHM of the (111) fcc reflex and the, by the modified Williamson-Hall calculated crystallite size, are presented in Figure 59 and compared with the height of the diffraction peak at 3.05°, which is attributed to an overlap of a harmonic bcc peak with the largest $YCrO_3$ reflection. Investigation of the FWHM confirms increased defect densities for the cryomilled specimen as suggested by XRD measurements in chapter 4.1.4. During heating with 100 K/min, the FWHM decreases steadily for all specimens until reaching 1100°C, after which the temperature was kept constant for 15 min before cooling with 100 K/min. The difference in the FWHM between the samples vanishes upon heating at approx. 670°C indicating a comparable defect density for all specimens from this point on. However, after the first minutes of holding at 1100°C, the FWHM of the 48h/CT sample further decreases and eventually reaches the instrumental broadening of the synchrotron beamline – LaB_6 reference sample - while the 48h/RT and 48h/RT+6h/CT specimen stay at a higher steady-state FWHM implying that at the 48h/CT sample an increased annihilation of defects is present at this temperature.
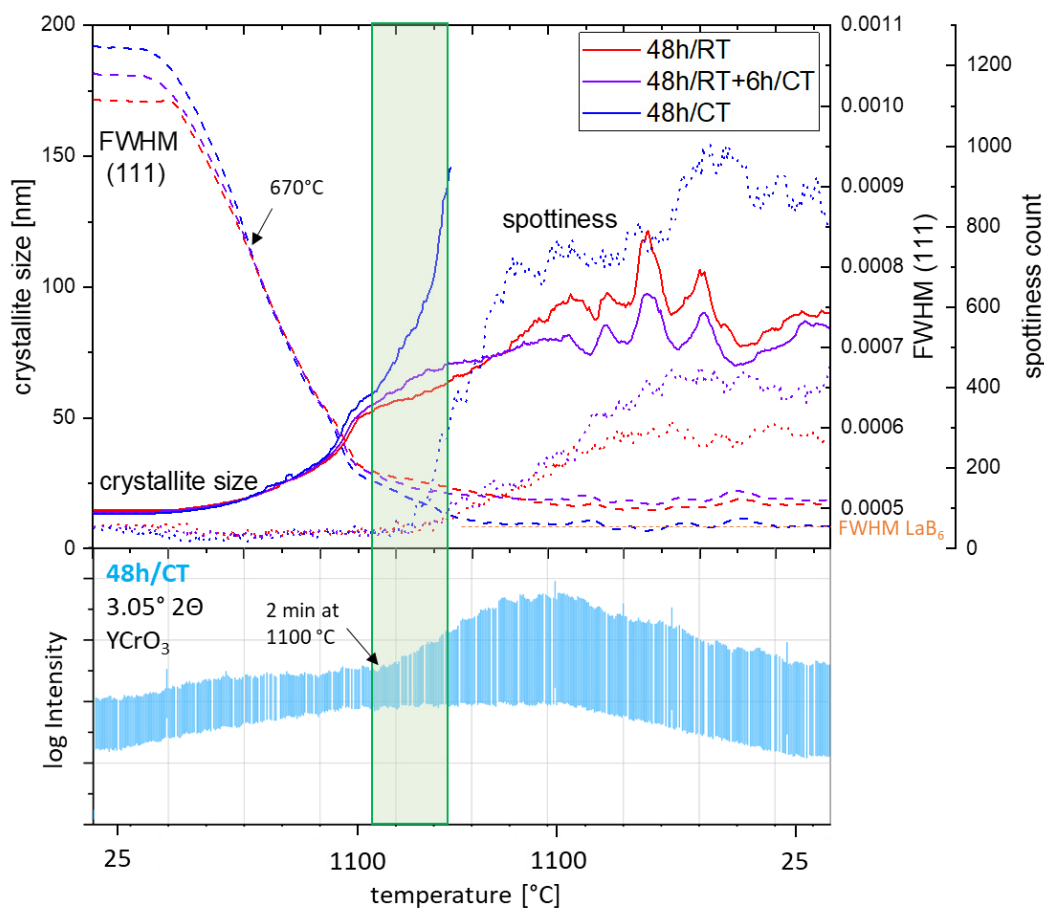
Figure 59: Evolution of the FWHM of the (111) peak and the crystallite size within the milled powders during heating in comparison with the peak height of the reflection containing $YCrO_3$ in the 48h/CT specimen. The spottiness count, according to Moreno [114], is presented, indicating an increased number of spots in the (111) diffraction ring of the 48h/CT sample after reaching the holding temperature. The marked area shows a correlation between a decreasing FWHM and increasing crystallite size and spottiness in the 48h/CT specimen with the increasing peak height at 3.05°. Heating and cooling rate are 100K/min between RT and 1100°C, holding time at 1100°C is 15 min.

The crystallite size starts at 13 nm and slowly increases during heating showing no significant differences between the powders up to 1100°C – i.e. the start of the holding time. The 48h/RT and 48h/RT+6h/CT samples seem to approach a steady-state at approx. 80 nm during holding at 1100°C. Nevertheless, the crystallite size of the 48h/CT specimen increases rapidly from 1100°C, suggesting a significantly faster growth of the crystallites. At a crystallite size of approx. 150 nm, the applied method fails to calculate a reasonable result as the FWHM reaches values of the LaB_6 reference sample and thus, no influence of the defects, including the crystallite size, can be

detected. Therefore, the extremely strong defect annihilation obtained from the FWHM and the fast-growing crystallites suggests abnormal grain growth or so-called secondary recrystallization in the 48h/CT specimen. This indication of abnormal grain growth can also be seen from the spottiness of the diffraction rings. Increasing spottiness indicates fewer statistics during diffraction caused by increased grain size. Figure 60 depicts parts of the diffraction rings of the (111) and (222) reflection after heating showing similar amounts of spots in the 48h/RT and 48h/RT+6h/CT samples presented in Figure 60a and b, respectively whereas more spots can be seen in the cryomilled 48h/CT sample (Figure 60c). Line profile analysis according to Moreno [114] in Figure 59 shows an increased number of such spots in the (111) diffraction ring of the 48h/CT sample compared to the 48h/RT and 48h/RT+6h/CT specimen. The results of the number of spots are presented and compared to the FWHM and the crystallite size in Figure 59, confirming the visual appearance of Figure 60. Note that the spottiness increases slightly later than the start of the recrystallization as single spots have to get large enough to be detected.
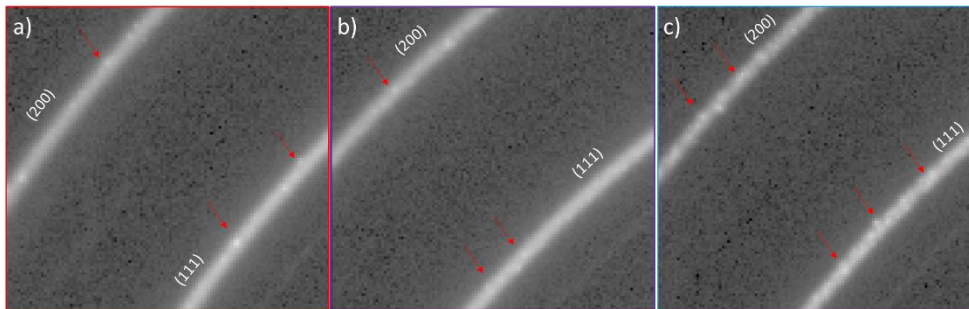
Figure 60: Representative parts of the fcc (111) and (200) diffraction reflexes after heating for a) 48h/RT, b) 48h/RT+6h/CT and c) 48h/Ct specimen indicating more spots in the cryomilled sample.

In order to confirm the above interpretation, Figure 61 presents representative SEM-BSE images of the 48h/RT and 48h/CT samples after inductive heating, showing significantly larger grains along with some finer grains within the 48h/CT specimen. This type of bimodal grain structure indicates abnormal grain growth [75,77,149] and therefore corroborates the findings of the HE-XRD evaluation.
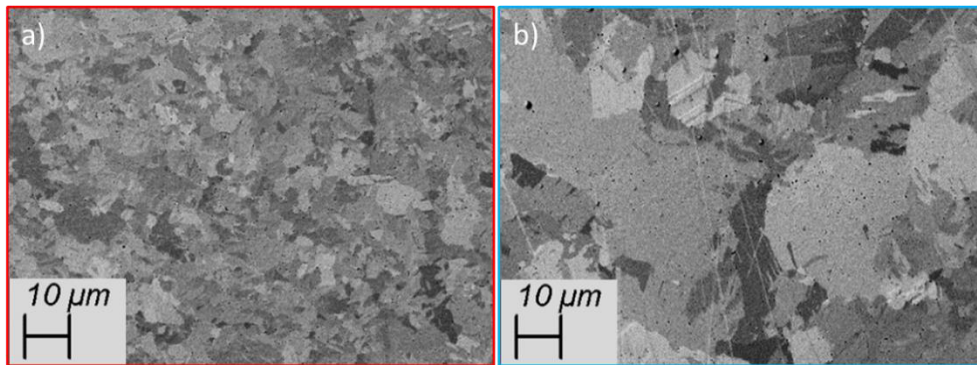
Figure 61: Representative SEM-BSE images of the a) 48h/RT and b) 48h/CT specimen after heating within the synchrotron beamline.

Comparing the defect evolution with the peak at 3.05° within the 48h/CT specimen shows that the $YCrO_3$ exceeds the harmonic bcc peak at the same point where the FWHM derives from the other samples towards smaller values and the crystallite size starts to increase. This correlation suggests a relation between the precipitation of $YCrO_3$ and the decrease of lattice defects within the 48h/CT sample upon inductive heating which will be discussed in the following paragraph.

Using in-situ XRD measurements on ferritic ODS powders, Sallez et al. [81] observed a similar trend in the crystallite size during heating. The authors attributed this observation to abnormal grain growth – i.e. secondary recrystallization, which was confirmed by SEM images indicating abnormally large grains together with some nanograined regions. According to previous literature [74,80,150], especially small second phase particles such as Y_2O_3 retard abnormal grain growth, whereas coarse particles are less effective in hindering grain boundary movement. Furthermore, internally stored energy provided by lattice defects is believed to promote abnormal grain growth, which means in turn, preserving the internal energy up to higher temperatures should foster secondary recrystallization [74,78]. To this end, in comparison with literature and based on the results of the crystallite size and the spottiness of the diffraction rings, abnormal grain growth for the 48h/CT sample is suggested to occur, whereas the 48h/RT and 48h/RT+6h/CT samples show normal recrystallization. A reason for the different recrystallization behavior of the samples might be found in the correlation between the $YCrO_3$ peak shown in Figure 59 and

91

the Y_2O_3 precipitation, as discussed in chapter 4.2.1. By this, in the 48h/RT and 48h/RT+6h/CT samples, mainly Y_2O_3 precipitates at approx. 700°C while within the 48h/CT, mostly $YCrO_3$ seems to precipitate at approx. 1100°C. Furthermore, Y and O enriched nanoclusters are expected to hinder dislocation motion [45], which preserves higher stored energy within the sample up to high temperatures which gets released when the clusters re-precipitate. Therefore, even though the FWHM drops significantly during heating, the stored energy seems large enough to initiate secondary recrystallization within the 48h/CT specimen as the precipitation of $YCrO_3$ releases the, in lattice defects stored, energy at a higher temperature compared to the 48h/RT specimen. This is further supported by the FWHM reaching the value of the LaB_6 reference sample, indicating that defect densities decrease below a measurable value in the inductively heated 48h/CT specimen. However, the other specimen, 48h/RT and 48h/RT+6h/CT, still exhibit a measurably amount of lattice defects after heating.

These results and conclusions are in contrast to the grain size in the SPSed specimen, as shown in Figure 56 and Figure 57, where no abnormally large grains were observed. This might be an indication that the processes of SPS and inductive heating within the synchrotron beamline are not comparable, which is further supported by the absence of Cr-Mn-O and Cr-N in the HE-XRD pattern. This difference might be a result of a slower heating rate within the SPS specimen compared to inductive heating. Even though the heating parameters were set to be the same, the SPS specimens were much larger than the encapsulated powder and a regulation of the heating rate over the whole volume is therefore more difficult to maintain. Slow heating rates lead to increased recovery processes, and thus, less energy is preserved at high temperatures potentially limiting the ability for abnormal grain growth. Furthermore, it is reported that the FeCrMnNiCo alloy exhibits phase instabilities [20,21] which are faster within highly deformed samples [21], possibly explaining the occurrence of Cr-Mn-O and Cr-N within the SPSed samples.

4.2.3 Summary of Microstructural processes during consolidation via spark plasma sintering

Investigation of the consolidation process conducted in this thesis showed a bimodal grain size distribution in the 48h/RT samples after SPS, whereas a mostly nanograined microstructure was observed in the 48h/CT and 48h/RT+6h/CT specimen. Detailed SEM investigations proved that this is attributed to an inhomogeneous yttria distribution as nearly no yttria precipitated within large-grained areas, i.e. no grain boundary pinning occurred. However, the nanograined areas showed no difference in grain size between the SPSed specimen reaching approx. 100–200 nm. Nevertheless, EDS analysis showed the precipitation of large Cr-Mn-O and, only in the 48h/CT specimen, also Cr-N, indicating the presence of excess oxygen and nitrogen. Y_2O_3 was found to precipitate finely dispersed within the grains as well as at grain boundaries. *In-situ* HE-XRD investigations found no Cr-Mn-O or Cr-N peaks within the inductively heated samples, however, Y_2O_3 and $YCrO_3$ peaks could be identified clearly showing a higher fraction of $YCrO_3$ and less precipitated Y_2O_3 in the heated 48h/CT sample, whereas for the 48h/RT and 48h/RT+6hCT samples this behavior reverses. Furthermore, Y_2O_3 was found to start precipitating at approx. 700°C during heating while $YCrO_3$ precipitates at the beginning of the holding time at 1100°C. Therefore, it is postulated that increased stability of the Y and O enriched nanocluster after cryomilling leads to precipitation of these elements at a higher temperature, at which precipitation of $YCrO_3$ is favored over Y_2O_3 as proposed by literature.

Furthermore, in-situ analysis of the crystallite size shows slightly increasing crystallite sizes from initially 13 nm to approx. 50 nm upon heating. The 48h/RT and 48h/RT+6h/CT samples then recrystallize, showing approx. 80 nm crystallite sizes after heating. However, the crystallite size of the cryomilled 48h/CT sample increases rapidly until the Warren-Averbach method fails to calculate trustful values indicating abnormal grain growth or so-called secondary recrystallization. The occurring recrystallization processes are confirmed by the spottiness count of the diffraction rings as well as SEM-BSE images. The spottiness of the 48h/CT sample shows

significantly higher numbers of spots – i.e. large fully recrystallized grains while SEM images confirm significantly larger grains within the 48h/CT sample. In this context, the FWHM of the 48h/CT sample reaches the same value as the LaB_6 reference sample indicating a strong annihilation of defects below a detectable level, further supporting the assumption of abnormal grain growth as this process needs internally stored energy in the form of defects to happen. This means in turn that after abnormal grain growth, a nearly full annihilation of defects such as dislocations is present. Here it is assumed that the occurrence of abnormal grain growth as well as the type of precipitated oxide is linked with the stability of the nanoclusters after milling and, therefore, the milling temperature. The assumption is based on the theory that abnormal grain growth requires high stored energy providing sufficient driving force for grain boundary movement at a high temperature. In the case of precipitation hardened alloys, this driving force has to be even large enough to overcome the pinning effect of precipitates.

Another conclusion based on the results shows that SPS and inductive heating processes are not comparable in terms of oxide precipitation and defect evolution during heating. This assumption is based on the observation of Cr-Mn-O and Cr-N in the SPSed sample, whereas no Cr-Mn-O or Cr-N could be identified in the HE-XRD pattern. Furthermore, the SPSed samples did not exhibit abnormal grain growth, which, however, happened during inductive heating of the milled powders. This observation might be linked to a lower present heating rate due to the larger size of the SPSed specimen. A lower heating rate potentially fosters phase segregation and therefore, the precipitation of Cr-Mn-O and Cr-N which are then stable enough to persist even at elevated temperatures. It might also hinder abnormal grain growth due to increased recovery processes during slow heating and thus, less preserved energy at elevated temperatures.

5 Conclusion

This chapter summarizes the main conclusions of the current work on the refinement and dissolution of yttria dependent on the milling temperature and the subsequent microstructural evolution during consolidation.

- During milling, the powder particle size increases due to cold welding of the ductile fcc FeCrMnNiCo alloy forming relatively spherical particles. However, cryomilling results in smaller particles than RT milling probably as a result of an increased strength of the matrix alloy at low temperatures shifting the cold-welding and fracturing balance towards increased fracturing. In this context and especially for cryomilling, 48h milling time seems to be long enough for a homogeneous milling microstructure, which is much shorter than reported in literature and thus, shows the high energy input of the used milling design.

- For the refinement and dissolution of yttria, two size ranges are proposed with a transition at approx. 10 nm. Particles larger than 10 nm exhibited an yttria crystal structure and were observed to be crushed remnants of the initial yttria, while particles below 10 nm are postulated to be dissolved in form of nanoclusters.

- For particles larger than 10 nm, the increased strength at low milling temperatures shows a beneficial effect of cryomilling on the refinement of yttria, lowering the equilibrium particle size as it shortens the necessary time needed to refine a substantial amount of yttria. Furthermore, cryomilling, even for 6h after 48h of RT milling, resulted in an increased yttria homogeneity within the milled powders.

- Independent of the milling temperature, two-thirds of the initially added yttria is refined below 10 nm and dissolved into nanoclusters. These findings are valid for milling

durations of 48h. These clusters are proposed to be smaller within the cryomilled sample due to an increased density of vacancies that stabilize smaller nanoclusters.

- Compared to RT milling, cryomilling resulted in a more homogeneous grain size distribution after SPS, which is attributed to a more uniform yttria distribution pinning grain boundaries. Therefore, this observation confirms increased yttria homogeneity within the milled powders.

- After inductive heating within the synchrotron beamline, a milling temperature dependent type and precipitation temperature of oxides was observed. Within the cryomilled sample, mostly $YCrO_3$ precipitated at approx. 1100°C during holding time whereas within the room temperature milled sample mostly Y_2O_3 precipitating at approx. 700°C. Therefore, a higher stability of the nanoclusters in the cryomilled samples is suggested, resulting in a higher precipitation temperature at which, precipitation of $YCrO_3$ is reported in literature to be favored over Y_2O_3, even though the oxygen content was comparable.

- During heating of the cryomilled sample, HE-XRD suggests abnormal grain growth whereas normal recrystallization was observed after RT milling. This phenomenon is again proposed to be a result of the increased cluster stability of the 48h/CT sample, which leads to a release of the internally stored energy at a higher temperature, thus, providing sufficient driving force for abnormal grain growth.

- The absence of abnormal grain growth in the SPSed specimen indicates that the SPS and inductive heating processes used in this work are not comparable. Even though the process parameters were chosen to be similar, this observation possibly stems from slower heating rates within the larger SPS specimen resulting in changed and therefore not equivalent process parameters.

6 Outlook

The results and conclusions presented in this thesis provide detailed insights into the mechanism of mechanical alloying and subsequent consolidation and are therefore useful for improving the manufacturing of an fcc ODS FeCrMnNiCo alloy. However, some open questions and challenges remain as they exceed the scope of this thesis.

The first challenge will be the application of the gained knowledge regarding the mechanism of mechanical alloying of an fcc ODS alloy towards new material classes and further optimizing the process. Therefore, open questions are if shorter milling times as the detailed investigated 48h are possible to achieve a dissolution of a substantial amount of yttria and quantify the amount of time-saving due to cryomilling. Furthermore, it has to be evaluated if the applied temperature of -150°C is necessary or if higher temperatures allow for an alternative and possibly cheaper cooling solution. By this, meaningful information about the economic feasibility of the process will be gained, possibly qualifying it for industrial applications. However, all such acquired knowledge depends on the used powder material. Regarding the dissolution of yttria, more in-depth investigations on atomic scale to support the postulated assumptions might help to get even deeper insights into the mechanism of mechanical alloying. This knowledge then leads to a detailed understanding of the parameters influencing the dissolution of yttria, allowing novel alloy designs for ODS alloys.

Preliminary investigations regarding the mechanical properties of the SPSed ODS FeCrMnNiCo alloy did not yield desirable results regarding yield strength, ductility and creep resistance, especially at high temperatures. Therefore, more work is needed to understand the challenges and improve the performance of such alloys. As main challenges, the precipitation of Cr-Mn-O and Cr-N and the relatively small grains (20 μm) within the SPSed sample were identified, resulting in intercrystalline fracture. A possible remedy to suppress the formation of Cr-Mn-O is the substitution of Y_2O_3 with metallic Y, as combustion analysis yielded a high amount of excess oxygen even though a high vacuum of 10^{-3} mbar was applied. By this, less oxygen

is available for the formation of Cr-Mn-O. Besides the precipitated oxide, the grain size must be increased to achieve desirable creep resistance. A possible way to achieve a coarse-grained microstructure in a short time, where oxide coarsening is not significant, is abnormal grain growth. This thesis suggested abnormal grain growth in the cryomilled samples using inductive heating, which is, however, postulated to be linked to the stability of the nanoclusters. A key topic in this context is the comparison of the processes of SPS and inductive heating which were proposed to yield different microstructural features. As another consolidation technique, hot-rolling possibly promotes secondary recrystallization due to its deformation during consolidation and resulting ability to retain a significant amount of lattice defects up to high temperatures. To this end, the phenomenon of abnormal grain growth dependent on cluster stability and possibly heating rate needs to be evaluated in detail in order to improve high-temperature mechanical properties.

7 References

[1]   J. Browne, Seven elements that have changed the world: Iron, carbon, gold, silver, uranium, titanium, silicon, Weidefeld & Nicolson, 2013.

[2]   Pavlenko N, Searles S, Assessing the sustainability implications of alternative aviation fuels - International Council on Clean Transportation, (2021). https://theicct.org/publication/assessing-the-sustainability-implications-of-alternative-aviation-fuels/.

[3]   Eurocontrol, EUROCONTROL Forecast Update 2021-2027, (2021).

[4]   J.H. Perepezko, The hotter the engine, the better, Science (80-.). 326 (2009) 1068–1069. doi:10.1126/science.1179327.

[5]   H. Long, S. Mao, Y. Liu, Z. Zhang, X. Han, Microstructural and compositional design of Ni-based single crystalline superalloys – A review, J. Alloys Compd. 743 (2018) 203–220. doi:10.1016/J.JALLCOM.2018.01.224.

[6]   Rolls-Royce, the Jet engine, fifth ed., Rolls-Royce, 1996.

[7]   W. Du, L. Luo, Y. Jiao, S. Wang, X. Li, B. Sunden, Heat transfer in the trailing region of gas turbines – A state-of-the-art review, Appl. Therm. Eng. 199 (2021) 117614. doi:10.1016/J.APPLTHERMALENG.2021.117614.

[8]   M.H. Tsai, J.W. Yeh, High-entropy alloys: A critical review, Mater. Res. Lett. 2 (2014) 107–123. doi:10.1080/21663831.2014.912690.

[9]   B.S. Murty, High-Entropy Alloys, 2019. doi:10.1016/b978-0-12-816067-1.09987-2.

[10] B. Cantor, I.T.H. Chang, P. Knight, A.J.B. Vincent, Microstructural development in equiatomic multicomponent alloys, Mater. Sci. Eng. A. 375–377 (2004) 213–218. doi:10.1016/j.msea.2003.10.257.

[11] G. Gottstein, Materialwissenschaft und Werkstofftechnik, 4th ed., Springer Vieweg, 2014.

[12] E. Arzt, Size effects in materials due to microstructural and dimensional constraints: A comparative review, J. Econ. Psychol. 50 (2015) 135–137. doi:10.1016/j.joep.2015.08.002.

[13] C. Suryanarayana, Mechanical Alloying and Milling, Marcel Dekker, 2004.

[14] N. Stepanov, M. Tikhonovsky, N. Yurchenko, D. Zyabkin, M. Klimova, S. Zherebtsov, A. Efimov, G. Salishchev, Effect of cryo-deformation on structure and properties of CoCrFeNiMn high-entropy alloy, Intermetallics. 59 (2015) 8–17. doi:10.1016/j.intermet.2014.12.004.

[15] G. Ressel, D. Holec, A. Fian, F. Mendez-Martin, H. Leitner, Atomistic insights into milling mechanisms in an Fe-Y2O3model alloy, Appl. Phys. A Mater. Sci. Process. 115 (2014) 851–858. doi:10.1007/s00339-013-7877-y.

[16] D.B. Miracle, O.N. Senkov, A critical review of high entropy alloys and related concepts, Acta Mater. 122 (2017) 448–511. doi:10.1016/j.actamat.2016.08.081.

[17] S. Gorsse, M.H. Nguyen, O.N. Senkov, D.B. Miracle, Database on the mechanical properties of high entropy alloys and complex concentrated alloys, Data Br. 21 (2018) 2664–2678. doi:10.1016/j.dib.2018.11.111.

[18] M. Laurent-Brocq, A. Akhatova, L. Perrière, S. Chebini, X. Sauvage, E. Leroy, Y. Champion, Insights into the phase diagram of the CrMnFeCoNi high entropy alloy, Acta Mater. 88 (2015) 355–365. doi:10.1016/j.actamat.2015.01.068.

[19] E.J. Pickering, R. Muñoz-Moreno, H.J. Stone, N.G. Jones, Precipitation in the equiatomic high-entropy alloy CrMnFeCoNi, Scr. Mater. 113 (2016) 106–109. doi:10.1016/j.scriptamat.2015.10.025.

[20] K.G. Pradeep, D. Raabe, M. Kuběnová, G. Eggeler, A. Dlouhý, F. Otto, E.P. George, Decomposition of the single-phase high-entropy alloy CrMnFeCoNi after prolonged anneals at intermediate temperatures, Acta Mater. 112 (2016) 40–52. doi:10.1016/j.actamat.2016.04.005.

[21] B. Schuh, F. Mendez-Martin, B. Völker, E.P. George, H. Clemens, R. Pippan, A. Hohenwarter, Mechanical properties, microstructure and thermal stability of a nanocrystalline CoCrFeMnNi high-entropy alloy after severe plastic deformation, Acta Mater. 96 (2015) 258–268. doi:10.1016/j.actamat.2015.06.025.

[22] F. Otto, A. Dlouhý, C. Somsen, H. Bei, G. Eggeler, E.P. George, The influences of temperature and microstructure on the tensile properties of a CoCrFeMnNi high-entropy alloy, Acta Mater. 61 (2013) 5743–5755. doi:10.1016/j.actamat.2013.06.018.

[23] K.V.S. Thurston, A. Hohenwarter, G. Laplanche, E.P. George, B. Gludovatz, R.O. Ritchie, On the onset of deformation twinning in the CrFeMnCoNi high-entropy alloy using a novel tensile specimen geometry, Intermetallics. 110 (2019) 106469. doi:10.1016/j.intermet.2019.04.012.

[24] B. Gludovatz, A. Hohenwarter, D. Catoor, E.H. Chang, E.P. George, R.O. Ritchie, A fracture-resistant high-entropy alloy for cryogenic applications, Science (80-.). 345 (2014) 1153–1158. doi:10.1126/science.1254581.

[25] S. Huang, W. Li, S. Lu, F. Tian, J. Shen, E. Holmström, L. Vitos, Temperature dependent stacking fault energy of FeCrCoNiMn high entropy alloy, Scr. Mater. 108 (2015) 44–47. doi:10.1016/j.scriptamat.2015.05.041.

[26] D. Choudhuri, B. Gwalani, S. Gorsse, M. Komarasamy, S.A. Mantri, S.G. Srinivasan, R.S. Mishra, R. Banerjee, Enhancing strength and strain hardenability via deformation twinning in fcc-based high entropy alloys reinforced with intermetallic compounds, Acta Mater. 165 (2019) 420–430. doi:10.1016/j.actamat.2018.12.010.

[27] P.E.J. Rivera-Díaz-del-Castillo, H. Fu, Strengthening mechanisms in high-entropy alloys: Perspectives for alloy design, J. Mater. Res. 33 (2018) 2970–2982. doi:10.1557/jmr.2018.328.

[28] R.L. Klueh, J.P. Shingledecker, R.W. Swindeman, D.T. Hoelzer, Oxide dispersion-strengthened steels: A comparison of some commercial and experimental alloys, J. Nucl. Mater. 341 (2005) 103–114. doi:10.1016/j.jnucmat.2005.01.017.

[29] C. Cayron, E. Rath, I. Chu, S. Launois, Microstructural evolution of Y2O3and MgAl2O4ODS EUROFER steels during their elaboration by mechanical milling and hot isostatic pressing, J. Nucl. Mater. 335 (2004) 83–102. doi:10.1016/j.jnucmat.2004.06.010.

[30] Y. Miao, K. Mo, Z. Zhou, X. Liu, K.C. Lan, G. Zhang, M.K. Miller, K.A. Powers, Z.G. Mei, J.S. Park, J. Almer, J.F. Stubbins, On the microstructure and strengthening mechanism in oxide dispersion-strengthened 316 steel: A coordinated electron microscopy, atom probe tomography and in situ synchrotron tensile investigation, Mater. Sci. Eng. A. 639 (2015) 585–596. doi:10.1016/j.msea.2015.05.064.

[31] H. Hadraba, Z. Chlup, A. Dlouhy, F. Dobes, P. Roupcova, M. Vilemova, J. Matejicek, Oxide dispersion strengthened CoCrFeNiMn high-entropy alloy, Mater. Sci. Eng. A. 689 (2017) 252–256. doi:10.1016/j.msea.2017.02.068.

[32]   B. Gwalani, R.M. Pohan, O.A. Waseem, T. Alam, S.H. Hong, H.J. Ryu, R. Banerjee, Strengthening of Al 0.3 CoCrFeMnNi-based ODS high entropy alloys with incremental changes in the concentration of Y2O3, Scr. Mater. 162 (2019) 477–481. doi:10.1016/j.scriptamat.2018.12.021.

[33]   F. Dobeš, H. Hadraba, Z. Chlup, A. Dlouhý, M. Vilémová, J. Matějíček, Compressive creep behavior of an oxide-dispersion-strengthened CoCrFeMnNi high-entropy alloy, Mater. Sci. Eng. A. 732 (2018) 99–104. doi:10.1016/j.msea.2018.06.108.

[34]   C.C. Koch, R.O. Scattergood, K.M. Youssef, E. Chan, Y.T. Zhu, Nanostructured materials by mechanical alloying: New results on property enhancement, J. Mater. Sci. 45 (2010) 4725–4732. doi:10.1007/s10853-010-4252-7.

[35]   M. Mayer, G. Ressel, J. Svoboda, The Effect of Cryogenic Mechanical Alloying and Milling Duration on Powder Particles' Microstructure of an Oxide Dispersion Strengthened FeCrMnNiCo High-Entropy Alloy, Metall. Mater. Trans. A. (2021). doi:10.1007/s11661-021-06532-x.

[36]   M. Brocq, B. Radiguet, S. Poissonnet, F. Cuvilly, P. Pareige, F. Legendre, Nanoscale characterization and formation mechanism of nanoclusters in an ODS steel elaborated by reactive-inspired ball-milling and annealing, J. Nucl. Mater. 409 (2011) 80–85. doi:10.1016/j.jnucmat.2010.09.011.

[37]   Z.W. Zhang, J.E. Zhou, S.Q. Xi, G. Ran, P.L. Li, W.X. Zhang, Formation of crystalline and amorphous solid solutions of W–Ni–Fe powder during mechanical alloying, J. Alloys Compd. 370 (2004) 186–191. doi:10.1016/J.JALLCOM.2003.09.012.

[38]   I. Lucks, P. Lamparter, E.J. Mittemeijer, Uptake of iron, oxygen and nitrogen in molybdenum during ball milling, Acta Mater. 49 (2001) 2419–2428. doi:10.1016/S1359-6454(01)00154-9.

[39]   R.B. Schwarz, Microscopic Model For Mechanical Alloying, (1998).

[40] Y. Ashkenazy, N.Q. Vo, D. Schwen, R.S. Averback, P. Bellon, Shear induced chemical mixing in heterogeneous systems, Acta Mater. 60 (2012) 984–993. doi:10.1016/j.actamat.2011.11.014.

[41] Y.D. Ou, W.S. Lai, Vacancy formation and clustering behavior in Y2O3 by first principles, Nucl. Instruments Methods Phys. Res. Sect. B Beam Interact. with Mater. Atoms. 269 (2011) 1720–1723. doi:10.1016/j.nimb.2010.11.077.

[42] H. Zhao, C.L. Fu, M. Krcmar, M.K. Miller, Effect of strain on the stabilization of oxygen-enriched nanoclusters in Fe-based alloys, Phys. Rev. B - Condens. Matter Mater. Phys. 84 (2011) 2–6. doi:10.1103/PhysRevB.84.144115.

[43] J. Xu, C.T. Liu, M.K. Miller, H. Chen, Nanocluster-associated vacancies in nanocluster-strengthened ferritic steel as seen via positron-lifetime spectroscopy, Phys. Rev. B - Condens. Matter Mater. Phys. 79 (2009) 1–4. doi:10.1103/PhysRevB.79.020204.

[44] C.L. Fu, M. Krčmar, G.S. Painter, X.Q. Chen, Vacancy mechanism of high oxygen solubility and nucleation of stable oxygen-enriched clusters in Fe, Phys. Rev. Lett. 99 (2007) 1–4. doi:10.1103/PhysRevLett.99.225502.

[45] Z.W. Zhang, L. Yao, X.L. Wang, M.K. Miller, Vacancy-controlled ultrastable nanoclusters in nanostructured ferritic alloys, Sci. Rep. 5 (2015) 1–9. doi:10.1038/srep10600.

[46] F.D. Fischer, J. Svoboda, E. Kozeschnik, Interstitial diffusion in systems with multiple sorts of traps, Model. Simul. Mater. Sci. Eng. 21 (2013). doi:10.1088/0965-0393/21/2/025008.

[47] J. Svoboda, W. Ecker, V.I. Razumovskiy, G.A. Zickler, F.D. Fischer, Kinetics of interaction of impurity interstitials with dislocations revisited, Prog. Mater. Sci. 101 (2019) 172–206. doi:10.1016/j.pmatsci.2018.10.001.

[48] Y. Kimura, S. Takaki, S. Suejima, R. Uemori, H. Tamehiro, Ultra Grain Refining and Decomposition of Oxide during Super-heavy Deformation in Oxide Dispersion Ferritic Stainless Steel Powder., ISIJ Int. 39 (1999) 176–182. doi:10.2355/isijinternational.39.176.

[49] M.P. Phaniraj, D.I. Kim, J.H. Shim, Y.W. Cho, Microstructure development in mechanically alloyed yttria dispersed austenitic steels, Acta Mater. 57 (2009) 1856–1864. doi:10.1016/j.actamat.2008.12.026.

[50] D.B. Witkin, E.J. Lavernia, Synthesis and mechanical behavior of nanostructured materials via cryomilling, Prog. Mater. Sci. 51 (2006) 1–60. doi:10.1016/j.pmatsci.2005.04.004.

[51] C.C. Koch, Synthesis of nanostructured materials by mechanical milling: Problems and opportunities, Nanostructured Mater. 9 (1997) 13–22. doi:10.1016/S0965-9773(97)00014-7.

[52] H.J. Fecht, Mechanical formation by mechanical attrition, Nanostructured Mater. 6 (1995) 33–42.

[53] T. Sakai, A. Belyakov, R. Kaibyshev, H. Miura, J.J. Jonas, Dynamic and post-dynamic recrystallization under hot, cold and severe plastic deformation conditions, Prog. Mater. Sci. 60 (2014) 130–207. doi:10.1016/j.pmatsci.2013.09.002.

[54] F.A. Mohamed, A dislocation model for the minimum grain size obtainable by milling, Acta Mater. 51 (2003) 4107–4119. doi:10.1016/S1359-6454(03)00230-1.

[55] A.H. Chokshi, A. Rosen, J. Karch, H. Gleiter, On the validity of the hall-petch relationship in nanostructured materials, Sctipa Metall. 23 (1989). doi:10.1016/j.egypro.2009.02.038.

[56] J.H. Kim, C.H. Park, Effect of milling temperature on nanoclusters and ultra fine grained microstructure of oxide dispersion strengthened steel, J. Alloys Compd. 585 (2014) 69–74. doi:10.1016/j.jallcom.2013.09.085.

[57] B.Q. Han, J. Ye, F. Tang, J. Schoenung, E.J. Lavernia, Processing and behavior of nanostructured metallic alloys and composites by cryomilling, J. Mater. Sci. 42 (2007) 1660–1672. doi:10.1007/s10853-006-0907-9.

[58] N. Kumar, C.S. Tiwary, K. Biswas, Preparation of nanocrystalline high-entropy alloys via cryomilling of cast ingots, J. Mater. Sci. 53 (2018) 13411–13423. doi:10.1007/s10853-018-2485-z.

[59] J.H. Gwon, J.H. Kim, K.A. Lee, Effects of cryomilling on the microstructures and high temperature mechanical properties of oxide dispersion strengthened steel, J. Nucl. Mater. 459 (2015) 205–216. doi:10.1016/j.jnucmat.2015.01.032.

[60] J.H. Kim, T.S. Byun, E. Shin, J.B. Seol, S. Young, N.S. Reddy, Small angle neutron scattering analyses and high temperature mechanical properties of nano-structured oxide dispersion-strengthened steels produced via cryomilling, J. Alloys Compd. 651 (2015) 363–374. doi:10.1016/j.jallcom.2015.08.100.

[61] C. Kaviarasu, M. Ravichandran, Nanomaterials Through Powder Metallurgy: Production, Processing, and Potential Applications Toward Energy and Environment BT - Handbook of Nanomaterials and Nanocomposites for Energy and Environmental Applications, in: O.V. Kharissova, L.M. Torres-Martínez, B.I. Kharisov (Eds.), Springer International Publishing, Cham, 2021: pp. 859–897. doi:10.1007/978-3-030-36268-3_127.

[62] H.E. Exner, E. Arzt, Sintering Processes, Phys. Metall. (1990) 3–8. doi:10.1007/978-94-009-0741-6_10.

[63] P. Cavaliere, Spark Plasma Sintering of Materials, 2019. doi:10.1007/978-3-030-05327-7.

[64] D.M. Hulbert, A. Anders, J. Andersson, E.J. Lavernia, A.K. Mukherjee, A discussion on the absence of plasma in spark plasma sintering, Scr. Mater. 60 (2009) 835–838.

doi:10.1016/J.SCRIPTAMAT.2008.12.059.

[65] Z.H. Zhang, Z.F. Liu, J.F. Lu, X.B. Shen, F.C. Wang, Y.D. Wang, The sintering mechanism in spark plasma sintering – Proof of the occurrence of spark discharge, Scr. Mater. 81 (2014) 56–59. doi:10.1016/J.SCRIPTAMAT.2014.03.011.

[66] M.J. Alinger, G.R. Odette, D.T. Hoelzer, On the role of alloy composition and processing parameters in nanocluster formation and dispersion strengthening in nanostuctured ferritic alloys, Acta Mater. 57 (2009) 392–406. doi:10.1016/j.actamat.2008.09.025.

[67] P. He, T. Liu, A. Möslang, R. Lindau, R. Ziegler, J. Hoffmann, P. Kurinskiy, L. Commin, P. Vladimirov, S. Nikitenko, M. Silveir, XAFS and TEM studies of the structural evolution of yttrium-enriched oxides in nanostructured ferritic alloys fabricated by a powder metallurgy process, Mater. Chem. Phys. 136 (2012) 990–998. doi:10.1016/J.MATCHEMPHYS.2012.08.038.

[68] S. Chung, B. Lee, S.Y. Lee, C. Do, H.J. Ryu, The effects of Y pre-alloying on the in-situ dispersoids of ODS CoCrFeMniNi high-entropy alloy, J. Mater. Sci. Technol. 85 (2021) 62–75. doi:10.1016/j.jmst.2020.11.081.

[69] Z. Mao, L. Xiong, S. Liu, The formation of the complex oxide in Ni-based alloy powder during mechanical milling and heat treatment, J. Alloys Compd. 879 (2021) 160333. doi:10.1016/J.JALLCOM.2021.160333.

[70] K.I. Kawamura, T. Maruyama, K. Nagata, The equilibrium oxygen pressure over the Cr-Y2O3-YCrO3 coexistence measured with the galvanic cell using stabilized ZrO2 solid electrolyte, Metall. Mater. Trans. B. 26 (1995) 289–294. doi:10.1007/BF02660971.

[71] H. Zhang, M.J. Gorley, K.B. Chong, M.E. Fitzpatrick, S.G. Roberts, P.S. Grant, An in situ powder neutron diffraction study of nano-precipitate formation during processing of oxide-dispersion-strengthened ferritic steels, J. Alloys Compd. 582 (2014) 769–773. doi:10.1016/j.jallcom.2013.08.069.

[72] X.L. Wang, C.T. Liu, U. Keiderling, A.D. Stoica, L. Yang, M.K. Miller, C.L. Fu, D. Ma, K. An, Unusual thermal stability of nano-structured ferritic alloys, J. Alloys Compd. 529 (2012) 96–101. doi:10.1016/j.jallcom.2012.02.143.

[73] X. Yan, X. Zhang, F. Wang, T. Stockdale, Y. Dzenis, M. Nastasi, B. Cui, Fabrication of ODS Austenitic Steels and CoCrFeNi High-Entropy Alloys by Spark Plasma Sintering for Nuclear Energy Applications, Adv. Manuf. Nucl. Energy. 71 (2019) 2856–2867. doi:10.1007/s11837-019-03531-7.

[74] H.K.D.H. Bhadeshia, Recrystallisation of practical mechanically alloyed iron-base and nickel-base superalloys, Mater. Sci. Eng. A. 223 (1997) 64–77. doi:10.1016/S0921-5093(96)10507-4.

[75] F.J. Humphreys, M. Matherly, Recrystallization and Related Annealing Phenomena, 2004.

[76] R. Bürgel, H.-J. Maier, T. Niendorf, Handbuch Hochtemperatur-Werkstofftechnik, 4th Editio, Vieweg+Teubner, 2011.

[77] N. Sallez, Recrystallization , abnormal grain growth and ultrafine microstructure of ODS ferritic steels To cite this version : HAL Id : tel-01153888 DOCTEUR DE L ' UNIVERSIT É DE GRENOBLE Recrystallization , abnormal grain growth and, (2015).

[78] M. Hillert, On the theory of normal and abnormal grain growth, Acta Metall. 13 (1965) 227–238. doi:10.1016/0001-6160(65)90200-2.

[79] F. Haessner, Recrystallization of Metallic Materials, 2nd ed., Riederer-Verlag, 1978. https://books.google.at/books?id=zToIAQAAIAAJ.

108

[80] E. Nes, N. Ryum, O. Hunderi, On the Zener drag, Acta Metall. 33 (1985) 11–22. doi:10.1016/0001-6160(85)90214-7.

[81] N. Sallez, X. Boulnat, A. Borbély, J.L. Béchade, D. Fabrègue, M. Perez, Y. De Carlan, L. Hennet, C. Mocuta, D. Thiaudière, Y. Bréchet, In situ characterization of microstructural instabilities: Recovery, recrystallization and abnormal growth in nanoreinforced steel powder, Acta Mater. 87 (2015) 377–389. doi:10.1016/J.ACTAMAT.2014.11.051.

[82] J.I. Goldstein, D.E. Newbury, J.R. Michael, N.W.M. Ritchie, J.H.J. Scott, D.C. Joy, Microscopy and X-Ray Microanalysis, 2018.

[83] A. Suri, A. Pratt, S. Tear, C. Walker, C. Kincal, U. Kamber, O. Gurlu, M. El-Gomati, Analysis and detection of low-energy electrons in scanning electron microscopes using a Bessel box electron energy analyser, J. Electron Spectros. Relat. Phenomena. 241 (2020) 0–1. doi:10.1016/j.elspec.2019.02.002.

[84] J. Cazaux, Material contrast in SEM: Fermi energy and work function effects, Ultramicroscopy. 110 (2010) 242–253. doi:10.1016/j.ultramic.2009.12.002.

[85] W.C.H. Kuo, M. Briceno, D. Ozkaya, Characterisation of catalysts using secondary and backscattered electron in-lens detectors, Platin. Met. Rev. 58 (2014) 106–110. doi:10.1595/147106714X680113.

[86] D.B. Williams, C.B. Carter, Transmission electron microscopy: A textbook for materials science, 2009. doi:10.1007/978-0-387-76501-3.

[87] R.F. Egerton, Physical principles of electron microscopy, 2005. doi:10.1016/s1369-7021(05)71290-6.

[88] H.-J. Penkalla, Modern Methods of Specimen Preparation for TEM including Focused Ion Beam (FIB), Proc. 1st Summer Sch. Adv. Electron Microsc. (2003).

[89] R. Wirth, Focused Ion Beam (FIB) combined with SEM and TEM: Advanced analytical tools for studies of chemical composition, microstructure and crystal structure in geomaterials on a nanometre scale, Chem. Geol. 261 (2009) 217–229. doi:10.1016/j.chemgeo.2008.05.019.

[90] G. Baptiste, M.P. Moody, J.M. Cairney, S.P. Ringer, Atom Probe Microscopy, Springer US, 2012.

[91] T.L. Martin, A.J. London, B. Jenkins, S.E. Hopkin, J.O. Douglas, P.D. Styman, P.A.J. Bagot, M.P. Moody, Comparing the Consistency of Atom Probe Tomography Measurements of Small-Scale Segregation and Clustering between the LEAP 3000 and LEAP 5000 Instruments, Microsc. Microanal. 23 (2017) 227–237. doi:10.1017/S1431927617000356.

[92] C. Hatzoglou, B. Radiguet, G. Da Costa, P. Pareige, M. Roussel, M. Hernandez-Mayoral, C. Pareige, Quantification of APT physical limitations on chemical composition of precipitates in Fe–Cr alloys, J. Nucl. Mater. 522 (2019) 64–73. doi:10.1016/J.JNUCMAT.2019.05.022.

[93] C. Hatzoglou, B. Radiguet, F. Vurpillot, P. Pareige, A chemical composition correction model for nanoclusters observed by APT - Application to ODS steel nanoparticles, J. Nucl. Mater. 505 (2018) 240–248. doi:10.1016/J.JNUCMAT.2018.03.057.

[94] Periodic Table of the Isotopes for Atom Probe Tomography, (n.d.).

[95] R. Lawitzki, P. Stender, G. Schmitz, Compensating Local Magnifications in Atom Probe Tomography for Accurate Analysis of Nano-Sized Precipitates, Microsc. Microanal. 27 (2021) 499–510. doi:10.1017/S1431927621000180.

[96] M.K. Miller, K.F. Russell, Atom probe specimen preparation with a dual beam SEM/FIB miller, Ultramicroscopy. 107 (2007) 761–766. doi:10.1016/j.ultramic.2007.02.023.

[97] F.A. Stevie, C.B. Vartuli, L.A. Giannuzzi, T.L. Shofner, S.R. Brown, B. Rossie, F. Hillion, R.H. Mills, Application of focused ion beam lift-out specimen preparation to TEM, SEM, STEM, AES and SIMS analysis, Surf. Interface Anal. 31 (2001) 345–351. doi:10.1002/sia.1063.

[98] M.K. Miller, R.G. Forbes, Atom-probe tomography: The local electrode atom probe, Atom-Probe Tomogr. Local Electrode Atom Probe. 9781489974 (2014) 1–423. doi:10.1007/978-1-4899-7430-3.

[99] L.T. Stephenson, M.P. Moody, P. V. Liddicoat, S.P. Ringer, New techniques for the analysis of fine-scaled clustering phenomena within Atom Probe Tomography (APT) data, Microsc. Microanal. 13 (2007) 448–463. doi:10.1017/S1431927607070900.

[100] R.P. Kolli, D.N. Seidman, Comparison of compositional and morphological atom-probe tomography analyses for a multicomponent Fe-Cu steel, Microsc. Microanal. 13 (2007) 272–284. doi:10.1017/S1431927607070675.

[101] S. Zeisl, A. Lassnig, A. Hohenwarter, F. Mendez-Martin, Precipitation behavior of a Co-free Fe-Ni-Cr-Mo-Ti-Al maraging steel after severe plastic deformation, Mater. Sci. Eng. A. 833 (2022) 142416. doi:10.1016/J.MSEA.2021.142416.

[102] J. Čížek, Characterization of lattice defects in metallic materials by positron annihilation spectroscopy: A review, J. Mater. Sci. Technol. 34 (2018) 577–598. doi:10.1016/J.JMST.2017.11.050.

[103] A. Somoza, A. Dupasquier, Positron studies of solute aggregation in age-hardenable aluminum alloys, J. Mater. Process. Technol. 135 (2003) 83–90. doi:10.1016/S0924-0136(02)01043-9.

[104] M. Butterling, Positron Annihilation Spectroscopy at the HZDR, (n.d.). https://www.hzdr.de/db/Cms?pOid=35245&pNid=3225&pLang=en.

[105] J. V. Olsen, P. Kirkegaard, N.J. Pedersen, M. Eldrup, PALSfit: A new program for the evaluation of positron lifetime spectra, Phys. Status Solidi Curr. Top. Solid State Phys. 4 (2007) 4004–4006. doi:10.1002/pssc.200675868.

[106] W.L. Bragg, The Structure of Some Crystals as Indicated by their Diffraction of X-rays. Crystals as Indicated by their Diffraction of X-rays, Proc. R. Soc. Lond. A (1913) 248–277. doi:http://doi.org/10.1098/rspa.1913.0083.

[107] T. Ungár, Microstructural parameters from X-ray diffraction peak broadening, Scr. Mater. 51 (2004) 777–781. doi:10.1016/j.scriptamat.2004.05.007.

[108] T. Ungár, S. Ott, P.G. Sanders, A. Borbély, J.R. Weertman, Dislocations, grain size and planar faults in nanostructured copper determined by high resolution X-ray diffraction and a new procedure of peak profile analysis, Acta Mater. 46 (1998) 3693–3699. doi:10.1016/S1359-6454(98)00001-9.

[109] V. Soleimanian, M. Mojtahedi, A comparison between different X-ray diffraction line broadening analysis methods for nanocrystalline ball-milled FCC powders, Appl. Phys. A Mater. Sci. Process. 119 (2015) 977–987. doi:10.1007/s00339-015-9054-y.

[110] T. Ungár, Á. Révész, A. Borbély, Dislocations and Grain Size in Electrodeposited Nanocrystalline Ni Determined by the Modified Williamson-Hall and Warren-Averbach Procedures, J. Appl. Crystallogr. 31 (1998) 554–558. doi:10.1107/S0021889897019559.

[111] M. Bahramyan, S. Hossein Nedjad, X-ray diffraction line broadening analysis of nanostructured nickel powder, Phys. Met. Metallogr. 118 (2017) 839–845. doi:10.1134/S0031918X17090022.

[112] M.S. Paterson, X-ray diffraction by face-centered cubic crystals with deformation faults, J. Appl. Phys. 23 (1952) 805–811. doi:10.1063/1.1702312.

[113] B.E. Warren, X-ray studies of deformed metals, Prog. Met. Phys. 8 (1959) 147–202. doi:10.1016/0502-8205(59)90015-2.

[114] M. Moreno, J. Teixeira, G. Geandier, J.C. Hell, F. Bonnet, M. Salib, S.Y.P. Allain, Real-time investigation of recovery, recrystallization and austenite transformation during annealing of a cold-rolled steel using high energy X-ray diffraction (HEXRD), Metals (Basel). 9 (2019). doi:10.3390/met9010008.

[115] NIST, Line Position and Line Shape Standard for Powder Diffraction (Lanthanum Hexaboride Powder), Natl. Inst. Stand. Technol. US Dep. Commer. Gaithersburg, MD. (2015) 1–5. https://www-s.nist.gov/srmors/certificates/660C.pdf?CFID=35608137&CFTOKEN=7e602cd95cb32152-D56C3582-CDD9-D727-1A32D16FDB2CF208.

[116] H.G. Brokmeier, M. Müller, P. Pranzas, Klaus, A. Schreyer, P. Staron, The High Energy Materials Science Beamline (HEMS) at PETRA III, Mater. Sci. Forum. 772 (2013) 57–61. doi:https://doi.org/10.4028/www.scientific.net/MSF.772.57.

[117] J. Zbiral, Tensile properties of mechanically alloyed Ni-based alloys, (1994).

[118] G. Laplanche, A. Kostka, O.M. Horst, G. Eggeler, E.P. George, Microstructure evolution and critical stress for twinning in the CrMnFeCoNi high-entropy alloy, Acta Mater. 118 (2016) 152–163. doi:10.1016/j.actamat.2016.07.038.

[119] O. Bouaziz, Strain-hardening of twinning-induced plasticity steels, Scr. Mater. 66 (2012) 982–985. doi:10.1016/j.scriptamat.2011.11.029.

[120] D. Wimler, S. Kardos, J. Lindemann, H. Clemens, S. Mayer, Aspects of powder characterization for additive manufacturing, Prakt. Metallogr. Metallogr. 55 (2018) 620–636. doi:10.3139/147.110547.

[121] S. Vock, B. Klöden, A. Kirchner, T. Weißgärber, B. Kieback, Powders for powder bed fusion: a review, Prog. Addit. Manuf. 4 (2019) 383–397. doi:10.1007/s40964-019-00078-6.

[122] K.H. Chung, J. He, D.H. Shin, J.M. Schoenung, Mechanisms of microstructure evolution during cryomilling in the presence of hard particles, Mater. Sci. Eng. A. 356 (2003) 23–31. doi:10.1016/S0921-5093(02)00833-X.

[123] Y. Guo, M. Li, C. Chen, P. Li, W. Li, Q. Ji, Y. Zhang, Y. Chang, Oxide dispersion strengthened FeCoNi concentrated solid-solution alloys synthesized by mechanical alloying, Intermetallics. 117 (2020) 106674. doi:10.1016/j.intermet.2019.106674.

[124] R.M. Pohan, B. Gwalani, J. Lee, T. Alam, J.Y. Hwang, H.J. Ryu, R. Banerjee, S.H. Hong, Microstructures and mechanical properties of mechanically alloyed and spark plasma sintered Al0.3CoCrFeMnNi high entropy alloy, Mater. Chem. Phys. 210 (2018) 62–70. doi:10.1016/j.matchemphys.2017.09.013.

[125] M. Li, Y. Guo, H. Wang, J. Shan, Y. Chang, Microstructures and mechanical properties of oxide dispersion strengthened CoCrFeNi high-entropy alloy produced by mechanical alloying and spark plasma sintering, Intermetallics. 123 (2020) 106819. doi:10.1016/j.intermet.2020.106819.

[126] K.H. Chung, R. Rodriguez, E.J. Lavernia, J. Lee, Grain growth behavior of cryomilled INCONEL 625 powder during isothermal heat treatment, Metall. Mater. Trans. A Phys. Metall. Mater. Sci. 33 (2002) 125–134. doi:10.1007/s11661-002-0011-y.

[127] S.H. Joo, H. Kato, M.J. Jang, J. Moon, E.B. Kim, S.J. Hong, H.S. Kim, Structure and properties of ultrafine-grained CoCrFeMnNi high-entropy alloys produced by mechanical alloying and spark plasma sintering, J. Alloys Compd. 698 (2017) 591–604. doi:10.1016/j.jallcom.2016.12.010.

[128] I.C. Albayrak, S. Basu, A. Sakulich, O. Yeheskel, M.W. Barsoum Z Z, Elastic and Mechanical Properties of Polycrystalline Transparent Yttria as Determined by Indentation Techniques, (n.d.). doi:10.1111/j.1551-2916.2010.03669.x.

[129] F. De Geuser, W. Lefebvre, F. Danoix, F. Vurpillot, B. Forbord, D. Blavette, An improved reconstruction procedure for the correction of local magnification effects in three-dimensional atom-probe, Surf. Interface Anal. 39 (2007) 268–272.

[130] G. Ressel, S. Primig, H. Leitner, The evolution of y distribution during the processing route of mechanically alloyed iron studied by means of atom probe tomography, Int. J. Mater. Res. 104 (2013) 1088–1095. doi:10.3139/146.110964.

[131] C.A. Williams, P. Unifantowicz, N. Baluc, G.D.W. Smith, E.A. Marquis, The formation and evolution of oxide particles in oxide-dispersion- strengthened ferritic steels during processing, Acta Mater. 61 (2013) 2219–2235. doi:10.1016/j.actamat.2012.12.042.

[132] M. Brocq, B. Radiguet, J.M. Le Breton, F. Cuvilly, P. Pareige, F. Legendre, Nanoscale characterisation and clustering mechanism in an Fe–Y2O3 model ODS alloy processed by reactive ball milling and annealing, Acta Mater. 58 (2010) 1806–1814. doi:10.1016/J.ACTAMAT.2009.11.022.

[133] G. Ressel, P. Parz, S. Primig, H. Leitner, H. Clemens, W. Puff, New findings on the atomistic mechanisms active during mechanical milling of a Fe-Y2O3model alloy, J. Appl. Phys. 115 (2014) 1–8. doi:10.1063/1.4869787.

[134] M. Saber, W. Xu, L. Li, Y. Zhu, C.C. Koch, R.O. Scattergood, Size effect of primary Y2O3 additions on the characteristics of the nanostructured ferritic ODS alloys: Comparing as-milled and as-milled/annealed alloys using S/TEM, J. Nucl. Mater. 452 (2014) 223–229. doi:10.1016/j.jnucmat.2014.05.014.

[135] P. Scherrer, Bestimmung der inneren Struktur und der Größe von Kolloidteilchen mittels Röntgenstrahlen, Kolloidchem. Ein Lehrb. 277 (1912) 387–409. doi:10.1007/978-3-662-33915-2_7.

[136] B. Schuh, R. Pippan, A. Hohenwarter, Tailoring bimodal grain size structures in nanocrystalline compositionally complex alloys to improve ductility, Mater. Sci. Eng. A. 748 (2019) 379–385. doi:10.1016/j.msea.2019.01.073.

[137] X. Sauvage, G. Wilde, S. V. Divinski, Z. Horita, R.Z. Valiev, Grain boundaries in ultrafine grained materials processed by severe plastic deformation and related phenomena, Mater. Sci. Eng. A. 540 (2012) 1–12. doi:10.1016/J.MSEA.2012.01.080.

[138] J.H. Kim, K.R. Lim, J.W. Won, Y.S. Na, H.S. Kim, Mechanical properties and deformation twinning behavior of as-cast CoCrFeMnNi high-entropy alloy at low and high temperatures, Mater. Sci. Eng. A. 712 (2018) 108–113. doi:10.1016/j.msea.2017.11.081.

[139] Y.H. Wang, Z.F. Zhang, S.J. Sun, H.J. Yang, Y.Z. Tian, H.R. Lin, X.G. Dong, Transition of twinning behavior in CoCrFeMnNi high entropy alloy with grain refinement, Mater. Sci. Eng. A. 712 (2017) 603–607. doi:10.1016/j.msea.2017.12.022.

[140] V.I. Razumovskiy, D. Scheiber, O. Peil, A. Stark, G. Ressel, A. Stark, M. Mayer, Thermodynamics of Vacancy Formation in the CoCrFeMnNi High Entropy Alloy from DFT Calculations, Asp. Min. Miner. Sci. 8 (2022). doi:10.31031/AMMS.2022.08.00069.

[141] L. Resch, M. Luckabauer, N. Helthuis, N.L. Okamoto, T. Ichitsubo, R. Enzinger, W. Sprengel, R. Würschum, Search for vacancies in concentrated solid-solution alloys with fcc crystal structure, Phys. Rev. Mater. 4 (2020) 60601. doi:10.1103/PhysRevMaterials.4.060601.

[142] M. Elsayed, R. Krause-Rehberg, C. Eisenschmidt, N. Eißmann, B. Kieback, Defect Study in CoCrFeMnNi High Entropy Alloy by Positron Annihilation Lifetime Spectroscopy, Phys. Status Solidi Appl. Mater. Sci. 215 (2018) 1–4. doi:10.1002/pssa.201800036.

[143] S. Abhaya, R. Rajaraman, S. Kalavathi, G. Amarendra, Positron annihilation studies on FeCrCoNi high entropy alloy, J. Alloys Compd. 620 (2015) 277–282. doi:10.1016/J.JALLCOM.2014.09.137.

[144] H. Ohkubo, Z. Tang, Y. Nagai, M. Hasegawa, T. Tawara, M. Kiritani, Positron annihilation study of vacancy-type defects in high-speed deformed Ni, Cu and Fe, Mater. Sci. Eng. A. 350 (2003) 95–101. doi:10.1016/S0921-5093(02)00705-0.

[145] J. Schiotz, T. Leffers, B.N. Singh, Dislocation nucleation and vacancy formation during high-speed deformation of fcc metals, Philos. Mag. Lett. 81 (2001) 301–309. doi:10.1080/09500830110041657.

[146] M. Kiritani, Y. Satoh, Y. Kizuka, K. Arakawai, Y. Ogasawara, S. Arai, Y. Shimomura, Anomalous production of vacancy clusters and the possibility of plastic deformation of crystalline metals without dislocations, Philos. Mag. Lett. 79 (1999) 797–804. doi:10.1080/095008399176616.

[147] N. Oono, S. Ukai, Precipitation of oxide particles in oxide dispersion strengthened (ODS) ferritic steels, Mater. Trans. 59 (2018) 1651–1658. doi:10.2320/matertrans.M2018110.

[148] H.Z. Fang, S.L. Shang, Y. Wang, Z.K. Liu, D. Alfonso, D.E. Alman, Y.K. Shin, C.Y. Zou, A.C.T. Van Duin, Y.K. Lei, G.F. Wang, First-principles studies on vacancy-modified interstitial diffusion mechanism of oxygen in nickel, associated with large-scale atomic simulation techniques, J. Appl. Phys. 115 (2014). doi:10.1063/1.4861380.

[149] K. Mino, Y.G. Nakagawa, A. Ohtomo, Abnormal grain growth behavior of an, Metall. Trans. A. 18 (1987) 777–784. doi:10.1007/BF02646920.

[150] G.S. Rohrer, Introduction to grains, phases, and interfaces-an interpretation of microstructure, 2010. doi:10.1007/s11661-010-0215-5.

8 Publications

Two publications are appended to this work, which are both a fundamental part of chapter 4.1 (Temperature effect of the refinement and dissolution of yttria during mechanical alloying).

Publication A focuses on the evolution of the powder morphology and refinement of yttria as a function of milling time and temperature. Conclusions are drawn regarding the mechanism of the yttria refinement and the efficiency of cryogenic mechanical alloying.

Publication B investigates the refinement and dissolution mechanism of yttria in an fcc matrix during mechanical allying more deeply. Furthermore, the effect of the milling temperature on the dissolution of yttria is described and discussed.

8.1 List of publications

Publication A:

M. Mayer, G. Ressel, J. Svoboda

The Effect of Cryogenic Mechanical Alloying and Milling Duration on Powder Particles' Microstructure of an Oxide Dispersion Strengthened FeCrMnNiCo High-Entropy Alloy

Metallurgical and Materials Transactions A (2021)

Publication B:

M. Mayer, J. Svoboda, F. Mendez-Martin, C. Gammer, V. Razumovskiy, W. Sprengel, L. Resch, A. Stark, S. Zeisl, G. Ressel

From microscopic to atomistic scale: Temperature effect on yttria distribution in milled FeCrMnNiCo powder particles

Submitted to Acta Materialia on Oct. 25th, 2022

Publication A

M. Mayer, G. Ressel, J. Svoboda

The Effect of Cryogenic Mechanical Alloying and Milling
Duration on Powder Particles' Microstructure of an Oxide
Dispersion Strengthened FeCrMnNiCo High-Entropy Alloy

CRediT author contribution statement

M. Mayer: Conceptualization, Methodology, Software, Validation,
Formal analysis, Investigation (milling experiments), Writing -
Original Draft. **G. Ressel:** Conceptualization, Writing - Review &
Editing, Supervision, Project administration, Funding acquisition. **J.
Svoboda:** Writing - Review & Editing, Supervision

The Effect of Cryogenic Mechanical Alloying and Milling Duration on Powder Particles' Microstructure of an Oxide Dispersion Strengthened FeCrMnNiCo High-Entropy Alloy

MICHAEL MAYER, GERALD RESSEL, and JIRI SVOBODA

Oxide dispersion strengthened materials are commonly used for high-temperature applications. Among other possibilities, these oxides are mostly introduced by mechanical alloying comprising cold welding and fracturing of powders by high-impact loads during milling. However, despite their outstanding high-temperature performance, these materials are still not established because of their laborious and thus expensive processing. Therefore, to improve mechanical alloying's efficiency, the effect of lower milling temperatures is investigated on an oxide-dispersion strengthened high-entropy-alloy in the proposed study. To this end, prealloyed FeCrMnNiCo powders were milled together with yttria at cryogenic and room temperature by using a novel attritor cryomill. Powders milled at both temperatures were subsequently compared regarding their macroscopic morphology, amount and size distribution of detectable yttria as well as defect structure by means of high-resolution scanning electron microscopy and X-ray diffraction, respectively. Investigations showed a significant decrease of powder particle size and an insignificant influence on their aspect-ratio at cryogenic conditions. Furthermore, the phase fraction of detectable yttria got reduced by cryomilling, indicating increased dissolution or at least refinement. Additionally, a higher full width at half maximum accompanied by increased stacking fault probability of the fcc FeCrMnNiCo matrix gained by X-ray diffraction measurements suggests an improved milling efficiency during cryomilling intensified by higher defect density as well as strength of FeCrMnNiCo powders.

MICHAEL MAYER and GERALD RESSEL are with the Materials Center Leoben Forschung GmbH, Roseggerstraße 12, 8700 Leoben, Austria. Contact e-mail: Michael.Mayer@mcl.at JIRI SVOBODA is with the Institute of Physics of Materials, Academy of Sciences of the Czech Republic, Zizkova 22, 616 62 Brno, Czech Republic.
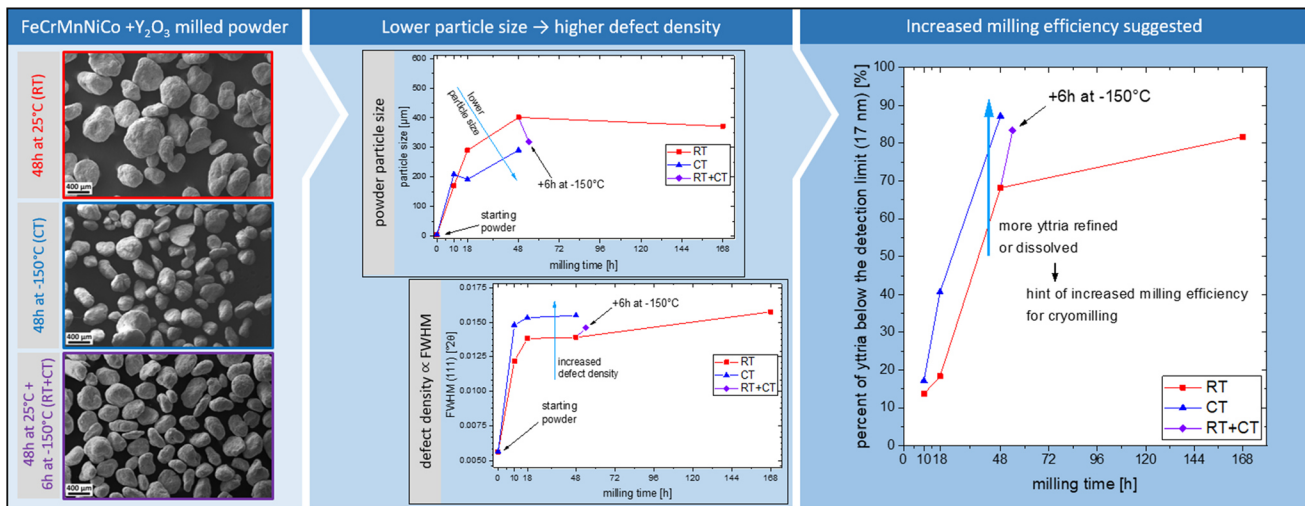
I. INTRODUCTION

THE efficiency of thermodynamic cyclic processes present in energy conversion or propulsion systems is increased with higher operation temperatures.[1,2] Consequently, as these operation temperatures are limited exceptionally by the materials applied, this means in turn that materials with increased load-bearing capacity at elevated or high temperatures lead to improved fuel efficiencies of these systems.[1] Nowadays, commonly used materials for these applications are Ni-based superalloys, which are already getting close to their limit as intermetallic particles coarsen and dissolve. Therefore, new material concepts are in focus of research to overcome this limit with high potential for enormous environmental as well as economic impact. One concept is high entropy alloys (HEA) as a new class of materials. Especially the so-called Cantor alloy, i.e., an equiatomic FeCrMnNiCo alloy, is already considered a promising candidate for applications at elevated temperatures because of its highly distorted, face-centered cubic (fcc) matrix and thus probably reduced diffusivity.[2] This so-called sluggish diffusion effect is one of the core effects of this class of alloys. It is expected that in HEAs, due to the mixed atomic structure and therefore locally different energetic sites, diffusing atoms become trapped at low energy sites and diffusion is slowed down.[2] However, other studies report contradictory results as no significant change of the diffusion coefficient compared to the elemental metals is found when the data are normalized to the melting temperature T_m.[3] The deformation behavior of this single-phase fcc FeCrMnNiCo alloy is already intensively studied and shows strong temperature-dependent mechanical properties with a low stacking fault energy.[4–10] Stepanov et al. showed that upon cryo-deformation the number of twinned grains increases but the dislocation density decreases compared to room temperature deformation,[11] which results in an increased strain hardening and a higher yield strength.[12] However, at elevated temperatures, the yield strength of this alloy is relatively low compared to Ni-based superalloys, which is, however, essential for application at these temperatures.

Therefore, one way to overcome this limit is the incorporation of nanometer-scaled oxidic particles, also known as oxide dispersion strengthening (ODS), which has proven to be an effective high-temperature strengthening mechanism. Among others,[13] these oxides are mostly introduced by mechanical alloying comprising cold welding and fracturing of at least two different types of input powders by high-impact loads during milling. Recently, also ODS FeCrMnNiCo alloys were produced via mechanical alloying at room temperature[14–16] as well as cryogenic temperatures[17] showing improved tensile properties at room and high temperatures[15,17] as well as lower compressive creep strain rates than the base alloy without dispersion strengthening.[16] However, the process of incorporating these small oxides via mechanical alloying is still time-consuming and therefore expensive.

Suryanarayana[18] described three stages of mechanical alloying of ODS materials. During the first stage, the ductile matrix gets flattened while the brittle oxide particles fracture and become occluded by the ductile constituents forming a lamellae structure with the oxide particles in between. During the second stage, work hardening of the ductile component promotes the fracture of the particles leading to a refinement of the lamella structure,[19,20] and the oxides become more finely distributed.[18] Depending on whether the oxides are soluble in the ductile constituent, during the third

milling stage, alloying occurs and homogeneity is achieved or the oxide particles are very finely distributed without being dissolved. Miller et al.[21] used atom probe tomography to analyze the oxide clusters in consolidated ODS steels and described different O:Y ratios compared to the added yttria concluding that the found oxide particles are not crushed remnants of the initial yttria.[21] Furthermore, other studies showed for mechanically alloyed body-centered cubic (bcc) steels that yttria dissolves at defects during milling,[22–26] and Ressel et al.[23] as well as Alinger et al.[24] found vacancies to play an important role in the dissolution of yttria in bcc steels. Upon subsequent consolidation, these metastable phases precipitate forming finely dispersed nanoparticles. However, Phaniraj et al.[27] concluded for fcc austenitic steels that yttria does not get dissolved but is finely dispersed in the matrix.

As a result of this repeated fracturing and cold welding of the powders during mechanical alloying, severe plastic deformation takes place in the powder particles.[18] In literature, studies[28–32] report on high densities of vacancy clusters—so-called stacking fault tetrahedrons—in fcc metals produced by severe plastic deformation and that their formation is further promoted at lower stacking fault energies (SFEs). These clusters are highly stable and can grow to extend up to 18 nm in Al[29] or even 100 nm[30] in Au. It is further assumed that the defect density is increased by lowering the deformation temperature as recovery and recrystallization processes are suppressed. As a result, milling at lower temperatures reduces the particle sizes because of a shift of the balance between fracturing and cold welding by incorporating more defects.[19] Furthermore, calculations on the interaction kinetics of interstitials at dislocation showed a T^{-3} dependence, leading to more interstitials being attracted by dislocations at lower temperatures.[33,34]

Although cryomilling has been investigated over the last decades, especially for bcc steels,[19,35,36] a direct investigation of the influence of the milling temperature during the mechanical alloying of ODS-HEAs has not been reported in the literature so far. Therefore, to close this gap and to get a fundamental understanding of increased milling efficiency, this study focuses on the effect of cryogenic mechanical alloying on the powder particle's microstructure and the evolution of yttria dispersions in an fcc FeCrMnNiCo HEA. The microstructure and defect structure of the milled powders are analyzed by X-ray diffraction (XRD). Additionally, scanning electron microscope (SEM) investigations reveal the powder particle's size and morphology whereas high-resolution SEM (HR-SEM) resolves the phase fraction and size of yttria particles at cross sections of the milled powders to obtain insights into the refinement process of these oxide particles.
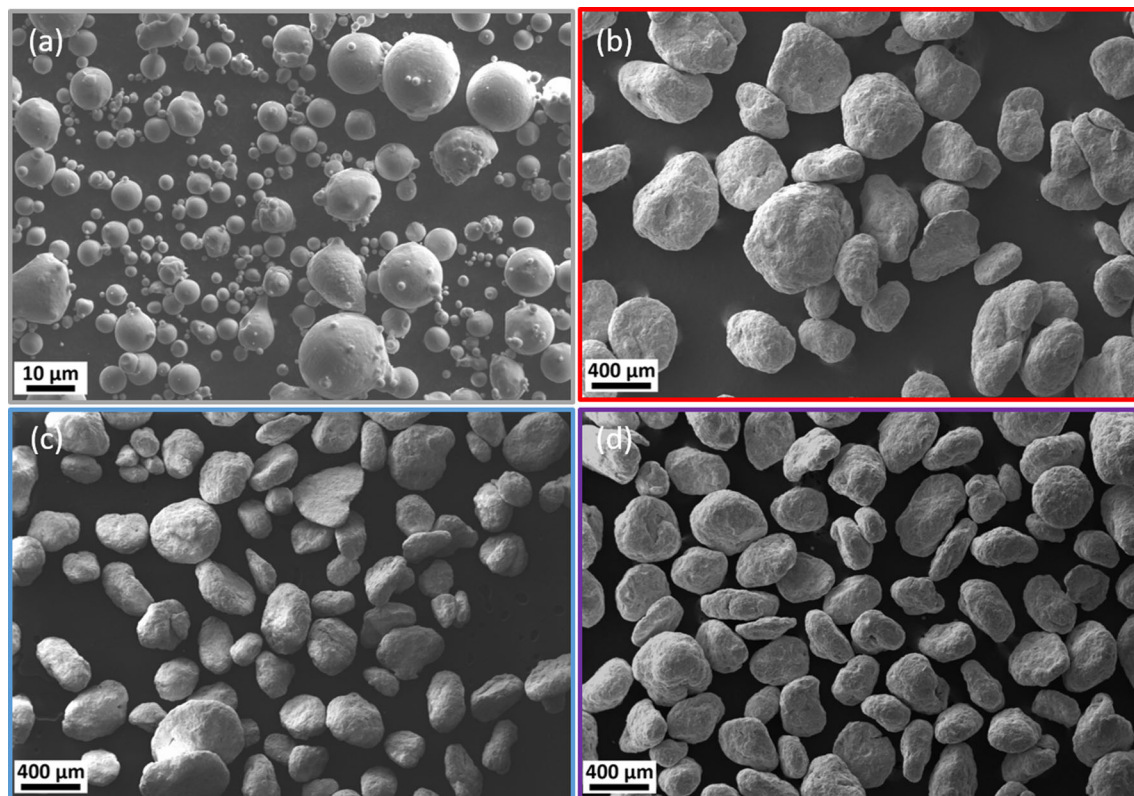

Fig. 1—Representative SEM images of the (a) unmilled powder and the (b) 48 h/RT, (c) 48 h/CT and (d) 48 h/RT + 6 h/CT milled powders showing a particle size increase with milling time and a decrease at lower milling temperatures.
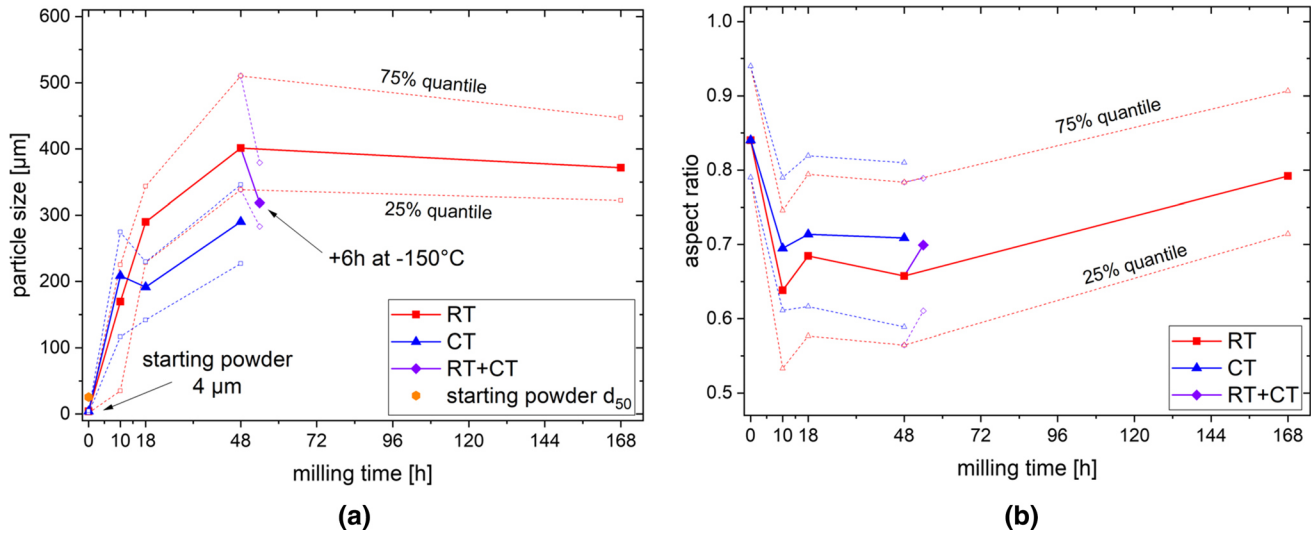
Fig. 2—(*a*) Powder particle size for the room temperature and cryomilled powders as a function of the milling time, indicating an increase with milling time and a decrease at lower milling temperatures. (*b*) Aspect ratio against the milling time showing no significant temperature dependence.

II. METHODS

For mechanical alloying, pre-alloyed, gas-atomized FeCrMnNiCo powders with a nominal composition of 20Fe–20Cr–20Mn–20Ni–20Co (at pct) were mechanically alloyed with 1 mol pct of Y_2O_3 in a stainless steel (X6CrNiMoTi17-12-2) grinding vial. The FeCrMnNiCo powders had a mean particle size of 4 μm while the Y_2O_3 particles showed a d_{90} of 1.16 μm. Milling was carried out using a novel high-energy attritor ball mill with an operation speed of 300 rpm. Furthermore, the milling setup comprised Inconel 825 balls with a diameter of 6.35 mm and a ball-to-powder weight ratio (BPR) of 10:1 (5 kg ball mass and 0.5 kg powder mass). To prevent the final powder from contamination of atmosphere, a vacuum of 10^{-3} mbar was applied. To investigate the influence of the milling time and the milling temperature, individual experiments with alternating milling times (10, 18, 48 and 168 hours) and milling temperatures (room temperature RT and cryogenic temperature CT) were performed as well as the combination of both temperatures (6 hours milling at CT added to 48 hours milled at RT). The RT experiments were water cooled, whereas for cryomilling experiments liquid nitrogen was used to maintain a temperature of approximately − 150 °C outside the grinding vial.

The powder morphology was investigated using a Zeiss Evo MA25 and the captured images analyzed by applying an in-house programmed python code (Python 3.7) using image detection. Therein, powder particles are detected, and a circle- and an ellipse-fit is conducted onto each particle exhibiting the same area as the projection of the particle. By using the diameter of the fitted circle as well as the breadth and length of the ellipse, the particle size and the aspect ratio of the particles were calculated, respectively.

To analyze the chemical composition, the microstructure and the yttria dispersions, the milled powders were hot mounted and cross sections were prepared using standard metallographic methods including active oxide suspensions (OPS). To determine the overall chemistry, EDX measurements were conducted at 20 kV using a Zeiss GeminiSEM 450 and an Oxford Instruments Ultim Extreme detector. To enhance the statistical power, area measurements at six images were carried out and the mean values calculated. Evaluation of the yttria particle size distribution and phase fraction was conducted at 5 kV and at three magnifications (1 kX, 3 kX, 10 kX) to detect enough yttria particles using the InLens SE detector, where the yttria particles appeared as bright white spots. These images were analyzed by means of the same python software used for the powder morphology where particle dimensions below three pixels were generally excluded as they have a high chance of being incorrectly detected. To consider the different observed areas for each magnification, the particle size distributions were corrected using an area factor.

XRD measurements of the powders were carried out using a Bruker D8 Discovery with Cu-Kα radiation. The instrumental breadth was defined directly before the experiments by using a LaB$_6$ powder according to the National Institute of Standards and Technology.[37] The diffraction patterns were fitted using a Pseudo-Voight model and analyzed by using an in-house programmed python script (Python 3.7). Thereby, the full width at half maximum (FWHM) was measured. Evaluation regarding stacking fault probability was done from the asymmetric peak shift of the milled powders according to Warren[38] for the (111) and (200) neighboring peaks using the unmilled sample as a reference.
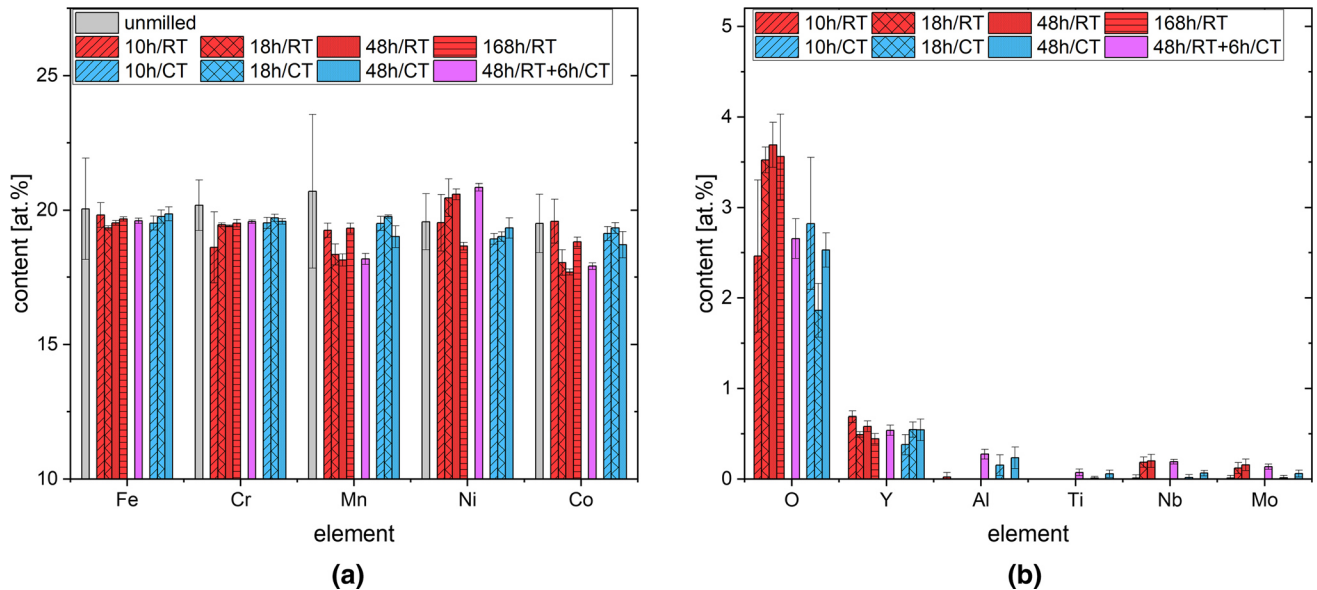
Fig. 3—Global chemistry measured with 20 kV EDX on cut sections of the powders for the (*a*) matrix elements and (*b*) yttria and other detected elements showing a nearly equiatomic matrix composition and similar Y contents in the milled powders.

III. RESULTS

A. *Temperature Effect on Powder Morphology and the Global Chemical Composition*

As mechanically alloying causes repeated cold welding and fracturing of the powders, the morphology and size are expected to be strongly milling time and temperature dependent. Figure 1 shows a representative image of the macroscopic shape of the 48 hours/CT milled powder with a rather spherical shape of the particles comparable to all other specimens.

Evaluation regarding particle size evolution during milling of the FeCrMnNiCo HEA with 1 mol pct Y_2O_3 at RT as presented in Figure 2(a) showed an increase of the particle size upon increasing milling time up to 400 μm. Milling at CT, however, also showed an increase of the particle size within the first 10 hours of milling similarly to the room temperature milled specimens, but lower particle sizes at longer milling times compared to the powders milled at RT. The temperature effect of lowering the particle size can also be seen at the specimen milled for 48 hours at RT followed by a 6 hours cryomilling experiment where the mean particle size decreases from approximately 400 to 300 μm. It should be mentioned that all cryogenically milled powders were smaller in mean size than the powder milled for 168 hours at RT.

As the aspect ratio presented in Figure 2(b) is a fundamental parameter of the flow ability of powders, the influence of the milling time and of the milling temperature is investigated in detail. It can be proposed that by applying the novel milling device the aspect ratio decreases during the first hours of milling from 0.84 to 0.7 and increases again to 0.8 with proceeding milling

times up to 168 hours. Lower milling temperatures cause a somewhat, however, insignificant increased steady state aspect ratio as depicted in Figure 2(b).

Furthermore, to analyze the global chemical composition of the powders and to show their comparability, EDX measurements on cross sections of the powders were done and are summarized in Figure 3. The main elements of the FeCrMnNiCo alloy (Figure 3(a)) show minor differences beside noticeably higher Ni and lower Mn and Cr content of the room temperature samples. This can be attributed to the incorporation of Inconel 718 and Inconel 825 as minor contaminations from former milling experiments as well as from the abrasion of the milling balls, respectively. This is also the reason for the existence of Nb and Mo in the same samples, which are alloying elements for Inconel 718 and Mo for Inconel 825 (Figure 3(b)). However, all chemical variations of FeCrMnNiCo show lower standard variations than the unmilled specimens and are insignificant.

Regarding the global Y content, it must be noted that variation of the overall Y content might be present because of measurement errors during the blending of the powders. The 10-hour CT sample and the 10-hour RT milled sample show an insignificantly lower and a higher Y mean content, respectively, but it is well met in the other specimens reaching a mean value of approximately 0.55 at pct Y, which is the equivalent Y content of 1 mol pct yttria. The associated low standard deviations indicate a homogeneous distribution of Y within all milled powders. Oxygen differs noticeably as well in the EDX measurements; nevertheless, it must be mentioned that the determination of oxygen by EDX is imprecise.

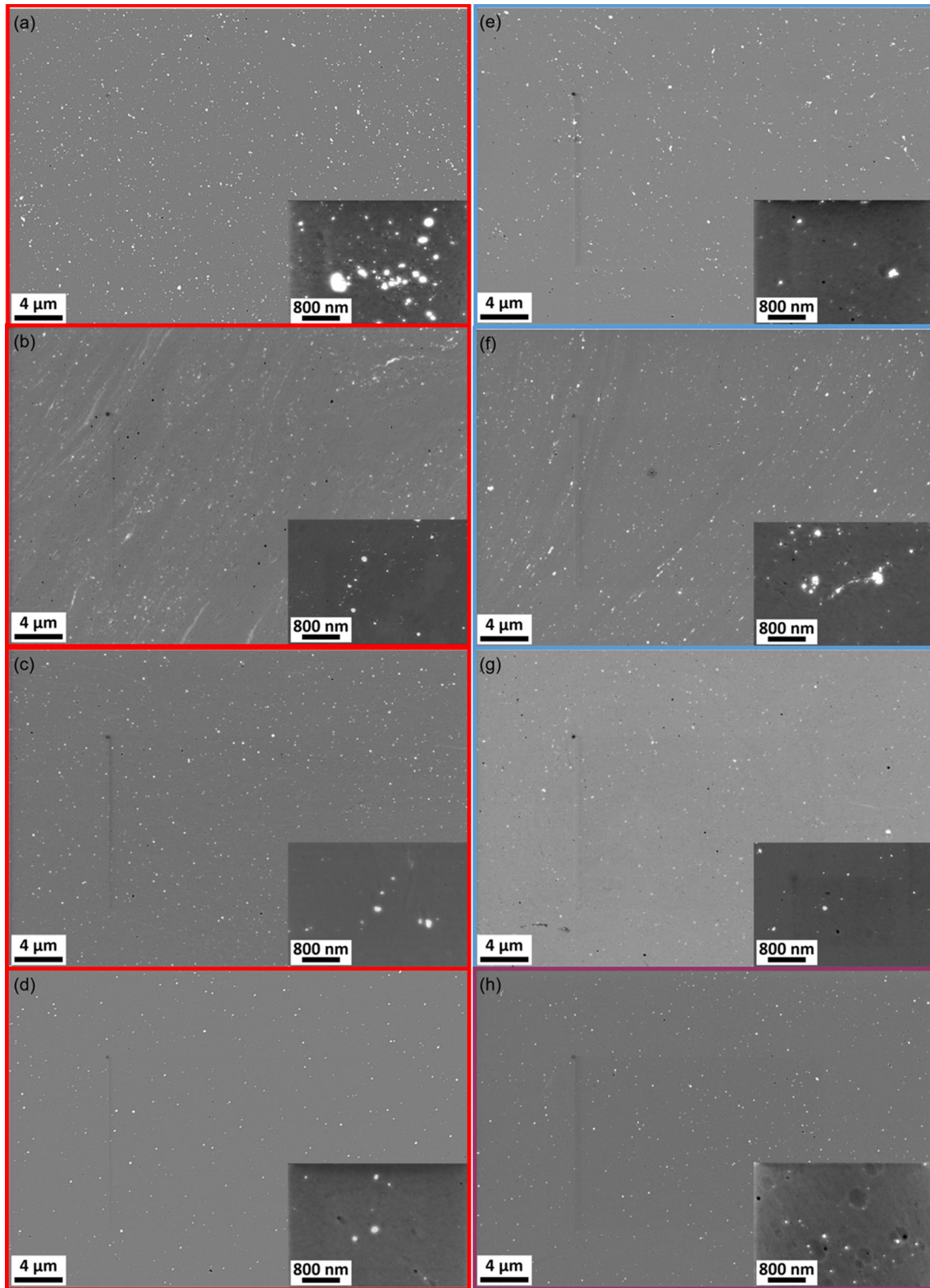Fig. 4—SE-InLens HR-SEM images indicating the distribution of yttria as bright white spots for the (*a*) 10 h, (*b*) 18 h, (*c*) 48 h and (*d*) 168 h samples milled at RT, (*e*) 10 h (*f*) 18 h and (*g*) 48 h samples milled at CT and (*h*) the sample milled for 48 h at RT and a subsequent milling for 6 h at CT. The detectable fraction of yttria decreases at longer milling times and cryogenic milling temperatures.
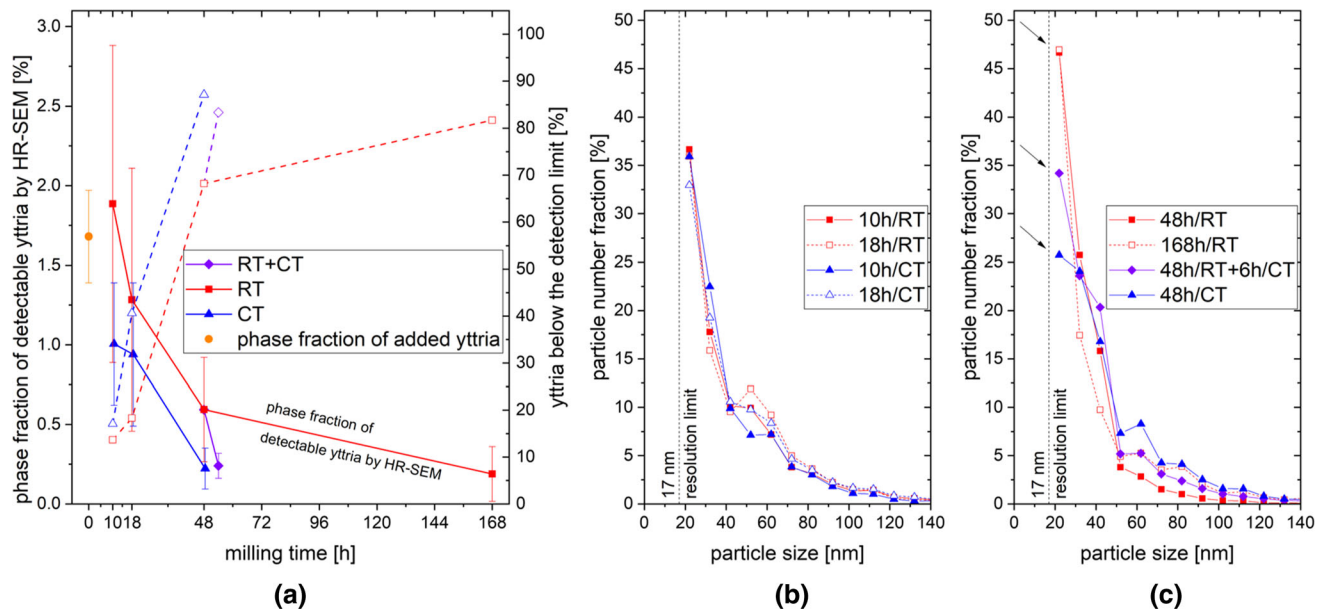
Fig. 5—(a) Phase fraction of detectable yttria by HR-SEM and percent of yttria below the detection limit of HR-SEM (< 17 nm) shown as a function of the milling time for specimens milled at room and cryogenic temperatures. The phase fraction of added yttria was calculated from the associated overall Y content measured by EDX and indicates a decrease upon longer milling times and cryogenic milling temperatures. (b) Milling time and temperature independent particle size distributions of 10 h and 18 h samples milled at RT and CT and (c) the particle size distributions of the 48 h/CT, 48 h/RT + 6 h/CT, 48 h/RT and 168 h/RT milled samples showing a decrease of the smallest particle fraction at lower milling temperatures.
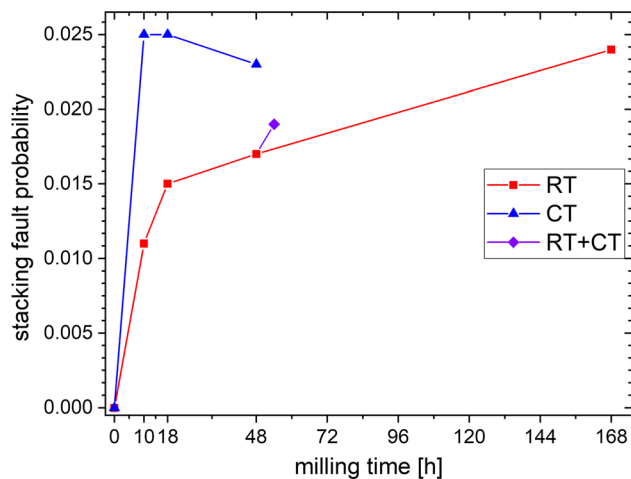
Fig. 6—Stacking fault probability calculated from the asymmetric peak shift of the (111) and (200) fcc reflections of FeCrMnNiCo as a function of milling duration at RT and CT as well as its combination showing a higher SFP for the cryomilled specimen.

B. Analysis of Detectable Yttria Particle Size Distribution and Phase Fraction

At longer milling times, the yttria particle sizes and detectable phase fractions are expected to decrease as a result of the continuous deformation and fracturing processes during mechanical alloying. Therefore, representative InLens HR-SEM images of cross sections are presented in Figure 4 with yttria particles indicated as bright white spots. Whereas Figures 4(a) through (d) shows the room temperature milled samples from 10 to 168 hours and Figure 4(h) represents the 48 hours/RT

+ 6 hours/CT milled specimens, Figures 4(e) through (g) shows the cryomilled samples.

Regarding milling times, the visible yttria phase fractions decrease and the dispersions seem more uniformly distributed for both temperatures at longer milling times whereas the 18-h milled specimens exhibit a typical lamella structure, indicating the second stage of mechanical alloying. It should be mentioned that due to the use of pre-alloyed powders, the matrix elements are homogeneously distributed, which was proven by EDS mappings (not presented in this article). The effect of the milling temperature can be seen by comparing the 48 hours/RT microstructure shown in Figure 4(c) with the states 48 hours/RT + 6 hours/CT and 48 hours/CT shown in Figures 4(h) and (g), respectively. By visual inspection, a decrease in the detectable phase fraction at comparable overall yttria contents shown in Figure 3(b) indicates an increased dissolution of yttria or at least smaller particles below the HR-SEM detection limit and a more uniform distribution of yttria upon milling at cryogenic temperatures.

To quantify the yttria dispersions, the measured phase fractions of the detectable yttria are shown in Figure 5(a), indicating a lower amount of yttria particles detectable by HR-SEM, i.e., > 17 nm or 3 pixels at a magnification of 10 kX, for longer milling times. Thus, an increased amount of yttria particles is below the before-mentioned detection limit as well as supersaturated in the FeCrMnNiCo matrix. This trend can be seen more clearly if the visible phase fraction is compared with the overall yttria as obtained by EDX, resulting in a percentage of undetected yttria of up to 87 vol pct for the 48 hours/CT specimen. Furthermore,
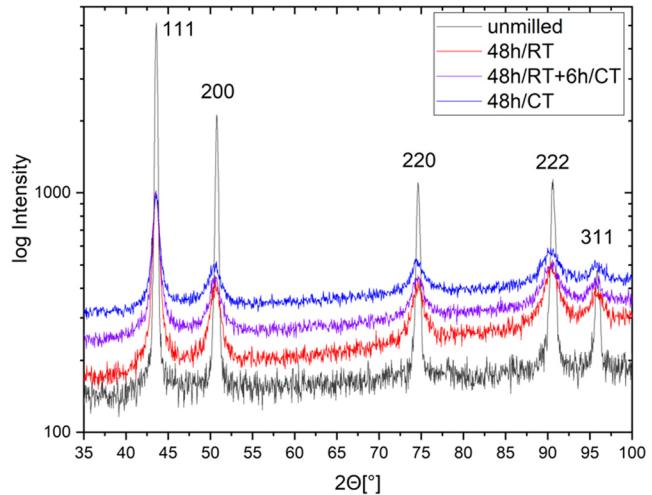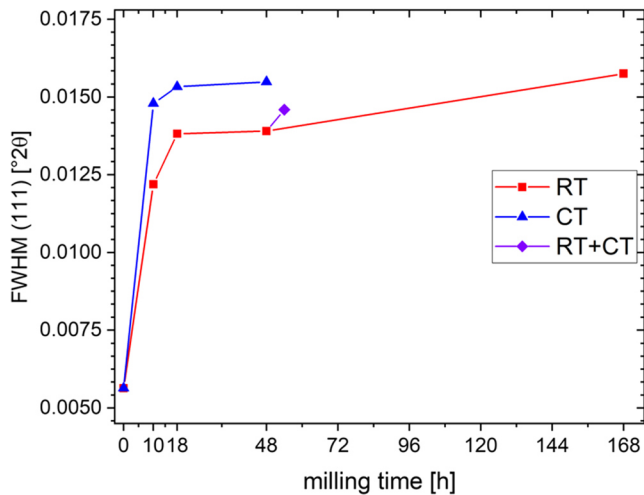
Fig. 7—(a) Full width at half maximum of the (111) reflection for all samples as a function of milling duration at RT and CT as well as its combination; (b) X-ray diffraction pattern of the unmilled, gas-atomized powder and the powders milled for 48 h at RT, 48 h at CT and the combination of both milling temperatures, respectively. Both figures confirm broader peaks after milling at CT compared to RT milling.

the standard deviation of the phase fraction significantly decreases upon longer milling times, indicating a more homogeneous yttria distribution. Comparing the RT with CT experiments reveals a slight tendency to lower phase fractions for the cryomilled samples suggesting a faster and more effective refinement or dissolution of yttria while at RT even milling for 168 hours does not reach the same amount of yttria below 17 nm as milling at CT.

For a detailed investigation on the fragmentation or dissolution behavior of yttria, Figures 5(b) and (c) shows the relative particle size distribution for all samples where each data point represents a range of 10 nm starting from the resolution limit of 17 nm toward larger dimensions. For shorter milling times up to 18 hours shown in Figure 5(b), no difference between the relative particle size distributions was found implying that the yttria particles get refined at all sizes at a comparable rate. However, at the longer milling times presented in Figure 5(c), cryomilling seems to reduce mainly oxide particles close to the detection limit as can be seen in the comparison between the 48, 168 and 48 hours/CT specimens (marked by arrows) where the fraction of oxide particles between 17 and 27 nm is significantly reduced for the cryomilled specimen. The 48 hours/RT + 6 hours/CT sample confirms this trend by lowering the fraction of small particles while milling at RT for 168 hours has a similar fraction close to the detection limit as the 48 hours/RT specimen but refines particles > 27 nm. Nevertheless, no pronounced temperature effect can be seen for particles > 27 nm for all specimens. Note that a lower particle number fraction of fine particles results in a proportionate higher fraction of larger particles.

C. Defect Evolution as a Function of Temperature and Milling Duration

Besides the evolution of the detectable particle sizes, the defect structure and sizes are highly relevant to obtain information on the effect of cryomilling on the ability to refine or dissolve yttria in the FeCrMnNiCo matrix. To obtain insights into temperature dependency on governing deformation mechanisms and thus to derive defect densities and formation mechanisms of the respective alloy, the stacking fault probability (SFP) of the cryomilled and room temperature milled powders is compared in Figure 6 and depicted as a function of milling time. Note: The SFP is the probability of finding a stacking fault between any two layers in the fcc stacking sequence and is therefore a measure for the formation of deformation-induced stacking faults.[38]

Evaluation reveals increased SFPs in all milling durations for the cryomilled powders compared to the powders milled at RT. Upon milling at CT, the SFP increases rapidly but stays rather constant at all performed milling durations at around 0.025, suggesting a stacking fault at every 40th atomic (111) plane. Conversely, milling at RT shows a lower increase of the SFP as a function of the milling time but reaches the same SFP as the cryomilled samples at 168 hours milling time. The tendency to a higher SFP with lower temperatures is corroborated by evaluation of the 48 hours/RT + 6 hours/CT sample, which shows an accelerated increase of the SFP compared to the powder milled for 48 hours at RT. Hence, it can be concluded that cryomilling as well as longer milling durations at RT promote the formation of an increased number of stacking faults.

XRD experiments further reveal an increased FWHM in the cryomilled samples compared to the RT milled specimens, as it shown in Figure 7(a) suggesting a higher defect density. According to the literature,[39] an increasing FWHM indicates a lower domain size or higher lattice strains (both indications for lattice defects) causing peak broadening in XRD diffraction patterns. During the first hours of milling, the FWHM increases rapidly up to 18 hours milling time continued by a lower increase for longer milling times. However, comparing the same milling times, milling at RT showed a lower FWHM compared to the cryomilled specimens resulting in comparable FWHM values for 48 hours milling at CT than 168 hours milling at RT, indicating a strong temperature effect on the peak broadening and thus defect densities of the investigated alloys. Furthermore, this is again supported by cryomilling for 6 hours subsequently to milling for 48 hours at RT as it causes a significantly steeper increase of the FWHM.

IV. DISCUSSION

To analyze the effect of cryogenic temperatures during attrition milling of an ODS HEA, in this work, series of advanced experiments were carried out. Powders were produced *via* mechanical alloying at room temperature as well as − 150 °C. The macroscopic powder morphology and the microscopic evolution of detectable yttria were analyzed by means of HR-SEM whereas XRD experiments reveal hints on the defect structure and deformation mechanisms, *i.e.*, formation of deformation-induced twinning, of investigated alloys.

According to Figure 2(a), the mean particle size increases upon milling at CT but also at RT in respective alloys agreeing with other studies dealing with milling of other fcc materials.[40] However, analysis of the aspect ratio reveals a decrease during milling, reaching a comparably high mean value between 0.65 and 0.8 after all milling durations, implying rather spherical shapes that qualify for potential additive manufacturing processes.[41,42] In literature some studies describe a flat or flaky powder shape[43,44] whereas others describe the opposite of achieving spherical particles[45–47] or in some cases a combination of both types of morphologies.[48,49] According to Surayanana,[18] the morphology is affected by the BPR. He proposed a dependency on the BPR, proposing that beyond a BPR of 10:1 milled powders tend to a spherical shape, whereas lower BPRs cause more flaky shapes. However, results of some other references[43,44] disagree with this assumption as in these experiments a BPR of 10:1 or higher was used achieving flaky particles. Consequently, a stronger effect of the ductility of the processed material as well as applied rotational speed combined with the design of the milling apparatus such as length of the milling pins and the distance to the milling container is suggested as the main factors influencing the powder's aspect ratio as they force the milling balls to rotate along the surface of the container.

Although the particle size increases during milling at cryogenic temperatures, the obtained cryomilled powders tend to be smaller than the room temperature milled powders allowing assumptions about the temperature-dependent deformation mechanism of this alloy. Generally, cold welding of powder particles upon the collision between the grinding balls causes an increase of the particle size while the continuous work hardening promotes their fracture.[18–20] As the cryomilled powders have a lower particle size compared to the room temperature milled specimens, it can be assumed that the repetitive and alternating processes of cold welding and fracturing shift more toward fracturing of the particles, resulting in smaller particles. Consequently, an increased work hardening ability and increasing yield strength of the investigated FeCrMnNiCo alloy at lower temperatures is implied, which is also found in References 7 and 8 and can also be directly related to deformation twinning as reported in Reference 12.

The proposed higher yield strength of the FeCrMnNiCo powder deformed at lower temperatures also suggests an accelerated refinement of yttria particles during mechanical alloying, resulting in a lower fraction of yttria > 17 nm detectable by HR-SEM as presented in Figure 5(a). The obtained temperature-independent particle size distribution for shorter milling times implies a refinement of the oxide particles at all sizes simultaneously, indicating the second stage of milling as suggested by Surayanana.[18] Therefore, considering the lower phase fraction of the cryomilled specimens, this refinement process is faster at lower temperatures and might be—as already discussed before—related to the higher yield strength of the cryomilled samples promoting oxide particle fracture.

Additionally, besides the direct evidence that lower temperatures seem to foster a dissolution of yttria or at least a refinement below the HR-SEM detection limit, Figure 5(b) supports this assumption as especially at longer milling times a decrease of the particle fraction close to the detection limit for the cryogenic milled powders was observed (marked by arrows). The further refinement of the smallest particle fraction is also the main root cause of the reduced phase fraction of the 48 hours/CT and the 48 hours/RT + 6 hours/CT samples compared to the 48 and 168 hours/RT samples. The particle size distributions shown in Figure 5(c) of the latter samples processed at RT seem to pile up close to the detection limit even more strongly than the CT samples, suggesting a stronger barrier-like effect preventing further refinement or dissolution during the third stage of mechanical alloying at RT. These results imply an increased amount of yttria being substantially refined or dissolved in the matrix at lower milling temperatures and longer milling times. However, whether yttria gets dissolved or just very finely dispersed (below the HR-SEM detection limit) cannot be

evidenced by the used methods, which will be, however, the focus of future work.

Besides the increased strength of the FeCrMnNiCo alloy, the accelerated refinement and possible subsequent increased solubility of Y_2O_3 can be explained by the formation of different defect structures at CT and RT. Previous studies on bcc steels proved defects such as vacancies or grain boundaries play an essential role in dissolution of yttria during mechanical alloying.[22–24,26] However, regarding fcc austenitic steels, studies, e.g., Phaniraj et al.,[27] report a fine dispersion of yttria and an impossibility of dissolution. Nevertheless, this conclusion is based on the observation of undissolved yttria in the milled powders after milling for 16 hours using XRD and X-ray photoelectron spectroscopy (XPS). However, from findings of this work it can be concluded that after 18 hours milling merely the second stage of milling was achieved where approximately 20 vol pct of the added yttria was refined below the detection limit at RT, suggesting that longer milling times or lower milling temperatures, i.e., increased defect densities and higher yield strengths, are needed to be able to detect a possible dissolution of yttria.

Therefore, to obtain detailed insights into the defect evolution during milling and their dependencies, this work investigated the FWHM and SFP as a function of milling duration and temperature by means of XRD. Analysis of the SFP as presented in Figure 6 reveals more stacking faults in both cryomilled samples—48 hours/CT and 48 hours/RT + 6 hours/CT—implying that deformation twinning is promoted at lower temperatures. This is in good agreement with studies proposed in the literature[5,8–11] suggesting that either low temperatures below RT or high stresses activate twinning deformation of the FeCrMnNiCo alloy. A higher SFP at lower deformation temperatures further confirms a low and temperature-dependent SFE as calculated by Huang et al.[5] According to Zhang et al.,[30] low SFEs in fcc metals promote the formation of stable vacancy cluster or so-called stacking fault tetrahedron. These clusters are reported to be highly stable and can hinder the motion of dislocations, thus effectively strengthening the material.[30] Supporting prior results, also subsequent milling for 6 hours at CT after 48 hours milling at RT increases the stacking fault probability; as a result, the powder particle size decreases more strongly, presumably because of increased twinning, possibly higher densities of the stacking fault cluster and hence increased work hardening and yield strength.

As the FWHM is a measure of the crystallite's domain size or lattice strains causing peak broadening in XRD diffraction patterns, it can give, besides the SFP, a fundamental indication for lattice defects. Therefore, also the FWHM is evaluated and presented in Figure 7, showing an increased FWHM in the cryomilled specimens, implying more defects present such as a lower domain size or higher lattice strains. Generally, lattice strains are caused by dislocations, vacancies, stacking faults or substitutional or interstitial elements.[39] As already discussed, more stacking faults are present in the cryomilled samples but their influence

on the peak broadening could not be determined quantitatively, and it can be assumed that dislocations and vacancies are present as well. Stepanov et al.[11] found a higher fraction of twinned grains but lower dislocation densities upon cryogenic deformation of a FeCrMnNiCo alloy whereas other studies reported high densities of vacancy clusters in heavily deformed fcc materials.[28–30,32] Therefore, the higher FWHM for the cryomilled specimens probably indicates smaller domain sizes as well as higher vacancy densities while especially vacancies are reported to play an important role in the dissolution of yttria into the matrix during milling as shown by Ressel et al. for bcc steels.[22,23]

The beneficial effect of cryomilling can be corroborated by calculations conducted by Svoboda et al.[33] and Fischer et al.[34] Although these calculations were done on the segregation of interstitials at edge dislocations in bcc steels, they are based on their molar volume and the strain field of dislocations and can be consequently adapted for the material in this study. It was found that the segregation capacity of interstitial atoms at edge dislocations depends as T^{-3} on the temperature, and, as a result, lowering the temperature enhances the segregation capability of interstitials at open volumes provided by defects. Considering the increase of lattice defects, this might explain the higher fraction of yttria below the resolution limit in the cryomilled specimens as presented in Figure 5(a), implying an increased amount of yttria being dissolved at lattice defects during milling at low temperatures. Thus, the lower temperature during cryomilling might reduce the time to achieve a certain amount of dissolved yttria, but no evidence was found that milling at room temperature does not reach the same amount of dissolved yttria upon milling for much longer times than the already investigated 168 hours.

V. CONCLUSIONS

The current work presents novel findings regarding the effect of cryogenic temperatures on the milling behavior of ODS FeCrMnNiCo HEA powders. Generally, it can be proposed that cryomilling might enhance the milling process of fcc FeCrMnNiCo and yttria resulting in an increased time efficiency of this generally long-lasting alloying process. The following detailed conclusions can be drawn:

- The powder particle size generally increased with milling time independently from milling temperature, whereas cryomilling resulted in smaller particles compared to RT milling, indicating a shift from cold welding to fracturing in conjunction with a higher yield strength at lower temperatures.
- Cryomilling resulted in an enhanced refinement of especially small yttria particles allowing shorter milling times to achieve a similar fraction of finely dispersed or dissolved yttria compared to the RT milled powders.
- XRD revealed increased FWHM values for cryomilled specimens, implying higher defect densities such as twins (corroborated by increased stacking

fault probability) and presumably higher densities of vacancies and vacancy cluster.

- It is implied that the increased density of lattice defects during cryomilling promotes the refinement or dissolution of especially the smallest fraction of yttria, as cryomilled specimens show a lower fraction of yttria particles between 17 and 27 nm (near the HR-SEM resolution limit).

CONFLICT OF INTEREST

On behalf of all authors, the corresponding author states that there is no conflict of interest.

REFERENCES

1. Rolls-Royce: *The Jet Engine*, 5th ed., Rolls-Royce, London, 1996.
2. M.H. Tsai and J.W. Yeh: *Mater. Res. Lett.*, 2014, vol. 2, pp. 107–23, https://doi.org/10.1080/21663831.2014.912690.
3. D.B. Miracle and O.N. Senkov: *Acta Mater.*, 2017, vol. 122, pp. 448–511, https://doi.org/10.1016/j.actamat.2016.08.081.
4. M. Naeem, H. He, S. Harjo, T. Kawasaki, F. Zhang, B. Wang, S. Lan, Z. Wu, Y. Wu, Z. Lu, C.T. Liu, and X.L. Wang: *Scripta Mater.*, 2020, vol. 188, pp. 21–25, https://doi.org/10.1016/j.scriptamat.2020.07.004.
5. S. Huang, W. Li, S. Lu, F. Tian, J. Shen, E. Holmström, and L. Vitos: *Scripta Mater.*, 2015, vol. 108, pp. 44–47, https://doi.org/10.1016/j.scriptamat.2015.05.041.
6. K.V.S. Thurston, A. Hohenwarter, G. Laplanche, E.P. George, B. Gludovatz, and R.O. Ritchie: *Intermetallics*, 2019, https://doi.org/10.1016/j.intermet.2019.04.012.
7. G. Laplanche, A. Kostka, O.M. Horst, G. Eggeler, and E.P. George: Microstructure evolution and critical stress for twinning in the CrMnFeCoNi high-entropy alloy *Acta Mater.*, 2016, vol. 118, pp. 152–63, https://doi.org/10.1016/j.actamat.2016.07.038.
8. F. Otto, A. Dlouhý, C. Somsen, H. Bei, G. Eggeler, and E.P. George: *Acta Mater.*, 2013, vol. 61, pp. 5743–55, https://doi.org/10.1016/j.actamat.2013.06.018.
9. Y.H. Wang, Z.F. Zhang, S.J. Sun, H.J. Yang, Y.Z. Tian, H.R. Lin, and X.G. Dong: *Mater. Sci. Eng. A.*, 2017, vol. 712, pp. 603–07, https://doi.org/10.1016/j.msea.2017.12.022.
10. J.H. Kim, K.R. Lim, J.W. Won, Y.S. Na, and H.S. Kim: *Mater. Sci. Eng. A*, 2018, vol. 712, pp. 108–13, https://doi.org/10.1016/j.msea.2017.11.081.
11. N. Stepanov, M. Tikhonovsky, N. Yurchenko, D. Zyabkin, M. Klimova, S. Zherebtsov, A. Efimov, and G. Salishchev: *Intermetallics*, 2015, vol. 59, pp. 8–17, https://doi.org/10.1016/j.intermet.2014.12.004.
12. O. Bouaziz: *Scripta Mater.*, 2012, vol. 66, pp. 982–85, https://doi.org/10.1016/j.scriptamat.2011.11.029.
13. F. Bergner, I. Hilger, J. Virta, J. Lagerbom, G. Gerbeth, S. Connolly, Z. Hong, P.S. Grant, and T. Weissgärber: *Metall. Mater. Trans. A Phys. Metall. Mater. Sci.*, 2016, vol. 47A, pp. 5313–24, https://doi.org/10.1007/s11661-016-3616-2.
14. B. Gwalani, R.M. Pohan, O.A. Waseem, T. Alam, S.H. Hong, H.J. Ryu, and R. Banerjee: *Scripta Mater.*, 2019, vol. 162, pp. 477–81, https://doi.org/10.1016/j.scriptamat.2018.12.021.
15. H. Hadraba, Z. Chlup, A. Dlouhy, F. Dobes, P. Roupcova, M. Vilemova, and J. Matejicek: *Mater. Sci. Eng. A*, 2017, vol. 689, pp. 252–56, https://doi.org/10.1016/j.msea.2017.02.068.
16. F. Dobeš, H. Hadraba, Z. Chlup, A. Dlouhý, M. Vilémová, and J. Matějíček: *Mater. Sci. Eng. A*, 2018, vol. 732, pp. 99–104, https://doi.org/10.1016/j.msea.2018.06.108.
17. S. Chung, B. Lee, S.Y. Lee, C. Do, and H.J. Ryu: *J. Mater. Sci. Technol.*, 2021, vol. 85, pp. 62–75, https://doi.org/10.1016/j.jmst.2020.11.081.
18. C. Suryanarayana: *Mechanical Alloying and Milling*, Marcel Dekker, New York, 2004.
19. D.B. Witkin and E.J. Lavernia: *Prog. Mater. Sci.*, 2006, vol. 51, pp. 1–60, https://doi.org/10.1016/j.pmatsci.2005.04.004.
20. H. Wen, T.D. Topping, D. Isheim, D.N. Seidman, and E.J. Lavernia: *Acta Mater.*, 2013, vol. 61, pp. 2769–82, https://doi.org/10.1016/j.actamat.2012.09.036.
21. M.K. Miller: *Microsc. Res. Tech.*, 2006, vol. 69, pp. 359–65, https://doi.org/10.1002/jemt.20291.
22. G. Ressel, D. Holec, A. Fian, F. Mendez-Martin, and H. Leitner: *Appl. Phys. A Mater. Sci. Process.*, 2014, vol. 115, pp. 851–58, https://doi.org/10.1007/s00339-013-7877-y.
23. G. Ressel, P. Parz, S. Primig, H. Leitner, H. Clemens, and W. Puff: *J. Appl. Phys.*, 2014, vol. 115, pp. 1–8, https://doi.org/10.1063/1.4869787.
24. M.J. Alinger, S.C. Glade, B.D. Wirth, G.R. Odette, T. Toyama, Y. Nagai, and M. Hasegawa: *Mater. Sci. Eng. A*, 2009, vol. 518, pp. 150–57, https://doi.org/10.1016/j.msea.2009.04.040.
25. N. Oono and S. Ukai: *Mater. Trans.*, 2018, vol. 59, pp. 1651–58, https://doi.org/10.2320/matertrans.M2018110.
26. L.L. Hsiung, M.J. Fluss, S.J. Tumey, B.W. Choi, Y. Serruys, F. Willaime, and A. Kimura: *Phys. Rev. B Condens. Matter Mater. Phys.*, 2010, vol. 82, pp. 1–13, https://doi.org/10.1103/PhysRevB.82.184103.
27. M.P. Phaniraj, D.I. Kim, J.H. Shim, and Y.W. Cho: *Acta Mater.*, 2009, vol. 57, pp. 1856–64, https://doi.org/10.1016/j.actamat.2008.12.026.
28. M. Kiritani, Y. Satoh, Y. Kizuka, K. Arakawai, Y. Ogasawara, S. Arai, and Y. Shimomura: *Philos. Mag. Lett.*, 1999, vol. 79, pp. 797–804, https://doi.org/10.1080/095008399176616.
29. X.L. Wu, B. Li, and E. Ma: *Phys. Lett.*, 2007, vol. 91, pp. 1–4, https://doi.org/10.1063/1.2794416.
30. L. Zhang, C. Lu, G. Michal, G. Deng, and K. Tieu: *Scripta Mater.*, 2017, vol. 136, pp. 78–82, https://doi.org/10.1016/j.scriptamat.2017.04.019.
31. S. Kojima, Y. Satoh, H. Taoka, I. Ishida, T. Yoshiie, M. Kiritani, and M. Kiritani: *Philos. Mag. A Phys. Condens. Matter Struct. Defects Mech. Prop.*, 1989, vol. 59, pp. 519–32, https://doi.org/10.1080/01418618908229782.
32. J. Schiotz, T. Leffers, and B.N. Singh: *Philos. Mag. Lett.*, 2001, vol. 81, pp. 301–09, https://doi.org/10.1080/09500830110041657.
33. J. Svoboda, W. Ecker, V.I. Razumovskiy, G.A. Zickler, and F.D. Fischer: *Prog. Mater. Sci.*, 2019, https://doi.org/10.1016/j.pmatsci.2018.10.001.
34. F.D. Fischer, J. Svoboda, and E. Kozeschnik: *Model. Simul. Mater. Sci. Eng.*, 2013, https://doi.org/10.1088/0965-0393/21/2/025008.
35. J.H. Kim and C.H. Park: *J. Alloys Compd.*, 2014, vol. 585, pp. 69–74, https://doi.org/10.1016/j.jallcom.2013.09.085.
36. J.H. Kim, T.S. Byun, E. Shin, J.B. Seol, S. Young, and N.S. Reddy: *J. Alloys Compd.*, 2015, vol. 651, pp. 363–74, https://doi.org/10.1016/j.jallcom.2015.08.100.
37. NIST: Line Position and Line Shape Standard for Powder Diffraction (Lanthanum Hexaboride Powder), Natl. Inst. Stand. Technol. US Dep. Commer. Gaithersburg, MD. (2015) 1–5. https://www-s.nist.gov/srmors/certificates/660C.pdf?CFID = 35608137

&CFTOKEN = 7e602cd95cb32152-D56C3582-CDD9-D727-1A32D 16FDB2CF208.

38. B.E. Warren: *XProg. Met. Phys.*, 1959, vol. 8, pp. 147–202, https://doi.org/10.1016/0502-8205(59)90015-2.
39. T. Ungár: *Scripta Mater.*, 2004, vol. 51, pp. 777–81, https://doi.org/10.1016/j.scriptamat.2004.05.007.
40. J. Zbiral: *Metall. Mater. Trans. A*, 1994, vol. 27A, pp. 1371–77.
41. D. Wimler, S. Kardos, J. Lindemann, H. Clemens, and S. Mayer: *Prakt. Metallogr. Metallogr.*, 2018, vol. 55, pp. 620–36, https://doi.org/10.3139/147.110547.
42. S. Vock, B. Klöden, A. Kirchner, T. Weißgärber, and B. Kieback: *Prog. Addit. Manuf.*, 2019, vol. 4, pp. 383–97, https://doi.org/10.1007/s40964-019-00078-6.
43. J. Zbiral: *Charakterisierung von Verteilungs-, Legierungs und Homogenisierungsprozessen beim mechanischen Legieren*, Technische Universität Wien, Vienna, 1990.
44. K.H. Chung, J. He, D.H. Shin, and J.M. Schoenung: *Mater. Sci. Eng. A*, 2003, vol. 356, pp. 23–31, https://doi.org/10.1016/S0921-5093(02)00833-X.
45. M. Li, Y. Guo, H. Wang, J. Shan, and Y. Chang: *Intermetallics*, 2020, vol. 123, art. no. 106819https://doi.org/10.1016/j.intermet.2020.106819.
46. Y. Guo, M. Li, C. Chen, P. Li, W. Li, Q. Ji, Y. Zhang, and Y. Chang: *Intermetallics*, 2020, vol. 117, art. no. 106674https://doi.org/10.1016/j.intermet.2019.106674.
47. R.M. Pohan, B. Gwalani, J. Lee, T. Alam, J.Y. Hwang, H.J. Ryu, R. Banerjee, and S.H. Hong: *Mater. Chem. Phys.*, 2018, vol. 210, pp. 62–70, https://doi.org/10.1016/j.matchemphys.2017.09.013.
48. K.H. Chung, R. Rodriguez, E.J. Lavernia, and J. Lee: *Metall. Mater. Trans. A Phys. Metall. Mater. Sci.*, 2002, vol. 33A, pp. 125–34, https://doi.org/10.1007/s11661-002-0011-y.
49. S.H. Joo, H. Kato, M.J. Jang, J. Moon, E.B. Kim, S.J. Hong, and H.S. Kim: *J. Alloys Compd.*, 2017, vol. 698, pp. 591–604, https://doi.org/10.1016/j.jallcom.2016.12.010.

Publication B

M. Mayer, J. Svoboda, F. Mendez-Martin, S. Fellner, C. Gammer, V. Razumovskiy, W. Sprengel, L. Resch, A. Stark, S. Zeisl, G. Ressel

From microscopic to atomistic scale: Temperature effect on yttria distribution in milled FeCrMnNiCo powder particles

CRediT author contribution statement

1   **From microscopic to atomistic scale: Temperature effect on yttria distribution**

2   **in mechanically alloyed FeCrMnNiCo powder particles**

3   Michael MAYER[a,*], Jiri SVOBODA[b], Francisca MENDEZ-MARTIN[c], Simon FELLNER[d], Christoph
4   GAMMER[d], Vsevolod RAZUMOVSKIY[a], Laura RESCH[e], Wolfgang SPRENGEL[e], Andreas STARK[f], Stefan
5   ZEISL[c], Gerald RESSEL.[a]

6   *corresponding author; e-mail: Michael.Mayer@mcl.at

7

8   [a] Materials Center Leoben Forschung GmbH, Roseggerstraße 12, 8700 Leoben, Austria
9   [b] Institute of Physics of Materials, Academy of Science of the Czech Republic, 616 62 Brno, Czech Republic
10   [c] Department of Materials Science, Montanuniversität Leoben, Franz-Josef-Straße 18, 8700 Leoben, Austria
11   [d] Erich Schmid Institute of Materials Science, Austrian Academy of Sciences, 8700 Leoben, Austria
12   [e] Institute of Materials Physics, Graz University of Technology, Petersgasse 16, 8010 Graz, Austria
13   [f] Helmholtz-Zentrum Hereon, Institute of Materials Physics, Max-Planck-Straße 1, 21503 Geesthacht, Germany

14

15   **Abstract:**

16   The key state-of-the-art processing step to produce oxide dispersion strengthened (ODS) materials

17   with outstanding mechanical properties at high temperatures is mechanical alloying (MA). However,

18   its deficiency regarding time and costs hinders a broader applicability. Any efforts to increase its time-

19   efficiency are of high interest for the scientific community and producers. Therefore, in order to

20   investigate the effect of cryogenic MA temperatures and to understand the mechanism behind the

21   refinement and dissolution of yttria, pre-alloyed face-centered cubic Cantor powders (FeCrMnNiCo)

22   are mechanically alloyed together with 1 m.% yttria using a novel cryogenic attritor. MA was

23   performed at both, room and cryogenic temperatures in order to investigate the effect of temperature

24   on the yttria dispersions. Mechanically alloyed powders are thus analyzed and compared using a

25   comprehensive set of experimental methods. Transmission electron microscopy reveals a stronger

26   decrease of the oxide particle size upon cryogenic MA while at both temperatures the hereby observed

27   particles in a size over 10 nm still show yttria crystal structure. Nevertheless, a substantial amount of

28   yttria is refined below 10 nm forming nanoclusters without detectable crystal structure. Positron

29   annihilation spectroscopy suggests a vacancy assisted dissolution of yttria into these nanoclusters

30   while detailed investigation of these nanoclusters by atom probe tomography suggests smaller clusters

31   in the cryoalloyed sample. The results imply that this vacancy assisted dissolution seems to be

32   enhanced at cryogenic temperatures as first principle calculations and a change of the chemical

33   composition of the nanoclusters imply higher vacancy densities at cryogenic MA temperatures

34   stabilizing smaller nanoclusters.

35

36

37 **Graphical Abstract:**
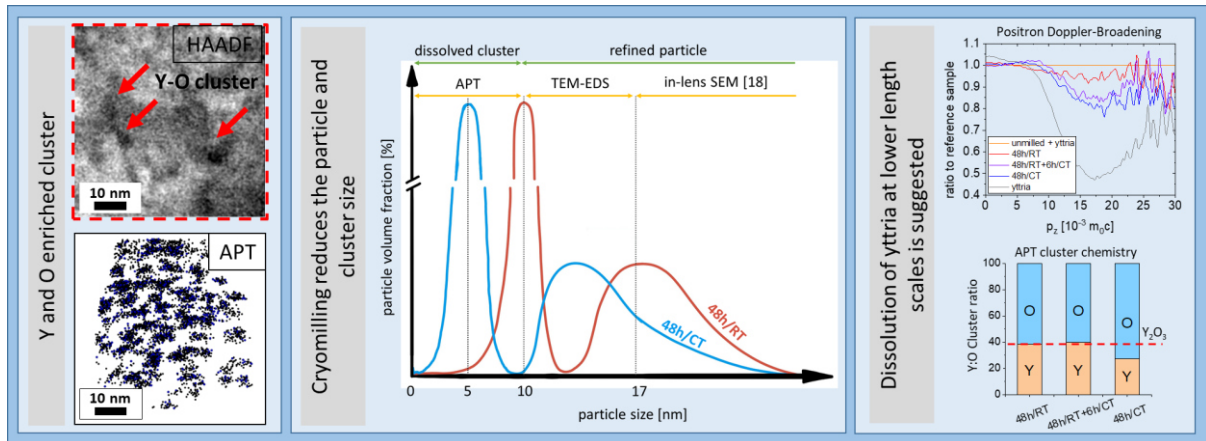
39 **Keywords:**

40 high-entropy alloys; oxide dispersion strengthening; mechanical alloying; transmission electron

41 microscopy; atom probe tomography; positron annihilation spectroscopy; first-principle calculations

42 **1. Introduction**

43 Nowadays used Ni-based superalloys for high-temperature applications such as the CMSX-4 show

44 excellent performance regarding strength and creep resistance [1,2]. However, besides their expensive

45 production, their strength significantly decreases at high temperature due to coarsening of γ' particles

46 and their dissolution into the matrix. Thus, application of these alloys at higher process temperatures

47 requires advanced material cooling during application. However, this cooling causes a significant

48 efficiency loss of the thermodynamic process [3]. As a result, materials sustaining higher application

49 temperatures are still of high interest as they increase the process efficiency, reduce efforts of cooling

50 systems and allow simpler and potentially cheaper solutions [2]. Therefore, alternatives to Ni-based

51 superalloys are in the focus of research over the last decades including high-entropy alloys (HEA) as

52 the most recent candidate for advanced high-temperature applications.

53 The core reason that high entropy alloys could replace Ni-based alloys at elevated temperatures lies

54 in their highly distorted matrix. In such compositionally complex alloys, the local atomic configuration

3

55   consists of low-energy sites and high-energy sites possibly trapping moving atoms and thus slowing

56   down diffusion [4]. However, new contradictory findings report no change in the diffusion coefficient

57   if the data is normalized to homological temperature T_m [5] and thus showing that this effect cannot

58   be clearly understood yet.

59   The most investigated HEA is the equiatomic face-centred cubic FeCrMnNiCo alloy, or so-called Cantor

60   alloy, with a low stacking fault energy showing strong temperature-dependent mechanical properties

61   [6–11]. Previous studies on the deformation mechanism of the FeCrMnNiCo alloy at low temperatures

62   report rather high strength and rather high strain hardening as a consequence of deformation twinning

63   but lower dislocation densities [8,9,12]. At elevated temperatures, however, this HEA lacks in strength

64   compared to Ni-based superalloys limiting the possibilities for substitution without additional

65   strengthening.

66   In metals, there are several mechanisms to strengthen alloys but the incorporation of small oxide

67   particles, known as oxide dispersion strengthening (ODS), has proven to be the most effective one in

68   high temperature applications [13]. These stable oxide particles in the size of a few nanometers

69   effectively impede the dislocation motion as a result of an attractive pinning force once the

70   dislocations climbed over the particles [14]. To prevent the particles from coarsening or dissolving into

71   the matrix, highly stable oxides such as Y_2O_3 (yttria) or Y-Ti-O ($Y_2Ti_2O_7$ or Y_2TiO_5) are incorporated

72   forming an incoherent interface with the matrix after consolidation [15]. Such highly stable and

73   insoluble oxides have to be incorporated into the matrix by MA, a process known for alloying

74   immiscible elements via the formation of non-equilibrium states [16].

75   Mechanical alloying (MA) is a process where during the collisions of milling balls repeated cold welding

76   and fracturing of the in-between trapped powder particles occurs. By this rapid energizing by severe

77   plastic deformation and subsequent quenching, a refinement and homogeneous distribution of the

78   oxide particles takes place. Furthermore, high densities of lattice defects such as dislocations, small

4

79   grains and vacancies [16–20] are introduced. However, whether these refined oxide particles are finely

80   distributed or dissolved forming a metastable supersaturated solid solution is still not decided. Some

81   studies suggest that in bcc steels yttria completely dissolves at lattice defects [21–25] while especially

82   vacancies are reported to play a crucial role in the dissolution [19,26,27]. Ressel et al. [25] conducted

83   positron annihilation spectroscopy (PAS) measurements, found that the vicinity of vacancies is

84   enriched with yttrium and oxygen after MA and concluded that vacancy defects are responsible for

85   the dissolution. Fu et al. [26] used first-principle calculations and found that O is strongly attracted by

86   vacancies [28,29] and as a result of this interaction, the formation energy of yttria nanoclusters is lower

87   than that of the stable oxide. Highly stable O-vacancy pairs are formed near interstitial octahedral sites

88   [26] and other solutes such as Ti and Y are attracted by neighboring lattice sites to minimize their

89   energy [21,26]. Xu et al. [30] confirmed these calculations by conducting PAS measurements. In the

90   samples without vacancies, no yttria nanoclusters are observed but in the samples containing high

91   vacancy densities many small and stable oxygen-enriched clusters are detected

92   Kimura et al. [23] proposed a model assuming an amorphous phase around crystalline grains enriched

93   with Y and O. The grains, as well as yttria, need to become refined to a nanometric scale during MA

94   providing a sufficient driving force for the decomposition of yttria into these amorphous regions. On

95   the contrary, based on X-ray diffraction (XRD) and X-ray photoelectron spectroscopy (XPS), Phaniraj et

96   al. [31] concluded for that yttria did not dissolve in austenitic steels during MA for 18 hours.

97   Some papers already focused on the strengthening of HEAs by oxide dispersion. Recently,

98   Hadraba et al. [32] reported improved high-temperature tensile properties while Dobes et al. [33]

99   focused on compressive creep and found a significant reduction of the creep rate at 800°C. Chung et

100   al. [34] investigated the oxide dispersion in FeCrMnNiCo alloy consolidated after cryogenic MA and

101   found a homogeneous elemental distribution together with fragmented yttria finely distributed within

102   the alloy. The influence of the MA temperature on the powder particles microstructure was studied

103 by Mayer et al. [18] at a microscopic scale. They found an increased number of lattice defects and a

104 lower phase fraction of yttria >17 nm concluding a higher MA efficiency for cryogenic MA. In their

105 cryoalloyed sample, 87 % of the added yttria is refined below 17 nm leaving the open question of what

106 happens with the oxide particle below this size. Whether yttria is dissolved or it is finely dispersed

107 cannot be answered by the methods used in [18].

108 While for bcc ODS alloys a detailed investigation of the powders' microstructure has been published

109 [19,22,35,36], more research is needed for fcc materials, particularly for the FeCrMnNiCo alloy.

110 Additionally, investigations on the influence of MA temperature on the yttria evolution were not

111 conducted down to atomic scale so far. In order to close this gap and to get insights into the MA

112 mechanism of ODS alloys, this study deals with the dependence of yttria evolution on the MA

113 temperature at microscale (> 10 nm) and nanoscale (<10 nm). The yttria particles of the powders

114 alloyed for 48h at room temperature (RT) and cryogenic temperature (CT), as well as a sample alloyed

115 for 48h at RT followed by 6h of cryoalloying, are investigated by transmission electron microscopy

116 (TEM) with focus on the oxide distribution and crystal structure. APT measurements are carried out to

117 get detailed insight into the formation of Y- and O-enriched nanoclusters and together with first-

118 principle methods and PAS, a model for the temperature-dependent alloying mechanism of yttria

119 strengthened fcc FeCrMnNiCo HEA is proposed.

120

2.   Methods

2.1. Specimen preparation

123   For mechanical alloying, gas-atomized, pre-alloyed $Fe_{20}Cr_{20}Mn_{20}Ni_{20}Co_{20}$ (at.%) powders with a d_{50} of

124   25.5 µm were blended with 1 m.% Y_2O_3 and a d_{90} of 1.16 µm and put into a grinding vial made of

125   stainless steel (X6CrNiMoTi17-12-2). MA was performed in a novel high-energy attritor ball mill

126   operated at 300 rpm and under high-vacuum (10^{-3} mbar) to prevent atmospheric contamination. As

127   grinding media, Inconel 825 balls with a diameter of 6.35 mm were used during the whole process, the

128   ball-to-powder-weight-ratio (BPR) was 10:1 – i.e. 5 kg ball mass together with 0.5 kg of powder mass.

129   In order to investigate the influence of the milling temperature, the powders were milled for 48h at

130   room temperature (RT) and at cryogenic temperatures (CT) as well as at a combination of both milling

131   temperatures where the powder was milled for 48h at RT and subsequently for 6h at CT. At both milling

132   temperatures, cooling was performed outside the grinding vial where at RT the temperature was

133   regulated to around 25°C using circulating water while for CT a temperature of approximately -150°C

134   outside the grinding vial was maintained using liquid nitrogen.

135   **2.2. Microstructural investigation**

136   High-Energy X-Ray diffraction was carried out at 25°C and 1100°C at the HEMS beamline of PETRA III

137   [37] at Deutsches Elektronen-Synchrotron (DESY) in Hamburg using high-energy synchrotron radiation.

138   The milled powder specimen were put into an Nb-capsule and heated to 1100°C with a heating rate of

139   100 K/min. The detector distance was 1.4 m and the wavelength of the used beam 0.14235 Å. The

140   calibration was obtained using a LaB6 standard. The X-ray beam was not perfectly monochromatic but

141   also a small fraction (about 1 %) of the first higher harmonic wavelength (0.071175 Å) was present.

142   This results in very weak additional reflections at the positions of 2Θ/2. To convert the 2D diffraction

143   image into a 1D diffraction pattern, the whole diffraction ring was integrated using an in-house Python

144   code. The lattice parameter of the measured diffraction patterns was analyzed from the Pseudo-Voight

7

145   fit of the peaks and the corresponding peak positions used for lattice parameter calculations. Due to

146   planar faults present in the milled powders and to eliminate their influence, the resulting asymmetric

147   peak shifts were corrected using the theoretical formula described by Warren [38] and an error-

148   minimization approach for all investigated peaks.

149   In order to obtain the yttria X-ray diffraction peaks, a diffraction pattern of the used yttria powder was

150   measured at a Bruker D8 Discover using Cu-Kα radiation with a wavelength of 1.54 Å. The hereby

151   obtained peak positions of the most prominent peaks were re-calculated to synchrotron wavelength

152   using Bragg's law [39].

153   For detailed investigations, TEM lamellae were extracted from the powder using the focused ion beam

154   lift-out technique. To study the chemical composition at lower magnification, energy-dispersive X-ray

155   spectroscopy (EDS) was performed on the TEM lamellae using a Zeiss GeminiSEM 450 operated at 20

156   kV using an Oxford Instruments Ultim Extreme detector. At higher magnifications, EDS maps were

157   obtained using a JEOL JEM-2200 FS TEM, at an acceleration voltage of 200 kV. The microstructure was

158   imaged using bright-field (BF) TEM and scanning TEM (STEM). For accurate phase characterization, a

159   combination between high-resolution TEM (HRTEM) imaging and selected area diffraction (SAD) was

160   used. To obtain information on the phases at the nanoscale, a TVIPS USG scan generator was employed

161   alloying to acquire a full diffraction pattern at each probe position during STEM imaging. The resulting

162   nanodiffraction map was analyzed using custom code written in Digital Micrograph [40].

163   **2.3. Atom-probe tomography**

164   The atom probe tomography (APT) data was generated with a CAMECA LEAP 3000X HR microscope.

165   All measurements were conducted in the pulsed voltage mode using a pulse fraction of 20%, a pulse

166   rate of 200 kHz at a specimen temperature of 50 K. The specimens were prepared with a focused ion

167   beam lift-out method using a FEI 3D DualBeam workstation. The APT data was evaluated using the

168   IVAS 3.6 software. The cluster analysis was performed using the maximum separation method (MSM).

169   The parameters for the MSM (d_{Max} and N_{Min}) were obtained with the aid of the nearest-neighbour

170   distribution, cluster size distribution and cluster count distribution. The chemical composition of the

171   clusters was determined by performing a peak decomposition on the mass-spectrum.

172   **2.4. First principle calculations**

173   The effective vacancy formation energies in the 5-component equimolar FeCrMnNiCo alloy with 20%

174   of each atomic species have been obtained using a combination of the projector augmented-wave

175   (PAW) method calculations [41], as implemented in the Vienna ab-initio simulation package (VASP)

176   [42,43], the EMTO-LSGF calculations (exact muffin-tin orbitals - locally self-consistent Green function

177   method) [44–47] within the disordered local moment (DLM) and the coherent potential

178   approximations (CPA) [48,49] for the magnetic and compositional disorder. The magnetic entropy

179   contribution at elevated temperatures has been included in a model form of longitudinal spin

180   fluctuations (LSF) [50] corresponding to 298 and 1373K. All calculations have been performed at the

181   corresponding to these temperatures experimental lattice constants. A detailed methodology of the

182   effective vacancy formation energy calculations employed in this works follows the methodology

183   proposed in [51] as it is described in [52] in detail.

184   **2.5. Positron Annihilation Spectroscopy**

185   For the positron annihilation measurements, the powder samples were pressed to small discs with a

186   diameter of 10 mm using 3 GPa pressure and a [22]Na positron source was sandwiched between pairs of

187   two identically treated samples. For the positron lieftime measurements the lifetime spectra were

188   acquired using an analog fast-fast positron lifetime spectrometer with a time resolution of 163 ps

189   (FWHM). Each lifetime spectrum contained more than 10^6 counts and was analyzed after background

190   and source correction using the program PALSFIT [18]. For the measurments of the Doppler

191   broadening of the positron-electron annihilation line a coincidence set-up consisting of two high-purity

9

192   germanium detectors were used. For the analysis of these measurements spectra of more than 10^7

193   counts were used.

3. Results

3.1. Effect of milling temperature on yttria size distribution from micro- to nanoscale

As the temperature has a strong influence on the mechanical properties of the FeCrMnNiCo matrix powder, a temperature dependence on the refinement of yttria is expected. Figure 1 presents the Y-EDS maps of the milled powders obtained at different length scales by STEM in the TEM and SEM as well in-lens SEM images of the same specimen where yttria appears as white spots. By inspecting the in-lens SEM images, a higher fraction of white spots – i.e. yttria particles – is observed in the 48h/RT specimen while the 48h/CT specimen indicates the lowest fraction of the observed samples. Investigations of the TEM–EDS maps of the 48h/RT sample shown in Figure 1a-c show a high fraction of yttria particles in the lowest magnification (Figure 1c) whereas no detectable yttria particles seem to be present even in the highest magnification map presented in Figure 1a. It has to be mentioned that the shown pictures are representatives of various analyzed positions. In contrast, the EDS maps of the 48h/CT sample shown in Figure 1i-k indicate, apparently, an increased number density of yttria particles at the highest magnification suggesting that yttria particles get stronger refined during cryomilling compared to milling at RT. This assumption is further supported by the 48h/RT+6h/CT specimen as this specimen indicates an in-between state concerning the amount of particles at each magnification implying a further refinement caused by 6 h milling at CT towards smaller yttria particle sizes. The smallest by TEM-EDS detectable particle size yielded 10 nm in the 48h/CT sample.

11
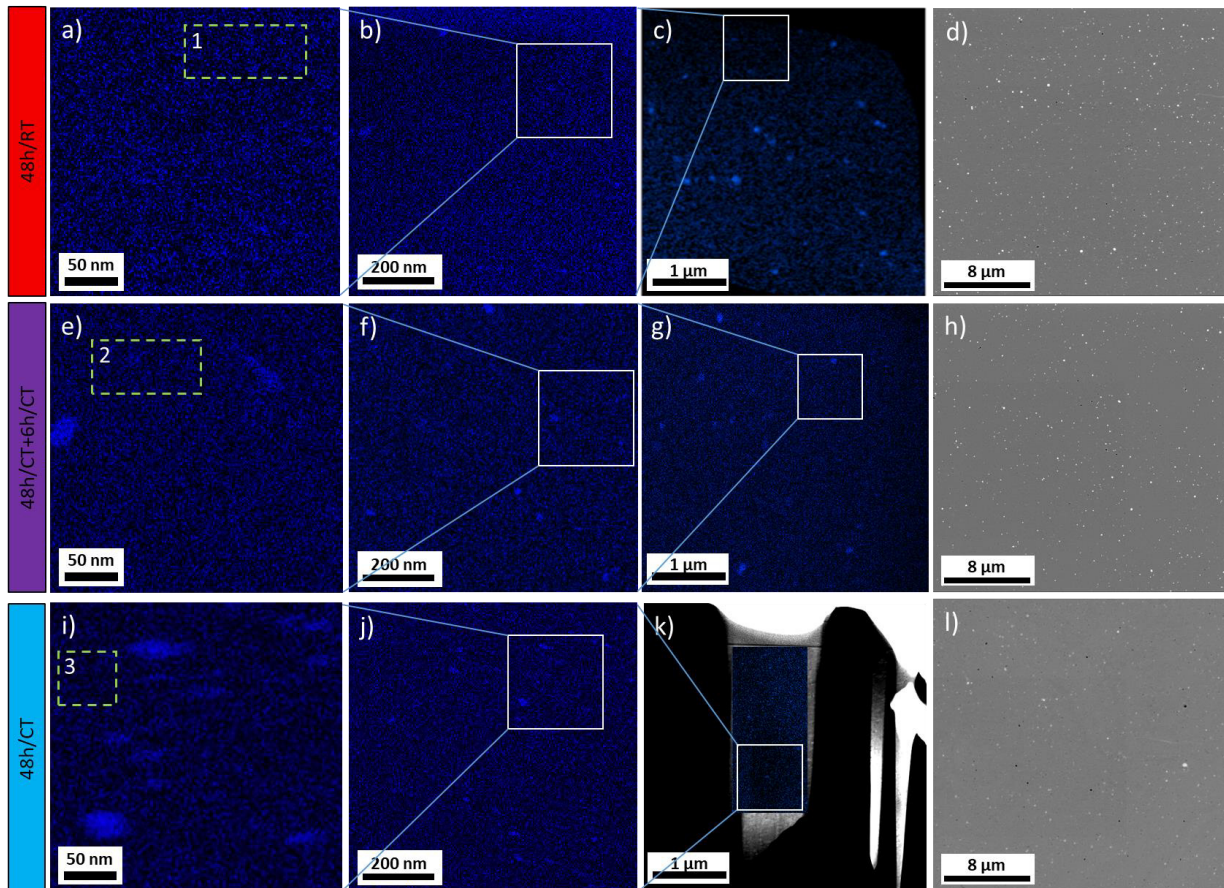
Figure 1: Y-TEM-EDS maps of the 48h/RT (a, b), 48h/RT+6h/CT (e, f) and 48h/CT (i, j) specimens at different magnifications compared with the corresponding Y-STEM-EDS-maps (c, g, k) and in-lens SEM images where yttria appears as white spots (d,h,l). Note that in k), the TEM lamellae was smaller compared to the other specimen and thus, a smaller EDS-map is shown here, overlaid with the SEM image of the TEM lamellae. These images suggest a finer yttria distribution for the samples milled at lower temperatures. The dashed areas (1-3) represent the area from where the matrix chemistry was measured via TEM-EDS. Results of the Y-matrix content yield 1) 0.42 at.%Y, 2) 0.41 at.%Y and 3) 0.39 at.%Y showing no difference between the measured specimen.

In order to compare the Y content in a size range below the detected particles with a size of 10 nm, areas in TEM-EDS maps shown by dashed lines in Figure 1a, -d and -g without visible yttria particles were evaluated. Evaluation of the Y content yielded 0.42, 0.41 and 0.39 at.% Y for the 48h/RT, 48h/RT+6h/CT and 48h/CT specimens, respectively. Therefore, it is suggested that within the detection limit of the used method, the matrix composition does not show any milling temperature dependence and consequently, indicates a saturation of the matrix at lower length scales. Comparing the

226 approximately 0.4 at.% Y below 10 nm in all milled specimen as obtained by TEM-EDS with the 0.55

227 at.% overall amount of Y – i.e. the amount of Y in 1 m.% yttria – yields that approximately two thirds

228 of the added yttria is refined below 10 nm in all milled samples.

229 These findings are corroborated in this work by APT measurements in order to shed light on the

230 chemical composition but also on the distribution of yttria in the matrix on a nanometric scale. Figure

231 2 shows the clusters and the distribution of Y and O atoms of the 48h/RT, 48h/RT+6h/CT and 48h/CT

232 specimens as well as the mean Y-content. No significant variation of the overall Y-content between the

233 measured samples were observed, confirming the results from the TEM-EDS measurements.

234 Furthermore, the volume fraction of the clusters yielded 4 vol.% for all three samples, which is

235 considerably larger than the 1.7 vol.% of the added yttria, indicating that also matrix elements are

236 within these clusters.

237

238

13
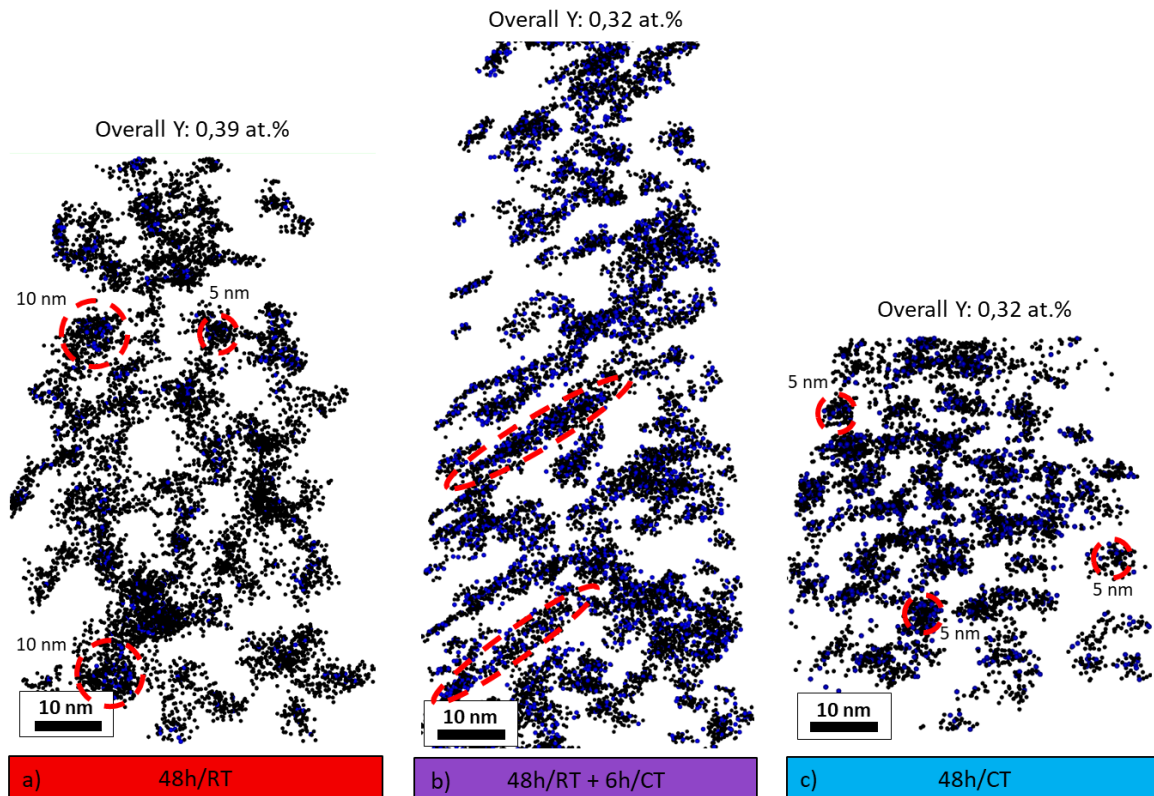
Figure 2: Y and O cluster analysis of APT Tips of the a) 48h/RT, b) 48h/RT+6h/CT, and c) 48h/CT specimen showing smaller cluster sizes for the CT specimen while the combination of both milling temperatures shows a transition state. The respective Y-content of the entire tip is shown above each tip. Y-atoms are marked black and O-atoms are presented blue.

The visual inspection of the clusters revealed a network-like structure of connected clusters. Furthermore, the clusters in the cryomilled specimen 48h/CT specimen appeared smaller than in the milled 48h/RT specimen. This is corroborated by the cluster appearance of the 48h/RT+6h/CT specimen showing elongated clusters in Figure 2b. As in this specimen, both milling temperatures were combined, their appearance suggest to represent a transition stage from a RT to a CT stable cluster size and structure, where the CT structure is not yet finished after 6 h of cryomilling subsequent to 48 h of milling at RT. The size of the clusters could not be quantified because of the network-like connections but visual estimation suggests maximum 10 nm sized clusters in the 48h/RT specimen and clusters of about 5 nm in the 48h/CT sample. Therefore, the cryomilled specimen is suggested to

14

252   exhibit smaller cluster sizes while the volume fraction of the clusters does not depend on the milling

253   temperature.

254   In order to compare the size and shape of the observed clusters, Figure 3c and f depict TEM images

255   together with the clusters of the APT-tips shown in Figure 3g at the same scale for the 48h/CT

256   specimen, in which the particle refinement is expected to be the most pronounced. The size and shape

257   of the clusters corresponds well with the black structures in the high angle annular dark field (HAADF)

258   STEM images, highlighted with red arrows. As Y is heavier than the matrix elements, Y-enriched

259   segregations are expected to appear darker in such HAADF-TEM images which is confirmed by

260   comparison of the HAADF image and the EDS map in Figure 3b and d, respectively. This implies that

261   these black areas are enriched with Y and by including the APT cluster analysis, this indicates that these

262   areas are Y and O-enriched nanoclusters. Furthermore, the location of the extracted HAADF STEM

263   images in the BF STEM images suggests that most of these clusters are located within the nanograins.

264   Therefore, the Y and O-enriched clusters are suggested to be located within the nanometric grains of

265   this ODS-FeCrMnNiCo alloy. Even though both investigations just yield visual estimations about the

266   size and structure of these Y and O enriched clusters, the correlative approach using both methods

267   strengthens the assumption of smaller cluster sizes within the 48h/CT specimen.

268   **3.2. Differentiation between clusters and particles at a size below 10 nm**

269   To get an insight into whether the by TEM-EDS detected yttria particles are finely dispersed with

270   separate crystal structure or in the fcc matrix dissolved and arranged as clusters, a nanodiffraction map

271   of the 48h/CT specimen was acquired at the same location as the EDS map and analyzed regarding the

272   crystal structure of yttria particles. The results are shown in Figure 3 including the BF and HAADF

273   images together with the EDS map, all shown in Figure 3a, b and d, and three representative

274   nanodiffraction patterns extracted from the diffraction map presented in Figure 3e.

15
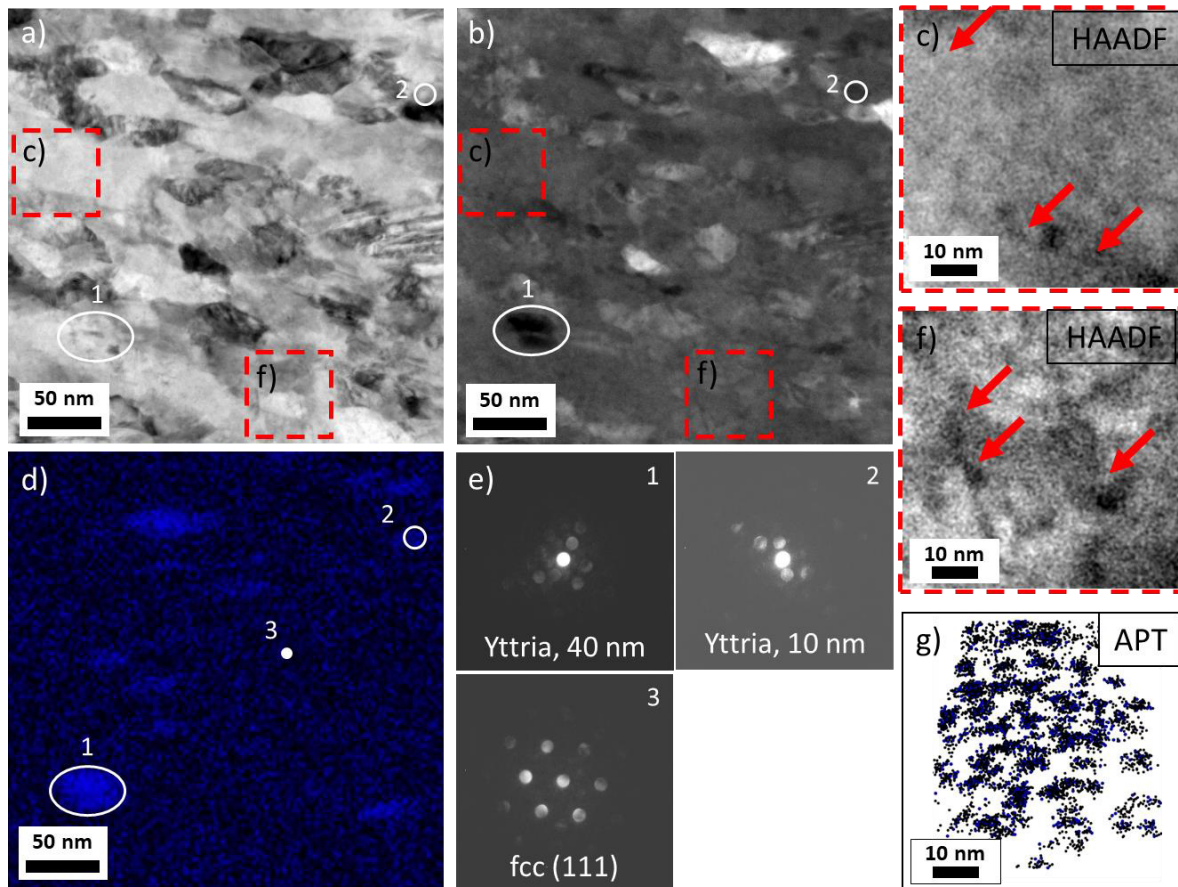
Figure 3: (a, b, d, e): Evaluation of yttria's and matrix' crystal structure of the 48h/CT specimen by comparing a) BF-STEM, b) HAADF STEM, d) Y-TEM-EDS-map and e) selected diffraction patterns obtained from diffraction map. The results confirm an yttria crystal structure down to particles sizes of about 10 nm. (c, f): HAADF image taken from the areas marked in a) and b) showing Y-clusters as black areas. f) APT tip of the 48h/CT specimen indicating a correlation of the black areas in the TEM images with the nanoclusters obtained by APT. Note that the APT-tips and TEM-lamellae were not prepared from the same position.

The matrix is single phased fcc as depicted in the diffraction pattern in Figure 3e-3 while a larger yttria particle with the size of 40 nm (Figure 3e-1) indicates a complex oxide diffraction pattern for which, analysis showed that yttria fits best. A smaller particle of about 10 nm (Figure 3e-2) shows a similar pattern as the large yttria particle indicating that this particle exhibits yttria crystal structure as well. Therefore, both investigated yttria particles remain crystalline after cryomilling with a complex oxide crystal structure, consequently qualifying the authors to denote them as particles. For particles smaller than 10 nm it was not possible to identify a crystal structure of yttria. This implies that, at this size

16

289   range, yttria is present in the form of clusters. However, it has to be mentioned that this fact has to be

290   treated with care as due to the thickness of the TEM lamellae and limit of the method uncertainties

291   are available.

292   Therefore, and as TEM measurements show very local results of the crystallinity of yttria particles, HE-

293   XRD measurements can give a much broader information. Therefore, analysis regarding the

294   crystallinity of yttria was conducted using synchrotron high-energy X-ray diffraction. The measured

295   diffraction patterns of the milled specimen are presented in Figure 4 together, exemplary, with the

296   diffraction pattern of the heated 48h/RT sample.
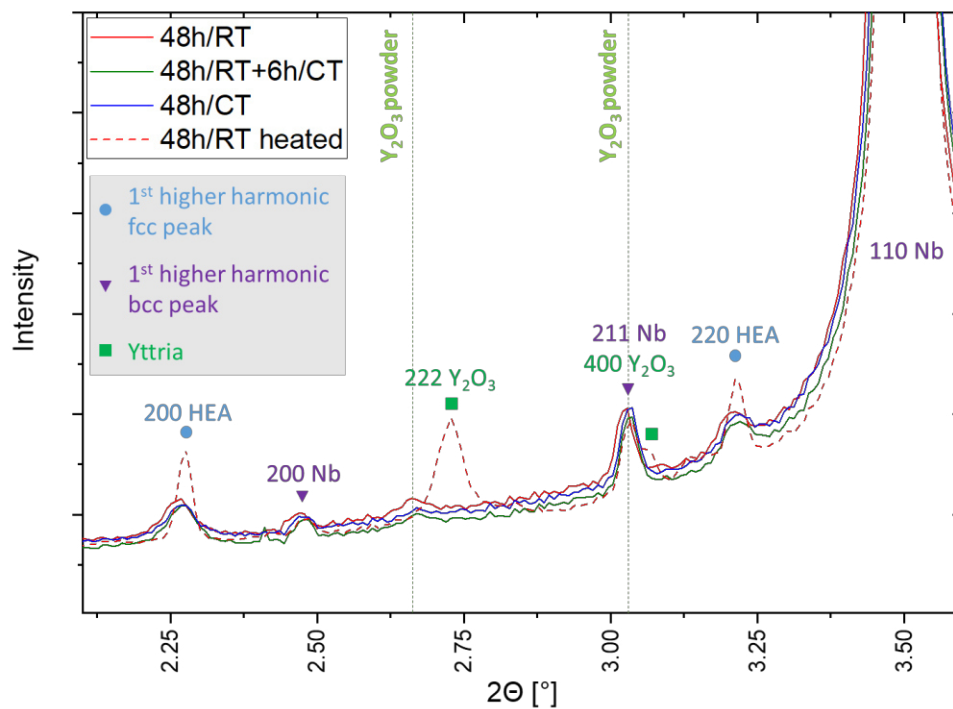
297

298   *Figure 4: HE-XRD pattern of the milled specimen 48h/RT, 48h/RT+6h/CT and 48h/CT overlaid with the 48h/RT specimen after*

299   *the heating up to 1100°C and subsequent cooling to RT indicating the growth and shift of the yttria peaks upon heating. Fcc*

300   *and bcc peaks correspond to the FeCrMnNiCo HEA matrix and the Nb capsule, respectively.*

301   The diffraction pattern of the as-milled specimen (48h/RT, 48h/RT+6h/CT and 48h/CT) do not differ

302   significantly from each other and the positions of the yttria peaks - obtained from XRD-measurements

303   of the initial yttria powders - are marked with dashed lines. In the milled specimen, at 2.7°, small yttria

        17

304   peaks for the 48h/RT and the 48h/RT+6h/CT specimen are visible while no peak could be distinguished

305   from the background for the 48h/CT sample. The second measured yttria peak at 3.05° is not

306   detectable in the milled samples due to the overlap with the 1st higher harmonic 211 Nb bcc peak of

307   the capsule.

308   However, after heating the 48h/RT powder up to 1100 °C, yttria peaks increase and are clearly visible

309   at larger 2Θ diffraction angles compared to the initial yttria powder, indicating a decrease of the lattice

310   parameter which was also observed by Zhang et al. [53]. This observation suggests that the phase

311   fraction of crystalline yttria in the as-milled condition is considerably lower compared to the heated

312   condition strengthening the previous assumption of increased amount of yttria clusters and lower

313   fraction of crystalline particles with yttria crystal structure present after milling. The heated 48h/CT

314   and 48h/RT+6h/CT specimens show the same trend as 48h/RT and are thus not shown in this work.

315   **3.3. Effect of milling temperature on defects and their interaction with yttria**

316   Mechanical alloying causes severe plastic deformation in the milled powders upon which, yttria

317   particles get fractured and refined within the matrix powder. The resulting microstructures are

318   presented in Figure 5 showing representative BF TEM images of the milled revealing severely deformed

319   and highly distorted microstructures in all powder particles. The grain size of the 48h/CT specimen

320   shown in Figure 5-c is significantly smaller compared to the 48h/RT sample presented in Figure 5-a

321   while in the combination of both milling temperatures (Figure 5-b) grain boundaries are not clearly

322   visible. The corresponding diffraction pattern for the 48h/RT specimen shows increased spottiness

323   compared to the 48h/CT sample indicating less and therefore larger grains within the observed volume

324   while the diffraction ring of the 48h/CT specimen suggests nanocrystalline grains. For the combined

325   sample, 48h/RT+6h/CT, the diffraction pattern indicates a deformation texture suggesting that the

326   grains are not uniformly deformed. Grain sizes evaluated visually ranged from 50-100 nm in the 48h/RT

327   sample to 20-40nm in the 48h/CT sample.

18
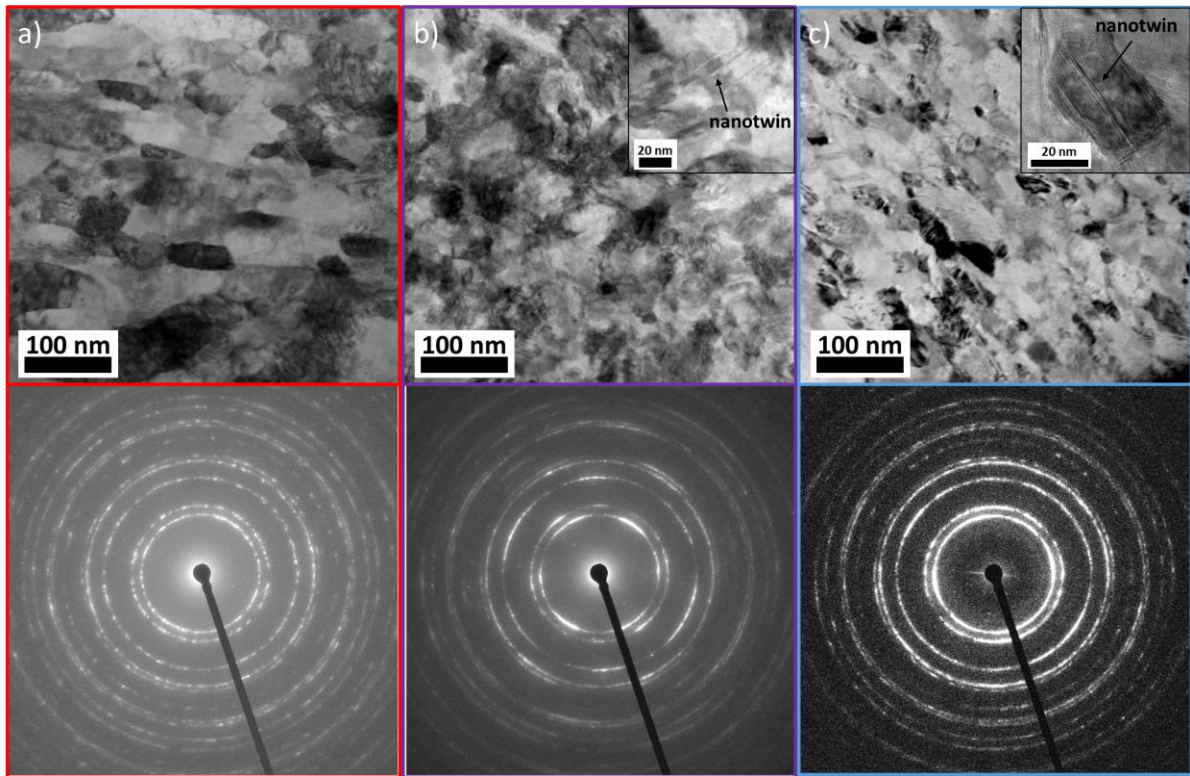
Figure 5: TEM-BF microstructure images with corresponding diffraction patterns of the a) 48h/RT, b) 48h/RT+6h/CT and c) 48h/CT specimen indicating smaller grains at lower milling temperatures. Magnified inserts in b) and c) show the existence of nanotwins due to milling at cryogenic temperatures.

Lattice defects are assigned to play a crucial role in the formation and stability of nanoclusters and were therefore investigated in detail in the milled specimen. Therefore, inserts in Figure 5 show TEM investigations of selected nanograins of each milled specimen revealing insights into the defect structure of the milled powders. By this, the tendency to form nanotwins at cryogenic temperatures seems to be increased as nanotwins were found in the 48h/CT and 48h/RT+6h/CT specimen while in the 48h/RT sample they seem not to be present. It should be mentioned that different positions of powder particles were investigated showing all the same tendency. Regarding other defects, such as vacancies, no reliable statement can be proposed by TEM.

Additional information about vacancies can be obtained by a combination of PALS and *ab-initio* calculations. Whereas PALS can give an experimental information about the presence of open volumes

19

342   directly after milling, *ab-initio* calculations can provide information on the formation energy of

343   vacancies both at 0 K and at elevated temperatures [52,54], which might be directly associated with

344   the concentration of vacancies in the alloy. The *ab-initio* results on the vacancy formation energies in

345   the HEA of this study have been obtained for the fcc phase at 300 K taking into account effects of the

346   paramagnetic state at the measured lattice parameters as reported in Table 1. According to

347   experimental XRD measurements presented in Figure 4, the measured lattice parameter increases

348   from 3.5978 Å for the RT milled sample to 3.6003 Å due to milling at cryogenic temperatures indicating

349   a lower vacancy formation energy for both cryomilled specimen. The vacancy formation in

350   mechanically alloyed powders, which is activated via severe plastic deformation, is therefore expected

351   to be easier at lower milling temperatures and the corresponding concentration of these point defects

352   is expected to be higher. This observation implies a tendency towards increased vacancy densities in

353   the cryomilled specimen 48h/CT compared to the 48h/RT sample with the 48/RT+6h/CT specimen in-

354   between.

355   *Table 1: Lattice parameter of the milled specimen and the corresponding calculated vacancy formation energy indicating*

356   *easier vacancy formation at lower milling temperatures. PALS results show an increase of the mean positron lifetime upon*

357   *milling which indicates an increase in the concentration and/or size of the open volume.*

Specimen name	XRD lattice parameter [A]	Vacancy formation Energy [eV]	Mean positron lifetime [ps]
unmilled, no yttria	3.5928	2,13	175
48h/RT	3.5978	2,11	200
48h/RT+6h/CT	3.5990	2,11	201
48h/CT	3.6003	2,10	200

358   In order to experimentally extend the results of the above calculations, positron annihilation

359   spectroscopy (PAS) is a useful technique to examine open volume defects such as vacancies. The

360   lifetime of positrons in the materials investigated is a direct measure for the concentration and/or size

361   of the open volume defects where positrons can get trapped. Therefore, to evaluate the presence of

20

362 vacancies in the specimens investigated, positron annihilation lifetime spectroscopy (PALS)

363 measurements were performed.

364 The results of the PALS investigation are listed in Table 1 showing an increase of the mean positron

365 lifetime from 175 ps for the unmilled samples to 200 ps for the 48h/RT milled specimen. However, no

366 significant difference in the mean positron lifetime between the different milling states was found.

367 This could be either due to fact that the free volume concentration does not change or that so-called

368 positron saturation trapping occurs. The upper detection limit for the concentration of free volume

369 sites is about 10^{-3}. If there is an increase in the concentration beyond that range, changes cannot be

370 detected. A positron lifetime in the range of 170-180 ps in these alloys is usually associated with

371 monovacancies in the constituent elements [55,56]. Furthermore, a positron lifetime of 186 ps has

372 been reported for FeCrMnNiCo after electron irradiation and that can be attributed to irradiation-

373 induced monovacancies. The milled samples provide lifetimes that also fall in the range of lifetimes

374 reported for di-vacancies in Ni [57] or more than 200 ps for di-vacancies in FeCrMnNiCo alloy [56]. As

375 for the positron lifetime in the defect-free state of the FeCrMnNiCo HEA matrix, a value in the range

376 from 113 to 117 ps can be assumed [58]. A comparison with the measured mean positron lifetime in

377 this work indicates an overall increase in concentration and size of open volumes for all alloys

378 investigated.

379 While PALS gives information about the size of open volume defects, Positron Doppler Broadening

380 (PAS-DB) yields insights into the chemical surrounding at the annihilation site of the positrons. Figure

381 6 presents the PAS-DB results of the milled specimens as ratio curves with respect to the blend of

382 unmilled FeCrMnNiCo powder mixed with 1 m.% Y_2O_3 as reference line (1.0). The other extreme case

383 represents the signature of yttria where annihilation events occur at open volumes in the vicinity of

384 yttrium atoms.
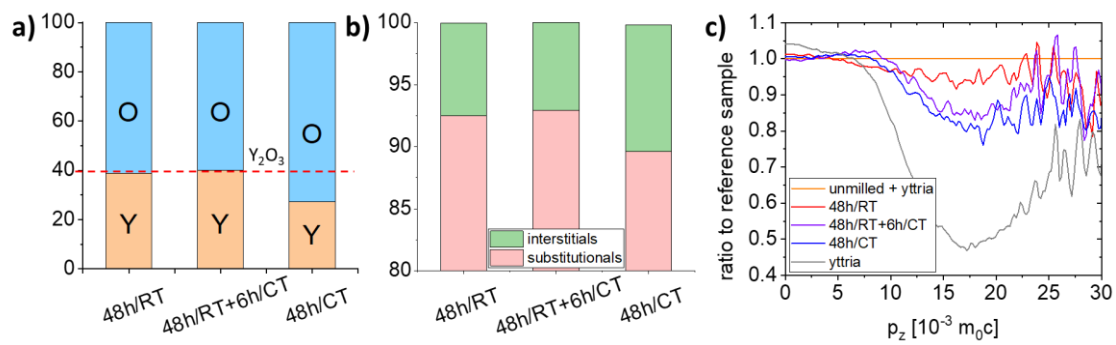
21

Figure 6: a) Y:O ratio of the clusters showing a lower Y:O ratio for the 48h/CT sample while the 48h/RT and the 48h/RT+6h/CT specimen yield yttria stoichiometry. b) Ratio of interstitial and substitutional elements within the clusters showing the same tendency. c) PAS-DB showing the chemical signature of the milled specimens together with the result from a pure yttria sample as ratio curves normalized to the unmilled powder with 1 m.% yttria. The curves indicate that the close vicinity of the open volume in the milled samples is decorated with yttrium. This effects intensifies for the cryomilled specimens.

The results show a clear tendency of the 48h/CT and the 48h/RT+6h/CT specimen towards the yttria signature indicating an enrichment of yttria in the vicinity of open volumes in these specimens compared to the 48h/RT specimen. The signature of the 48h/RT samples shows a less pronounced trend towards yttria and thus, less yttria at open volume defects is suggested. According to these results it can be stated that milling at CT, even for 6h after 48h of RT milling, has an increased tendency towards vacancy formation and these vacancies or open volumes are significantly enriched with yttria.

Besides the Y and O cluster size and structure, the Y:O ratio within the clusters was evaluated as an important parameter in understanding the influence of the milling temperature on the yttria cluster constitution. The Y:O ratio as presented in Figure 6a shows yttria stoichiometric clusters for the 48h/RT and 48h/RT+6h/CT samples while the ratio is significantly lower for the 48h/CT specimen. To get further insights into the change of the cluster Y:O ratio with different milling temperatures, Figure 6b depicts the ratio of interstitial elements such as Fe, Cr, Mn, Ni, Co and Y to substitutional elements such as O and N. By comparison, a slight decrease of lattice elements and thus increase of interstitial elements at the 48h/CT specimen can be proposed.

22

4. Discussion

A series of advanced experiments and calculations were carried out to get insights into the mechanism of mechanical alloying of an fcc ODS-FeCrMnNiCo powder. Therefore, the milled powders were investigated from micro- to nanoscale with focus on the influence of the milling temperature on the oxide particle- and cluster size and structure. The microscale analysis of the yttria distribution were based on SEM and TEM investigations including TEM-EDS maps and a diffraction map. A more detailed TEM microstructure analysis, HE-XRD and APT experiments gave insights into the particle size and structure at nanoscale below 10 nm whereas ab-initio calculations together with PAS investigated the role of vacancies in the refinement process of yttria during high-energy mechanical alloying.

4.1. Effect of milling temperature on yttria size distribution from micro- to nanoscale

At microscale, investigation of the yttria dispersions presented in Figure 1 show a lower amount of large and thus a higher amount of smaller yttria particles in the cryomilled specimen compared to the RT milled sample. This is corroborated by the combination of both milling temperatures, represented by the 48h/RT+6h/CT specimen, which indicates a transition state as observed particle sizes were between particle sizes at RT and at CT milling. Thus, an enhancing effect of cryomilling on the efficiency of yttria refinement can be proposed in this work. This is corroborated with our previous work [18] already suggesting by detailed SEM and XRD experiments that cryomilling increases the milling efficiency towards shorter milling times necessary to refine a substantial amount of yttria which is the governing mechanism during the second stage of mechanical alloying according to Suryanarayana [16]. In this context it has to be mentioned that yttria possessed a much higher yield strength of 7 GPa [58] compared to the yield strength of 2 GPa of the at RT severely deformed FeCrMnNiCo alloy [9] implying that even a highly deformed matrix cannot simply crush yttria particles. Therefore, concerning the refinement of incoherent particles – such as yttria in fcc [59,60] – during mechanical alloying, Ashkenazy [61] proposed a model where dislocations pile up around the particle causing an amorphous shell. These high defect densities cause high stresses at the particle-matrix interface resulting in a

23

432   refinement of the particle. Other studies investigating the temperature dependent deformation

433   behavior of the FeCrMnNiCo alloy found a higher strength and work-hardening ability at cryogenic

434   deformation temperatures [8,10], which means in turn that higher defect densities are expected.

435   Previous conclusions concerning the refinement of yttria [18] were based on the observation of smaller

436   oxide particle sizes and a lower phase fraction of yttria larger than 17 nm in the cryomilled specimen.

437   Therefore, TEM-EDS investigations of yttria particle sizes in this work extend the observation of an

438   increased yttria refinement due to cryomilling towards smaller particle sizes. As a result, it is suggested

439   that at microscale, an increased strength and higher defect densities of the FeCrMnNiCo matrix alloy

440   at lower deformation- and thus milling temperatures lead to an enhanced refinement of yttria particles

441   during milling as described by Ashkenazy [61]. Considering the 48h/RT+6h/CT specimen with particle

442   sizes in-between the 48h/RT and 48h/CT samples suggests a milling temperature-dependent

443   equilibrium oxide particle size at microscale, which transition is not yet finished for the 48h/RT+6h/CT

444   sample. Therefore, the final oxide particle size at microscale is suggested to depend on the strength

445   and defect density of the matrix which increases with decreasing deformation temperature [8,10].

446   However, the Y-content according to TEM-EDS investigations of the matrix shows that approx.

447   two-thirds of the added yttria is refined below 10 nm in all milled specimen. This milling temperature

448   independent Y content at nanoscale is confirmed by the overall Y content by APT. However, visual

449   analysis of Y and O atom cluster maps of all investigated states suggest pronounced differences in size

450   and shape. Lower milling temperature seems to lower the size of the smallest clusters, while the

451   volume fraction of the clusters stays the same for all three samples. Again, the 48h/RT+6h/CT sample

452   indicates a transition state between them as they exhibit an elongated shape compared to rather

453   spherical but connected clusters in the 48h/CT and 48h/CT sample. In literature, such small clusters,

454   also called nanoclusters, were already observed in mechanically alloyed ODS-steels using APT

455   [19,22,36] describing distinct clusters [22,36] as well as percolated structures [19] in the size of a few

456   nanometers. To estimate their size and stability, Zhao et al. [62] used first-principle theory at bcc steels,

       24

457 concluding that strain is an important factor defining the stable size of these nanoclusters. In his

458 calculations, strain originated from solute-solute repulsion forces and the presence of increased O in

459 form of O-vacancy pairs - i.e. increased strain - yield smaller clusters. For the current alloy, higher

460 micro-strains at lower milling temperatures were already reported by Mayer et al. [18] using XRD

461 correlating well with the observations in this paper finding smaller Y and O enriched clusters at lower

462 milling temperatures. Therefore, it can be concluded that these higher lattice strains observed in the

463 cryomilled specimens might lead to smaller Y and O-enriched clusters. Whether the source of the strain

464 is due the solute-solute repulsion or due to O-vacancy interactions cannot be concluded at this stage.

465 By comparing the size and shape of the nanoclusters obtained by APT with TEM microstructure images

466 presented in Figure 5, it is suggested that the observed nanoclusters are not at grain boundaries but

467 within the grains forming network-like structures similar in shape to the percolated aspect described

468 by Brocq et al. [19]. Kimura et al. suggested using APT and TEM that these with Y and O enriched areas

469 represent an amorphous phase around nanocrystalline grains [23]. However, even though in the

470 current study the size and shape of the nanoclusters correlated well with the theory of Kimura et al.

471 [23], the observed clusters are within nanocrystalline grains and no signs of amorphous phases were

472 found.

473 As a result, based on the observations in this paper, two size regions for the refinement of yttria are

474 suggested – micro- and nanoscale – with 10 nm as a proposed transition while the matrix at nanoscale

475 seems to be saturated with yttria milling temperature independently. However, milling at CT is

476 expected to lower the equilibrium particle and cluster size. Thus, based on findings of this and previous

477 work [18] an attempt is made to illustrate schematically the yttria size distribution of the RT and CT

478 milled specimens shown in Figure 7. It is depicted that at microscale, the equilibrium particle size is

479 lowered due to cryomilling and at nanoscale, representative bars schematically indicate the decreased

480 cluster size in the cryomilling specimen showing the beneficial effect of cryomilling on the refinement

481 of yttria.
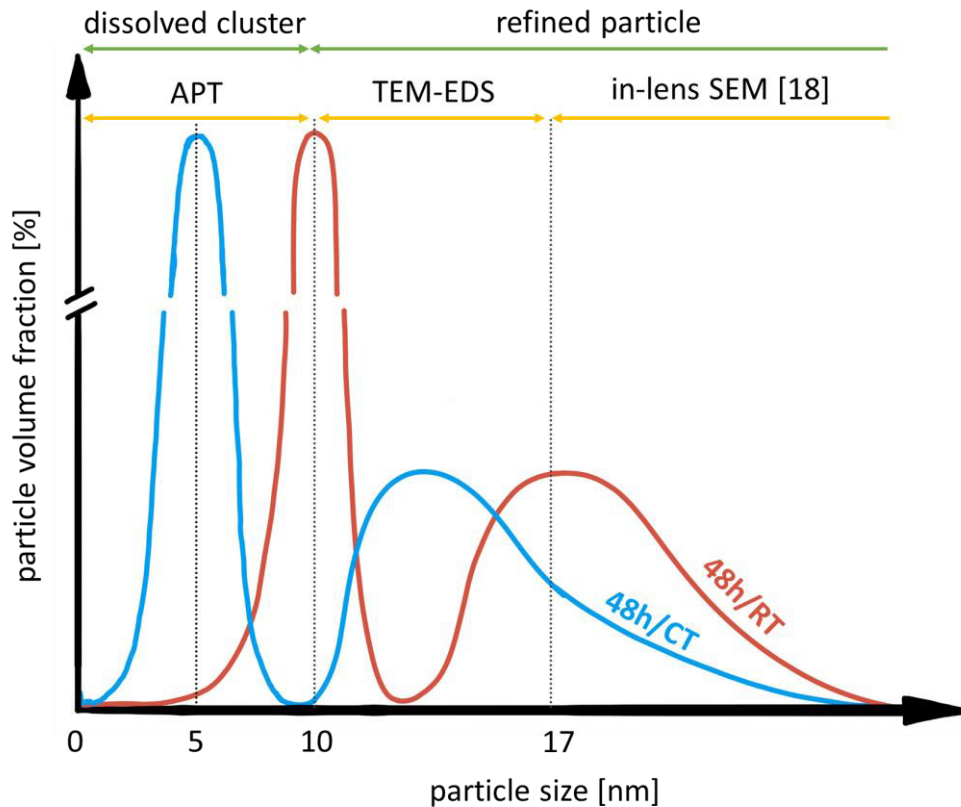
25

4.2. Differentiation between clusters and particles

In this study, the smallest by TEM-EDS observable particles were 10 nm in diameter and are presented in Figure 3 for the 48h/CT sample. Spots extracted from TEM diffraction maps confirm their complex crystal structure potentially originating from typical yttria crystal structure indicating that these are still yttria particles with their own crystal structure. Therefore, particles larger 10 nm are suggested to be crushed remnants of the initial yttria powders exhibiting no structural change. However, as reported in the previous chapter, in all investigated specimen, approximately two-thirds of the added yttria were observed in the matrix by TEM-EDS and APT measurements shown in Figure 1 and Figure 2 implying that a significant amount of yttria was refined below 10 nm. While the observable particles at microscale exhibit yttria crystal structure, the results of HE-XRD presented in Figure 4 imply that

26

496 yttria loses its crystal structure at nanoscale possibly forming clusters as the yttria peak at all as-milled

497 states is not present, whereas heating provokes a formation and precipitation of yttria particles

498 causing a distinct yttria peak in the HE-XRD pattern after consolidating at 1100°C. Nevertheless, in the

499 current study, the observed diffraction peaks in the as-milled HE-XRD pattern were smaller than

500 expected considering that one third of the added yttria is expected to exhibit yttria crystal structure.

501 A possible explanation for this is based on the Scherrer equation [63] for the size broadening of

502 diffraction peaks. According to Scherrer [63], crystallite – i.e. yttria – sizes below 100-200 nm broaden

503 the peak significantly causing a superposition of its signal by background signal. Therefore, the smaller

504 the yttria particles are, the broader and consequently less intensive the peak appears.

505 Note: The authors define clusters as elemental enrichment without own crystal structure, whereas

506 particles exhibit their own crystal structure. However, to best of the author's knowledge a precise

507 definition of the difference between the terms cluster and particle have not been published and in

508 many cases both definitions are mixed.

509 Many previous investigations focused on the question whether yttria dissolves [25,64] or refines

510 [31,65] while a saturation of the matrix with dissolved yttria was suggested by Saber et al. [66] for bcc

511 steels. However, he concluded that larger but not dissolved yttria forms amorphous phases and thus,

512 even in his samples with 10 m.% yttria, applying TEM investigations, no yttria crystal diffraction rings

513 were observed. This observation is in contrast to the findings in this paper suggesting yttria particles

514 with yttria crystal structure to a size of approx. 10 nm. Therefore, in analogy the section before, in this

515 work, two size regimens are proposed with larger yttria particles being crushed remnants of the

516 initially added yttria while yttria below 10 nm is suggested to be dissolved into clusters. However,

517 detailed insights into the dissolution mechanism of yttria in this FeCrMnNiCo alloy will be discussed in

518 the next section.

519

4.3. Effect of milling temperature on defects and their interaction with yttria

At microscale, BF-TEM images in Figure 5 show a significant grain size reduction of about 50 nm for the 48h/CT specimen compared to the 48h/RT sample. These measurements by visual inspection are supported by the diffraction patterns showing increased spottiness at a similar investigated volume. Similar findings were proposed by Stepanov et al. [12] as they investigated the temperature dependent deformation behavior of the FeCrMnNiCo alloy by rolling. They found an accelerated grain refinement at 77K and attributed this fact to increased twinning accompanied with a strong deformation texture due to rolling. He further concluded that twinning results in an increased subdivision of the grains by introducing new interfaces [12] which is a key component of grain refinement [67]. As a result of this change in the microstructure, the mechanical properties of this alloy are strongly temperature dependent showing a higher yield strength at low temperatures [8–10,12]. The combination of both milling temperatures – 48h/RT+6h/CT sample - therefore represents an in-between state from the RT to the CT equilibrium, which is supported by the absence of clear grain boundaries and the deformation texture observed in the diffraction pattern. Hence, it can be assumed that the grain refinement of this specimen due to 6 h of milling at CT is not finished yet as the defect density within the grains seems to increase compared to the 48h/RT sample but they did not yet rearrange to form smaller grains as in the 48h/CT sample. Therefore, suppressed recovery of lattice defects at low temperatures increases the defect density within the grains which leads to smaller grain sizes upon longer milling.

In deformed metals, lattice defects include dislocations, vacancies as well as interstitial and substitutional elements but especially vacancies are reported to be crucial for the dissolution of yttria [25,30]. Therefore, PAS measurements together with first-principle methods were conducted to get deeper insights into the formation and stability of the observed nanoclusters. The results of PALS show an increase in the size of the open volumes after mechanical alloying indicating mono- or divacancies in the milled specimen without significant difference in the lifetimes and therefore size of the open

28

544   volumes. However, no densities of these open volumes could be acquired as lifetimes of different

545   defects superimpose due to the present complex defect structure. Nevertheless, *ab-initio* calculations

546   accounting for the temperature effect on the formation energy of vacancies reveal that at lower milling

547   temperatures, increased vacancy densities can be generated upon deformation. To the best of the

548   author's knowledge, no reports on the influence of deformation temperature on the positron lifetime

549   have been conducted so far. However, concerning the generation of vacancies, Ohkubo et al. [57]

550   conducted PAS showing that conventional rolling of Ni at RT results in monovacancies and even

551   stronger deformation does not increase the positron lifetime. For high-speed deformation of Ni, he

552   also observed mainly monovacancies but also low densities of a larger positron lifetimes corresponding

553   to vacancy clusters. Kiritani et al. [68] reported high numbers of vacancies after high speed

554   deformation of fcc thin foils suggesting a vacancy assisted deformation mechanism at high

555   deformation speeds. During the ball-to-ball collisions of mechanical alloying, high deformation speeds

556   of the in-between trapped powder particles occur and therefore, milling at cryogenic temperatures

557   seems to introduce higher vacancy densities as a combination of actual *ab-initio* calculations and PAS

558   suggests, stabilizing smaller nanoclusters, which were observed by APT cluster analysis and HR-TEM

559   investigations.

560   The interaction of yttria with open volumes as a function of milling temperature was studied using

561   PAS-DB and the chemical composition of APT cluster analysis. Signatures of PAS-DB measurements of

562   the milled specimen show a stronger tendency to yttria for the CT sample indicating an increased

563   amount of vacancies present at yttria. APT measurements presented in Figure 6a show that especially

564   the finest clusters of the 48h/CT specimen show sub-stoichiometric yttria composition while the

565   48h/RT as well as the 48h/RT+6h/CT specimen exhibit the exact Y:O ratio of the initial yttria. Previous

566   studies on the nanoscale behavior of yttria during mechanical alloying of bcc steels suggested a

567   dissolution of yttria during mechanical alloying at lattice defects such as vacancies [19,21,22,26] or

568   dislocations [24] created during the severe plastic deformation of mechanical alloying. Especially

569   vacancies were further reported to strongly interact with O forming O-vacancy pairs [26,69] lowering

570   the formation energy of nanoclusters below that of the stable oxide [26] while Y is attracted by these

571   O-vacancy pairs to minimize its energy [21,26]. Despite most of these calculations were done for bcc

572   steels, the results of Fang et al. modelling the role of vacancies in the diffusion of O in Ni [69] suggest

573   that they can be used for interpretations of fcc alloys as well. Inspecting the overall elemental ratios

574   of the APT cluster compositions indicates that less lattice elements are present in the cluster, which

575   are compensated by increased amounts of interstitial elements such as O and N. Nevertheless, O and

576   N are not supposed to occupy lattice sites but dissolve interstitially and therefore this observation

577   indicates an increased presence of not occupied lattice sites – i.e. vacancies – inside the clusters of the

578   48h/CT specimen. Therefore, these interpretations together with a strong yttria signature of PAS-DB

579   within the cryomilled sample implies a strong interaction of yttria with vacancies whereas calculations

580   from literature suggest a dissolution of yttria at these vacancies forming Y and O enriched

581   nanoclusters.

582

5.　Conclusion

The current work investigated the influence of cryogenic mechanical alloying on the distribution and dissolution of yttria at micro- and nanoscale. Generally, it can be concluded that at all milling temperatures a substantial amount of yttria – approximately two thirds - is potentially dissolved in the matrix forming nanoclusters without yttria crystal structure, whereas the larger yttria in diameter beyond 10 nm is present as particles with the complex yttria crystal structure. Thus, for refined yttria, two size regimes are proposed: micro- and nanoscale with 10 nm as a proposed transition between refined and dissolved yttria. Yttria particles or clusters are present at all investigated length scales. At microscale, lower milling temperatures yield smaller yttria particle sizes but yttria at this size still shows yttria crystal structure and is therefore not dissolved. The increased refinement of yttria in the cryomilled specimen is believed to be due to less defect recovery resulting in higher strains and a higher strength of the matrix. By this, a higher strength of the matrix at lower milling temperatures enables yttria particles to be refined to smaller sizes. At nanoscale, a vacancy-assisted dissolution of yttria is proposed. Vacancies lower the formation energy of Y and O enriched nanoclusters below the energy of yttria and thus, allowing Y and O to dissolve into these small nanoclusters. During cryomilling, suppressed defect recovery, as well as lower vacancy formation energies result in higher vacancy densities of this fcc FeCrMnNiCo matrix alloy. Higher vacancy densities promote the nucleation and stabilization of smaller nanoclusters. This study provides substantially new insight into the mechanism during mechanical alloying and the effect of temperature in order to increase milling's time-efficiency. The results obtained may help in the future to conduct time-efficient milling processes and targeted design of novel ODS materials especially with fcc matrices.

31

612

Literature:

613

614   [1]   H. Long, S. Mao, Y. Liu, Z. Zhang, X. Han, Microstructural and compositional design of Ni-based

615   single crystalline superalloys — A review, J. Alloys Compd. 743 (2018) 203–220.

616   https://doi.org/10.1016/J.JALLCOM.2018.01.224.

617   [2]   Rolls-Royce, the Jet engine, fifth ed., Rolls-Royce, 1996.

618   [3]   J.H. Perepezko, The hotter the engine, the better, Science (80-.). 326 (2009) 1068–1069.

619   https://doi.org/10.1126/science.1179327.

620   [4]   M.H. Tsai, J.W. Yeh, High-entropy alloys: A critical review, Mater. Res. Lett. 2 (2014) 107–123.

621   https://doi.org/10.1080/21663831.2014.912690.

622   [5]   D.B. Miracle, O.N. Senkov, A critical review of high entropy alloys and related concepts, Acta

623   Mater. 122 (2017) 448–511. https://doi.org/10.1016/j.actamat.2016.08.081.

624   [6]   B. Cantor, I.T.H. Chang, P. Knight, A.J.B. Vincent, Microstructural development in equiatomic

625   multicomponent   alloys,   Mater.   Sci.   Eng.   A.   375–377   (2004)   213–218.

626   https://doi.org/10.1016/j.msea.2003.10.257.

627   [7]   S. Gorsse, M.H. Nguyen, O.N. Senkov, D.B. Miracle, Database on the mechanical properties of

628   high entropy alloys and complex concentrated alloys, Data Br. 21 (2018) 2664–2678.

629   https://doi.org/10.1016/j.dib.2018.11.111.

630   [8]   F. Otto, A. Dlouhý, C. Somsen, H. Bei, G. Eggeler, E.P. George, The influences of temperature

631   and microstructure on the tensile properties of a CoCrFeMnNi high-entropy alloy, Acta Mater.

632   61 (2013) 5743–5755. https://doi.org/10.1016/j.actamat.2013.06.018.

633   [9]   B. Schuh, F. Mendez-Martin, B. Völker, E.P. George, H. Clemens, R. Pippan, A. Hohenwarter,

634   Mechanical properties, microstructure and thermal stability of a nanocrystalline CoCrFeMnNi

635   high-entropy alloy after severe plastic deformation, Acta Mater. 96 (2015) 258–268.

33

636   https://doi.org/10.1016/j.actamat.2015.06.025.

637   [10]   B. Gludovatz, A. Hohenwarter, D. Catoor, E.H. Chang, E.P. George, R.O. Ritchie, A fracture-

638   resistant high-entropy alloy for cryogenic applications, Science (80-.). 345 (2014) 1153–1158.

639   https://doi.org/10.1126/science.1254581.

640   [11]   S. Huang, W. Li, S. Lu, F. Tian, J. Shen, E. Holmström, L. Vitos, Temperature dependent stacking

641   fault energy of FeCrCoNiMn high entropy alloy, Scr. Mater. 108 (2015) 44–47.

642   https://doi.org/10.1016/j.scriptamat.2015.05.041.

643   [12]   N. Stepanov, M. Tikhonovsky, N. Yurchenko, D. Zyabkin, M. Klimova, S. Zherebtsov, A. Efimov,

644   G. Salishchev, Effect of cryo-deformation on structure and properties of CoCrFeNiMn high-

645   entropy alloy, Intermetallics. 59 (2015) 8–17. https://doi.org/10.1016/j.intermet.2014.12.004.

646   [13]   G. Gottstein, Materialwissenschaft und Werkstofftechnik, 4th ed., Springer Vieweg, 2014.

647   [14]   E. Arzt, Size effects in materials due to microstructural and dimensional constraints: A

648   comparative review, J. Econ. Psychol. 50 (2015) 135–137.

649   https://doi.org/10.1016/j.joep.2015.08.002.

650   [15]   S. Yamashita, S. Ohtsuka, N. Akasaka, S. Ukai, S. Ohnuki, Formation of nanoscale complex oxide

651   particles in mechanically alloyed ferritic steel, Philos. Mag. Lett. 84 (2004) 525–529.

652   https://doi.org/10.1080/09500830412331303609.

653   [16]   C. Suryanarayana, Mechanical Alloying and Milling, Prog. Mater. Sci. 46 (2001) 184.

654   [17]   C.C. Koch, R.O. Scattergood, K.M. Youssef, E. Chan, Y.T. Zhu, Nanostructured materials by

655   mechanical alloying: New results on property enhancement, J. Mater. Sci. 45 (2010) 4725–4732.

656   https://doi.org/10.1007/s10853-010-4252-7.

657   [18]   M. Mayer, G. Ressel, J. Svoboda, The Effect of Cryogenic Mechanical Alloying and Milling

658   Duration on Powder Particles ' Microstructure of an Oxide Dispersion Strengthened

34

659   FeCrMnNiCo High-Entropy Alloy, Metall. Mater. Trans. A. (2021).

660   https://doi.org/10.1007/s11661-021-06532-x.

661   [19] M. Brocq, B. Radiguet, S. Poissonnet, F. Cuvilly, P. Pareige, F. Legendre, Nanoscale

662   characterization and formation mechanism of nanoclusters in an ODS steel elaborated by

663   reactive-inspired ball-milling and annealing, J. Nucl. Mater. 409 (2011) 80–85.

664   https://doi.org/10.1016/j.jnucmat.2010.09.011.

665   [20] Z.W. Zhang, J.E. Zhou, S.Q. Xi, G. Ran, P.L. Li, W.X. Zhang, Formation of crystalline and

666   amorphous solid solutions of W–Ni–Fe powder during mechanical alloying, J. Alloys Compd.

667   370 (2004) 186–191. https://doi.org/10.1016/J.JALLCOM.2003.09.012.

668   [21] G. Ressel, D. Holec, A. Fian, F. Mendez-Martin, H. Leitner, Atomistic insights into milling

669   mechanisms in an Fe-Y2O3model alloy, Appl. Phys. A Mater. Sci. Process. 115 (2014) 851–858.

670   https://doi.org/10.1007/s00339-013-7877-y.

671   [22] G. Ressel, S. Primig, H. Leitner, The evolution of y distribution during the processing route of

672   mechanically alloyed iron studied by means of atom probe tomography, Int. J. Mater. Res. 104

673   (2013) 1088–1095. https://doi.org/10.3139/146.110964.

674   [23] Y. Kimura, S. Takaki, S. Suejima, R. Uemori, H. Tamehiro, Ultra Grain Refining and

675   Decomposition of Oxide during Super-heavy Deformation in Oxide Dispersion Ferritic Stainless

676   Steel Powder., ISIJ Int. 39 (1999) 176–182. https://doi.org/10.2355/isijinternational.39.176.

677   [24] N. Oono, S. Ukai, Precipitation of oxide particles in oxide dispersion strengthened (ODS) ferritic

678   steels, Mater. Trans. 59 (2018) 1651–1658. https://doi.org/10.2320/matertrans.M2018110.

679   [25] G. Ressel, P. Parz, S. Primig, H. Leitner, H. Clemens, W. Puff, New findings on the atomistic

680   mechanisms active during mechanical milling of a Fe-Y2O3model alloy, J. Appl. Phys. 115 (2014)

681   1–8. https://doi.org/10.1063/1.4869787.

35

682   [26]   C.L. Fu, M. Krčmar, G.S. Painter, X.Q. Chen, Vacancy mechanism of high oxygen solubility and

683   nucleation of stable oxygen-enriched clusters in Fe, Phys. Rev. Lett. 99 (2007) 1–4.

684   https://doi.org/10.1103/PhysRevLett.99.225502.

685   [27]   Z.W. Zhang, L. Yao, X.L. Wang, M.K. Miller, Vacancy-controlled ultrastable nanoclusters in

686   nanostructured ferritic alloys, Sci. Rep. 5 (2015) 1–9. https://doi.org/10.1038/srep10600.

687   [28]   F.D. Fischer, J. Svoboda, E. Kozeschnik, Interstitial diffusion in systems with multiple sorts of

688   traps, Model. Simul. Mater. Sci. Eng. 21 (2013). https://doi.org/10.1088/0965-

689   0393/21/2/025008.

690   [29]   J. Svoboda, W. Ecker, V.I. Razumovskiy, G.A. Zickler, F.D. Fischer, Kinetics of interaction of

691   impurity   interstitials   with   dislocations   revisited,   Prog.   Mater.   Sci.   (2019).

692   https://doi.org/10.1016/j.pmatsci.2018.10.001.

693   [30]   J. Xu, C.T. Liu, M.K. Miller, H. Chen, Nanocluster-associated vacancies in nanocluster-

694   strengthened ferritic steel as seen via positron-lifetime spectroscopy, Phys. Rev. B - Condens.

695   Matter Mater. Phys. 79 (2009) 1–4. https://doi.org/10.1103/PhysRevB.79.020204.

696   [31]   M.P. Phaniraj, D.I. Kim, J.H. Shim, Y.W. Cho, Microstructure development in mechanically

697   alloyed   yttria   dispersed   austenitic   steels,   Acta   Mater.   57   (2009)   1856–1864.

698   https://doi.org/10.1016/j.actamat.2008.12.026.

699   [32]   H. Hadraba, Z. Chlup, A. Dlouhy, F. Dobes, P. Roupcova, M. Vilemova, J. Matejicek, Oxide

700   dispersion strengthened CoCrFeNiMn high-entropy alloy, Mater. Sci. Eng. A. 689 (2017) 252–

701   256. https://doi.org/10.1016/j.msea.2017.02.068.

702   [33]   F. Dobeš, H. Hadraba, Z. Chlup, A. Dlouhý, M. Vilémová, J. Matějíček, Compressive creep

703   behavior of an oxide-dispersion-strengthened CoCrFeMnNi high-entropy alloy, Mater. Sci. Eng.

704   A. 732 (2018) 99–104. https://doi.org/10.1016/j.msea.2018.06.108.

36

705   [34]   S. Chung, B. Lee, S.Y. Lee, C. Do, H.J. Ryu, The effects of Y pre-alloying on the in-situ dispersoids

706   of ODS CoCrFeMniNi high-entropy alloy, J. Mater. Sci. Technol. 85 (2021) 62–75.

707   https://doi.org/10.1016/j.jmst.2020.11.081.

708   [35]   M.K. Miller, K.F. Russell, D.T. Hoelzer, Characterization of precipitates in MA/ODS ferritic alloys,

709   J. Nucl. Mater. 351 (2006) 261–268. https://doi.org/10.1016/j.jnucmat.2006.02.004.

710   [36]   C.A. Williams, P. Unifantowicz, N. Baluc, G.D.W. Smith, E.A. Marquis, The formation and

711   evolution of oxide particles in oxide-dispersion- strengthened ferritic steels during processing,

712   Acta Mater. 61 (2013) 2219–2235. https://doi.org/10.1016/j.actamat.2012.12.042.

713   [37]   H.G. Brokmeier, M. Müller, P. Pranzas, Klaus, A. Schreyer, P. Staron, The High Energy Materials

714   Science Beamline (HEMS) at PETRA III, Mater. Sci. Forum. 772 (2013) 57–61.

715   https://doi.org/https://doi.org/10.4028/www.scientific.net/MSF.772.57.

716   [38]   B.E. Warren, X-ray studies of deformed metals, Prog. Met. Phys. 8 (1959) 147–202.

717   https://doi.org/10.1016/0502-8205(59)90015-2.

718   [39]   W.L. Bragg, The Structure of Some Crystals as Indicated by their Diffraction of X-rays. Crystals

719   as Indicated by their Diffraction of X-rays, Proc. R. Soc. Lond. A (1913) 248–277.

720   https://doi.org/http://doi.org/10.1098/rspa.1913.0083.

721   [40]   C. Gammer, V. Burak Ozdol, C.H. Liebscher, A.M. Minor, Diffraction contrast imaging using

722   virtual apertures, Ultramicroscopy. 155 (2015) 1–10.

723   https://doi.org/10.1016/J.ULTRAMIC.2015.03.015.

724   [41]   P.E. Blöchl, PAW, Phys. Rev. B. 50 (1994) 17953.

725   [42]   G. Kresse, J. Hafner, Ab initio molecular dynamics for open-shell transition metals, Phys. Rev. B.

726   48 (1993) 13115–13118. https://doi.org/10.1103/PhysRevB.48.13115.

727   [43]   G. Kresse, J. Furthmüller, Efficiency of ab-initio total energy calculations for metals and

728   semiconductors using a plane-wave basis set, Comput. Mat. Sci. 6 (1996) 15.

729   https://doi.org/10.1016/0927-0256(96)00008-0.

730   [44] O.E. Peil, A. V. Ruban, B. Johansson, Self-consistent supercell approach to alloys with local

731   environment effects, Phys. Rev. B. 85 (2012) 165140.

732   https://doi.org/10.1103/PhysRevB.85.165140.

733   [45] L. Vitos, Total-energy method based on the exact muffin-tin orbitals theory, Phys. Rev. B. 64

734   (2001) 14107. https://doi.org/10.1103/PhysRevB.64.014107.

735   [46] L. Vitos, Computational Quantum Mechanics for Materials Engineers: The EMTO Method and

736   Applications, Springer, 2007.

737   [47] I. Abrikosov, A. Niklasson, S. Simak, B. Johansson, A. Ruban, H. Skriver, Order- N Green's

738   Function Technique for Local Environment Effects in Alloys, Phys. Rev. Lett. 76 (1996) 4203–

739   4206. https://doi.org/10.1103/PhysRevLett.76.4203.

740   [48] P. Soven, Coherent-Potential Model of Substitutional Disordered Alloys, Phys. Rev. 156 (1967)

741   809–813. https://doi.org/10.1103/PhysRev.156.809.

742   [49] B.L. Gyorffy, Coherent-Potential Approximation for a Nonoverlapping-Muffin-Tin-Potential

743   Model of Random Substitutional Alloys, Phys. Rev. B. 5 (1972) 2382–2384.

744   https://doi.org/10.1103/PhysRevB.5.2382.

745   [50] A. V. Ruban, M. Dehghani, Atomic configuration and properties of austenitic steels at finite

746   temperature :, Phys. Rev. B. 94 (2016) 104111. https://doi.org/10.1103/PhysRevB.94.104111.

747   [51] A. V. Ruban, Thermal vacancies in random alloys in the single-site mean-field approximation,

748   Phys. Rev. B. 93 (2016) 1–5. https://doi.org/10.1103/PhysRevB.93.134115.

749   [52] V.I. Razumovskiy, D. Scheiber, O. Peil, A. Stark, G. Ressel, A. Stark, M. Mayer, Thermodynamics

750   of Vacancy Formation in the CoCrFeMnNi High Entropy Alloy from DFT Calculations, Asp. Min.

38

751   Miner. Sci. 8 (2022). https://doi.org/10.31031/AMMS.2022.08.00069.

752 [53] H. Zhang, M.J. Gorley, K.B. Chong, M.E. Fitzpatrick, S.G. Roberts, P.S. Grant, An in situ powder

753   neutron diffraction study of nano-precipitate formation during processing of oxide-dispersion-

754   strengthened ferritic steels, J. Alloys Compd. 582 (2014) 769–773.

755   https://doi.org/10.1016/j.jallcom.2013.08.069.

756 [54] A. Ruban, V.I. Razumovskiy, Spin-wave method for the total energy of paramagnetic state, Phys.

757   Rev. B. 85 (2012) 174407. https://doi.org/10.1103/PhysRevB.85.174407.

758 [55] M. Elsayed, R. Krause-Rehberg, C. Eisenschmidt, N. Eißmann, B. Kieback, Defect Study in

759   CoCrFeMnNi High Entropy Alloy by Positron Annihilation Lifetime Spectroscopy, Phys. Status

760   Solidi Appl. Mater. Sci. 215 (2018) 1–4. https://doi.org/10.1002/pssa.201800036.

761 [56] S. Abhaya, R. Rajaraman, S. Kalavathi, G. Amarendra, Positron annihilation studies on FeCrCoNi

762   high entropy alloy, J. Alloys Compd. 620 (2015) 277–282.

763   https://doi.org/10.1016/J.JALLCOM.2014.09.137.

764 [57] H. Ohkubo, Z. Tang, Y. Nagai, M. Hasegawa, T. Tawara, M. Kiritani, Positron annihilation study

765   of vacancy-type defects in high-speed deformed Ni, Cu and Fe, Mater. Sci. Eng. A. 350 (2003)

766   95–101. https://doi.org/10.1016/S0921-5093(02)00705-0.

767 [58] I.C. Albayrak, S. Basu, A. Sakulich, O. Yeheskel, M.W. Barsoum Z Z, Elastic and Mechanical

768   Properties of Polycrystalline Transparent Yttria as Determined by Indentation Techniques,

769   (n.d.). https://doi.org/10.1111/j.1551-2916.2010.03669.x.

770 [59] K.H. Chung, J. He, D.H. Shin, J.M. Schoenung, Mechanisms of microstructure evolution during

771   cryomilling in the presence of hard particles, Mater. Sci. Eng. A. 356 (2003) 23–31.

772   https://doi.org/10.1016/S0921-5093(02)00833-X.

773 [60] V.A. Shabashov, A. V. Litvinov, V. V. Sagaradze, K.A. Kozlov, N.F. Vil'Danova, Mechanosynthesis

774   of ODS alloys with an fcc lattice on the basis of the Fe-Ni system, Phys. Met. Metallogr. 105

775   (2008) 157–167. https://doi.org/10.1007/s11508-008-2008-2.

776 [61] Y. Ashkenazy, N.Q. Vo, D. Schwen, R.S. Averback, P. Bellon, Shear induced chemical mixing in

777   heterogeneous   systems,   Acta   Mater.   60   (2012)   984–993.

778   https://doi.org/10.1016/j.actamat.2011.11.014.

779 [62] H. Zhao, C.L. Fu, M. Krcmar, M.K. Miller, Effect of strain on the stabilization of oxygen-enriched

780   nanoclusters in Fe-based alloys, Phys. Rev. B - Condens. Matter Mater. Phys. 84 (2011) 2–6.

781   https://doi.org/10.1103/PhysRevB.84.144115.

782 [63] P. Scherrer, Bestimmung der inneren Struktur und der Größe von Kolloidteilchen mittels

783   Röntgenstrahlen, Kolloidchem. Ein Lehrb. 277 (1912) 387–409. https://doi.org/10.1007/978-3-

784   662-33915-2_7.

785 [64] M. Brocq, B. Radiguet, J.M. Le Breton, F. Cuvilly, P. Pareige, F. Legendre, Nanoscale

786   characterisation and clustering mechanism in an Fe–Y2O3 model ODS alloy processed by

787   reactive   ball   milling   and   annealing,   Acta   Mater.   58   (2010)   1806–1814.

788   https://doi.org/10.1016/J.ACTAMAT.2009.11.022.

789 [65] L. Dai, Y. Liu, Z. Dong, Size and structure evolution of yttria in ODS ferritic alloy powder during

790   mechanical milling and subsequent annealing, Powder Technol. 217 (2012) 281–287.

791   https://doi.org/10.1016/j.powtec.2011.10.039.

792 [66] M. Saber, W. Xu, L. Li, Y. Zhu, C.C. Koch, R.O. Scattergood, Size effect of primary Y2O3 additions

793   on the characteristics of the nanostructured ferritic ODS alloys: Comparing as-milled and as-

794   milled/annealed   alloys   using   S/TEM,   J.   Nucl.   Mater.   452   (2014)   223–229.

795   https://doi.org/10.1016/j.jnucmat.2014.05.014.

796 [67] D.B. Witkin, E.J. Lavernia, Synthesis and mechanical behavior of nanostructured materials via

40

797   cryomilling, Prog. Mater. Sci. 51 (2006) 1–60. https://doi.org/10.1016/j.pmatsci.2005.04.004.

798   [68]   M. Kiritani, Y. Satoh, Y. Kizuka, K. Arakawai, Y. Ogasawara, S. Arai, Y. Shimomura, Anomalous

799   production of vacancy clusters and the possibility of plastic deformation of crystalline metals

800   without   dislocations,   Philos.   Mag.   Lett.   79   (1999)   797–804.

801   https://doi.org/10.1080/095008399176616.

802   [69]   H.Z. Fang, S.L. Shang, Y. Wang, Z.K. Liu, D. Alfonso, D.E. Alman, Y.K. Shin, C.Y. Zou, A.C.T. Van

803   Duin, Y.K. Lei, G.F. Wang, First-principles studies on vacancy-modified interstitial diffusion

804   mechanism of oxygen in nickel, associated with large-scale atomic simulation techniques, J.

805   Appl. Phys. 115 (2014). https://doi.org/10.1063/1.4861380.

806